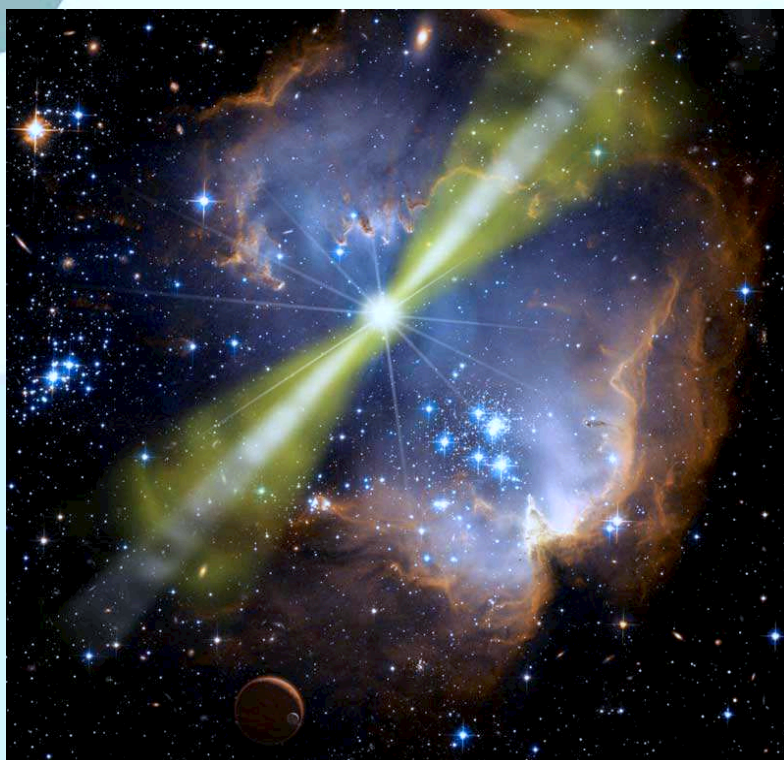


Spectroscopy of High Redshift Sightlines



Thesis submitted for the degree of
Doctor of Philosophy (PhD)
on *February 15, 2011*
Defended in Copenhagen on *April, 2011*

Tayyaba Zafar

Supervisor: Darach Watson
Co-Supervisor: Johan P. U. Fynbo

Dark Cosmology Centre, Niels Bohr Institute
Faculty of Science, University of Copenhagen

www.dark-cosmology.dk

SPECTROSCOPY OF HIGH REDSHIFT SIGHTLINES

TAYYABA ZAFAR

Dissertation
Submitted for the Degree

DOCTOR OF PHILOSOPHY

Dark Cosmology Centre
Niels Bohr Institute
Faculty of Science
University of Copenhagen

Submission: *February 15th, 2011*

Defence: *April, 2011*

Supervisor: *Assoc. Prof. Dr. Darach Watson*

Co-Supervisor: *Assoc. Prof. Dr. Johan P. U. Fynbo*

Opponents: XXX
XXX

CONTENTS

Contents	iii
Acronyms	ix
List of Figures	xi
List of Tables	xiv
Acknowledgments	xvii
Abstract	xix
1 Introduction	3
1.1 When history made the future	3
1.2 The Compton Gamma-Ray Observatory	4
1.3 BeppoSAX and HETE	4
1.4 The <i>Swift</i> revolution	5
1.5 Progenitors	7
1.5.1 Long duration GRBs	7
1.5.2 Short duration GRBs	8
1.6 Fireball model	10
1.7 GRB afterglows	11
1.7.1 Dark GRBs	13
1.8 Quasars	13
1.8.1 Damped $\text{Ly}\alpha$ absorbers	14
1.8.2 $\text{Ly}\alpha$ blobs	16
1.9 Dust extinction	16
1.9.1 Dust at high redshift	19
1.10 Structure of the thesis	20

2	SED modelling and absorption line spectroscopy	21
2.1	GRBs as cosmological probes	21
2.2	Spectral Energy Distribution	22
2.2.1	X-ray data	22
2.2.2	Optical/NIR data	23
2.3	SED modelling	25
2.4	Dust models	26
2.4.1	Supernova extinction curve	28
2.5	Absorption line systems	30
2.5.1	Metallicities	32
2.6	X-shooter data reduction	33
3	Multi Epoch SED analysis of GRB 050904 at $z \sim 6.3$	37
3.1	Introduction	38
3.2	Multi-wavelength observations of the afterglow	39
3.2.1	X-ray analysis	39
3.2.2	Near-IR and optical imaging	39
3.2.3	Grism spectroscopy	41
3.3	SED analysis	41
3.3.1	Afterglow compound SED	41
3.3.2	Comparing the z -band filter responses	42
3.4	Discussion	45
3.4.1	Dust in the GRB 050904 host galaxy	45
3.4.2	X-ray absorption	47
3.4.3	Gas-to-dust ratio	48
3.4.4	The origin of dust in the early Universe	49
3.5	Conclusions	49
4	Dust extinction at high redshift	51
4.1	Introduction	52
4.2	Multi-wavelength data	52
4.3	Results	54
4.3.1	Multi epoch SED of GRB 050904	55
4.3.2	Multi epoch SED of GRB 080913	55
4.3.3	Multi epoch SED of GRB 090423	57
4.4	Discussion	57
4.5	Conclusions	61
5	The extinction curves of star-forming regions from $z = 0.1$ to 6.7	63
5.1	Introduction	65
5.2	Multi-wavelength observations and data reduction	67

5.2.1	Ensemble selection criteria	67
5.2.2	Optical spectroscopy	67
5.2.3	Photometry	68
5.2.4	X-ray data	68
5.3	Data analysis	72
5.3.1	Dust models	72
5.4	Results	74
5.4.1	The SED of the afterglow	74
5.4.2	Dust extinction	76
5.5	Discussion	76
5.5.1	The 2175 Å feature	76
5.5.2	Constraints on R_V	79
5.5.3	Gas-to-dust ratios	82
5.5.4	Metals-to-dust ratios	85
5.5.5	The effect of metallicity	87
5.6	Conclusions	90
5.7	Details on the spectroscopic GRB afterglow sample	93
5.7.1	GRB 050401	93
5.7.2	GRB 050730	93
5.7.3	GRB 050824	93
5.7.4	GRB 060115	94
5.7.5	GRB 060512	94
5.7.6	GRB 060614	95
5.7.7	GRB 060707	95
5.7.8	GRB 060708	95
5.7.9	GRB 060714	96
5.7.10	GRB 060729	96
5.7.11	GRB 060904B	96
5.7.12	GRB 060906	97
5.7.13	GRB 060926	97
5.7.14	GRB 060927	97
5.7.15	GRB 061007	98
5.7.16	GRB 061021	98
5.7.17	GRB 061110A	99
5.7.18	GRB 061110B	99
5.7.19	GRB 070110	99
5.7.20	GRB 070125	99
5.7.21	GRB 070129	100
5.7.22	GRB 070318	100
5.7.23	GRB 070506	101

5.7.24	GRB 070611	101
5.7.25	GRB 070721B	101
5.7.26	GRB 070802	101
5.7.27	GRB 071020	102
5.7.28	GRB 071031	102
5.7.29	GRB 071112C	103
5.7.30	GRB 071117	103
5.7.31	GRB 080210	103
5.7.32	GRB 080319B	104
5.7.33	GRB 080520	104
5.7.34	GRB 080605	105
5.7.35	GRB 080607	105
5.7.36	GRB 080707	106
5.7.37	GRB 080721	106
5.7.38	GRB 080805	106
5.7.39	GRB 080905B	107
5.7.40	GRB 080913	107
5.7.41	GRB 080916A	107
5.7.42	GRB 080928	108
5.8	Additional notes	128
5.8.1	Photometric data	128
5.8.2	Spectral change	134
5.8.3	Constraining R_V	140
6	Spectroscopic studies of QSO pair Q 0151+048	145
6.1	Introduction	147
6.2	Observations and data reduction	148
6.2.1	The NOT/ALFOSC data	148
6.2.2	VLT/X-shooter data	149
6.3	Results	150
6.3.1	The NOT/ALFOSC data	150
6.3.2	VLT/X-shooter data	152
6.4	Absorption line analysis	160
6.4.1	Absorption lines of the DLA system	161
6.4.2	Photo-ionization model of the DLA	163
6.4.3	Intervening absorbers	165
6.5	Discussion: What is the Q 0151+048A&B/DLA/Ly α -blob system?	166
6.5.1	Geometry of the system	167
6.5.2	Dynamical state of the system	169
6.5.3	Black Hole and Dark Matter Halo masses	169

6.6	Conclusions	170
7	Conclusions and future prospects	173
7.1	Conclusions	173
7.2	Future prospects	177
7.2.1	Extension of the sample	177
7.2.2	X-shooter	177
7.2.3	Possible mass-dust relation	178
7.2.4	Metal rich GRBs	179
	Bibliography	181
	co-Author statements	199

ACRONYMS

2MASS	Two micron all sky survey
AGB	Asymptotic giant branch
AGN	Active galactic nuclei
ALFOSC	Andalucia faint object spectrograph and camera (installed at NOT)
BAL QSO	Broad absorption line quasar
BAT	Burst alert telescope (onboard <i>Swift</i>)
BH	Black hole
DLA	Damped Lyman alpha absorber
DM	Dark matter
ESO	European southern observatory
EW	Equivalent width
FOCAS	Faint object camera and spectrograph (installed at Subaru telescope)
FORS1/2	Focal reducer and low dispersion spectrograph 1/2 (installed at VLT)
FWHM	Full-width half maximum
GRB	Gamma-ray Burst
IR	Infrared
IGM	Intergalactic medium
ISM	Interstellar medium
LAE	Lyman alpha emitter
LBG	Lyman break galaxy
LMC	Large Magellanic Cloud
MIDAS	Munich image data analysis system
MW	Milky Way
NIR	Near-infrared
NOT	Nordic Optical Telescope (La Palma/Spain)
PDLA	Proximate damped Lyman alpha absorber
PSF	Point Spread Function
QSO	Quasi-stellar Object
SDSS	Salon digital sky survey
SED	Spectral energy distribution

SINFONI	Spectrograph using integral field observations in the near-infrared
SMC	Small Magellanic Cloud
SN	Supernova
ToO	Target-of-Opportunity (proposal type/fast observation mode)
UV	Ultra violet
UKIRT	United Kingdom infrared telescope
VLT	Very Large Telescope (Paranal/Chile)
WFCAM	Wide field infrared camera (Imaging camera on UKIRT)
XRT	X-ray telescope (onboard <i>Swift</i>)

LIST OF FIGURES

1.1	Sky positions for all GRBs detected during the CGRO/BATSE mission	4
1.2	Satellites dedicated to GRB study	6
1.3	Long and short duration GRBs	8
1.4	Optical afterglow of GRB 050709	9
1.5	The canonical fireball model	11
1.6	Synchrotron emission spectra	12
1.7	Distribution of H I column densities	15
1.8	The Horsehead Nebula	16
1.9	Absorption and scattering of light by dust	18
2.1	X-ray Lightcurves	23
2.2	<i>J</i> and <i>I</i> band lightcurve of GRB 0909026A	24
2.3	UVOT filters lightcurves of GRB 080605	25
2.4	Local Group extinction curves	27
2.5	SN-origin extinction curves	28
2.6	Curve of growth	31
2.7	H I column density of GRB 050904	32
2.8	NOT spectra of Q 0151+048	34
3.1	Optical spectrum of GRB 050904 with different <i>z</i> -band transmission curves	42
3.2	Multi epoch SED of GRB 050904	44
3.3	Multi epoch NIR SED of GRB 050904 fitted with SN and SMC dust models	48
4.1	Multi epoch SED of GRB 080913	55
4.2	Optical/NIR SED of GRB 080913 consistent with a power-law	56
4.3	Multi epoch SED of GRB 090423	57
4.4	Redshift distribution of spectroscopic GRB sample	60
5.1	$\Delta\beta$ against the X-ray spectral slope	75
5.2	Distribution of A_V of the GRB sample	78
5.3	A_V against spectroscopically measured NH I	81

5.4	Visual extinction against UV metal abundances	83
5.5	A_V measurements versus $N_{H,X}$ for the GRB sample	84
5.6	$N_{H,X}/A_V$ distribution of spectroscopic GRB sample	86
5.7	Restframe A_V and $(N_{H,X}/A_V)$ for GRB sample	88
5.8	Restframe A_V measurements versus GRB metallicity	89
5.9	Gas-to-dust ratio versus metallicity for GRB sub sample	91
5.10	Metals-to-dust ratio versus metallicity for the GRB sub sample.	92
5.11	SEDs of GRB afterglow sample	109
5.11	110
5.11	111
5.11	112
5.11	113
5.11	114
5.11	115
5.11	116
5.11	117
5.11	118
5.11	119
5.12	Absolute extinction curves of the GRB sample	120
5.12	121
5.12	122
5.12	123
5.12	124
5.12	125
5.12	126
5.12	127
5.13	Contour plots of χ^2 as a function of A_V and $\Delta\beta$	135
5.13	Continued.	136
5.14	Contour plots of χ^2 as a function of A_V and ν_{break}	137
5.14	Continued.	138
5.15	$\Delta\beta$ versus optical slope β_1	139
5.16	$\Delta\beta$ versus cooling break ν_{break}	139
5.17	Contour plots of χ^2 as a function of A_V and R_V	141
5.17	Continued.	142
5.17	Continued.	143
5.18	Metals-to-dust ratios $(N_{H,X}/A_V)$ versus redshift	144
5.19	$N_{H,X}$ against UV metal abundances	144
6.1	NOT and X-shooter slit positions for the observation of Q0151+048	149
6.2	PSF subtracted spectrum of the Ly α blob	151

6.3	Velocity profile of the DLA	152
6.4	X-shooter spectra of Q 0151+048	153
6.5	Q 0151+048 H α emission lines	156
6.6	Q 0151+048A H β emission line	157
6.7	X-shooter PSF subtraction of Q 0151+048	161
6.8	Voigt profile fitting of the DLA	162
6.9	ΔV determination of the DLA	164
6.10	Metallicity vs. velocity width relation and DLA	165
6.11	Cloudy model calculation for DLA at $z = 1.934$	166
6.12	Rotation curve of Ly α blob and other spiral galaxy	167
6.13	Density profile of Q 0151+048 DM halo	170
6.14	X-shooter UVB-arm spectra of Q 0151+048	172
7.1	Equivalent widths of Fe II versus Zn II	178
7.2	Visual extinction versus Zn II equivalent width	179

LIST OF TABLES

3.1	Best Fit parameters of GRB 050904 SED at different epochs	46
4.1	Best fit parameters of high- z GRB afterglow SEDs	53
5.1	Complete log of spectroscopic GRB sample	69
5.2	Results of fits to the afterglow SEDs	71
5.3	Parameters of the best fit with the SMC extinction curve	77
5.4	Parameters of the best fit with the FM extinction model	78
5.5	GRB sample X-ray and optical derived column densities	80
5.6	GRB sub-sample metallicities	90
5.7	Photometric data for GRB 050401	129
5.8	Photometric data for GRB 060512	129
5.9	Photometric data for GRB 060614	129
5.10	Photometric data for GRB 060708	129
5.11	Photometric data for GRB 060714	129
5.12	Photometric data for GRB 060729	129
5.13	Photometric data for GRB 060906	129
5.14	Photometric data for GRB 060927	129
5.15	Photometric data for GRB 061007	129
5.16	Photometric data for GRB 061021	129
5.17	Photometric data for GRB 070110	129
5.18	Photometric data for GRB 070125	130
5.19	Photometric data for GRB 070129	130
5.20	Photometric data for GRB 070318	130
5.21	Photometric data for GRB 070802	130
5.22	Photometric data for GRB 071020	130
5.23	Photometric data for GRB 071031	130
5.24	Photometric data for GRB 071112C	130
5.25	Photometric data for GRB 080210	130
5.26	Photometric data for GRB 080319B	130
5.27	Photometric data for GRB 080520	130

5.28	Photometric data for GRB 080605	131
5.29	Photometric data for GRB 080607	131
5.30	Photometric data for GRB 080721	131
5.31	Photometric data for GRB 080913	131
5.32	Photometric data for GRB 080928	131
5.33	Results of the SED fits	132
6.1	Log of spectroscopic observation of Q 0151+048	149
6.2	Emission line redshifts of Q 0151+048	155
6.3	Voigt profile fitting measurements of the DLA	158
6.4	BH and DM masses of Q 0151+048	168

ACKNOWLEDGMENTS

*As we express our gratitude, we must
never forget that the highest appreciation
is not to utter words, but to live by them.
John F. Kennedy (1917-1963)*

Three years - time flew very fast - but contribution of many people made my PhD a wonderful experience. I owe my deepest gratitude to many people who helped me to reach this goal, my PhD.

First of all, I would like to thank my marvelous advisor Darach Watson for taking me as his PhD student, for guidance, assistance and tireless support throughout my time at DARK. I appreciate him for his excellent advices, many motivating discussions and words of wisdom. I am enormously indebted to him for his kind support in the last six months while I was sick and he put all his energies to make life easier for me in view of my ill health. I will not be able to forget his phrase “*I hate to do this to you*” which he used for the analysis and re-analysis of our GRB sample during the last couple of months. We both came up with something that we forgot or interesting to implement on the data. He actually re-hated and I re-did it for a number of times. Thank you for everything!

A very special thanks to my co-supervisor, Johan Fynbo, a fabulous Dane, the fantastic astronomer. I went to him with the most irritating problems and he solved them in the blink of an eye. I will always be indebted to him for his extensive help and relentless support.

I’m grateful to all the people at DARK for their help and support: Daniele Malesani, with 250 GRB memory all filled with references and interesting ideas; Jens Hjorth, who introduced to me the theory of non-speculation; Anja Andersen, for encouraging me with a pleasant smile and motivating words; Marianne Vestergaard, for explaining to me the difference between a presentation and a book; Sune Toft, for interesting discussions; Paul Vreeswijk for exciting ideas; Kristian Pedersen and Steen Hansen for their ever inspiring words; my office mates, Radek Wojtak and Martina Falco for nice chats; Antonio de Ugarte Postigo, for helpful discussions. I also thank the DARK administrative staff: Michelle Løkkegaard, Sarah Pearson and Corinne Toulouse-Aastrup for

making all administrative matters as smooth as silk; Julie Meier Hansen for the endless kindness; Brian Lindgren Jensen for fixing stupid computer problems. I am also thankful to my collaborators Palle Møller and Cédric Ledoux for having patience during the course of our project and explaining me the emission and absorption line fitting. I'm deeply grateful to Andrew J. Levan, Nial Tanvir and Rhaana Starling for their support. I jointly thank DARK folks for always being friendly and creating a lively work place. I'm very happy to have met them all. All in all if these people were not there it would have been impossible for a person like me to have stayed here for three years and remained sane, in short these would have been the longest three years of my life if not for them.

Thank you DARK for turning me into an astronomer.

Special thanks to my parents, Rai Zafar Ali and Naseem Zafar, for all their love, affection, assistance and support in my life and career. I particularly thank my youngest brother Farzduk Mehdi who is the joy of my life, he usually remained online and this is how we shared our bond of love during these three years, Atyab Mehdi who is now always comparing my life in Copenhagen with his life in London and telling how much better off I am. Bundle of thanks to my other siblings Qudsia, Faliha, Samana and Wila for endless love, I would not imagine life without them. I appreciate Dr. Mujahid Kamran for motivating me throughout my PhD life. I will always be grateful to my uncles Syed Muhammad Hassan and Muhammad Hussain Akbar who always encouraged me and pushed me to the limits where I achieved the success which in their words is my right. I'm sure I forgot someone but it is not on purpose.

Last but not the least I would like to acknowledge the financial support from the Faculty of Science, University of Copenhagen and the Dark Cosmology Centre.

Thank you all!

ABSTRACT

This thesis deals with the absorption studies of two kinds of cosmological objects: gamma-ray bursts (GRBs) and quasars (QSO), using spectroscopy and spectral energy distribution (SED) analysis. GRBs are the most powerful explosions in the Universe. After the discovery of these cosmological events in 1967, a lot of progress has been made in investigating their properties which divided them into two subcategories of long and short bursts. Both GRB classes have different origins and properties. Long duration GRBs are signposts of star formation due to their association with the deaths of short-lived, massive stars. The launch of the *Swift* satellite in 2004, mainly devoted to GRB observations, has marked a dramatic improvement in our understanding of GRB physics. The initial burst of γ -rays is followed by slowly fading emission at lower frequencies, which is termed the “afterglow”. GRB afterglows are excellent and sensitive probes of gas and dust in star-forming galaxies at all epochs. The X-ray to optical/near-infrared SED analysis of GRB afterglows can reveal intrinsic host galaxy properties. The brightness of these transient sources and their occurrence in young, blue galaxies make them excellent tools to study star forming regions in the distant Universe.

The first chapter presents an introduction to the history of GRB research, different progenitor models and afterglow phases. The chapter also provides an introduction to the damped $\text{Ly}\alpha$ absorbers (DLAs) usually seen in the spectra of background QSOs. The second chapter summarizes the different dust models used for afterglow SED modeling. It also describes absorption line fitting techniques.

The third and fourth chapter provide the SED analysis of all known $z > 6$ GRB afterglows: GRB 090423, 080913 and 050904, at $z = 8.2$, 6.69, and 6.295, respectively. A completely new reduction of the available photometric, spectroscopic and the X-ray data is made and multi-epoch SEDs are generated. The X-ray-NIR SEDs are jointly fitted with single and broken power-laws including dust models. This provides information about the kind of dust and how much dust is present at these cosmic epochs. For GRB 050904, the claimed evidence for unusual (supernova (SN)-origin) dust in its host galaxy is addressed by a thorough SED analysis. I find that the afterglow SED at all times can be reproduced without dust, and at 1.25 days in particular, strict limits to the extinction can be set. The data of GRB 090423 were well fit with no dust using a broken power-law. There is possible evidence for a low level of ($A_V = 0.12 \pm 0.03$)

extinction in GRB 080913. In this analysis I find no GRBs at high redshift with $A_V > 0.1$. Comparison with my lower redshift sample where the average extinguished burst has $A_V \sim 0.3$, suggests a decrease in dust content in star-forming environments at $z \geq 4$ despite the very small statistics.

The fifth chapter focuses on the SED analysis of a sample of 41 GRBs using spectroscopy. This is the largest ever sample studied to derive absolute extinction curves outside the Local Group. The chapter discusses the spectral shapes of GRBs and their consistency with the synchrotron emission model. In our spectroscopic GRB sample, a spectral break between the X-ray and optical wavelengths is found for 22 cases. More than 95% of this subsample is well described by a spectral change of $\Delta\beta = \beta_2 - \beta_1 = 0.5$ as predicted by the fireball model. In this chapter, I also examine GRB circumburst environments by comparing their gas-to-dust and metals-to-dust ratios, and metallicities to that of Local Group environments. The gas-to-dust ratios of GRBs display a large scatter suggesting that a large fraction of gas is ionized by the GRB. The metals-to-dust ratios of GRB environments are found to be 3–30 times higher than the Local Group. GRBs span a range of metallicities from approximately solar to $\sim 1/100$ solar, hinting that this remarkable variation in metals-to-dust ratios are not due to any metallicity effects.

63% of the sample is well fits with SMC-type extinction. Three of approximately twelve objects where a 2175 Å bump could have been detected had a bump. This fraction of 25%, may represent a lower limit: the spectra with a bump are all more extinguished than any other burst in our sample ($A_V > 1$), suggesting that this type of extinction is in fact common and we may be missing many more highly extinguished events with bumps because of selection effects and sample incompleteness.

Chapter six discusses the interesting case of the QSO pair Q 0151+048. The complex system brings together several types of objects at $z \sim 2$, which are usually seen separately on the sky: a QSO pair, a Ly α blob, and a DLA. In the spectrum of the brighter member of this pair, Q 0151+048A, a DLA is observed at a higher redshift than the QSO. I seek to constrain the geometry of the system and understand the possible relations between the DLA, the Ly α blob, and the two QSOs. We measure systemic redshifts of $z_{\text{em(A)}} = 1.92924 \pm 0.00036$ and $z_{\text{em(B)}} = 1.92863 \pm 0.00042$ from the H β and H α emission lines, respectively. In other words, the two QSOs have identical redshifts within 2σ . Line-profile fitting techniques are employed, to measure the metallicity of the DLA, and photo-ionization modeling was done to characterize the DLA further. Residual continuum in the DLA trough is detected which is interpreted as emission from the host galaxy of Q 0151+048A. No absorption is detected in the spectrum of Q 0151+048B at or near the redshift of the DLA which implies that the spatial extent of the DLA must be smaller than about 28 kpc.

Chapter seven proposes conclusions and directions for future work.

*To the most wonderful parents
on this planet Naseem Zafar
and Rai Zafar Ali and
my brother Farzduk Mehdi*

1

INTRODUCTION

1.1 WHEN HISTORY MADE THE FUTURE

On August 5, 1963, the Nuclear Test Ban Treaty was signed by the governments of the Soviet Union, the United Kingdom and the United States in Moscow. The treaty prohibited nuclear weapon tests inside and outside the Earth's atmosphere as well as under water. The main motivation behind this treaty was to slow down the growing arms race and to save Earth's atmosphere from the nuclear fallout. The US suspected that the Soviet Union might attempt to conduct secret nuclear explosions without being noticed. To monitor this the United States designed a space mission capable of searching for the traces of nuclear explosions by measuring the γ -radiation pulses produced by the explosion. The mission was started in 1965 with the launch of the Vela 3 and Vela 4 military satellites designed by the team of the Los Alamos Scientific Laboratory in New Mexico. With improved detectors, Vela 5a and 5b, the successors of Vela3 and 4, were launched in May 1969. These satellites found no illegal nuclear explosion testing but led to a scientific discovery.

On 1967 July 2 at 14:19 UT, the Vela 3 and 4 spacecrafts detected mysterious double peaked gamma ray flashes. These γ -ray pulses came from the sky rather than the Earth or the moon. The team of the Los Alamos Scientific Laboratory led by Ray Klebesadel and Roy Olson filed the data for further investigation. Rough estimates of the sky positions were determined from the arrival time differences of the γ -ray flashes at both instruments. This clearly excluded any solar or terrestrial origin of these pulses. It was realized very soon that these were the products of extremely complicated cosmic phenomena. This was the detection of the first gamma-ray burst, GRB 670702. The results were published in 1973 by Klebesadel et al. (1973). In total sixteen GRBs were detected by the four Vela military satellites. GRBs are named by their discovery year, month, date and an alphabetical letter in cases where several bursts are detected per day. Since 2010, the name of the first burst of every day always has a letter 'A'.

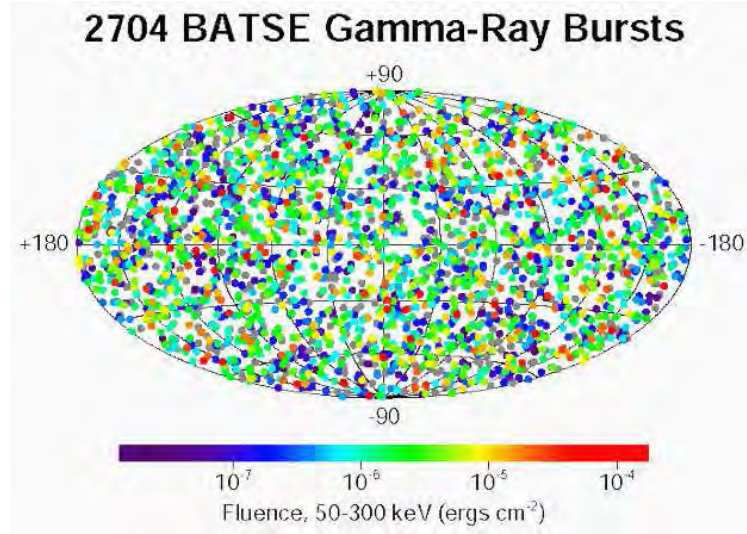


Figure 1.1: Angular distribution of GRBs detected during the nine years of the CGRO/BATSE mission. The burst positions are color-coded based on their fluence. Bright bursts appear in red and faint bursts in purple.

1.2 THE COMPTON GAMMA-RAY OBSERVATORY

The major advances in this subject began with the launch of the Compton Gamma Ray Observatory (CGRO) in April 1991 by NASA (Fishman et al. 1989; Fishman & Meegan 1995), with the Burst and Source Transient Experiment (BATSE) and the Energetic Gamma Ray Experiment Telescope (EGRET) onboard. CGRO with BATSE covered the energy range from 20 keV to ~ 2 MeV and EGRET covered 20 MeV to 30 GeV. BATSE consisted of eight identical detectors, one at each corner of the spacecraft. Even with a large detector area and high sensitivity, BATSE could still determine the position of a GRB only down to a few degrees. The all sky survey indicated that GRBs are isotropically distributed on the sky with no direction biases (see Fig. 1.1; Meegan et al. 1993; Briggs et al. 1993, 1996). The data showed that GRBs are not concentrated in the Galactic plane and must come from far outside the Milky Way (Piran 1992; Paczynski 1995). BATSE also found that GRBs come in two different classes, short and long duration (see Sect. 1.5 for more detail). The CGRO mission also provided a wealth of γ -ray lightcurves and spectra. Over nine years around 3000 bursts were registered with a typical detection rate of ~ 1 burst day^{-1} .

1.3 BEPPoSAX AND HETE

Gamma rays alone did not provide enough information, therefore searches were made to detect radiation from the bursts at other wavelengths. The next major step ahead was made with the launch of the BeppoSAX satellite on 30 April 1996 (Boella et al.

1997). BeppoSAX was operated by the Italian Space Agency with the participation of the Netherlands Space Agency. BeppoSAX was named in honour of the Italian physicist Giuseppe (Beppo) Occhialini and SAX stands for Satellite for X-ray astronomy. BeppoSAX helped to find more precise locations for GRBs and made GRB follow-up observations possible. On 28 February, 1997 the “afterglow” phenomenon was discovered with BeppoSAX with the first observation of the X-ray afterglow of GRB 970228 at $z = 0.695$ (Costa et al. 1997). The redshift estimate was based on emission lines from the host galaxy. The distribution of the position enabled optical and radio follow-up with the William Herschel Telescope (WHT), the Westerbork Radio Telescope and the Very Large Array (VLA). GRB 970508 was also detected by BeppoSAX. A spectrum of the afterglow was obtained with the Keck telescope and the redshift determined to be $z = 0.8349$ from absorption lines in the afterglow. The upper limit on the redshift based on the absence of a Ly α forest was $\lesssim 2.3$ (Metzger 1997; Metzger et al. 1997). The redshift determinations allowed estimates to be made of the distances and energetics of GRBs. Following the first optical detection, BeppoSAX also discovered GRB 980425 at $z = 0.0085$ which later showed a supernova (SN) at the same location as the GRB and is considered the first direct evidence of the GRB-SN connection (Galama et al. 1998a; Kulkarni et al. 1998). In total BeppoSAX discovered 55 GRBs.

The High Energy Transient Explorer (HETE) also known as Explorer 79 was an American astronomical satellite with international contributions mainly from Japan and France. The HETE and BeppoSAX satellites were launched in the same year but unfortunately HETE was lost during launch in November 1996. The second HETE was launched on 9 October, 2000. HETE-2 consisted of UV, X-ray and γ -ray instruments. The primary objective of HETE-2 was to carry out follow-up observations of GRBs at UV, X-ray and γ -ray wavelengths. HETE-2 was capable of localizing GRBs with around 10 arc second accuracy and transmitting these positions to a network of receivers at ground based telescopes enabling radio, optical and infrared (IR) follow-up studies. HETE-2 detected the famous GRB 030329 at $z = 0.1685$, the first GRB clearly connected to a SN (Hjorth et al. 2003b; Stanek et al. 2003). The detection of the short GRB with the first optical afterglow detection (Hjorth et al. 2005), GRB 050709, is also credited to HETE-2 (see section 1.5.2).

1.4 THE *Swift* REVOLUTION

A multi-wavelength space observatory, the *Swift* satellite was launched on 20 November 2004 with the main goal of GRB detection, localization and follow up (Gehrels et al. 2004). It consists of three instruments, the Burst Alert Telescope (BAT), the X-ray Telescope (XRT) and the Ultraviolet/Optical Telescope (UVOT). BAT searches the sky for new GRBs with a localization accuracy of 1–4 arcmin radius. The satellite slews automatically to the GRB position after the BAT trigger and the XRT provides a position

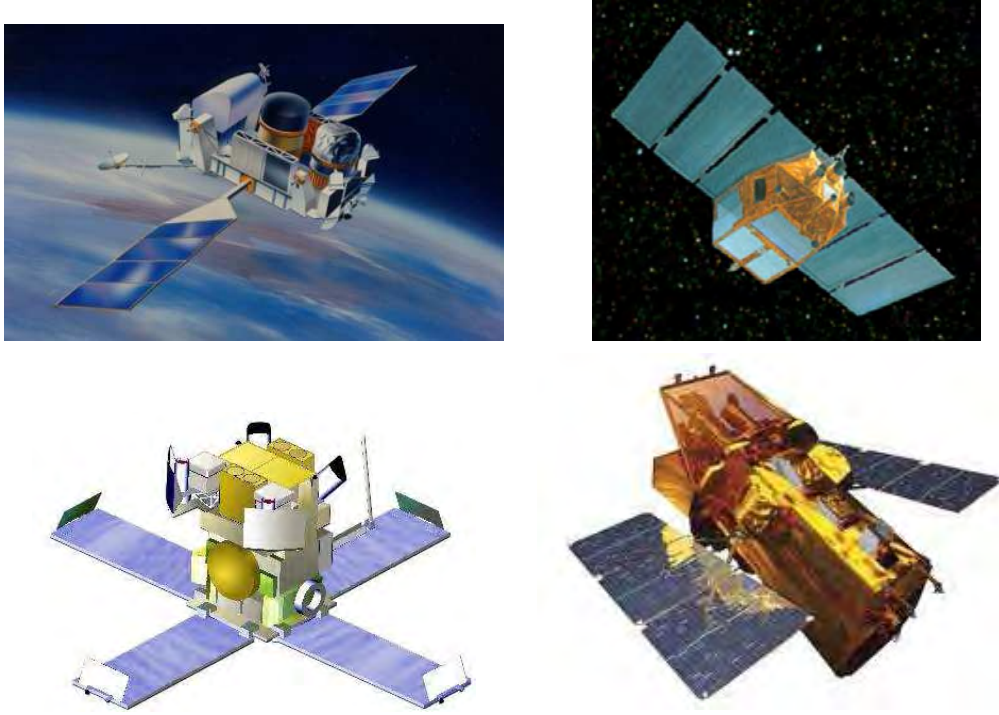


Figure 1.2: The CGRO, BeppoSAX, HETE-2 and Swift satellites.

with an error circle of 1–4 arcsec. The UVOT, equipped with three UV and three optical filters covering a wavelength range from 1700 to 6000 Å, detects the UV/optical counterpart of the GRB. The autonomy of the *Swift* spacecraft allows it to perform the X-ray, UV and optical observations within 20–70 s after the γ -ray trigger. The high BAT sensitivity allows detection of faint bursts. The *Swift* mission solved many enigmas and posed new questions related to GRB science. The rapid response of *Swift* provided a large sample of afterglows with a detection rate of more than 100 bursts year⁻¹. *Swift* holds the record for detecting the most distant GRB, at redshift $z = 8.2$ (GRB 090423; Tanvir et al. 2009; Salvaterra et al. 2009). So far, four other spectroscopically confirmed GRBs have been detected at redshift $z > 5$ (GRB 050904 ($z = 6.295$): Haislip et al. 2006; Kawai et al. 2006; Tagliaferri et al. 2005; GRB 060522 ($z = 5.11$): Cenko et al. 2006a; GRB 060927 (5.4636): Ruiz-Velasco et al. 2007; GRB 080913 ($z = 6.69$): Greiner et al. 2009) and many others with photometric redshift determinations. *Swift* even detected a “naked-eye” burst, GRB 080319B, with a uniquely bright peak visual magnitude of 5.3 at $z = 0.937$ (Racusin et al. 2008; Woźniak et al. 2009; Bloom et al. 2009). This is optically the brightest burst observed to date.

1.5 PROGENITORS

The prompt observable emission time for GRBs spans from milliseconds to a few minutes. GRBs have been categorized into two populations according to their observable emission durations. The dividing line between the two populations is at $T_{90} = 2$ s (Kouveliotou et al. 1993). T_{90} , introduced by the BATSE team, is the time interval in which 90% of the γ -ray photon fluence is detected. These two classes are termed long and short duration GRBs. These categories also differ spectroscopically, with short duration GRBs having harder spectra than the long duration ones (Dezalay et al. 1992).

1.5.1 LONG DURATION GRBs

The gamma-ray events with $T_{90} > 2$ s are classified as long duration GRBs. Long GRBs last typically from 2 s to several minutes with an average duration of ~ 30 s. These are the most commonly observed events and have been studied in great detail. These immensely bright events can occur near the farthest edges of the observable Universe. The favoured model describing long GRB physics is the so called “collapsar model” (Woosley 1993; Paczynski 1998; MacFadyen & Woosley 1999). A typical case is the iron core implosion of a 20-30 M_{\odot} rotating Wolf-Rayet star. The massive star loses its hydrogen through stellar winds and collapses further to a black hole (BH).

Stars during their main-sequence evolutionary phase convert hydrogen into helium through nuclear fusion in their cores. As the hydrogen runs out, the core contracts and heats up and starts to fuse heavier elements, such as oxygen and carbon. At this stage a sufficiently massive star evolves to a supergiant star. The star fuses heavier and heavier elements in its core until it produces iron. Iron fusion uses energy instead of releasing it. So the star suddenly finds itself out of any usable fuel. This results in a sudden collapse where the core turns into a neutron star and the remainder is ejected into space via a SN explosion. Theory predicts that stars with initial masses exceeding 20 M_{\odot} will collapse into a BH rather than a neutron star. If the progenitor star has considerable angular momentum then material far from the axis does not fall straight into the BH but it forms an accretion disk which feeds the BH. Dissipative mechanisms in the accretion disk convert kinetic energy into heat. The material accretes in an equatorial disk and this infall creates a low density region around the poles. The energy deposition around the disk poles leads to a reverse of the infall and creates a powerful outflow of material in the form of relativistic jets perpendicular to the accretion disk. The jets contain matter and antimatter in the form of electrons, protons, positrons and photons. If the outer layers of the star are not too thick, then the jet will reach the surface within a few seconds. The jet is a “fireball” which shock-accelerates the particles of the ISM to relativistic velocities and these particles are able to radiate through synchrotron emission. SNe produced in this collapse are more energetic than ordinary SNe and are called “hypernovae”. Therefore, the model suggests that long duration GRBs are associated with

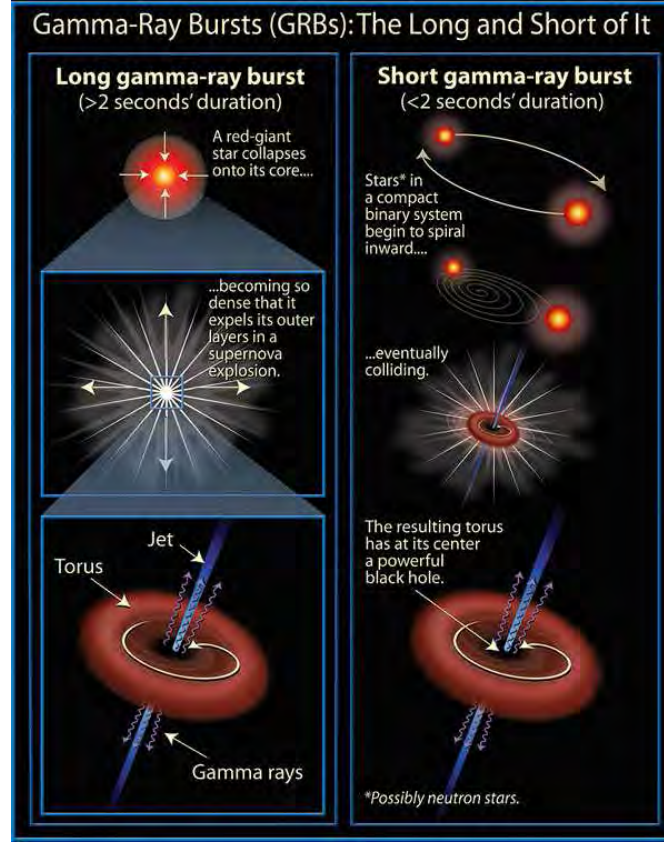


Figure 1.3: Illustration of long and short duration gamma-ray bursts. Credit: Andrew J. Levan.

the deaths of massive, young stars and usually associated with hypernovae, providing ten times the energy of a regular supernova. From an observer's perspective, the matter is accelerated towards her, resulting in a blueshift to gamma ray energies. This first detection of high energy photons is the gamma-ray burst.

1.5.2 SHORT DURATION GRBs

Gamma-ray bursts with $T_{90} < 2$ s are termed short duration GRBs. Short GRBs last from a few ms to 2 s with an average duration of 300 ms. Short GRBs are believed to be due to the merger of two compact objects, such as a binary system containing neutron stars or a system containing a BH and a neutron star (e.g. Eichler et al. 1989; Paczynski 1990; Narayan et al. 1992; Mészáros & Rees 1992). The two compact objects spiral toward each other and eventually merge. Merging neutron stars should be powerful sources of gravitational waves. The gravitational waves causes these objects to spiral towards each other. These objects then collide, form a single BH surrounded by a disk, and release an incredible amount of energy which is beamed out of the newly forming BH (see Fig. 1.3). Gamma ray bursts produced in this way are expected to be located in a

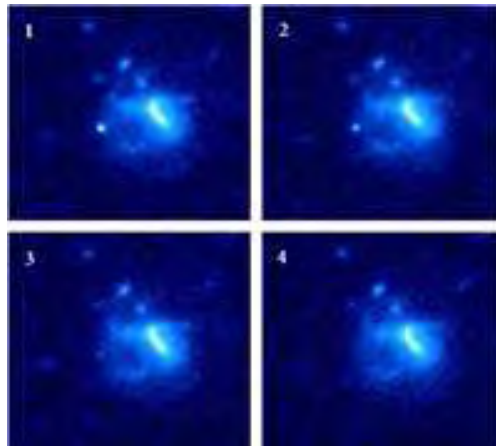


Figure 1.4: Visible light images of the afterglow of GRB 050709. The images were taken at 5.6, 9.8, 18.6 and 34.7 days after the burst. Adapted from: Fox et al. (2005)

range of normal star forming and elliptical galaxies. Short GRBs can be located in the outskirts of their host galaxies which is the usual location of old merging binaries. This location is due to the fact that these systems have experienced two SNe explosions, which imparted a significant kick velocities. By the time the merger happened, the system has travelled far away from its birth place reaching the outskirts of the galaxy. The star formation rates, metallicities, sizes and offsets of short GRB hosts are distinct from those of long GRB hosts. This too indicates that their progenitors are not related to a young star forming population. It is now widely believed that short GRBs are diverse and probably contain sub-classes (e.g., Tanvir et al. 2005). The short GRB discovery rate is about 1 event per month.

HETE-2 detected a short GRB on July 9, 2005. The Chandra X-ray Observatory and the *Swift* satellite observed the X-ray afterglow (Fox et al. 2005). Hubble and many ground based telescopes observed the optical source at the same location, thus making the first optical observation of a short GRB (see Fig. 1.4, Hjorth et al. 2005, Fox et al. 2005).

The association of long GRBs with hypernovae supports the notion that they occur in areas of active star formation within galaxies. A massive star blows up a few million years after its birth, so its deathbed is close to its birth-point. On the other hand, binaries may take from ~ 10 Myr to > 10 Gyr to merge. Some do explode on their birth sites (see e.g. Belczynski et al. 2010). Short GRBs are also closer to us with: $z = 0.1$ to 1 compared to long GRBs, which have $z = 0.0086 - 8.2$. The brightness of short GRBs is on the average 1,000 times less than long GRBs.

1.6 FIREBALL MODEL

After the GRB onset, the second step is the origin of the electromagnetic radiation from GRBs which is explained by the so called “standard fireball model” (e.g., Mészáros 2002; Piran 2004). Most of the energy created by the collapse of the stellar core is released in the form of thermal neutrinos with energies of 10–30 MeV. Searches are underway for ultra-high energy neutrino signals from GRBs, which are expected to be measured with the IceCube neutrino detector in Antarctica (Abbasi et al. 2010). In the case of coalescence of compact objects, most of the energy is released in the form of gravitational waves which are so far undetected. Searches are also in hand for gravitational waves with the Laser Interferometer Gravitational-wave Observatory (LIGO) in Washington and Louisiana and the Virgo interferometer in Cascina, near Pisa, Italy.

A small fraction of energy goes into an ultra-relativistic fireball consisting of electrons, positrons, gamma-rays and baryons. Most of the baryons remain close to the central engine, otherwise the fireball could not reach ultra-relativistic velocities. γ -rays are emitted as a result of internal shock waves within the expanding fireball that arise from colliding shells which have been sent out by the central engine with different Lorentz factors (Mészáros & Rees 1992). Inside the fireball, density, pressure and temperature vary. This leads to a series of internal shock waves moving back and forth within the fireball. The faster moving blobs take over the slower moving blobs in the expanding material (see Fig. 1.5). The fireball expands very close to the speed of light. According to the principles of relativity the observer sees gamma-rays that last for only a few seconds, even if it took a day or more to produce them in the co-moving frame. The GRB fireball then behaves like a shock wave, plows into and sweeps up material in the ISM.

The γ -ray pulses vary significantly in shape and duration. Some GRBs show a single (also called a fast rise exponential decay, FRED), peak while others show several spikes and sometimes substructures. Short duration bursts usually have harder spectra, higher peak energies and lower luminosities than long duration GRBs. The observed gamma-ray spectrum typically follows the Band function (Band et al. 1993), described at low energies by a power-law continuum with an exponential cutoff and at high energies by a steeper power-law. The two power-laws are joined smoothly at a break energy $E_0(\alpha - \beta)$:

$$N_E(E) \propto \begin{cases} E^\alpha e^{-E(\alpha+2)/E_0} & E \leq E_0(\alpha - \beta)/(\alpha + 2) \\ E^\beta & E > E_0(\alpha - \beta)/(\alpha + 2) \end{cases}$$

where α and β are the slopes and E_0 is the peak energy, typically ranging from as low as 100 keV to 1 MeV.

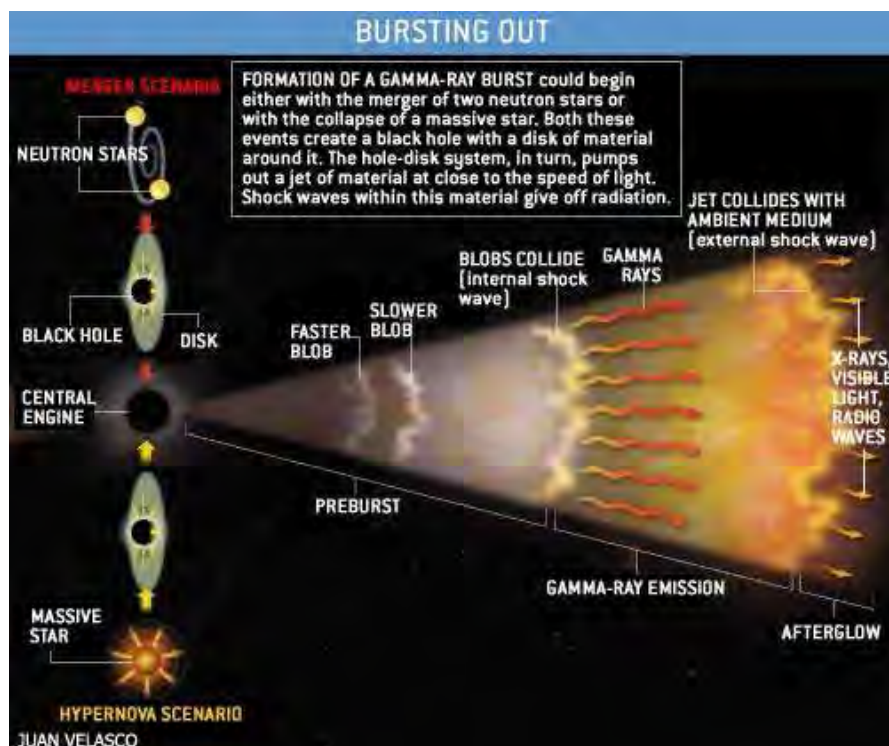


Figure 1.5: *The canonical fireball model.* Credit: Neil Gehrels, Luigi Piro and Peter J. T. Leonard, Scientific American December 2002.

1.7 GRB AFTERGLOWS

The afterglow is produced when the shock wave reaches the local medium, shocks it, and create a wide array of less energetic radiation. The initial burst of γ -rays is followed by slowly fading emission, its spectral peak moving from gamma-rays to the X-rays to visible light and finally to radio waves. In general, the GRB pulses are assumed to be produced by synchrotron emission from collisions between ultra-relativistic conical shells ejected during the explosion, while the GRB afterglow is assumed to be synchrotron radiation emitted when the merged shells collide with the ISM and drive a forward blast wave into the ISM and a reverse shock into the merged shells. The afterglows persists for longer times with a gradual shift to lower frequencies peaking initially at the X-ray and moving towards radio wavelengths.

The external shock produces a power-law distribution of electrons described as $N(\gamma_e) \propto \gamma_e^{-p}$ for $\gamma > \gamma_m$ where p is the electron energy index and γ_e is the Lorentz factor. Theoretically afterglow spectra and light curves are described in Sari et al. (1998) and Granot & Sari (2002). The afterglow evolution is described by three characteristic frequencies, ν_a , ν_m and ν_c . The electrons with minimum Lorentz factor γ_m preferentially radiate at ν_m . ν_c is the cooling frequency with Lorentz factor γ_c and ν_a is the frequency below which the flux is self absorbed. The spectral and temporal evolution of these

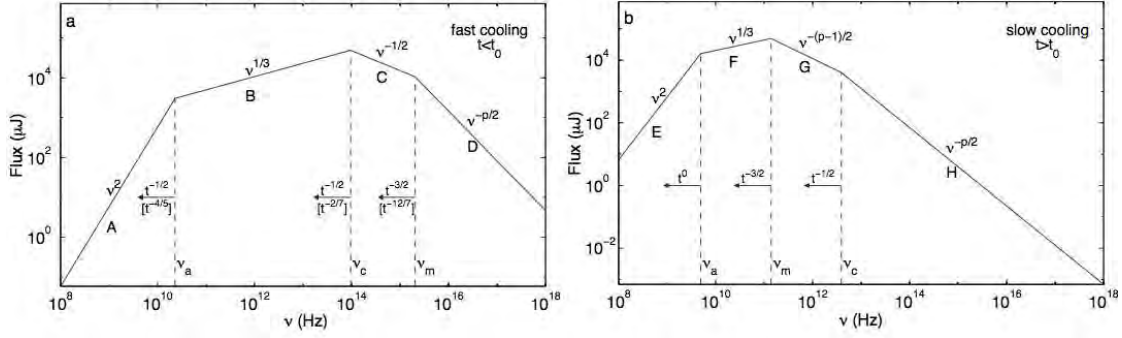


Figure 1.6: Synchrotron emission spectra in the fast cooling and slow cooling phases from Sari et al. (1998).

frequencies is a power-law as $F_\nu(t) \propto \nu^{-\beta} t^{-\alpha}$ where β is the spectral index and α is the temporal index. There are now two different cases, depending on whether $\gamma_m > \gamma_c$ or $\gamma_m < \gamma_c$. When $\gamma_m > \gamma_c$ then all electrons cool down to γ_c and this case is called fast cooling (see Fig. 1.6). The flux F_ν for this case is given as

$$F_\nu = \begin{cases} F_{\nu,0}(\nu/\nu_c)^{1/3} & \nu_c > \nu \\ F_{\nu,0}(\nu/\nu_c)^{-1/2} & \nu_m > \nu > \nu_c \\ F_{\nu,0}(\nu_m/\nu_c)^{-1/2}(\nu/\nu_m)^{-p/2} & \nu > \nu_m \end{cases}$$

$F_{\nu,0}$ is the observed peak flux. According to the standard fireball model, explained by Sari et al. (1998), at late times the electron population accelerated by shock mechanisms is expected to radiate in the slow cooling regime where $\gamma_c > \gamma_m$, the electrons do not cool within a time t and the observed spectrum is

$$F_\nu = \begin{cases} F_{\nu,0}(\nu/\nu_m)^{1/3} & \nu_m > \nu \\ F_{\nu,0}(\nu/\nu_m)^{-(p-1)/2} & \nu_c > \nu > \nu_m \\ F_{\nu,0}(\nu_c/\nu_m)^{-(p-1)/2}(\nu/\nu_c)^{-p/2} & \nu > \nu_c \end{cases}$$

The proposed SEDs of the afterglows in both phases are shown in Fig. 1.6.

As mentioned above, the flux behaves like a power-law and the empirical temporal evolution of the afterglow lightcurve is described by the smoothly broken power-law shape (Beuermann et al. 1999) given as

$$F_\nu(t) = F_b(t) [(t/t_b)^{\alpha_1 n} + (t/t_b)^{\alpha_2 n}]^{-1/n}$$

where F_b is the normalization constant, t_b is the jet break time, α_1 the pre break slope, α_2 the post break slope, and n is the smoothness parameter as the jet break is not a sharp point in time. In reality, a well-sampled afterglow lightcurve is not a strict smooth power-law but instead shows several smaller and larger variations e.g. X-ray flares. The flares imply a second emission component, which may be due to a number of

causes, possibly related to direct activity of the GRB central engine (see Zhang et al. 2007).

1.7.1 DARK GRBs

A certain population of GRBs are termed “dark” or ghost GRBs (see Djorgovski et al. 2001; Jakobsson et al. 2004a). GRB afterglows are usually detected in X-rays but a large fraction of GRBs are not detected in visible light. In fact, about 60–70% of well localized GRBs are not accompanied by detections of optical afterglows (Fynbo et al. 2001b). Dark GRBs remain one of the unresolved issues in GRB physics. There are several explanations proposed for the missing optical counterparts of GRBs. One explanation is that these GRBs lie in regions of recent star formation, which tend to be filled with large amount of dust. Dust would absorb and scatter the visible photons but not the X-rays. Another intriguing possibility is that these dark GRBs occur at very high redshifts and are not detectable in the optical (e.g., Tanvir et al. 2008). This is because the relevant light wavelengths produced by these bursts would be absorbed by the neutral IGM. The third possibility is that these GRBs are inherently optically faint.

1.8 QUASARS

A quasi stellar radio source (contracted to “quasar”) is a very powerful, luminous and distant active galactic nucleus. The term quasar was coined by Hong-Yee Chiu in 1964. Some radio sources appeared to be point like objects like galactic stars, but their spectra were very peculiar, with strong, broad emission features that didn’t match any plausible features expected from stars. A quasar is an extremely compact region powered by accretion of material onto a supermassive rotating black hole at the center of a massive galaxy. The suggestion that supermassive BHs were involved appeared early (e.g. Zel’Dovich & Novikov 1964). It turned out that many quasars were not necessarily strong radio sources, and the term quasi-stellar objects (QSOs) is often used. According to their radio emission, QSOs are divided into radio loud and radio quiet classes. Only about 10% of QSOs are radio loud.

In the 1950s the first quasars were observed with radio telescopes finding that they have very small angular sizes. In 1959 hundreds of these objects were discovered (Edge et al. 1959). Finally an optical spectrum was obtained for the 3C 48 radio source, which showed that it had broad emission lines (Greenstein 1963). In 1963 Maarten Schmidt identified an optical source corresponding to a radio source, 3C 273. The star like appearance suggested it was relatively nearby. Maarten Schmidt obtained the optical spectrum using the Hale Telescope on Mount Palomar. Schmidt realized the emission lines seen in the spectrum were the hydrogen Balmer series and Mg II emission lines redshifted to $z = 0.158$ (Schmidt 1963). This finding revolutionized quasar science and

now many high redshift QSOs have been observed up to $z > 6$ (Fan et al. 2003, 2004, 2006). The Sloan Digital Sky Survey (SDSS) has found thousands of quasars. 26 out of the 30 most distant quasars known to date were found by the SDSS. The observations of quasars at $z \geq 6$ provide some clues to the cosmic reionization (Fan et al. 2004, 2006). Their spectra displaying a Gunn-Peterson trough, which is an absorption feature in the spectra due to neutral hydrogen in the IGM. This indicates that the IGM at that time was partly neutral and indicates that the end of the epoch of reionization occurred around these times.

Because quasars are so distant and so luminous, it has been difficult to study the host galaxies which contain them. It has been found that there is no simple relationship between a quasar and the morphology of its host galaxy (Malkan et al. 1984). Many quasar host galaxies are interacting or merging systems and there are also many host galaxies that appear to be normal ellipticals or spirals. It has also been found that the radio loud quasars tend to be found in elliptical and interacting galaxies whereas the radio quiet quasars (the QSOs) seem to be present in both elliptical and spiral host galaxies (Bahcall et al. 1994, 1995; Miller & Sheinis 2003; Wolf & Sheinis 2008).

Quasars are now known to be very luminous active galactic nuclei (AGN) buried in galaxies of normal luminosity. An AGN is a galaxy that has a very energetic central region powered by accretion onto a central supermassive blackhole. In the 1980s quasars were classified as a particular kind of active galaxy. Other types of AGNs include Seyfert galaxies, blazars, and radio galaxies. AGNs have six main observational properties: *i*) high luminosity; *ii*) compact angular size; *iii*) continuum emission from the core and this radiation ranges from radio to the X-ray; *iv*) emission lines, and *v*) sporadic variability of the continuum and spectral line emission.

This thesis discusses the studies of the QSO-pair Q0151+048. Q0151+048A is a radio quiet quasar, optically bright with V band magnitude of 17.63 mag, and has a faint companion quasar Q0151+048B with $V = 21.1$ mag. Q0151+048B lies 3.3'' to the NE of Q0151+048A and was first discovered by Meylan et al. (1990).

1.8.1 DAMPED $\text{Ly}\alpha$ ABSORBERS

Damped Lyman alpha absorbers (DLAs) are responsible for the strongest absorption lines present in bright QSO spectra with H I column densities $\text{NH I} \geq 2 \times 10^{20} \text{ cm}^{-2}$ (e.g., Wolfe et al. 2005), which is an indication of very large dark matter over-densities. DLAs comprise the neutral gas reservoir for star formation at high redshifts (Nagamine et al. 2004). Stars are likely to descend from cold neutral clouds, which are the predecessors of molecular clouds and the birth sites of stars (Wolfire et al. 2003). The study of DLAs provides critical information on the formation and evolution of galaxies. DLA surveys show systematic absorption from different ionized species (C IV, Si IV, O I, Al II, etc.), demonstrating the complex interstellar structure observed in present-day galaxies

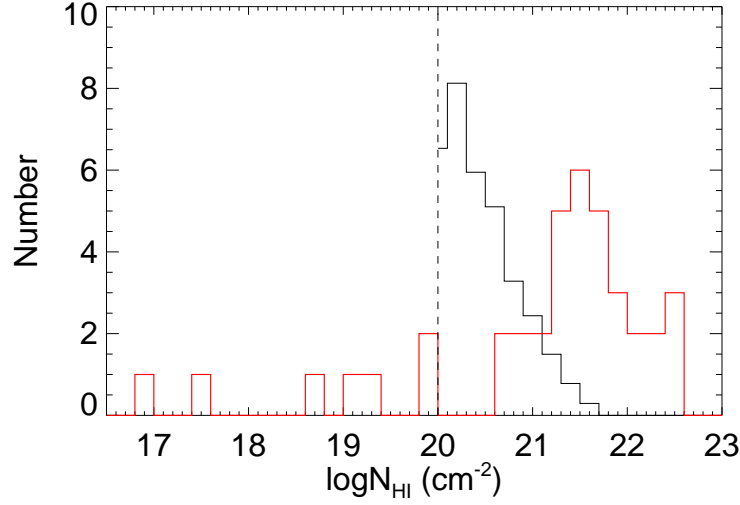


Figure 1.7: Distribution of H I column densities. Black: QSO-DLAs from (Noterdaeme et al. 2009). Red: GRB-DLAs from (Fynbo et al. 2009). Adapted from Fynbo et al. (2009).

(Wolfe & Prochaska 2000; Fox et al. 2007a,b). QSO-DLAs are usually considered to be representative of the ISM of the whole population of galaxies at high redshifts. The host galaxies of QSO absorbers are not only faint but also have small angular distances from the QSO itself and are therefore difficult to detect. However the host galaxies of QSO absorbers have been detected in a few cases via direct imaging (e.g. Warren et al. 2001; Fynbo et al. 2003).

QSO absorbers are sub-divided into populations according to their column density, the number of hydrogen atoms per unit area: *i*) DLAs and *ii*) Lyman limit systems (LLS). LLSs with $17 < \log N_{\text{HI}}/\text{cm}^{-2} < 20.3$ are thick enough that ultraviolet (UV) radiation does not get into their interiors (Péroux et al. 2003).

The DLAs are also observed in the spectra of GRB afterglows. QSO-DLAs are assumed to be the ISM of the galaxies located in front of the QSO, while GRB-DLAs are dominated by the GRB host galaxy rather than intervening absorbers (e.g., Hjorth et al. 2003a; Prochaska et al. 2008a). Although intervening absorbers are also seen in GRB afterglow spectra they are at lower redshift, and typically much lower column densities compared to the GRB-DLA. GRBs have on average higher metallicities than QSO absorbers. QSO-DLAs hardly extend out to $\log N_{\text{HI}}/\text{cm}^{-2} = 21.8$, whereas GRB-DLAs have been observed with $\log N_{\text{HI}}/\text{cm}^{-2} = 22.7$ (see Fig. 1.8; Prochaska et al. 2009). The main difference between QSO and GRB absorption spectroscopy is that QSOs are nearly stationary and stable in their emission, while GRBs are the most variable, transient and violent phenomena in the Universe. QSOs have enough time to ionize their own host galaxy along their lines of sight. While the physical, dynamical, and chemical status of the circumburst medium in GRB progenitors can be modified by the explosive



Figure 1.8: *The Horsehead Nebula* Credit: NASA.

event, through shock waves and ionizing photons. QSO-DLAs as well as GRB-DLAs display an evolution of metallicity with redshift in such a way that the metallicity decreases with increasing redshift (Fynbo et al. 2006b; Prochaska et al. 2007).

1.8.2 $\text{Ly}\alpha$ BLOBS

The $\text{Ly}\alpha$ emission line is a very promising tool for finding distant galaxies. Several searches have been conducted to discover objects in the high redshift Universe through $\text{Ly}\alpha$ emission. Recently a mysterious subclass of Lyman Alpha Emitters (LAEs) was found, namely $\text{Ly}\alpha$ “Blobs” (Steidel et al. 2000). $\text{Ly}\alpha$ blobs are very extended, up to more than 150 kpc, luminous up to $\log L_{\text{Ly}\alpha}/\text{erg s}^{-1} \gtrsim 43$ resembling the giant $\text{Ly}\alpha$ nebulae associated with high redshift radio galaxies. The proposed explanations for the production of energy needed to ionize the nebulae are: *i*) star formation in the starburst galaxies and thence superwinds from supernova explosions (Taniguchi et al. 2001; Ohyama et al. 2003; Mori et al. 2004); *ii*) Active Galactic Nuclei (AGN) heavily obscured from the line of sight (Haiman & Rees 2001; Weidinger et al. 2005) and *iii*) cold accretion: infalling gas onto a dark matter halo (Haiman et al. 2000; Fardal et al. 2001; Dekel & Birnboim 2006; Dijkstra et al. 2006a,b).

1.9 DUST EXTINCTION

When we look in different directions of the sky, we see dark patches in the distributions of stars. These are not gaps where there are no stars, but instead are interstellar dust clouds, such as the Horsehead nebula. Dust obscures light from internal objects as well as from objects in the background and can be detected in the optical through extinction and polarization. Extinction (and reddening) are discussed in detail below.

Dust comes not only in thick clouds, but also spread diffusely throughout interstel-

lar space. Studies of high redshift galaxies and star formation obscured by dust have shown the importance of dust extinction in the distant Universe. Dust extinction is the absorption and scattering of electromagnetic radiation along the line of sight emitted by some source. More than 30% of the UV and optical light from stars in the Universe may be absorbed and re-radiated thermally at infrared wavelengths by the obscuring dust (Lagache et al. 2005; Franceschini et al. 2008). The extinction due to dust is not equally effective at all wavelengths. Dust grains extinguish most strongly at short wavelengths i.e. optical and UV ranges. Because the dust grains are of order the same size as the wavelength of visible light, long wavelength light scatters less than shorter wavelength blue light. The degree of reddening can be determined by measuring the colour index $(B - V)$ of the object and comparing to its intrinsic colour index $(B - V)_0$ by

$$E(B - V) = (B - V) - (B - V)_0$$

Greater extinction will give more reddening. Each line of sight has its own extinction law and is usually expressed by the variation of extinction with wavelength (i.e. A_λ/A_V or $E(\lambda - V)/E(B - V)$). Interstellar extinction is commonly obtained through the *pair-method* by comparing spectra of reddened and unreddened stars of the same spectral type. Cardelli et al. (1989) showed that Galactic sightlines could be fairly well characterized by a single parameter R_V , though Fitzpatrick & Massa (2007) dispute this. The R_V parameter is a measurement of the total, A_V , to selective extinction $E(B - V)$ and is defined as

$$R_V = A_V/E(B - V)$$

For the MW the mean value of R_V is 3.1. The value of R_V varies for individual lines of sight.

The object seen through dust will generally appear fainter and redder than it would if there were no dust along the line of sight. However dust extinction causes a certain typical shape in the observed spectrum of an object depending on the properties of the dust. Known absorption features include the 2175 Å bump, the diffuse interstellar bands, the 3.1 μm water ice feature and the 10 and 18 μm silicate features.

The strongest spectroscopic dust absorption feature, in terms of FWHM, is the bump situated at 2175 Å or 4.6 μm^{-1} . The bump was firstly discovered in 1965 by Theodore P. Stecher. Immediately following the discovery by Stecher (1965), Stecher & Donn (1965) pointed out that small graphite particles would produce similar absorption. The central wavelength of the bump is nearly invariant from one sightline to another, with a mean deviation of 0.4% in λ_0^{-1} (Fitzpatrick & Massa 1986). The bump is present at all values of R_V in the Galaxy. The bump is very strong and must be produced by a very abundant material. Usually theories attribute it to carbon (e.g., Henrard et al. 1997). Other candidates responsible for the bump are also proposed in other theories. These candidates ranges from carbonaceous materials (Henrard et al. 1997) to iron poor silicate grains in the form of partially hydrogenated amorphous Mg_2SiO_4 particles (Steel

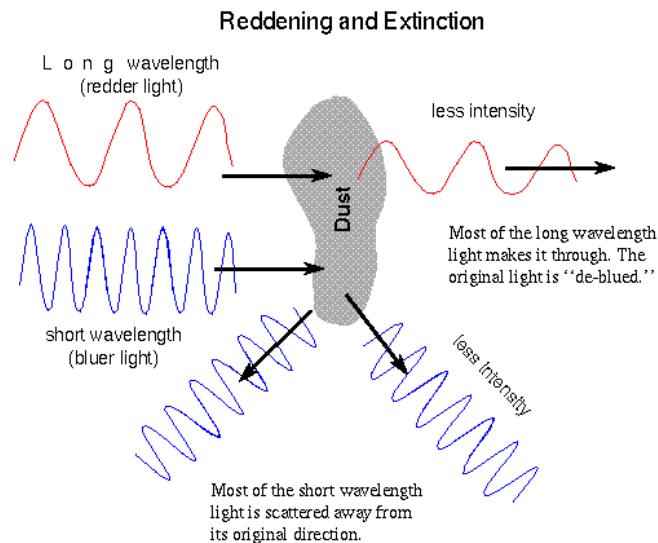


Figure 1.9: Absorption and scattering of light by dust particles at short and long wavelengths.

& Duley 1987). The dominant hypothesis is some form of carbonaceous material in small grains ($\lesssim 50 \text{ \AA}$), with polycyclic aromatic hydrocarbons (Duley & Seahra 1998; Duley 2006; Cecchi-Pestellini et al. 2008; Duley 2009; Cecchi-Pestellini et al. 2010) and graphite being popular choices (Stecher & Donn 1965; Mathis et al. 1977; Draine & Lee 1984; Draine 1989; Sorrell 1990; Mathis 1994; Rouleau et al. 1997; Will & Aannestad 1999; Andersen et al. 2002; Clayton et al. 2003; Fitzpatrick & Massa 2007).

Fitzpatrick & Massa (1986) studied the 2175 \AA bump in the direction of 45 reddened stars in the Milky Way (MW). The important characteristic of the MW extinction curve is the strong 2175 \AA bump. The 2175 \AA extinction bump is weaker in Large Magellanic Cloud (LMC) compared to the MW (Fitzpatrick 2004). A stronger far-UV extinction, more than elsewhere in the LMC and in the MW, is seen in the LMC2 supershell (Fitzpatrick & Massa 1986; Misselt et al. 1999). In the SMC there seems to be a lower value of R_V , almost no bump, and an even stronger far-UV rise. Although one out of the five lines of sight to the SMC does show the 2175 \AA bump (Lequeux et al. 1982; Gordon et al. 2003). The mixtures of carbonaceous and silicate grains are appropriate for explaining the observed LMC and SMC extinction law (Pei 1992; Weingartner & Draine 2001).

Previously it was believed that the different average extinction curves in the MW, LMC, and SMC were due to the different metallicities of the three environments. Later it was found that a few sightlines to the LMC and SMC have extinction curves similar to the MW and that the MW too has some extinction curves that look like those found in the LMC and SMC (Gordon et al. 2003; Clayton et al. 2000; Valencic et al. 2003). This gave rise to a new interpretation, according to which the variation in the extinction curves seen in MW, LMC and SMC environments may be caused by processing of dust grains by nearby star formation. This interpretation is supported by studies of starburst

galaxies (e.g., Calzetti et al. 1994; Meurer et al. 1999). Calzetti et al. (1994), Gordon et al. (1997) and Gordon et al. (2000) found that attenuation or extinction curves of the starburst galaxies lacked the 2175 Å bump.

Trumpler (1930) and Lindblad (1935) firstly recognized that reddening of distant stars are produced by submicron particles in the ISM. Dust formation in the local Universe takes place in the stellar winds of evolved asymptotic giant branch (AGB) stars (Dwek 1998; Tielens 1998). Dust is formed by a series of chemical reactions in which atoms or molecules from the gas phase combine to clusters of increasing size. Dust affects the temperature of the ISM. Dust not only provides cooling to the ISM, but also provides heating through electrons ejected photoelectrically from grains.

1.9.1 DUST AT HIGH REDSHIFT

Dust production at high redshift is a hotly debated topic. At high redshifts evidence for dust exists from the observations of DLAs (Pettini et al. 1994; Ledoux et al. 2002; Prochaska & Wolfe 2002) and from the detection of dust thermal emission from QSOs re-observed at millimeter (e.g. Carilli et al. 2001; Omont et al. 2001; Bertoldi et al. 2003; Beelen et al. 2006) and mid-IR wavelengths (e.g., Jiang et al. 2010). The inferred dust masses and star formation rates in these QSO host galaxies can be $\geq 10^8 M_{\odot}$ and up to $3000 M_{\odot} \text{ yr}^{-1}$ respectively (e.g., Bertoldi et al. 2003). Such high redshift quasars are, however, rare objects and are hardly representative of the dominant star forming population.

A transition in the dust properties is theoretically expected at $z \gtrsim 5$ (Dwek et al. 2007; Morgan & Edmunds 2003; Marchenko 2006; Todini & Ferrara 2001). In the local Universe, the major sources of interstellar dust are evolved AGB stars which require $\gtrsim 1$ Gyr to evolve to produce dust (Gehrz 1989; Morgan & Edmunds 2003; Marchenko 2006; Dwek et al. 2007). The dust is then distributed into the ISM through stellar winds. It is believed that AGB stars are not predominantly responsible for the dust seen at $z \gtrsim 5$ due to the short time from the Big Bang. Theories predict that on such short time scales, an alternative source of dust is required and that core-collapse SNe could dominate dust formation at these early times (Todini & Ferrara 2001; Morgan & Edmunds 2003; Nozawa et al. 2003; Dwek et al. 2007; Marchenko 2006; Hirashita et al. 2005). The grain condensation by SNe is fast enough to explain dust masses at high redshift. However observations of local SNe do not support the hypothesis of dust production in SN ejecta (Meikle et al. 2006; Smith & Jarvis 2007). Valiante et al. (2009) proposed that AGB stars could produce enough dust at high redshift under certain initial conditions. However Michałowski et al. (2010a) found that large dust masses observed in $z > 5$ QSOs could not be due to AGB stars. So far the dust production mechanism at high redshift is not clear.

1.10 STRUCTURE OF THE THESIS

This thesis deals with dust extinction in GRB host galaxies at low and high redshift. It also discusses the expected transitions of dust producers at high redshift. The interesting case of the QSO pair Q0151+048 is also presented in this thesis.

Chapter 2 will describe the methods adopted in this thesis to conduct absorption spectroscopy for GRB afterglows and QSOs. The chapter describes the data reduction procedures and SED modelling.

In Chapter 3 the afterglow of GRB050904 is reinvestigated to understand cosmic dust at high redshift. The claimed evidence of unusual SN-origin dust is addressed by multi-epoch SED analysis. The afterglow SED is derived at 0.47, 1.25 and 3.4 days after the burst trigger. This Chapter also discusses the origin of dust in the early Universe and the sources of dust in the late and early Universe.

Chapter 4 deals with the SED analysis of all known $z > 6$ GRB afterglows: GRB 090423, 080913 and 050904, at $z = 8.2$, 6.69, and 6.295, respectively. Multi-epoch SEDs are generated and fitted with single and broken power-laws including dust models. Comparison with the lower redshift GRB sample is also made to see the evolution of dust with the redshift.

In Chapter 5, focus on the SED analysis of a sample of 41 GRB afterglows. This chapter presents SED modelling of a large GRB sample using spectroscopy for the first time. This is the largest ever sample studied to derive absolute extinction curves outside the Local Group. In particular, the spectral shapes of GRB afterglows and their consistency with the synchrotron emission model are discussed here. The chapter also discusses GRB circumburst environments by comparing their gas-to-dust and metals-to-dust ratios and metallicities to those of other galaxies. The chapter also presents the SED analysis of all known GRBs where the 2175 Å bump is detected in the optical spectrum.

In Chapter 6 the case of the QSO pair Q0151+048 is discussed. The system consists of a QSO pair, a Ly α blob and a DLA at $z \sim 2$. This complex system has been observed with NOT and VLT/X-shooter, helping us to constrain the geometry of the system. The line-profile fitting techniques used to measure metallicity are discussed here. The systemic redshifts of the QSO pair are also investigated using the restframe optical emission lines.

In Chapter 7 the main conclusions and some future prospects are presented.

2

SED MODELLING AND ABSORPTION LINE SPECTROSCOPY

PART I

2.1 GRBS AS COSMOLOGICAL PROBES

The association of long GRBs with star forming galaxies, their immense brightness and prompt observations make GRBs useful probes to study matter in the star forming environments. The prompt emission alters the surrounding environment and affects the X-ray and optical afterglow out to radii of a few tens of pc (Perna & Loeb 1998; Perna & Lazzati 2002; Perna et al. 2003; Fox et al. 2003). The X-ray, optical/UV, and NIR observations can tell us about the gas density, gas ionization, dust content, and metallicity in the GRB environment (Kumar & Narayan 2003; Piro 2000; Stratta et al. 2004; Fynbo et al. 2009; Schady et al. 2010). The simple spectral shape from the X-ray to optical makes GRBs excellent tools to determine not only the effective reddening, but also the absolute extinction from the distant Universe (e.g. Stratta et al. 2004; Watson et al. 2006a; Starling et al. 2007; Schady et al. 2010; Greiner et al. 2011; Zafar et al. 2011). X-ray spectra provide useful information by measuring low energy absorption due to the photoelectric effect. The potential of GRB afterglows as probes of the early Universe was realized very early in the so-called afterglow era (e.g. Wijers et al. 1998; Lamb & Reichart 2000). $\text{Ly}\alpha$ and metal absorption systems, often observed in GRBs lines of sight, can be used to derive physical properties of the absorbing gas clouds, such as gas kinematics, metal column densities and metallicities (Vreeswijk et al. 2006; Fox et al. 2008; Ledoux et al. 2009). On the other hand, the spectral energy distribution (SED) provides information on both the dust inside the host galaxy and the spectral properties of the GRB afterglow itself (e.g. Starling et al. 2007; Schady et al. 2010). In the era of the *Swift* satellite and fast responding telescopes, well sampled GRB afterglow lightcurves and SEDs enable us to get more complete extinction curves. GRBs are transient sources and their nature is manifested through the detection of excited levels of the atom and fine structure lines

(e.g. O I, Fe II, Ni II, Si II and C II). Fine-structure features are identified in several GRB spectra, and are most probably excited by the intense UV afterglow flux. Multi-epoch spectroscopy indicates that they undergo variability, which cannot be explained with pure infrared excitation or collisional processes (Prochaska et al. 2006; Vreeswijk et al. 2007). The distance of the gas to the GRB can be computed by assuming UV pumping as the responsible mechanism for the production of these lines. This distance varies from a few hundred pc to a kpc (see Vreeswijk et al. 2007; Ledoux et al. 2009; D’Elia et al. 2010).

2.2 SPECTRAL ENERGY DISTRIBUTION

A significant fraction of the results presented in this thesis are based on the SED modeling using all available X-ray, spectroscopic and photometric optical/NIR data simultaneously for a given GRB afterglow. The SEDs in this paper are within the observing window of the optical to the X-ray (i.e. 10^{14} to 10^{18} Hz). The afterglow SEDs are generated at specific times: which are the mid time of the acquisition image photometry.

2.2.1 X-RAY DATA

The *Swift* XRT data for GRB afterglows were taken from the *Swift* data archive facility. The XRT has four observing modes: *i*) imaging mode, *ii*) photodiode mode, *iii*) windowed timing (WT) mode, and *iv*) photon counting (PC) mode. Imaging mode is similar to PC mode and takes images of the GRB region with typical exposure time of 0.1–2.5 s. Photodiode mode has been disabled on May 27, 2005 due to a micro-meteoroid hit. WT is a high gain mode with 1D imaging. PC retains full imaging and spectroscopic resolution. In PC mode pile-up occurs for count rates above about 0.6 counts s^{-1} . Pile-up in charge-coupled devices (CCD) happens when two or more photons reaches the same pixel of the detector before the detector is read out. The detector is unable to resolve individual signals and identifies them as a single event with energy equal to the sum of the two photons’ energies.

In this thesis XRT PC mode data are utilized for the X-ray afterglow analysis. For temporal analysis of each afterglow, the X-ray lightcurves in the 0.3–10 keV range are produced from the XRT data (Evans et al. 2007, 2010). The 0.3–10 keV is the energy band required for compatibility with the current calibration files. The X-ray lightcurves are fitted with a smoothly broken power-law (see Fig. 2.1). This lightcurve fitting was done for the following reasons: *i*) to get the possible X-ray continuum, *ii*) to avoid spectral contamination from afterglow flares and *iii*) to focus on the precise time frame to compute the GRB afterglow SED. The X-ray spectra are processed in the 0.3–10 keV energy range using the HEASoft software and the most recent calibration files. The sources counts were extracted within a circular region centered on the source with a

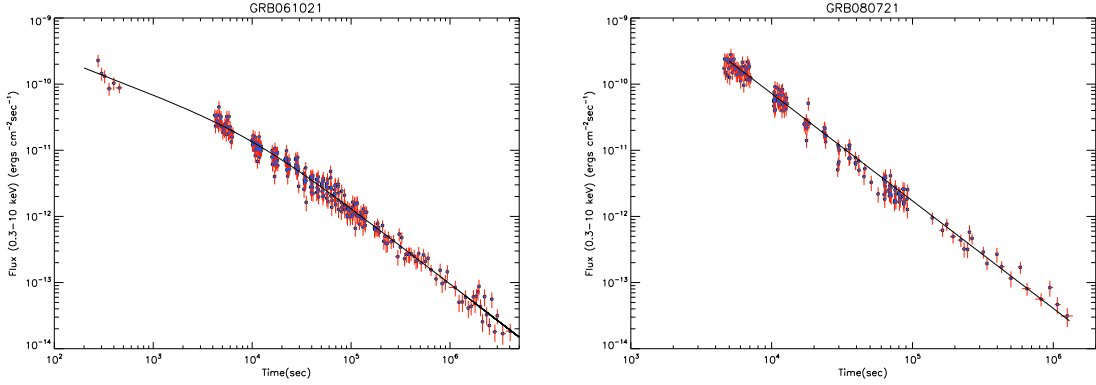


Figure 2.1: X-ray lightcurves of GRB 061021 and GRB 080721. The data points are shown in blue circles with red error bars. The black curve illustrates the power-law fit to the data.

radius ranging from 20 to 70 pixels, where one XRT pixel is $2.36''$. The background count rate was estimated from a circular region with an area approximately 10 times greater than the source region. XSELECT was utilized to extract spectra from the event data in the 0.3–10 keV range. To avoid pile-up, all X-ray spectra were taken in PC mode, in time intervals where the measured count rate was less than $0.6 \text{ counts s}^{-1}$. The XRTMKARF tool was used to create effective area response files. The standard response matrices from the *Swift* XRT archive were used. The X-ray spectral files were grouped to 12–20 counts per energy channel.

For precise analysis, it is important to obtain an accurate estimate of the absolute flux for these X-ray spectra. The X-ray spectra at specific times were obtained by taking the photon weighted mean time of the X-ray spectrum and normalizing to the lightcurve continuum at that specific time. The photon weighted mean time of the X-ray spectra were obtained by generating the events files of the spectra within XSELECT and calculating mean arrival time of the photons. The X-ray spectra were then fitted within XSPEC (Arnaud 1996) with an absorbed power-law. The spectra were corrected for fixed Galactic neutral hydrogen column density taken from Kalberla et al. (2005). The equivalent neutral hydrogen column density from the host galaxy of each GRB was estimated from the soft X-ray absorption (below $\sim 3 \text{ keV}$) and is denoted as $N_{H,X}$. $N_{H,X}$ is modeled within XSPEC where solar abundances were adopted from Asplund et al. (2006). The X-ray spectra were also corrected for this absorption to obtain the intrinsic power-law.

2.2.2 OPTICAL/NIR DATA

Most of the GRB afterglow spectra are taken with the Very Large Telescope (VLT) Focal Reducer and low dispersion Spectrographs (FORs1 and FORs2) except for GRB 050904 (Subaru telescope using the Faint Object Camera and Spectrograph, FOCAS), GRB 080607 (Keck telescope using the Low Resolution Imaging Spectrometer, LRIS) and

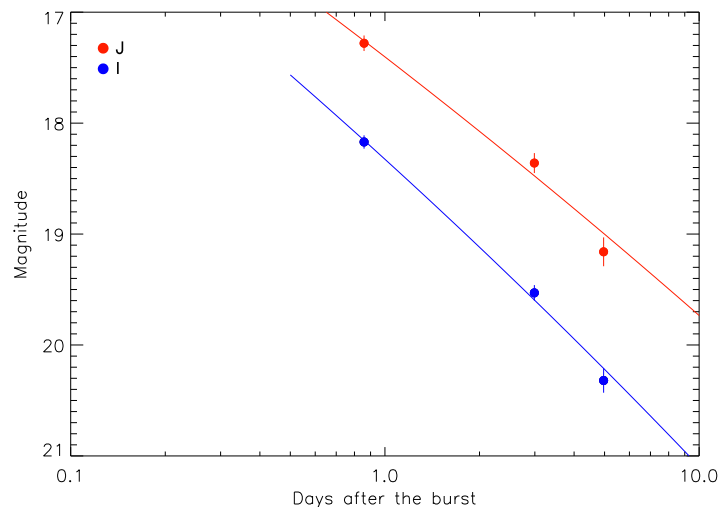


Figure 2.2: The *J* and *I* band lightcurve of GRB 090926A. The photometric data are taken from the ANDICAM instrument on the 1.3 m telescope at CTIO and given by Cobb (2009).

GRB 090423 (VLT using the Infrared Spectrometer And Array Camera, ISAAC and VLT Spectrograph using INtegral Field Observations in the Near Infrared, SINFONI). The optical spectra were reduced using the standard IRAF techniques for bias subtraction and flat-fielding. The spectra were then wavelength calibrated using the calibration lamp frames. The 1D spectra were flux calibrated using the observation of a spectrophotometric standard star from the same night.

The photometry in different optical/NIR bands is usually taken from the literature. For some cases aperture photometry was carried out with Gaia using the SDSS or Two Micron All Sky Survey (2MASS) catalogues for calibration. Moreover the magnitude of the GRB afterglows from the VLT FORS1/2 acquisition images were obtained using the ESO photometric zero-points¹ from the night of the observation. The photometric UV/optical data from UVOT on board the *Swift* satellite were also processed. UVOT contains three optical and three UV lenticular filters: *v*, *b*, *u*, *uvw1*, *uvm2* and *uvw2* (Roming et al. 2005). The UVOT lightcurves were extracted using the UVOT imaging data tool UVOTMAGHIST. The fluxes were then obtained by using the standard UVOT photometric calibration techniques defined by Poole et al. (2008).

The afterglow lightcurves in different bands were fitted using a power-law ($F(t) \propto t^{-\alpha}$) or smoothly broken power-law and the fluxes were obtained by interpolating or extrapolating the lightcurves to the time of interest (see e.g., Fig. 2.2 and 2.3). The SEDs were then constructed at certain epochs, usually the mid time of the acquisition image of the optical spectrum, and for this the optical spectrum was normalized to the level of the acquisition image photometry.

¹<http://www.eso.org/observing/dfo/quality/FORS2/qc/zeropoints/zeropoints.html>

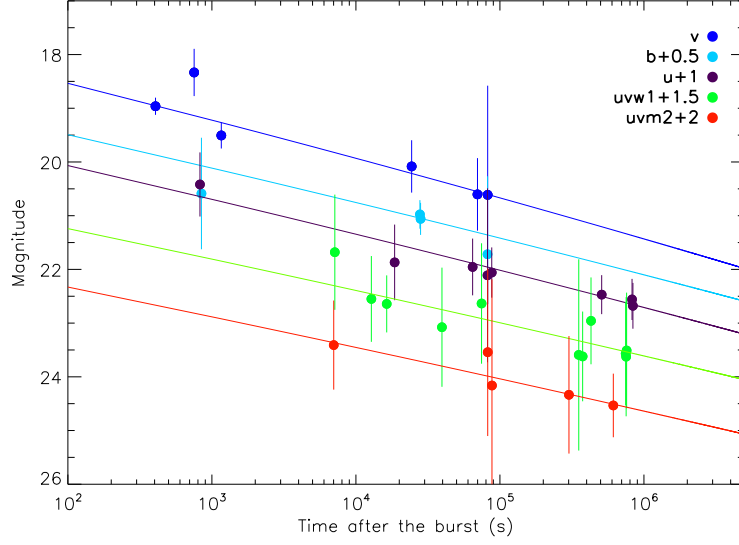


Figure 2.3: The UVOT bands v , b , u , $uvw1$ and $uvm2$ lightcurves of GRB 080605. For clarity the lightcurves are scaled by 0.5, 1.0, 1.5 and 2 for the b , u , $uvw1$ and $uvm2$ bands respectively. The fits to the afterglow lightcurves are also shown for each band.

2.3 SED MODELLING

The X-ray to optical SED is expected to be a single or broken power-law. The simple spectral shape of GRBs and the lack of absorption above ~ 3 keV allow us to place constraints not only on the dust reddening but also on the absolute extinction. Sari et al. (1998) predicted that the most energetic electron population accelerated by shock mechanisms may lose a significant fraction of their energy to radiation. This decrease in energy will give rise to a break at ν_c (corresponding to the critical Lorentz factor γ_c above which cooling by the synchrotron radiation is significant). The spectrum is given as $F_\nu \propto \nu^{-(p-1)/2}$ up to the cooling frequency ν_c and above ν_c it follows $F_\nu \propto \nu^{-p/2}$. The intrinsic spectral slope therefore should change by a value of half due to the decrease in energy by electrons through radiation.

In the simplest fireball model the spectral index, β , is governed by the energy distribution index of the electrons, p , and the location of the cooling break ν_c (e.g., Sari et al. 1998):

$$\beta(p) = \begin{cases} (p-1)/2 & \nu \leq \nu_c \\ p/2 & \nu \geq \nu_c \end{cases}$$

Hereafter this cooling break frequency ν_c will be denoted as ν_{break} . Observationally, the cooling break is frequently found to be located between the optical and X-ray regimes. The cooling break gives rise to a break in the intrinsic spectral distribution somewhere between the optical/NIR and X-ray wavelengths. The broken power-law model is

given as:

$$F_\nu = \begin{cases} F_{\nu,0} \nu^{-\beta_1} & \nu \leq \nu_{\text{break}} \\ F_{\nu,0} \nu_{\text{break}}^{\beta_2 - \beta_1} \nu^{-\beta_2} & \nu \geq \nu_{\text{break}} \end{cases}$$

where β_1 is the low energy (typically the optical/NIR) slope with $\beta_1 = (p - 1)/2$ and β_2 is high energy (typically the X-ray) slope with $\beta_2 = p/2$. In this simple picture the spectral change between the optical and X-ray wavelengths is given as $\Delta\beta = \beta_2 - \beta_1$. In this thesis, the spectral change $\Delta\beta$ is not fixed to 0.5 as predicted by Sari et al. (1998). This was done to test the consistency of the synchrotron emission model that GRB afterglows are powered by synchrotron emission of electrons accelerated in a relativistic shock.

2.4 DUST MODELS

The continuum emission from a GRB afterglow is believed to be synchrotron radiation (Sari et al. 1998). In the optical, the intrinsic flux of the GRB afterglow is described by a single power-law given as

$$F_\nu = F_{\nu,0} \nu^{-\beta}$$

where $F_{\nu,0}$ is the flux normalization, ν is the frequency and β is the intrinsic spectral slope. The observed flux is extinguished due to dust in our galaxy (the Milky Way), and intervening objects between our Galaxy and the GRB, the latter typically dominated by the GRB host galaxy. The extinction from the foreground sky is usually corrected using the Galactic extinction maps of Schlegel et al. (1998), decreased by 14%, following the analysis of Schlafly et al. (2010). After this correction the extinction will only be due to extragalactic dust. The simple spectral shapes of GRB afterglows allow us to determine the absolute extinction (A_λ) along the line of sight. With the knowledge of the redshift, the unextinguished spectral slope and restframe visual extinction, A_V , can be determined. The observed extinguished flux of the afterglow is given as

$$F_\nu^{\text{obs}} = F_\nu 10^{-0.4A_\lambda}$$

Here extinction at a wavelength λ is related to the extinction in the restframe V -band, A_V . The wavelength dependence on dust extinction observed in local disk galaxies is well reproduced by the standard dust models (Fitzpatrick & Massa 1986; Cardelli et al. 1989; Pei 1992). For the Small and Large Magellanic Clouds (SMC, LMC), and MW the extinction law introduced by Pei (1992) is given as

$$A_\lambda = A_V \left(\frac{1}{R_V} + 1 \right) \sum_{i=1}^6 \frac{a_i}{(\lambda/\lambda_i)^{n_i} + (\lambda_i/\lambda)^{n_i} + b_i}$$

For SED modeling we implemented the SMC parameterization from Pei (1992) where $R_V = 2.93$. The R_V parameter is the measure of the total A_V to selective extinction

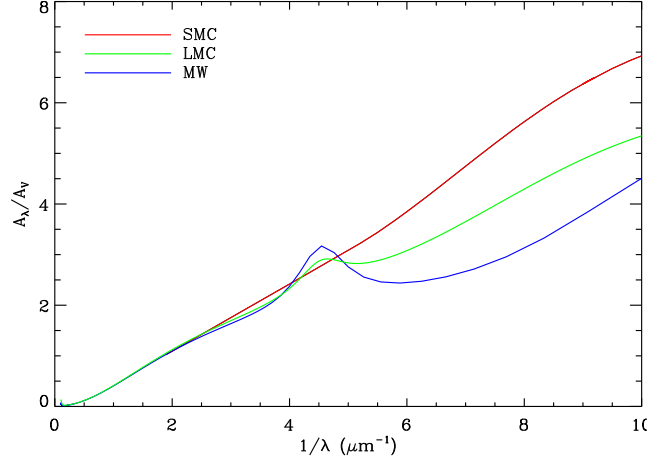


Figure 2.4: Extinction curves for different reddening laws implemented in this thesis. Extinction curves of SMC, LMC, and MW from Pei (1992) with $R_V = 2.93$, 3.08 and 3.16 respectively.

$E(B - V)$. A_V is the total extinction at the restframe V band at central wavelength of 5550 \AA . Low density regions have smaller R_V (steeper far-UV rise) and smaller dust grains; denser regions have larger R_V (flatter far-UV rise) and larger dust grains **references**. The parameters a_i , b_i , and n_i are different for the SMC ($R_V = 2.93$), LMC ($R_V = 3.16$), and MW ($R_V = 3.08$) extinction model (see Pei 1992 for complete parameter list). The peculiarity of the SMC law is the lack of 2175 \AA bump and even steeper rise in the far UV, rising faster than $1/\lambda$ (Prevot et al. 1984; Gordon et al. 2003). The LMC extinction curve is characterized by a weaker 2175 \AA bump and a stronger far-UV rise than the MW extinction curve (see Fig. 2.4; Nandy et al. 1981; Koornneef & Code 1981). Pei (1992) suggested that the absence or weakness of the bump in SMC and LMC sightlines can be explained by a difference in the relative abundances of graphite and silicate grains.

The important characteristic of the MW extinction law is the strongest 2175 \AA extinction bump and weakest far-UV curvature compared to the LMC and the SMC (see Fig. 2.4). The parameterization for the MW was advocated by Cardelli et al. (1989) with $R_V = 3.1$ to fit the Galactic average. It provides a better estimation of far UV curvature with fixed bump strength and varying R_V . It is defined as

$$A_\lambda = A_V \left(a(x) + \frac{b(x)}{R_V} \right) \quad \text{where } x = \lambda^{-1}$$

$a(x)$ and $b(x)$ are wavelength dependent polynomials controlling the UV, optical, and NIR regimes of the extinction curve. I also fitted the data with the Fitzpatrick & Massa (1986) extinction model. This was especially useful for the cases where there is clear evidence for a 2175 \AA extinction bump. The parameterization for the Fitzpatrick & Massa

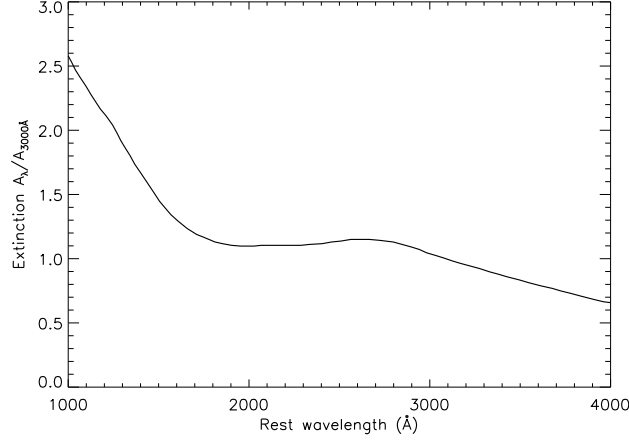


Figure 2.5: SN-origin extinction curve inferred from a BAL QSO at $z = 6.2$ (Maiolino et al. 2004).

(1986) extinction curve in the UV range is given as

$$A_\lambda = A_V \left(\frac{1}{R_V} k(\lambda - V) + 1 \right)$$

where

$$k(\lambda - V) = \begin{cases} c_1 + c_2x + c_3D(x, x_0, \gamma) & x \leq c_5 \\ c_1 + c_2x + c_3D(x, x_0, \gamma) + c_4(x - c_5)^2 & x > c_5 \end{cases}$$

and a Lorentzian-like Drude profile is given as

$$D(x, x_0, \gamma) = \frac{x^2}{(x^2 - x_0^2)^2 + x^2\gamma^2}$$

The entire underlying UV extinction component is specified by the intercept c_1 and the slope c_2 . c_3 is the strength of the 2175 Å bump, x_0 is the centroid of the bump and γ controls the width of the bump. These three parameters fit the 2175 Å absorption bump. c_4 and c_5 give the far UV curvature of the extinction curve. The extinction properties in the NIR and optical are characterized using spline interpolation points (see Fitzpatrick & Massa 2007). The Fitzpatrick & Massa (1986) parameterization provides a greater freedom for fitting the extinction curve than any of the other parameterizations. Particularly it is useful to fit the 2175 Å bump cases where we see variation in the strength and width of the bump.

2.4.1 SUPERNOVA EXTINCTION CURVE

The evolution of dust in the early Universe is still poorly understood. As discussed before, theoretically a transition in dust properties is expected at $z \gtrsim 5$ (Dwek et al. 2007; Morgan & Edmunds 2003; Marchenko 2006; Todini & Ferrara 2001). This scenario has

been tested through observations of a reddened quasars at high redshift (Maiolino et al. 2004; Gallerani et al. 2010). A peculiar, SN-origin, dust extinction curve was claimed in the spectrum of the broad absorption line QSO (BAL QSO) SDSS J1048 + 46 at $z = 6.2$ (Maiolino et al. 2004, but see (Gallerani et al. 2010)). The inferred dust extinction curve is different with respect to any of the extinction curves observed at low redshift (Hopkins et al. 2004). The SN-origin extinction curve is in good agreement with the extinction curve predicted for dust formed in SN ejecta using a simple model without dust destruction. So far this is the only direct evidence for a dominant SN-origin extinction curve in the early Universe. The unusual extinction curve is also claimed in GRB 071025 at $z \sim 5$ (Perley et al. 2010). The unusual extinction curve is rather flat at longer wavelengths and steeply rises at $\lambda_{\text{rest}} < 1700 \text{ \AA}$ (see Fig. 2.5). The extinction curve is computed in the wavelength range of $\lambda_{\text{rest}} = 1000 - 4000 \text{ \AA}$ and therefore the reference extinction is derived at 3000 \AA instead of restframe V -band. In this thesis I made use of the SN-origin extinction curve to study dust in the afterglows of high redshift GRBs and also to see the evolution of dust in distant Universe. I have found no evidence for the SN-origin extinction curve in any case.

PART II

2.5 ABSORPTION LINE SYSTEMS

Several intervening absorbers are detected in the spectra of high redshift quasars (e.g. Weymann et al. 1979; Sargent et al. 1980; Pettini et al. 1997; Rauch 1998; Impey et al. 1999; Wolfe et al. 2005). DLAs from the host galaxies of GRBs are also seen in GRB afterglow spectra (e.g. Watson et al. 2006a; Jakobsson et al. 2006a; Ledoux et al. 2009). These absorption systems pinpoint dark, diffuse and cold regions in the Universe. Because the DLA comprise the neutral gas reservoir for star formation at high redshifts, a determination of their metal content is useful to understand the chemical evolution of star forming galaxies.

The mass of metals per unit comoving volume that the DLA contribute indicates that these systems are chemically enriched. The chemical enrichment of gas is obtained from column density measurements of resonance lines. Abundance estimations for Silicon, Sulphur and Iron are possible because of the presence of different transitions with a wide range of oscillator strengths. The absorption lines in the ISM are naturally broadened owing to the finite lifetime of the upper energy state. In the rest frame the line is broadened by two mechanisms: *i*) Doppler broadening due to movement of atoms with different velocities and *ii*) natural broadening due to life time of different transitions. The convolution of these mechanisms is called Voigt profile where Doppler broadening produces a Gaussian profile and natural broadening produces a Lorentzian profile. The line profile $\phi(a, u)$ is defined as

$$\phi(a, u) = \frac{H(a, u)}{\Delta\nu_D \sqrt{\pi}}$$

$H(a, u)$ is the Voigt function which is used to compute the intensity of an atomic absorption line profile (see Armstrong 1967, for more detail).

$$H(a, u) = \frac{a}{\pi} \int_{-\infty}^{\infty} \frac{e^{-y^2}}{a^2 + (u - y)^2} dy$$

Here u is dimensionless frequency offset ($u = (\nu - \nu_o)/\Delta\nu_D$) and a is the damping parameter ($a = \Gamma/4\pi\Delta\nu_D$). The Doppler width $\Delta\nu_D$ and the transition rate Γ are given as $\Delta\nu_D = \nu_o b/c$ and $\Gamma = \gamma + 2\nu_{col}$. b is the Doppler parameter, defining the kinematics of the gas and given by $b = \sqrt{2kT/m}$.

The column density N of a certain ion is given as $N = \int n_l dl$ with n_l the density of atoms and l the path length of the absorbing matter. The relation between the equivalent width (EW) and the column density for different values of doppler parameter is known as the curve of growth (see Petitjean 1998). The curve of growth has three different regimes: *i*) For an unsaturated line with the optical depth of $\tau_0 < 0.1$, the EW

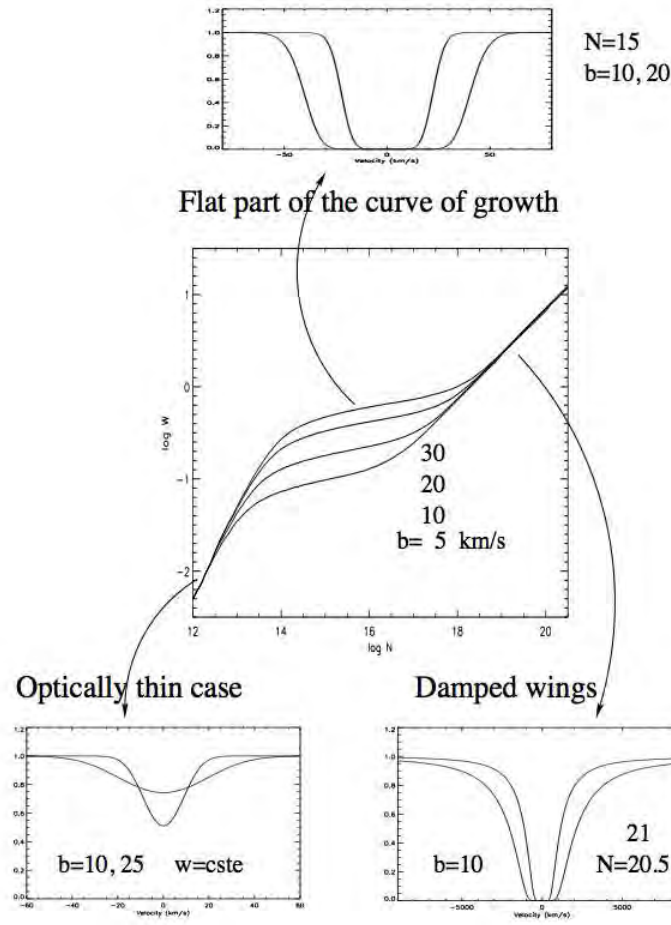


Figure 2.6: Curve of growth: EW and column density in log-log space. The three characteristics regions of the curve of growth are shown Credit: Patrick Petitjean.

does not depend on b and N and can be computed straightforward by the relation:

$$N \text{ (cm}^{-2}\text{)} = \frac{\text{EW}_{\text{rest}}}{\lambda^2 f} \frac{1.13 \times 10^{20} \text{ cm}^2}{\lambda^2 f}$$

here f is the oscillator strength which can be obtained for each transition from Morton (1991) and λ is the . *ii*) In the logarithmic regime (flat-part) N largely depends on b (km s⁻¹) at a given EW and this makes the determination of b and N very uncertain. At the center of the line EW will be

$$\text{EW}_{\text{rest}} = 2 \frac{b \lambda_o}{c} \sqrt{\ln(\tau_o)}$$

The optical depth, τ_o , of resonance lines is independent of density and temperature of the absorbing gas. The optical depth at the center of the line is given as

$$\tau_o = 1.497 \times 10^{-15} \frac{N f \lambda_o}{b}$$

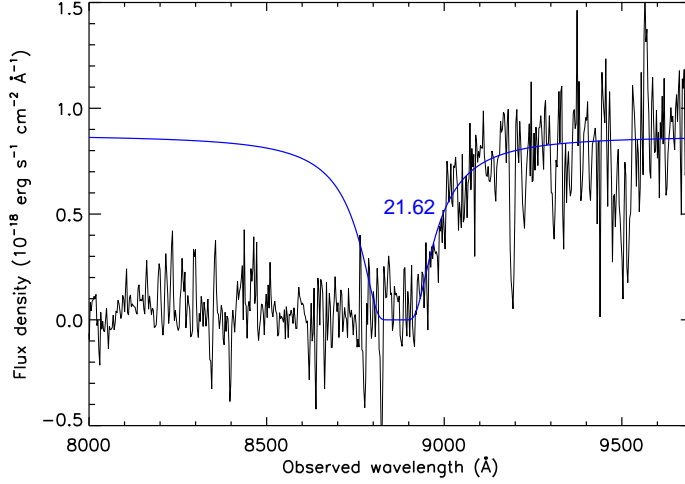


Figure 2.7: *H I column density of GRB 050904 at $z = 6.295$ at 3.4 days after the burst. The blue curve shows the fit to the DLA absorption. The black curve is the optical spectrum of GRB 050904 obtained with the Subaru Telescope.*

iii) In case of prominent damping wings, the EW does not depend on b and the column density determination is very accurate with

$$\text{EW}_{\text{rest}} = 2.64\lambda_o \frac{b\sqrt{a}}{c} \times \sqrt{\tau_o}$$

High resolution spectroscopy can resolve the actual shape of the line profile. This makes it easy to adopt Voigt profiles directly to fit the lines (see above). There are many software programs which read in the atomic data, laboratory wavelengths and oscillator strengths (Morton 1991) and fit the absorption lines. In this thesis, I used the ESO-MIDAS package FITLYMAN (Fontana & Ballester 1995) to fit the different lines. FITLYMAN takes the normalized spectrum, the error spectrum, the redshift of the object and line IDs and fit Voigt profiles to the absorption lines. FITLYMAN finds the best global fit using a χ^2 minimization algorithm which includes the spectral resolution and returns best fit parameters for central wavelength, column density and Doppler turbulent broadening as well as errors on each quantity. Fig. 2.7 shows an example of the DLA fit to the spectrum of GRB 050904.

2.5.1 METALLICITIES

A central aspect of the history of the Universe is the formation and evolution of galaxies, and their gradual build-up of metallicity (Pei & Fall 1995; Sommer-Larsen & Fynbo 2008; Fynbo et al. 2010). Abundance refer to the elements in the gas phase. Some fraction of each element could be depleted onto dust grains. Therefore metallicities are best measured from the volatile elements which are relatively undepleted in the ISM.

The best element to determine the metallicity is Zn as it is least dust depleted in the ISM (Jenkins 2004). If Zn is not available one can use S and O to obtain metallicity (Wolfe et al. 2005). Like Zn, S and O are volatile and are relatively undepleted in the ISM. The refractory element Si is mildly depleted in DLAs and can be used as an unbiased metallicity tracer (see for a review Wolfe et al. 2005). We can compare the measured abundance of elements with the one in the solar neighbourhood which then gives us the metallicity of the material. To obtain the metallicities we can use the relation:

$$[X/H] = \log \left(\frac{N_X}{N_H} \right)_{\text{object}} - \log \left(\frac{N_X}{N_H} \right)_{\text{solar}}$$

where X stands for a specific metal and N represents the column density of that element. The second part of the term is obtained from the solar element abundances for each metal species, given as

$$\log \epsilon_X = \log \left(\frac{N_X}{N_H} \right)_{\text{solar}} + 12$$

where $\log \epsilon_X$ is the astronomical scale for logarithmic abundance of element X. The value 12 is attributed to the solar hydrogen abundance i.e. $\log \epsilon_X - 12.0$. This implies that metallicities can be obtained for each transition observed in cosmological objects by using

$$[X/H] = \log \left(\frac{N_X}{N_H} \right)_{\text{object}} - \log \epsilon_X + 12$$

where solar abundances in $\log \epsilon_X$ are measured (see Asplund et al. 2009). $[X/H] = 0$ is the solar metallicity (Z_\odot), $[X/H] = -1$ corresponds to $1/10 Z_\odot$. The measured metallicity can be very different from the average metallicity of that galaxy because it only represents the metallicity along the line of sight.

2.6 X-SHOOTER DATA REDUCTION

As it is mentioned above that Q0151+048B is a faint quasar, therefore, it was not observed spectroscopically before. While spectra from different telescopes had been taken for the brightest member Q0151+048A, confirming the presence of a DLA with $z_{\text{abs}} \gtrsim z_{\text{em}}$. It was firstly expected like the quasar A its companion quasar B is also absorbed by the DLA. Later deep imaging unambiguously confirmed that Q0151+048B is not covered by the DLA (Fynbo et al. 1999). The spectra of the QSO pair were obtained with Nordic Optical Telescope (NOT) on 24 - 25 August 2008 during the summer school (see Fig. 2.8). It turned out that Q0151+048B is not covered by the DLA as suggested by Fynbo et al. (1999). To explore more on this particular object we asked for X-shooter observation.

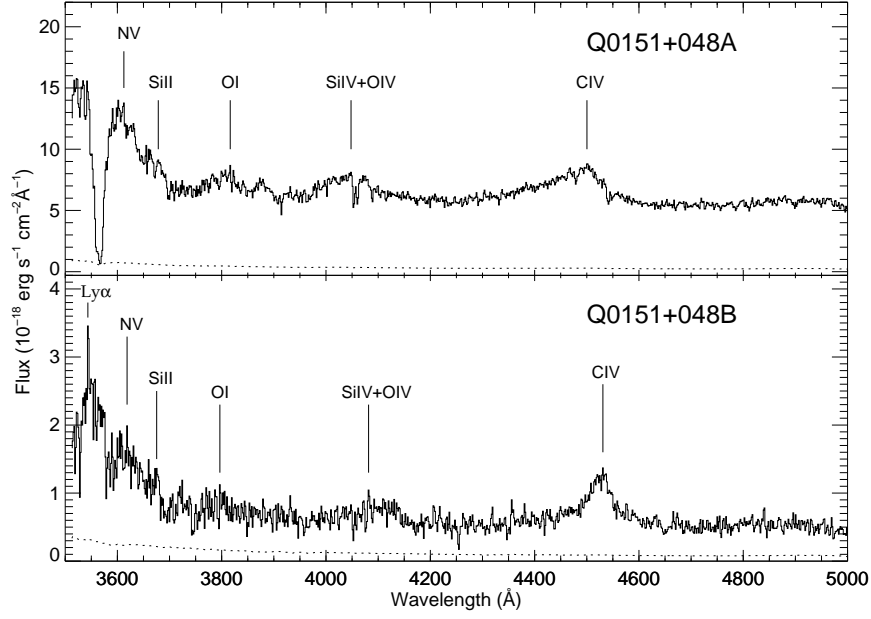


Figure 2.8: *Upper panel* : Optical spectrum of Q0151+048A showing the DLA absorption. *Lower panel* : Spectrum of Q0151+048B. The lower dotted line in both panels shows the 1σ noise spectrum.

X-shooter, mounted on ESO-VLT, is a single target echelle spectrograph that covers the spectral range from the UV to the K -band in a single exposure. X-shooter operates at intermediate resolutions in the three arms. The data were obtained during two observing runs. The QSO pair was integrated at the same time with both quasars lying on a single slit.

The X-shooter data were processed using the X-shooter data reduction pipeline (Goldoni et al. 2006; Modigliani et al. 2010). The pipeline takes in set of files which contain list of raw frames including flat, bias and science frames. Calibration files are also included to perform wavelength calibration and final order merging. The *xsh_util_physmod* recipe firstly generate theoretical maps containing the instrument spectral format. The pipeline corrected UVB and VIS raw frames for bias with the recipe *xsh_mbias* and NIR frames for dark current with *xsh_mdark*. This recipe *xsh_orderpos* traces accurately the order centers. After division by the flat field with *xsh_mflat* recipe, the pipeline performed background subtraction, corrected cosmic ray hits using the method developed by van Dokkum (2001) and subtracted sky emission lines using the Kelson (2003) method. The individual orders were extracted and rectified in wavelength space by *xsh_2dmap*. This was done by using the previously obtained wavelength solution from calibration frames. The pipeline then uses *xsh_scired_slit_stare* or *xsh_scired_slit_nod* recipe where individual orders were merged afterwards and in the overlapping regions the merging was weighted by the errors which were be-

ing propagated during the reduction process. From the final 2D merged spectrum one dimensional spectra for Q 0151+048A & B were extracted.

This chapter is based on:

T. Zafar, D. J. Watson, D. Malesani, P. M. Vreeswijk, J. P. U. Fynbo, J. Hjorth, A. J. Levan and
M. J. Michałowski – *No evidence for dust extinction in GRB 050904 at $z \sim 6.3$* A&A, 2010, 515, A94

3

MULTI EPOCH SED ANALYSIS OF GRB 050904 AT $z \sim 6.3$

ABSTRACT –

Gamma-ray burst (GRB) afterglows are excellent and sensitive probes of gas and dust in star-forming galaxies at all epochs. It has been posited that dust in the early Universe must be different from dust at lower redshifts. To date two reports in the literature directly support this contention, one of which is based on the spectral shape of the afterglow spectrum of GRB 050904 at $z = 6.295$. Here we reinvestigate the afterglow of GRB 050904 to understand cosmic dust at high redshift. We address the claimed evidence for unusual (supernova-origin) dust in its host galaxy by simultaneously examining the X-ray and optical/near-infrared spectrophotometric data of the afterglow. We derived the intrinsic spectral energy distribution (SED) of the afterglow at three different epochs, 0.47, 1.25, and 3.4 days after the burst. We made a fresh reduction of the Swift X-ray data, the 1.25 days FORS2 z -Gunn photometric data, the spectroscopic and z' -band photometric data at ~ 3 days from the Subaru telescope, as well as the critical UKIRT Z -band photometry at 0.47 days, upon which the claim of dust detection largely relies. We find no evidence of dust extinction in the SED at any time. We computed flux densities at $\lambda_{\text{rest}} = 1250 \text{ \AA}$ directly from the observed counts at all epochs. In the earliest epoch, 0.47 days, where the claim of dust is strongest, the Z -band suppression is found to be weaker ($0.3 \pm 0.2 \text{ mag}$) than previously reported and statistically insignificant ($< 1.5\sigma$). Furthermore, we find that the photometry of this band is unstable and difficult to calibrate. From the afterglow SED we demonstrate that there is no evidence of dust extinction in GRB 050904 – the SED at all times can be reproduced without dust, and at 1.25 days in particular, significant extinction can be excluded, with $A(3000 \text{ \AA}) < 0.27 \text{ mag}$ at 95% confidence using the supernova-type extinction curve. We conclude that there is no evidence of any extinction in the afterglow of GRB 050904 and that the presence of supernova-origin dust in the host of GRB 050904 must be viewed skeptically.

3.1 INTRODUCTION

Gamma-ray bursts (GRBs) can be detected up to the onset of reionization (e.g. Tanvir et al. 2009; Salvaterra et al. 2009) due to their brightness in the first few hours after the explosion (Lamb & Reichart 2000). GRBs are transient sources followed by long lasting afterglows, emitting energy intensely across the full range of the electromagnetic spectrum. GRB afterglows are effective and informative probes for the detailed study of cosmic dust at high redshifts due to their simple power-law spectra, high luminosities and locations in star-forming environments.

Interstellar dust has a crucial significance in the appearance and evolution of star formation in the early Universe. It is still under debate whether interstellar dust properties have evolved as a function of redshift. At high redshift ($z > 5-6$) it has been suggested that dust might originate in sources other than the evolved asymptotic giant branch stars that are the dominant source of dust production in the local Universe (Gehrz 1989; Dwek et al. 2007). Previous studies reported that dust in cosmological objects at $z > 6$ is predominantly produced in the ejecta of core-collapse supernovae (SNe), rather than the evolved stars which are missing on short timescales (Todini & Ferrara 2001; Morgan & Edmunds 2003; Nozawa et al. 2003; Dwek et al. 2007; Marchenko 2006; Hirashita et al. 2005). Recently, however, Valiante et al. (2009) calculated that the most massive asymptotic giant branch (AGB) stars could produce dust on time scales short enough to dominate dust production by $z \sim 6$. Observationally, Maiolino et al. (2004) found an unusual extinction curve in the most distant known broad absorption line quasar (BAL QSO) at redshift $z = 6.2$, consistent with what could be expected from dust produced in core-collapse SNe.

The progenitors of long-duration GRBs are known to be short-lived massive stars (Galama et al. 1998a; Hjorth et al. 2003b; Stanek et al. 2003; Malesani et al. 2004). GRB 050904 at $z = 6.295$ was a long duration GRB. It was extremely luminous and is the third most distant known GRB to date. GRB 050904 was detected by *Swift* on 2005 September 4 at $t_0 = 01:51:44$ UT (Cummings et al. 2005). Substantial multi-wavelength follow-up was carried out simultaneously for GRB 050904 with several ground based facilities. Previous analysis of the rest-frame UV afterglow found no evidence of dust (Tagliaferri et al. 2005; Haislip et al. 2006; Kann et al. 2007; Gou et al. 2007). Later Stratta et al. (2007) re-examined the afterglow SED at different epochs and claimed the detection of dust absorption with an extinction curve consistent with that used to explain the spectrum of the highest redshift BAL QSO, but inconsistent with the dust typical of the local Universe.

The claim of detection of SN-origin dust in GRB 050904 is of fundamental importance to the question of the origin of dust in the early Universe, a very vexed problem for high redshift sub-mm galaxies (see, e.g. the discussion in Michałowski et al. 2010b). It was the first only direct observational evidence of dust from SNe in a high redshift

star-forming environment. In this paper we review the relevant data to test whether dust is required by these observations and if so, what kind of dust is needed. The outline of the paper is as follows: In §2 we describe the detailed multi-band spectral analysis of the afterglow of GRB 050904 at different epochs. In §3 we present results from the SED of the afterglow. In §4 we discuss possible scenarios. In §5 we provide our conclusions.

3.2 MULTI-WAVELENGTH OBSERVATIONS OF THE AFTERGLOW

3.2.1 X-RAY ANALYSIS

Swift's X-ray Telescope (XRT) localized the afterglow of GRB 050904. The XRT data (in the 0.3–10.0 keV energy range) were extracted and reduced using the HEAsoft software (version 6.4). We computed the X-ray spectra at three epochs, specifically 0.47, 1.25 and 3.4 days post-burst, chosen as the epochs with the best spectroscopic and photometric optical/near-infrared coverage. X-ray spectra at three epochs were created in a standard way using the most recent calibration files.

For our analysis, it is important to obtain an accurate estimate of the absolute flux for these X-ray spectra. The X-ray lightcurve is extremely variable, exhibiting long lasting flaring activity (Watson et al. 2006b; Cusumano et al. 2006; Gendre et al. 2006). The flares suggest two separate components, which may be due to a number of causes, possibly activity of the GRB central engine (e.g. Burrows et al. 2007). At late times the X-ray count rate is very low (see Fig. 6.8), therefore, we aim to get an accurate estimation of the flux which includes the uncertainty due to the flares. We fitted the afterglow lightcurve by assuming a smoothly broken power-law (Beuermann et al. 1999) to get an approximate overall X-ray lightcurve. The fit to the afterglow lightcurve results in at most a 30 – 40% scatter around this fit at all epochs. We then normalized the X-ray spectra to the lightcurve fit at the relevant SED epoch. The procedure results in X-ray spectra with the best estimate of the slope and flux at the relevant SED epoch, and with an additional overall 30 – 40% uncertainty on their absolute flux levels.

3.2.2 NEAR-IR AND OPTICAL IMAGING

Several telescopes obtained photometric observations of the afterglow in the optical and near-infrared bands (Tagliaferri et al. 2005; Haislip et al. 2006; Price et al. 2006). For a comprehensive investigation of the SED, we gathered optical and near-infrared photometry at three epochs. Stratta et al. (2007) suggested unusual dust particularly on the basis of the *Z*-band observation at ~ 0.5 days, taken by the UK Infrared Telescope (UKIRT) equipped with WFCAM. Therefore, we re-reduced these *Z*-band data obtained at $t_0 + 0.47$ days. The object has low signal to noise. Our best estimate of the magnitude comes from point-spread function (PSF)-matched photometry, carried

out using the DAOPhot package within IRAF. For consistency we also carried out aperture photometry (with Gaia and IRAF/PHOT), and found the afterglow Z -band magnitude to be strongly sensitive to the chosen sky extraction annulus, being in some cases brighter by \sim half a magnitude, although with large errors. This uncertainty is worth noting.

At 1.25 days z -band photometry was obtained with the 8.2m ESO Very Large Telescope (VLT) by using the FOcal Reducer and low dispersion Spectrograph 2 (FORS2) z -Gunn filter. The object is detected with high signal to noise and using aperture photometry we could significantly reduce the error reported by Tagliaferri et al. (2005), which was likely mostly due to calibration issues.

At 3.3 days after the burst, z' -band photometry was carried out with the 8.2m Subaru telescope (Iye et al. 2004) using the Faint Object Camera and Spectrograph (FOCAS; Kashikawa et al. 2002). We re-analysed the photometric data using aperture photometry. We compared our FOCAS z' result with the Gemini South GMOS z' value at 3.16 days obtained by Haislip et al. (2006). Correcting for the time difference between the two observations using a broken power-law with $\alpha_1 = 0.72^{+0.15}_{-0.20}$, $\alpha_2 = 2.4 \pm 0.4$, $t_b = 2.6 \pm 1.0$ days (Tagliaferri et al. 2005), we found these photometric measurements to be consistent within the statistical uncertainties.

Other photometric data were taken from the literature (Haislip et al. 2006; Tagliaferri et al. 2005) when available at a time close to our nominal SED epochs (J -band at 0.49 days). All H and K_s data as well as J at 1.25 and 3.4 days were derived from the best-fit lightcurves of Haislip et al. (2006) and Tagliaferri et al. (2005). At 1.25 days we used the Y -band photometry from the lightcurve computed in this band (Haislip et al. 2006).

We corrected the observed magnitudes for extinction in the Milky Way (MW) using the Schlegel et al. (1998) maps with $R_V = 3.1$ and $E(B - V) = 0.081$ mag along the line of sight of the burst. Potential systematic uncertainties in the Galactic extinction correction have no significant effect on our results. The independent analysis of Dutra et al. (2003) confirms the Schlegel et al. (1998) maps for low $E(B - V)$. For the z -bands considered here, even assuming a 30% uncertainty in the Galactic value would correspond to an extinction uncertainty of 0.03 mag which is smaller than the statistical uncertainties we find for the extinction in the host galaxy (see Table 4.1). Effects in the J , H , and K_s bands will be smaller still. An under-estimate of the Galactic extinction would lead to a smaller host galaxy extinction than we find in the current analysis.

The z -Gunn, FOCAS z' , GMOS z' and Sloan Digital Sky Survey (SDSS¹; Fukugita et al. 1996) z filters have almost the same profile across the whole band and extend much redder than the UKIRT Z filter. It should be noted that since the $\text{Ly}\alpha$ absorption occurs in these bands, the filter wavelength coverage affects the observed magnitude significantly (see §3.2). Unless explicitly mentioned, in the rest of the paper we use the term “ z -band” to denote all of the three z filters, i.e. UKIRT Z , FORS2 z -Gunn and

¹<http://www.sdss.org/>

FOCAS z' .

3.2.3 GRISM SPECTROSCOPY

The optical spectrum of the afterglow was obtained with FOCAS at the Subaru telescope and the spectroscopic data were retrieved from the SMOKA science archive facility² (Baba et al. 2002). The afterglow was observed on 7 September 2005 for 4.0 hr. The exposure mid-time was 12:05 UT, corresponding to 3.4 days after the burst trigger (Kawai et al. 2006; Totani et al. 2006). The spectra were flux calibrated using the spectrophotometric standard star BD+28D4211 obtained on the same night. Individual spectra were combined following standard data reduction techniques using IRAF. The spectrum exhibits no flux below $\sim 8900 \text{ \AA}$, consistent with a break due to Ly α absorption at redshift $z \sim 6.3$ and the Ly α forest. The spectrum shows a flat continuum at the red wavelength end, revealing a series of metal absorption lines arising from different atomic species at $z = 6.295$, and an intervening C IV system at $z = 4.84$ (Kawai et al. 2006). The observed spectrum was corrected for Galactic extinction by assuming the Cardelli et al. (1989) extinction curve and as explained in §2.2 above.

We implemented Voigt profile fitting to the 3.4 day Subaru spectrum using the FIT-LYMAN package in MIDAS (Fontana & Ballester 1995). We measure a hydrogen column density of $\log \text{NH I (cm}^{-2}\text{)} = 21.62 \pm 0.02$, consistent with the value reported by Totani et al. (2006). It should be noted that z' -band photometry and spectroscopy of the afterglow were obtained with FOCAS at 3.3 and 3.4 days, respectively.

3.3 SED ANALYSIS

Stratta et al. (2007) studied the optical-UV rest-frame SED of the afterglow of GRB 050904 at 0.5, 1 and 3 day epochs and found a deficit in the z -band at 0.5 and 1 days, and (less significantly) at 3 days, compared to the JHK power-law extrapolation, claiming that dust reddening could explain the flux deficit. This required a SN-type extinction curve.

3.3.1 AFTERGLOW COMPOUND SED

Knowledge of the SED can address the z -band flux suppression issue, therefore, we computed the near-infrared to X-ray SED of GRB 050904 at three epochs, i.e. 0.47, 1.25 and 3.4 days. To facilitate comparison of the z -band flux, the SED at all epochs was normalized to the H -band flux, using the smoothly broken power-law presented by Tagliaferri et al. (2005). The normalized near-infrared photometry is generally consistent, but the X-ray spectra are much brighter at 0.47 and 1.25 days due to the intense afterglow flaring activity at these times. The consistency of the X-ray flux with the NIR SED extrapolation suggests that the X-ray afterglow at 3.4 days was relatively unaf-

²<http://smoka.nao.ac.jp/>

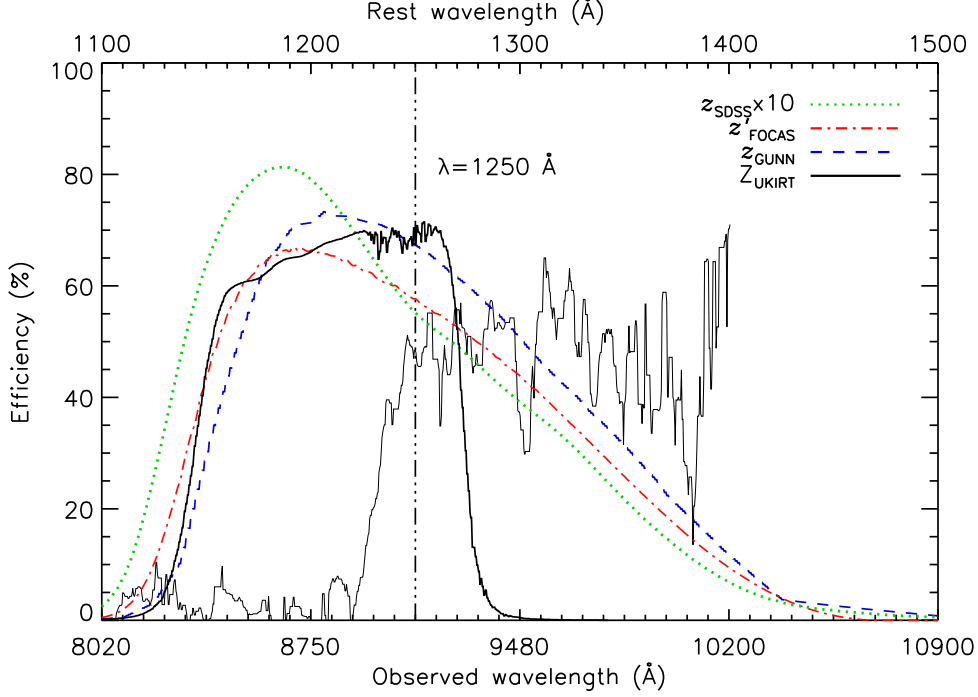


Figure 3.1: Filter transmission curves of SDSS z , FOCAS z' , FORS2 z -Gunn and UKIRT Z . The grey curve corresponds to the median-filtered optical spectrum at 3.4 days (arbitrarily normalized). The vertical triple black dot-dashed line represents the wavelength (1250 Å) where we computed the flux density (see § 3.2).

ected by flares. The composite SED of the afterglow of GRB 050904 at three different epochs is shown in Fig. 6.8.

3.3.2 COMPARING THE z -BAND FILTER RESPONSES

Since the z -band photometry is strongly affected by the $\text{Ly}\alpha$ absorption, we performed spectro-photometric analysis by utilizing the total effective filter transmission functions including detector responses (Fig. 3.1). We use the following method that allows for a clean comparison of the different z -band magnitudes of the afterglow, taken at 0.47, 1.25, and 3.4 days after the burst, with the filters UKIRT Z , VLT z -Gunn, and Subaru z' , respectively. The method essentially constructs the SEDs of stars in the field and uses these to make a direct comparison of the afterglow magnitudes at each epoch.

First, in each afterglow image we select several non-saturated reference stars with known SDSS and Two Micron All Sky Survey (2MASS³; Skrutskie et al. 2006) magnitudes. Using the 2MASS J -band, and the SDSS z and i , we construct a rudimentary SED for each reference star, where we convert the magnitudes to flux densities (in erg

³<http://www.ipac.caltech.edu/2mass/>

$\text{s}^{-1} \text{cm}^{-2} \text{\AA}^{-1}$) at the central wavelength of the SDSS and 2MASS filters. We connect these flux densities with a linear interpolation, and integrate the reference star SED convolved with the filter response curve relevant to that image, retrieving the band-integrated flux in $\text{erg s}^{-1} \text{cm}^{-2}$. Second, from the image we measure the counts for the reference stars using aperture or PSF photometry, determining the conversion factor between counts and flux. Using this factor, we eventually compute the (band-integrated) afterglow flux from its measured counts. We used several comparison stars to evaluate the accuracy of the procedure. At 0.47, 1.25, and 3.3 days, we find a scatter of 0.02, 0.04, and 0.02 mag using 8, 10, and 5 reference stars, respectively. The small scatter confirms the robustness of our method.

In the deep FORS2 and FOCAS z -band images, the brightest stars are heavily saturated, and suitable reference stars are lacking since the fainter stars have large uncertainties in the SDSS and 2MASS catalogues. Therefore, we calibrated a set of faint stars using the UKIRT J and z -band images, based on the 2MASS and SDSS catalogs. For the z band, due to the difference in the UKIRT and SDSS filters, appropriate color terms were taken into account, achieving a photometric accuracy of ≈ 0.02 mag. Given the higher sensitivity of the SDSS in the i band, suitable calibrators for the VLT and Subaru images were available directly from the SDSS catalog. Note that our calibration is entirely based on the SDSS and 2MASS catalogs, therefore, our analysis is not dependent on the sky conditions when the data have been acquired.

The third and final step is to convolve the relative afterglow spectral shape (as measured from the Subaru spectrum that was obtained at 3.4 days) with the three different z -band filter response curves, where the spectrum is rescaled in absolute terms to recover the band-integrated flux (in $\text{erg s}^{-1} \text{cm}^{-2}$) determined for each epoch (see above). We note that this method does not rely on the absolute flux calibration of the Subaru spectrum; it merely uses the photometry to rescale it, and therefore the errors only include the errors in the aperture/PSF photometry, the error from the conversion factor, and the Subaru noise error when convolving it with the filter response curves. After rescaling of the spectrum, the afterglow flux density (in $\text{erg s}^{-1} \text{cm}^{-2} \text{\AA}^{-1}$) can be compared at any pivot wavelength, after the H -band normalization. At all epochs we computed the flux density at $\lambda_{\text{rest}} = 1250 \text{\AA}$, which was selected since it is close to the peak of all the involved filter transmission curves (see Fig. 3.1), and is separated from the metal absorption lines visible in the spectrum (Kawai et al. 2006).

The single but important assumption in this method is that the spectral shape of the afterglow is not changing from 0.47 to 3.4 days. This is in some sense the null hypothesis that we are trying to test: dust destruction would produce a change in the relative spectral shape, and would therefore produce a change in the z -band brightness relative to the H -band normalization. Other effects, such as a variable HI column, or a change in the spectral slope due to e.g. the cooling frequency crossing the z -band, could also in principle cause such a change. However, if the resulting afterglow z -

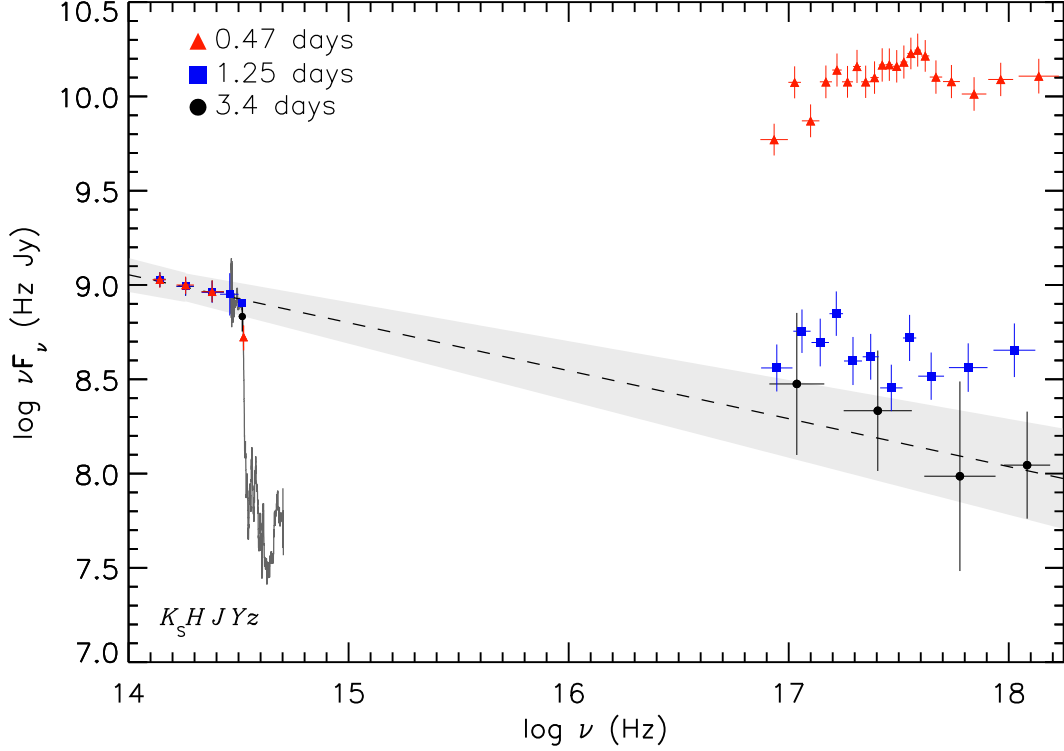


Figure 3.2: Near-infrared to X-ray spectral energy distribution of the afterglow of GRB 050904 at 0.47 (red triangles), 1.25 (blue squares) and 3.4 days (black circles) after the burst. The SED at 0.47 and 1.25 days is scaled to the H -band at 3.4 days. The solid grey curve represents the median-filtered optical spectrum at $t_0 + 3.4$ days. The black dashed line corresponds to a power-law fit to the near-infrared to the X-ray data at 3.4 days with a spectral index $\beta = 1.25 \pm 0.05$. The grey shaded area represents the 1σ uncertainty on the power-law.

band brightness (normalized to the H -band) between 0.47 and 3.4 days does not show a significant change, then this would provide strong support for the null hypothesis that the spectral shape is not changing.

Following the above procedure, we find the afterglow to have a flux density at 1250 Å of 14.7 ± 1.32 , 9.41 ± 0.24 and 2.13 ± 0.22 μJy at 0.47, 1.25 and 3.3 days, respectively. We find that the normalized 0.47 day UKIRT Z -band brightness is 0.27 ± 0.18 mag fainter than the FOCAS z' -band brightness at 3.3 days. At 1.25 days, the normalized FORS2 z -Gunn brightness is brighter by 0.17 ± 0.15 mag compared to the FOCAS z' -band brightness at 3.3 days. The uncertainties here also include the uncertainties in the normalization, i.e. the errors in the H -band photometry (0.06 mag). Therefore, there is no evidence for variability of the spectral shape around the z band. In particular, after taking into account the appropriate filter shapes and color effects, there is no significant deficiency of flux in the z -band flux at 0.47 days compared to later epochs (Haislip et al.

2006; Stratta et al. 2007).

3.4 DISCUSSION

At 0.47 days post-burst, we find a flux deficit in the UKIRT Z -band compared to the 3.3 days Subaru photometry that is only significant at $< 1.5\sigma$ level. This low significance result, combined with the difficulty in determining the Z -band magnitude at 0.47 days alluded to in §2.2, suggests that a change in the spectrum between 0.47 and 3.4 days does not have strong observational support. If the effect were real then such a flux deficit could be explained by: (i) dust extinction as suggested by Stratta et al. (2007) with a SN-origin extinction curve, or (ii) gas absorption. Previously Haislip et al. (2006) also suggested that absorption due to molecular hydrogen could give rise to the Z -band flux deficit at 0.47 days.

3.4.1 DUST IN THE GRB 050904 HOST GALAXY

The claim of SN-type dust in GRB 050904 is important because of the possibility of observing the evolution of cosmic dust at high redshift. Stratta et al. (2007) suggested SN-type dust extinction in the host galaxy of GRB 050904 with an extinction curve inferred for a BAL QSO at $z = 6.2$ (Maiolino et al. 2004). The unusual extinction curve is rather flat at longer wavelengths and steeply rises at $\lambda < 1700 \text{ \AA}$. The best-fit estimates of Stratta et al. (2007) of the extinction at 3000 \AA in the rest-frame, $A(3000 \text{ \AA})$, were 0.89 ± 0.16 , 1.33 ± 0.29 , and $0.46 \pm 0.28 \text{ mag}$ at 0.5, 1, and 3 days, respectively.

It is clear from our broad-band SED at 3.4 days (see Fig. 6.8) that the extrapolation of the near-infrared power-law is consistent with a single power-law to the X-ray spectrum, i.e. consistent with both the slope and flux level of the X-ray spectrum at that time. We can also clearly see that there is no evidence in the flux-calibrated optical/near-infrared spectrum at 3.4 days for any extinction – the continuum just redward of the $\text{Ly}\alpha$ absorption is consistent with the single JHK power-law. Both facts mean that there is no evidence for dust extinction at 3.4 days. We fitted a dust-attenuated power-law using a dust model for the Small Magellanic Cloud (SMC, $R_V = 2.93$; Pei 1992) and the SN-origin extinction model of Maiolino et al. (2004) to the 0.47, 1.25 and 3.4 day $zYJHK_s$ data (from the z -band, we compute the flux density at $\lambda_{\text{rest}} = 1250 \text{ \AA}$). The best fit parameters are reported in Table 4.1. With our revised z -band photometry, extinction at the level suggested by Stratta et al. (2007) can be ruled out at all three epochs (see Fig. 3.3). In no case the computed absorption is significant at more than 1.5σ level.

Extinction-correcting the 1.25 day SED at the level fitted by Stratta et al. (2007) makes its extrapolation overshoot the X-ray spectrum, hinting that $\sim 1 \text{ mag}$ of extinction at 3000 \AA is not required. More importantly, the Y -band photometry, with a central wavelength of 1400 \AA in the rest-frame, at 1.25 days (Haislip et al. 2006), is consistent

Table 3.1: Best fit parameters of the SED at different epochs.

Days	Model	β	$A(3000 \text{ \AA})$ (mag)	A_V^a (mag)
0.47	PL	1.28 ± 0.11
	PL+SN	1.22 ± 0.24	0.3 ± 0.22	...
	PL+SMC	1.23 ± 0.08	0.1 ± 0.07	0.05 ± 0.04
1.25	PL	1.24 ± 0.09
	PL+SN	1.27 ± 0.2	0.05 ± 0.11	...
	PL+SMC	1.17 ± 0.51	0.01 ± 0.04	0.01 ± 0.02
3.4	PL	1.25 ± 0.05
	PL+SN	1.23 ± 0.21	0.22 ± 0.24	...
	PL+SMC	1.24 ± 0.07	0.056 ± 0.059	0.042 ± 0.044

^aThe SN-origin extinction curve has been only computed in the range $\lambda_{\text{rest}} = 1000 - 4000 \text{ \AA}$, hence it is not possible to provide A_V .

with the near-infrared power-law extrapolation. Such consistency would not be expected in the Stratta et al. (2007) dust hypothesis since $A(1400 \text{ \AA})$ is about 1.75 times the $A(3000 \text{ \AA})$ in the Maiolino et al. (2004) model, and the Y -band photometry should therefore lie a factor of 2 below a power-law extrapolation, while it does not (Fig. 3.3), though its error is large. As it can be seen in the middle panel of Fig. 3.3, the SED at 1 day follows a simple power-law and provides strong constraints on dust absorption. Again, it seems likely that not only is there no evidence for SN-type extinction in GRB 050904 after 1.25 days, but that there is no evidence for any dust extinction at all at ~ 1 day or later.

There are also strong arguments against a SN-origin dust interpretation at 0.47 days. While dust reddening has been unequivocally observed in lower redshift GRBs (e.g. Kann et al. 2006; Fynbo et al. 2009; GRB 050401: Watson et al. 2006a; GRB 991216: Vreeswijk et al. 2006; GRB 050408: Foley et al. 2006; de Ugarte Postigo et al. 2007; GRB 070802: Elíasdóttir et al. 2009; GRB 080607: Prochaska et al. 2009), so far SN-origin dust has never been seen before in any GRB host. Moreover there is no compelling evidence of dust extinction in any GRB beyond $z = 5$. A possible exception is GRB 071025 (which has a photometric redshift $4.4 < z < 5.2$ Perley et al. 2010), which shows indications of a significant dust column. Notable are the two bursts at higher redshift than GRB 050904, i.e. GRB 080913 at $z = 6.7$ (Greiner et al. 2009), and GRB 090423 at $z = 8.2$ (Tanvir et al. 2009; Salvaterra et al. 2009), neither of which show any sign of extinction. Second, given that dust can be excluded at $t > 1$ day, having non-zero absorption at $t = 0.47$ days would require time-varying dust extinction, which has never been observed in any burst. If due to dust destruction, we would expect reddening

variations to be associated with intense episodes of emission, while there is no optical flaring or any significant feature in the restframe-UV lightcurve in this period that could be responsible for such dust destruction (see Haislip et al. 2006; Tagliaferri et al. 2005), and most dust destruction scenarios sublimate dust on timescales of only a few minutes after the burst at most (Perna et al. 2003; Fruchter et al. 2001). Stratta et al. (2007) suggested that varying extinction may also indicate that the emitting region had become larger than the obscuring cloud. While this cannot be excluded, such a geometry requires some tuning of the cloud and fireball parameters. The claim of dust in the host galaxy of GRB 050904, with an unusual extinction curve, relying principally on a smaller (0.3 mag) and $< 2\sigma$ flux deficit in a photometric observation, is not the most likely explanation. The most likely hypothesis is simply systematic uncertainties related to the Z -band calibration.

It is worth noting however that time-variable dust with an unusual extinction curve is not even the simplest explanation even if the original analysis had been reliable. Given that we know from the optical spectrum that a large quantity of gas is present in the system, a variability in the gas column density at early times is a less tortured hypothesis.

3.4.2 X-RAY ABSORPTION

The X-ray spectral analysis suggests a high metal column density in the afterglow of GRB 050904 (Watson et al. 2006b; Campana et al. 2007). Time-resolved X-ray spectroscopy reveals that the column density of metals within the first few hours is highly variable (Campana et al. 2007; Cusumano et al. 2006; Gendre et al. 2006). Due to the rapid changes in the X-ray spectrum this apparently variable column may be an artifact of the changing intrinsic spectrum resulting in a downturn at soft energies that disappears at later times (see Butler et al. 2006). However, even if the change in the soft X-rays is really due to a variable column density, i.e. due to increasing ionization of the metals, this effect occurs at early times ($\lesssim 10^3$ s) and cannot support the idea of dust destruction after 0.5 days. Indeed, a varying metal column density at < 1000 s argues against dust destruction at 0.5 days. If the varying metal column density is a real effect, destruction of any dust associated with the high metal column should have been completed long before 0.5 days. As a more general point, the optical and X-ray fluxes are at least one to two orders of magnitude lower after 0.5 days than before 1000 s. It is difficult to construct a scenario in which significant dust destruction occurs in the interval 0.5–3 days that did not occur before in the absence of a huge flare in the UV–X-ray, something which is not observed.

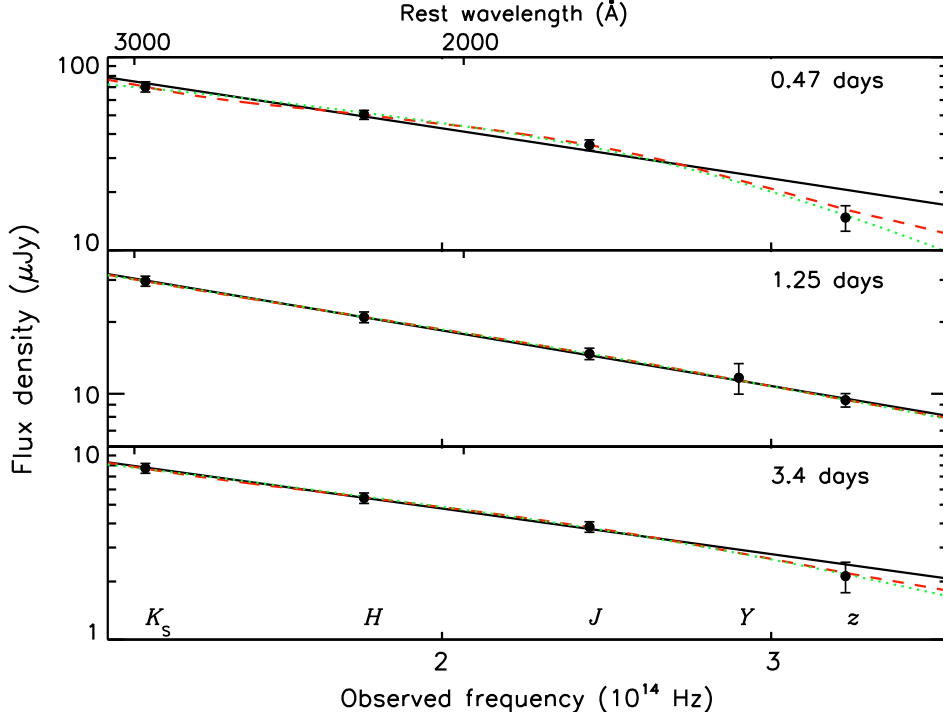


Figure 3.3: Near-infrared spectral energy distribution of the afterglow of GRB 050904 at 0.47 (top panel), 1.25 (middle panel) and 3.4 days (bottom panel) after the burst. The observed data are corrected for Galactic extinction (§ 2.2). The corresponding bands are identified in the bottom panel. The solid, dashed, and dotted lines represent the best fit with a power-law, a power-law with SN dust, and a power-law with SMC dust, respectively. At 1.25 days, the three lines almost overlap.

3.4.3 GAS-TO-DUST RATIO

GRBs typically occur in host galaxies with high gas to dust ratios (e.g. Jensen et al. 2001; Galama & Wijers 2001; Hjorth et al. 2003a; Stratta et al. 2004; Elíasdóttir et al. 2009). The H I column density of the host of GRB 050904 is very large while A_V is small. Using our limit on (SMC-type) dust at 1.25 days, $A_V \lesssim 0.05$ mag at 95% confidence, leads to a high gas-to-dust ratio $\text{NH I}/A_V \gtrsim 8.3 \times 10^{22} \text{ cm}^{-2} \text{ mag}^{-1}$. The Galactic relation between H I column density and dust reddening is $\text{NH I}/A_V = 4.93/R_V \times 10^{21} \text{ cm}^{-2} \text{ mag}^{-1}$ (Diplas & Savage 1994). Correcting for metallicity at 3.4 days ($Z = 0.1Z_\odot$; Kawai et al. 2006), this implies an $\text{NH I}/A_V$ ratio limit 5 times the Galactic value. A comparison with the SMC (Gordon et al. 2003), which has a similar metallicity to the environment of GRB 050904, yields a gas-to-dust ratio which is also more than 5–10 times larger in the host of GRB 050904.

3.4.4 THE ORIGIN OF DUST IN THE EARLY UNIVERSE

In the local Universe, the major sources of interstellar dust are AGB stars, the lower mass ranges of which require $\gtrsim 1$ Gyr to evolve to produce dust (Dwek et al. 2007). It has been suggested that for sources with large dust masses such as sub-mm galaxies, due to the short time available at $z \gtrsim 5$, an alternative source of dust is required and that core-collapse SNe could dominate dust formation at these times (Todini & Ferrara 2001; Morgan & Edmunds 2003; Nozawa et al. 2003; Dwek et al. 2007; Marchenko 2006; Hirashita et al. 2005). However, more complete theoretical models including dust destruction by supernova shock or grain growth/destruction in the interstellar medium obtain yields that are $\lesssim 0.01 M_{\odot}$ per SN (Bianchi & Schneider 2007), consistent with almost all observations of nearby SNe (Wooden et al. 1993; Elmhamdi et al. 2003; Meikle et al. 2006; Blair et al. 2007; Sakon et al. 2009). This is too little to produce the quantities of dust observed at high redshift. Recently Valiante et al. (2009) argued that on short timescales massive AGB stars could form much of the dust, depending on the assumed initial stellar metallicity and star formation history. The galaxy-SED modelling of sub-mm-selected galaxies of Michałowski et al. (2010b) suggests dust-formation timescales of order tens of millions of years in a few cases at $z \gtrsim 4$, which would clearly preclude even high-mass AGB dust-formation. While intriguing, these cases may be affected by active galactic nuclei (AGN) contamination and must be treated cautiously.

Observationally, after our analysis here of the afterglow of GRB 050904, the detection of a peculiar extinction curve in a BAL QSO spectrum at $z = 6.2$ (Maiolino et al. 2004) remains the only direct evidence for dominant SN-origin dust in the early Universe (but see recent work by Perley et al. (2010)). While the observational analysis of Maiolino et al. (2004) is carefully done, the relatively narrow wavelength coverage, the presence of strong, broad absorption and emission lines that dominate over the continuum at the blue end of the spectrum, and the use of composite QSO spectra, leave the result awaiting further confirmation. Furthermore, it is difficult to exclude that the dust is affected by the central AGN itself (Perna et al. 2003), so that the extinction curve may not tell us a lot about the origin of that dust.

3.5 CONCLUSIONS

In this work we reinvestigated the afterglow of GRB 050904 at 0.47, 1.25 and 3.4 day epochs to understand stellar environments and interstellar dust at high redshift. We find that the afterglow SED can be reproduced at all epochs without any dust extinction. The previous finding of dust extinction requiring a SN-type extinction curve by Stratta et al. (2007) relies mostly on a Z -band photometric point at 0.47 days which we find has calibration difficulties and with our new accurate analysis technique we find the flux deficit to be both smaller and less significant than reported by previous studies. We can reasonably exclude the presence of substantial quantities of any type of dust in

this GRB host galaxy at all epochs. We therefore conclude that there is no significant evidence of dust extinction in the afterglow of GRB050904.

Note added post-submission: A recent paper by Perley et al. (2010) reports significant SN-origin dust extinction in GRB071025 at $z \sim 5$ (Perley et al. 2010). We note that Perley et al. (2010) also independently attempted to model the dust profile of GRB050904 and found that the data are consistent with no extinction at all.

4

DUST EXTINCTION AT HIGH REDSHIFT

ABSTRACT –

The brightness of gamma-ray burst (GRB) afterglows and their occurrence in young, blue galaxies make them excellent probes to study star forming regions in the distant Universe. We here elucidate dust extinction properties in the early Universe through the analysis of the afterglows of all known $z > 6$ GRBs: GRB 090423, 080913 and 050904, at $z = 8.2$, 6.69 , and 6.295 , respectively. We gather all available optical and near-infrared photometry, spectroscopy and X-ray data to construct spectral energy distributions (SEDs) at multiple epochs. We then fit the SEDs at all epochs with a dust-attenuated power-law or broken power-law. We find no evidence for dust extinction in GRB 050904 and GRB 090423, with possible evidence for a low level of extinction in GRB 080913. We compare the high redshift GRBs to a sample of lower redshift GRB extinctions and find a lack of even moderately extinguished events ($A_V \sim 0.3$) above $z \gtrsim 4$. In spite of the biased selection and small number statistics, this result hints at a decrease in dust content in star-forming environments at high redshifts.

4.1 INTRODUCTION

Dust formation in the early universe is a hotly debated topic. The properties and quantity of dust at these times are essential not only to our understanding of how dust forms and evolves, but also to models of star-formation and the appearance of the first generations of stars and galaxies. Currently we extrapolate dust properties in the local group to very different environments that existed less than a billion years after the Big Bang. Long-duration gamma-ray bursts (GRBs), associated with the deaths of massive stars (Woosley 1993; Galama et al. 1998a; Hjorth et al. 2003b; Stanek et al. 2003; Malesani et al. 2004; Campana et al. 2006), have extremely bright and spectrally simple afterglows ($F_\nu \propto \nu^{-\beta}$) (Sari et al. 1998; Granot & Sari 2002), and so provide an opportunity to obtain not only effective reddening, but also absolute extinctions from distant galaxies (e.g. Watson et al. 2006a; Schady et al. 2010; Zafar et al. in prep). The recent tremendous advances in this subject were enabled by the dedicated GRB satellite, *Swift* (Gehrels et al. 2004), with its precise localization and fast responding X-ray and UV/optical telescopes, detecting the afterglow within only a few tens of seconds after the γ -ray trigger. The data from *Swift* have provided a very large sample of afterglows virtually complete in X-ray detections, and with a high completeness in the optical. It has also for the first time, enabled the discovery of GRBs at redshifts greater than or comparable to the most distant known galaxies and quasars (QSO) (see Kawai et al. 2006; Greiner et al. 2009; Tanvir et al. 2009; Salvaterra et al. 2009).

In this paper we collect for the first time all the available afterglow photometry and spectra from near-infrared (NIR) to X-ray at different epochs for all GRBs at $z > 6$: GRB 050904 ($z = 6.295$), GRB 080913 ($z = 6.69$) and GRB 090423 ($z \sim 8.2$). Since observations of these high- z GRBs are being made in the rest frame UV, they are in principle relatively sensitive to even small amounts of dust. We extract the SEDs at multiple epochs for all three GRBs and jointly fit the X-ray to NIR data to determine the properties of dust at $z > 6$. In §2 we describe multi-wavelength observations of the afterglows at different epochs carried out with different instruments. In §3 we present our results from the SED fitting. Based on our results, in §4 we discuss the origin of dust at high redshift and compare to the first large spectroscopic sample of GRB-derived extinction curves, the first spectroscopic sample of absolute extinction curves outside the local group. In §5 we provide our conclusions.

For all parameters we quote uncertainties at the 68% confidence level. We derive 3σ upper limits for the cases where detection is less than 2σ significant. A cosmology where $H_0 = 72 \text{ km s}^{-1} \text{ Mpc}^{-1}$, $\Omega_\Lambda = 0.73$ and $\Omega_m = 0.27$ is assumed throughout.

4.2 MULTI-WAVELENGTH DATA

The X-ray to NIR SED of GRB 050904 was analysed in detail in a previous work (see Zafar et al. 2010).

Table 4.1: Best fit parameters of the afterglow SEDs at different epochs with SMC type extinction. The provided upper limits are 3σ .

GRB	Epoch	A_V (mag)	β_1	β_2	$\log \nu_{break}$ Hz
050904	0.47d	< 0.17	1.23 ± 0.08
	1.25d	< 0.08	1.17 ± 0.51
	3.4d	< 0.16	1.24 ± 0.07
080913	10.5m	0.14 ± 0.06	0.78 ± 0.02
	26.9m	0.22 ± 0.11	0.65 ± 0.04
	1.88hr	0.12 ± 0.03	0.79 ± 0.03
	4.78d	< 0.40	0.94 ± 0.04
090423	16.7hr	< 0.10	0.45 ± 0.11	0.95 ± 0.11	15.1 ± 0.7
	1.65d	< 0.09	0.68 ± 0.13	1.18 ± 0.13	16.5 ± 0.9

On 2008 September 13 at 06:48:33.6 UT *Swift*-XRT began observing GRB080913. Telescopes at the European Southern Observatory (ESO), Gemini Observatories, and the Subaru all observed the field of GRB080913 in different optical and NIR bands (Greiner et al. 2009). On 2008 September 13, an optical spectrum of the afterglow of GRB080913 was secured at the Very Large Telescope (VLT) using the FOCal Reducer and low dispersion Spectrograph 2 (FORIS2) (Greiner et al. 2009; Fynbo et al. 2009; Patel et al. 2010). The spectrum shows a sharp break at $\sim 9400 \text{ \AA}$ supporting the detection of Ly α absorption at $z = 6.69$. We use this spectrum in addition to photometric data in the J , H and K bands from the lightcurves presented in Greiner et al. (2009). We corrected the data for extinction in the Milky Way (MW) of $E(B - V) = 0.043 \text{ mag}$ along the line of sight to this burst (Schlegel et al. 1998).

At 07:56:32 UT on 2009 April 23, *Swift*-XRT began observations of GRB090423. The afterglow of GRB090423 was observed in optical and NIR bands, with non-detection in $griz'$ and Y -band due to the high redshift (Tanvir et al. 2009). A NIR spectrum was obtained with the VLT Infrared Spectrometer And Array Camera (ISAAC) starting about 17.5 hours after the burst trigger. A redshift of ~ 8.2 was estimated from a break observed around $1.14 \mu\text{m}$ due to Ly α absorption by the neutral intergalactic medium (IGM). Another spectrum of the afterglow was obtained 40 hours after the burst with the VLT's Spectrograph using INtegral Field Observations in the Near Infrared (SINFONI) and confirms the analysis of the ISAAC spectrum (Tanvir et al. 2009). The finding was also confirmed with a spectrum obtained with Telescopio Nazionale Galileo (TNG) at ~ 14 hours after the burst (Salvaterra et al. 2009). We use the J , H and K band photometry of Tanvir et al. (2009). The data were corrected for Galactic extinction of $E(B - V) = 0.029 \text{ mag}$ (Schlegel et al. 1998).

For all three GRB afterglows the *Swift* XRT data were available and downloaded from the *Swift* data archive and reduced using HEASoft (version 6.10). Spectra and lightcurves were extracted in the 0.3–10.0 keV energy range. The X-ray spectra at different epochs were analyzed using the latest associated calibration files. All X-ray spectra were obtained near the time of optical/NIR spectra or relevant available photometry. To get an approximate X-ray flux level at each epoch, the afterglow lightcurves were obtained from the *Swift* XRT GRB light curve repository at the UK Swift Science Data Centre¹, created as described in Evans et al. (2007, 2010) and fitted by assuming a smoothly decay broken power-law (Beuermann et al. 1999). Considering the photon weighted mean time, the X-ray spectra were then normalized to the relevant SED time by using the lightcurve fit.

The XMM-*Newton* observations of the afterglows of GRB 080913 and GRB 090423 were performed at ~ 4.4 and ~ 2.2 days respectively. The data were collected from the XMM-*Newton* science archive (XSA)². The data were reduced in 0.3–10.0 keV band using Science Analysis System (SAS, version 10.0.0). The spectrum of GRB 080913 was fitted using a single power-law with a best fit photon index of $\Gamma = 2.4 \pm 0.4$ and frozen for Galactic X-ray absorption of $3.2 \times 10^{20} \text{ cm}^{-2}$ (using the nH FTOOL; Dickey & Lockman 1990). The best fit photon index for GRB 090423 is $\Gamma = 2.4 \pm 0.3$ with the fixed Galactic absorption of $3.1 \times 10^{20} \text{ cm}^{-2}$ (Dickey & Lockman 1990).

Parts of spectra with a restframe wavelength shortward of $\text{Ly}\alpha$ (i.e. $\lambda < 1216 \text{ \AA}$) are not included in the SED analysis to avoid absorption caused by the neutral IGM. The absorption lines arising from ionic species were removed from the spectrum of GRB 050904. Uncertainty in the Galactic extinction does not affect our results. The Dutra et al. (2003) reddening maps confirm the Schlegel et al. (1998) Galactic extinction maps up to $E(B - V) = 0.25 \text{ mag}$. Assuming an uncertainty of 15% (Schlafly et al. 2010) even for the case with the largest Galactic extinction (z' -band, GRB 050904), this corresponds to an uncertainty in the Galactic reddening value of $\lesssim 0.015 \text{ mag}$. This indicates that the uncertainty due to the Galactic extinction correction in the NIR is always smaller than our statistical uncertainties.

4.3 RESULTS

SEDs of the three GRB afterglows were obtained at multiple epochs. The data were fitted with dust-attenuated power-laws or broken power-laws. In addition to our standard extinction model (SMC type, see Zafar et al. 2010), we also fitted the data with the extinction curve inferred by Maiolino et al. (2004) to explain the spectrum of a QSO at $z = 6.2$ (although see Gallerani et al. 2010).

¹www.swift.ac.uk/xrt_curves

²<http://xmm.esac.esa.int/xsa/>

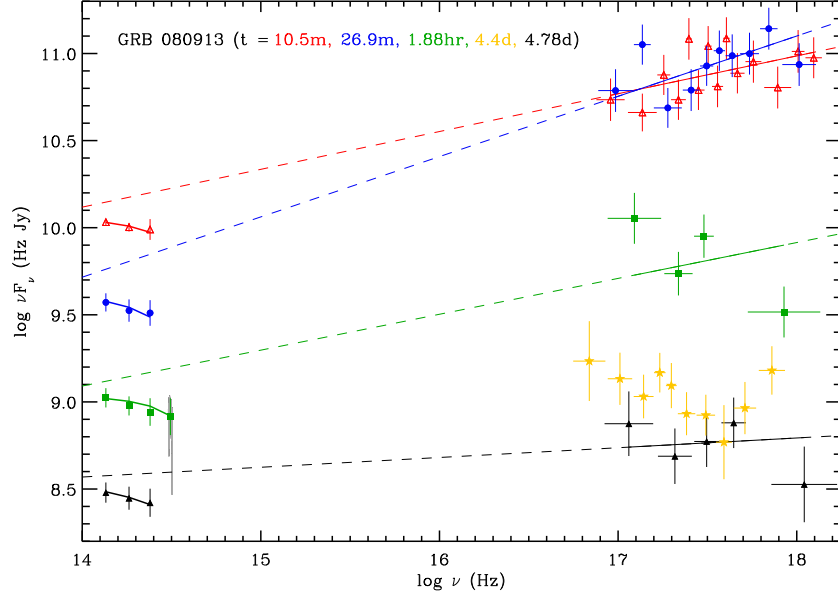


Figure 4.1: NIR to X-ray SED of the afterglow of GRB 080913 at 10.5 minutes (open red triangles), 26.85 minutes (blue circles), 1.88 hours (green squares) and 4.78 days (black triangles). Yellow stars correspond to XMM-Newton data at 4.4 days after the burst. The grey curve is the optical spectrum of the afterglow taken at $t_0 + 1.88$ hours. The solid lines represent the best-fit to the data; dashed lines illustrate the unextinguished power-law from the best fit. Being close in time, the X-ray spectra for the first two epochs are superimposed.

4.3.1 MULTI EPOCH SED OF GRB 050904

The SED of this burst was examined in detail in Zafar et al. (2010), where the SED of the afterglow of GRB 050904 is constructed at 0.47, 1.25 and 3.4 days after the burst. We use the results from the analysis here. The results of the SMC-extinction fits are reported in Table. 4.1 for completeness. The fits using supernova (SN)-origin extinction from Maiolino et al. (2004) suggest that there is no evidence in this burst for this type of extinction.

4.3.2 MULTI EPOCH SED OF GRB 080913

The SED of the afterglow of GRB 080913 is extracted at four epochs i.e. 10.5 and 26.9 minutes, 1.88 hours and 4.78 days after the burst (see Fig. 4.1). To get precise photometry in the z -band which is affected by strong $\text{Ly}\alpha$ absorption, we performed spectrophotometric analysis at 1.88 hours using the effective transmission function of the FORS2 z -Gunn filter. We constructed SEDs of the stars in the field using the Sloan Digital Sky Survey (SDSS; Fukugita et al. 1996) and Two Micron All Sky Survey (2MASS; Skrutskie et al. 2006) catalogues. We derived the count-to-flux conversion factor and es-

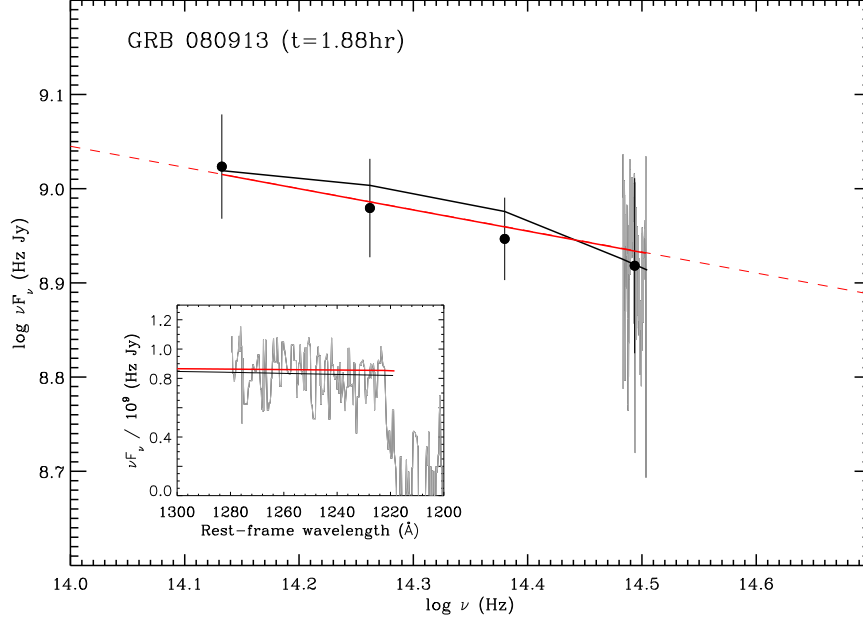


Figure 4.2: NIR and optical SED of the afterglow of GRB 080913 at 1.88 hours after the trigger. The grey curve represents the optical spectrum. The solid black curve corresponds to the best fit SMC-dust-attenuated power-law to the full NIR–X-ray SED, while the red line shows the best fit power-law to the NIR-optical data only with no extinction. Inset: Zoom of the optical spectrum and fits. The spectrum has been median filtered for display purposes.

timated the afterglow band-integrated flux from its measured counts. We computed the flux density at $\lambda_{\text{rest}} = 1250 \text{ \AA}$ using the procedure described in Zafar et al. (2010). At 1.88 hour the flux density at 1250 \AA was $2.66 \pm 0.63 \text{ \mu Jy}$. The NIR to X-ray SED at all epochs is well fitted with a single power-law and SMC type extinction. The combined fit for dust extinction at all epochs resulted in marginal dust reddening of $A_V = 0.12 \pm 0.03$. Fitting each epoch individually, we find dust extinction significant at the 2σ level at 10.5 and 26.9 min, at 4σ at 1.88 hours and 1σ at 4.78 days (see Table 4.1). We also fitted the data using the Maiolino et al. (2004) extinction curve, resulting in a significantly worse fit and zero extinction.

It is worth noting that the X-ray lightcurve for the afterglow of GRB 080913 shows some evidence of flaring, possibly resulting in harder spectra (see Evans et al. 2007; Greiner et al. 2009). If the SED of the afterglow of GRB 080913 is dominated by two separate components in optical-NIR and X-ray wavelengths, as observed at early times for GRB 050904, we should fit the optical-NIR data independent of the X-rays. Using this method, we obtain results consistent with a single power-law and no dust extinction, with a spectral slope of $\beta = 1.2 \pm 0.1$ and an upper limit of $A_V < 0.09$ (see Fig. 4.2).

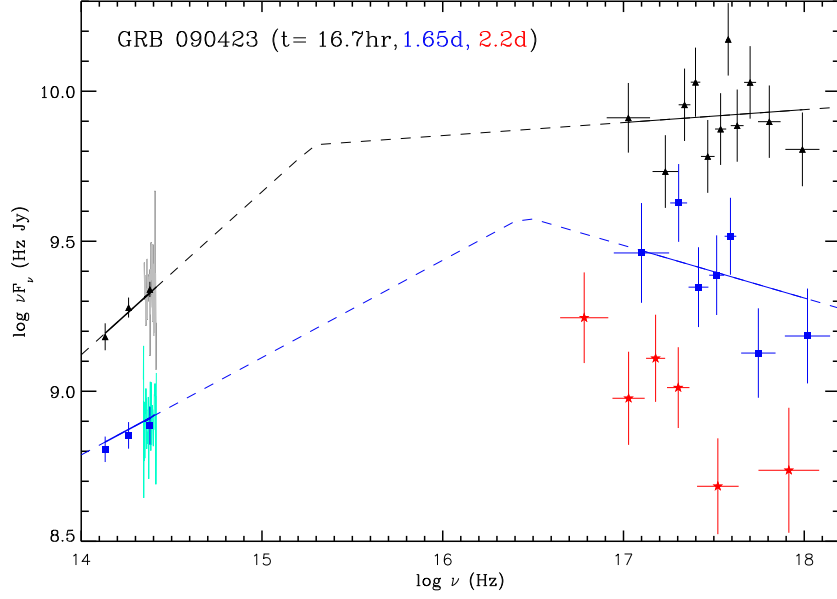


Figure 4.3: The NIR to X-ray SED of the afterglow of GRB 090423 at 16.7 hours (black triangles) and 1.645 days (blue squares). The corresponding lines show the best fits to the data. The ISAAC and SINFONI spectra are shown with the grey and cyan curves respectively. Red stars represent the XMM-Newton data taken at 2.21 days after the trigger.

4.3.3 MULTI EPOCH SED OF GRB 090423

The SED of the afterglow of GRB 090423 was constructed at 16.7 hours and 1.654 days (see Fig. 4.3). The VLT/ISAAC and SINFONI spectra, NIR photometry and X-ray spectra were fitted at both epochs. The data from both epochs were well fit with no dust using a broken power-law, with an evolution in the cooling break (see Table 4.1). The estimated 3σ upper limit on the A_V with SMC extinction is 0.10 and 0.09 mag at 16.7 hours and 1.654 epochs respectively.

4.4 DISCUSSION

Two apparently conflicting themes appear in studies of dust at high redshift. The first is the expected decline in extinction as we get to early in the Universe, where galaxies are younger and dust has less time to form. In the local Universe low and intermediate mass asymptotic giant branch (AGB) stars are believed to be the principal sources of interstellar dust, requiring $\gtrsim 1$ Gyr to evolve off the main sequence to produce dust (Gehrz 1989; Morgan & Edmunds 2003; Marchenko 2006; Dwek et al. 2007). Because of the time required to evolve to the giant branch, it has been posited that AGB stars should not contribute significantly to dust at $z \gtrsim 6$ (Dwek et al. 2007). Spectroscopic (Douglas et al. 2010) and photometric (Verma et al. 2007) studies of $z \sim 5$ lyman-break

galaxies seem to confirm the general trend of little dust at high redshifts, showing low extinctions, and the sample of z -band dropout galaxies ($z \sim 7$) shows little or no dust (González et al. 2010).

However, the second, at first paradoxical, theme is the very large dust masses discovered in quasar host galaxies at $z \sim 6$ from mm and sub-mm observations (e.g. Bertoldi et al. 2003; Carilli et al. 2001; Beelen et al. 2006; Wang et al. 2008; Michałowski et al. 2010a; Gall et al. 2011), and the mystery surrounding the origin of such large quantities of dust within a billion years of the Big Bang. It has been suggested that dust produced on short time scales could be produced in the ejecta of Type II SNe (Kozasa et al. 1991; Todini & Ferrara 2001; Morgan & Edmunds 2003; Nozawa et al. 2003; Dwek et al. 2007; Marchenko 2006; Hirashita et al. 2005), although observations of local SNe do not support this hypothesis (e.g. Meikle et al. 2006; Smith et al. 2008). Valiante et al. (2009) estimated that under certain conditions AGB stars could produce dust at earlier epochs, beginning to dominate between 150 and 500 Myr. However Michałowski et al. (2010a) found that given the stellar masses in high redshift QSO hosts, AGB stars could not be responsible for the large masses of dust observed in these objects at $z > 5$ (see Cherchneff & Dwek 2009; Pipino et al. 2011; Gall et al. 2010), and suggested rapid dust growth in the ISM as an alternative (see also Draine 2009). The modeling of Lyman alpha emitters at $z \sim 6$ suggests that the largest galaxies are the most dust enriched and that dust content decreases with increasing redshift (Lai et al. 2007; Finkelstein et al. 2009; Dayal et al. 2010). In spite of the emphasis in the literature on these QSO hosts, it may be that such very massive systems, being exceptional and rare, tell us little about typical star forming environments at very high redshift. And while, young star-forming galaxies at high redshift with strong nebular emission appear to be somewhat dust-obscured in spite of their blue continua (Schaerer & de Barros 2010; Watson et al. 2010), the quantities of dust are not large, consistent with the idea that in the early universe, most of the star-formation is likely to be less obscured than at later times. GRBs, associated as they are with the deaths of massive stars, usually occur in young, blue and sub-luminous galaxies with a high specific star formation rate (Le Floc'h et al. 2003; Courty et al. 2004; Christensen et al. 2004; Prochaska et al. 2004; Savaglio et al. 2009; Castro Cerón et al. 2010) and are therefore likely to be good probes of star-forming regions, especially at high redshift.

In this work, we have determined that all the identified $z > 6$ GRBs have low or negligible extinctions. By comparing these results with the first spectroscopic GRB extinction sample of Zafar et al. (in prep.), we find that at high-redshifts ($z \gtrsim 4$), GRB sightlines appear significantly less extinguished (see Fig. 4.4). The majority of reddened low-redshift GRBs are observed with $A_V \sim 0.3$ mag. While the numbers are small, the absence of any GRBs at $z \gtrsim 4$ with extinctions in this range is striking. The first explanation to examine is observational bias, where higher-redshift GRBs will be observed farther into the restframe UV where the extinction is likely to be more severe, possibly

preventing spectra from being obtained or the afterglow from being detected. For the $z > 6$ GRBs, a restframe $A_V = 0.3$ corresponds to 1–1.5 magnitudes of extinction in the observed J -band and 0.5–0.8 magnitudes in the observed K , for an SMC extinction curve. Considering the photometric observations given in Ruiz-Velasco et al. (2007); Haislip et al. (2006); Tagliaferri et al. (2005); Greiner et al. (2009); Tanvir et al. (2009), we found that even with $A_V = 0.3$ the GRBs at $z > 6$ could have been detected with relative ease and a photometric redshift obtained. In the case of GRB 050904, it seems likely that a spectroscopic redshift would have been obtained even with restframe $A_V = 0.3$. This work therefore hints at a low extinction of most $z > 4$ bursts, since it seems that our $z > 6$ bursts would have been found even with $A_V = 0.3$. Therefore we have looked at all known $z > 5$ GRB afterglows in the literature. There are four bursts with firm estimates of $z > 5$ known. Three of them have estimates of their dust extinction available. The four bursts are: GRB 050814 (Jakobsson et al. 2006c) at $z \sim 5.3$, GRB 060522 (Cenko et al. 2006a) at $z = 5.11$, GRB 060729 (Ruiz-Velasco et al. 2007; Zafar et al. in prep.) at $z = 5.46$ and GRB 071025 (Perley et al. 2010) at $z \sim 5$. Jakobsson et al. (2006c) obtained a photometric redshift of the afterglow of GRB 050814 and the SED is consistent with no dust reddening (P. Jakobsson, private communication). (Cenko et al. 2006a) give a spectroscopic redshift for GRB 060522 based on the $\text{Ly}\alpha$ break, however no estimate of the extinction is available so far in the literature. Ruiz-Velasco et al. (2007) obtained the spectroscopic redshift of the afterglow of GRB 060927. We have studied the SED of the afterglow of this burst in our spectroscopic sample of Zafar et al. (in prep.) and it is consistent with $A_V = 0$ (see Fig. 4.4). Moderate extinction is claimed in the case of GRB 071025 (Perley et al. 2010), with extinction corresponding to $A_V \sim 0.5$ (converting $A(3000\text{\AA})$ to A_V using the SMC extinction curve ratio). A Maiolino et al. (2004) extinction curve is required to fit the SED. With this extinction, GRB 071025 has a high enough extinction to begin to fill in the gap at high redshift around $A_V \sim 0.3$, though it is perhaps notable that it has the lowest redshift of all the bursts examined here. It is more anomalous in the sense that it has an apparently unique extinction curve since reanalyses have shown that no other QSO or GRB any longer require such a peculiar extinction (see Gallerani et al. 2008; Zafar et al. 2010).

The issues of bias and low number statistics are clearly important and we cannot resolve them with this sample. The fact that we infer very little dust in the afterglows studied here does not imply that dusty environments do not exist along sightlines to $z > 6$ GRBs, but it suggests that there is less dust in highly star-forming regions at $z \gtrsim 4$. This result is also potentially interesting in the context of dark bursts – suggesting that highly-extinguished bursts may not exist at high redshift, and that bright, very high redshift GRBs will be detectable as long as they are observed in the NIR.

Finally, the comparison to the column densities of metals is striking. In the cases of both GRB 050904 and GRB 090423, column densities of $N_{H,X} \sim 3 \times 10^{22}$ and 1×10^{23} are claimed (assuming solar abundances and neutral elements, Watson et al. 2006b; Cam-

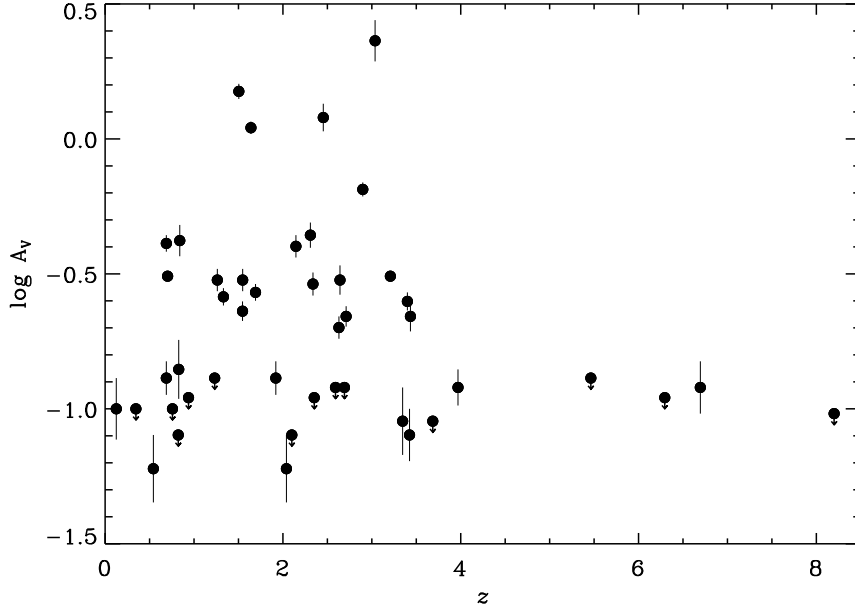


Figure 4.4: Extinction in GRB afterglow versus redshift. The three high redshift GRBs ($z > 6$) are from this work while the 42 low redshift GRBs are from a sample studied in Zafar et al. (in prep.). There seems to be a dearth of GRB afterglows at $z \gtrsim 4$ with $A_V \sim 0.3$.

pana et al. 2010a; Gendre et al. 2006; Tanvir et al. 2009; Starling et al. in prep.) from the soft X-ray absorption. The dust-to-metals ratios in both cases are at most a few percent of the value in the local group. Given that the metals are likely to be highly-ionized (Schady et al. 2010; Watson et al. 2007), the metal column must be substantially higher than found using neutral medium models. This could drive the dust-to-metals ratio down below a percent of local group values. While it is established that GRB environments can have low dust-to-metals ratios (Elíasdóttir et al. 2009; Watson et al. 2006a; Schady et al. 2010), these high-redshift objects are extreme. Such extreme ratios could be related to the more effective destruction of dust due to the high luminosity of these bursts (e.g. Fruchter et al. 2001); the effects of dust destruction may be discernible not only in very early colour changes in the GRB prompt phase UV emission, but also in the extinction curve at later times (Perna & Lazzati 2002). A very low dust-to-metals ratio could however, also be due to something more fundamental, such as the rapid production of metals in SNe but delayed formation and growth of the dust. For the metals to form before the dust suggests at least several million years between the formation of metals and the onset of significant dust growth. Observations of a larger sample may help to clarify this issue (see Zafar et al. in prep).

4.5 CONCLUSIONS

We have investigated cosmic dust at $z > 6$ using the afterglows of the highest redshift GRBs known. We performed multi-epoch NIR–X-ray SED analysis of GRB 050904, 080913, and 090423. We infer from our analysis that there is no evidence of dust in GRB 050904 and GRB 090423. We find possible evidence of low extinction in GRB 080913 consistent with an SMC extinction curve, however the optical spectrum and NIR photometry alone are consistent with a power-law with no dust extinction. In no case did we find evidence for any other extinction curve (e.g. the ‘SN-origin’ curve of Maiolino et al. 2004). Comparing to a much larger spectroscopic sample of GRB extinctions, we find a distinct absence of extinction at high redshifts. While the high redshift sample is very small and some of the effect may be explained by restframe UV-selection bias, this is not the whole picture, as all the $z > 6$ GRBs would have been detected at the typical A_V of lower redshift reddened bursts. This hints that there is less dust along sightlines to the highest redshift GRBs, indicating less dust in the early Universe. From these results, we also infer an extremely low dust-to-metals ratio in GRBs at high redshift, suggestive either of efficient dust destruction, or a delay of at least several million years between the formation of metals and the formation and growth of dust.

5

THE EXTINCTION CURVES OF STAR-FORMING REGIONS FROM $z = 0.1$ TO 6.7

ABSTRACT –

Studies of extinction curves provide insights into the properties of interstellar dust. Until recently, however, very few extinction curves existed outside the Local Group. GRB afterglows are well suited to extinction studies due to their brightness, simple power-law spectra and the occurrence of GRBs in distant star forming galaxies. In this paper we present results from the SED analysis of a sample of 41 GRB afterglows, from X-ray to NIR wavelengths. The sample is based on spectra from VLT-FORS, with additional data primarily from Swift. This is the largest sample of extinction curves outside the Local Group and, to date, the only extragalactic sample of absolute extinction curves based on spectroscopy. Estimates of the distribution of restframe visual extinctions, the extinction curves, and the intrinsic spectral shapes of GRB afterglows are obtained. Their correlation with H I column density as well as total and gas-phase metal column density are examined. The line-of-sight gas-to-dust and metals-to-dust ratios are determined and examined as a function of total column density, ISM metallicity and redshift. The intrinsic SEDs of the afterglows show that approximately half the sample require a cooling break between the optical and X-ray regimes. The broken power-law SEDs show an average change in the spectral index of $\Delta\beta = 0.51$ with a very small standard deviation of 0.02 (excluding the outlier GRB 080210). This is consistent with the expectation from a simple synchrotron model. Such a close convergence of values suggests that the X-ray afterglows of GRBs may be used with considerably more confidence to set the absolute flux level and intrinsic spectral indices in the optical and UV. Of the sample, 63% are well described by a featureless (SMC-type) extinction curve. Almost a quarter of our sample is consistent with no significant extinction (typically $A_V \lesssim 0.1$). The 2175 Å extinction bump is detected unequivocally in 7% of our sample (3 GRBs), which all have $A_V > 1.0$, while one afterglow has a very unusual extinction curve with a sharp UV rise. However, we can only say that the bump is not present in about a quarter of our sample because of low extinction or lack of coverage of the 2200 Å region. All the afterglows well fit with SMC type curves have moderate or low extinction, with $A_V < 0.65$. Because our sample is based on good-quality

optical spectra, it is likely to be heavily biased toward low extinction sightlines. This suggests that the SMC extinction curve is not as nearly-universal as previously believed and that extinction curves more similar to those found in the Galaxy and the LMC may be quite prevalent. We find an anti-correlation between gas-to-dust ratio and metallicity consistent with the Local Group relation; we find, however, no correlation between the metals-to-dust ratios and the metallicities, redshift and visual extinction; we find no strong correlation of the extinction column with metallicity either. Our metals-to-dust ratios derived from the soft X-ray absorption are always larger (3–30 times) than the Local Group value, which may mean that GRB hosts may be less efficient at turning their metals into dust. However, we find that gas, dust, and metal column densities are all likely to be influenced by photo-ionization and dust destruction effects from the GRB to differing extents and caution must be used in extrapolating the ratios of dust and gas-derived properties from GRB afterglows to the star-forming population in general.

5.1 INTRODUCTION

Extinction of light is the scattering and absorption of photons along the travel path from an object to the observer. Dust grains are the major contributor to extinction in the optical and ultraviolet (UV) range. More than 30% of the UV and optical light from stars in the Universe may be absorbed and re-radiated thermally at infrared and millimeter wavelengths by the obscuring dust (Lagache et al. 2005; Franceschini et al. 2008). Extinction curves are the standard tool to study dust in the optical and UV energy bands, revealing information about the dust grain size and composition by considering the amount of light lost due to scattering and absorption. The extinction curves of the Milky Way (MW), and the Large and Small Magellanic Clouds (LMC and SMC) have been modeled in a variety of ways (Fitzpatrick & Massa 1986; Cardelli et al. 1989; Pei 1992). These extinction laws vary significantly, largely due to the presence and relative strength of the 2175 Å extinction feature which is believed to be mainly due to absorption by graphite grains (Stecher & Donn 1965; Draine 2003). Extinction curves are typically obtained by comparing pairs of stars, however, outside the Local Group of galaxies, the method of estimating extinction curves from stellar atmosphere models is not applicable because individual stars are difficult or impossible to observe.

Long duration gamma-ray bursts (GRB) are signposts of star formation due to their association with the deaths of short-lived, massive stars (e.g., Woosley 1993; Galama et al. 1998a; Hjorth et al. 2003b; Stanek et al. 2003; Della Valle et al. 2003; Malesani et al. 2004; Campana et al. 2006; Starling et al. 2010). GRBs are excellent probes to study extinction curves in distant galaxies due to their intrinsic brightness, simple spectra and their occurrence in dense, star forming environments. GRB afterglows typically have intrinsically featureless piecewise power-law spectra from the X-ray to the optical/NIR and radio wavelengths. Theoretically, the most prominent explanation of GRB afterglows is the fireball model (e.g. Rees & Meszaros 1992; Meszaros & Rees 1997; Galama et al. 1998b; Sari et al. 1998; Piran 1999; Granot & Sari 2002; Zhang et al. 2006) which provides some notable successes in explaining the observations. According to the fireball model the GRB afterglow originates from synchrotron radiation produced by the interaction between the ultra-relativistic jet and the surrounding interstellar medium (ISM). It is believed that slow cooling in the synchrotron spectrum can sometimes place a cooling break between the X-ray and optical/NIR. In the fireball scenario, the cooling frequency will lead to a well-defined change in spectral slope of $\Delta\beta = \beta_2 - \beta_1 = 0.5$ resulting in a softer spectrum on the high energy side. Therefore, the X-ray–optical SED is expected to be a single or broken power-law. The simple spectral shape of GRBs and the lack of absorption above ~ 3 keV allow us to place constraints not only on the reddening due to dust, but on the absolute extinction and thereby obtain absolute extinction curves for sources at almost all redshifts ($z = 0.0086 - 8.2$).

In the era of the *Swift* satellite (Gehrels et al. 2004) and fast responding ground-based

telescopes, better-sampled GRB afterglow lightcurves and SEDs enable us to get more complete extinction curves and even samples of extinction curves. To date, SMC-type extinction (i.e. without a 2175 Å bump), has provided the best representation of GRB afterglow extinction (Bloom et al. 1998; Jensen et al. 2001; Fynbo et al. 2001a; Price et al. 2001; Savaglio & Fall 2004; Jakobsson et al. 2004b; Kann et al. 2006; Starling et al. 2007; Kann et al. 2010; Schady et al. 2010). The 2175 Å feature has been firmly detected in only two GRB afterglows so far: GRB 070802 (Elíasdóttir et al. 2009; Krühler et al. 2008) and GRB 080607 (Prochaska et al. 2009; Perley et al. 2011b). Grey/wavelength-independent extinction laws have also been claimed for a few GRB afterglows (Galama et al. 2003; Nardini et al. 2008; Perley et al. 2008). Dust with an unusual extinction curve, claimed to be due to supernova-origin dust, has been suggested in two cases, GRB 071025 (Perley et al. 2010) and GRB 050904 (Stratta et al. 2007), but ruled out for the latter case with revised multi-epoch SED analysis (Zafar et al. 2010).

In this paper, we present the SED analysis of a sample of forty one GRB afterglows observed mainly with the Very Large Telescope (VLT). This is the largest study to date of extinction curves outside the Local Group of galaxies. It is also unique as the first spectroscopic sample of absolute extinction curves (cf. Kann et al. 2006; Starling et al. 2007; Schady et al. 2007b, 2010; Kann et al. 2010; Krühler et al. 2010; Gallerani et al. 2010). Our main objectives are: *i*) to examine the extinction curves of star-forming galaxies at all redshifts, *ii*) to understand the properties of the dust and their relationship to the gas and metals in these galaxies, *iii*) to infer information about the typical spectral shapes of GRB afterglows.

To the best of our knowledge, this paper presents the first set of absolute extinction curves based on spectroscopy. Using spectroscopy in addition to photometry has significant benefits in such an analysis: *i*) the actual shape of the continuum and of the extinction curve can be determined, including the width, strength and central wavelength of the 2175 Å bump where it is present *ii*) the effects of gas absorption on the spectrum can be removed, including Ly α at $z \gtrsim 2$ and the Ly α forest at higher redshifts, *iii*) precise redshifts can be obtained from the spectrum, *iv*) the potential influence of intervening absorbers can be determined.

In §2 we describe the X-ray, UV/optical and NIR data reduction. In §3 we describe the different models used to fit the data. The results of our modeling are presented in §4. A discussion on the implications of our results is given in §5, and our conclusions are summarized in §6. A cosmology where $H_0 = 72 \text{ km s}^{-1} \text{ Mpc}^{-1}$, $\Omega_\Lambda = 0.73$ and $\Omega_m = 0.27$ (Spergel et al. 2003) is assumed. Throughout spectral indices are denoted by β where β_1 is the low energy (typically the optical/NIR) slope and β_2 is the high energy (typically X-ray) slope. The temporal indices are denoted by α : $F(\nu, t) \propto t^{-\alpha} \nu^{-\beta}$. All errors are 1σ unless otherwise specified. For the cases where there is no detection, 2σ upper limits are reported.

5.2 MULTI-WAVELENGTH OBSERVATIONS AND DATA REDUCTION

5.2.1 ENSEMBLE SELECTION CRITERIA

The sample consists of the flux-calibrated spectra from Fynbo et al. (2009, hereafter F09) taken with the Focal Reducer and low dispersion Spectrographs (FORS1 and FORS2) on the VLT with photometric observations in at least R or I -bands. Forty one GRB afterglows fulfilled our selection criteria (see Table 5.1). The spectra were obtained through target-of-opportunity (ToO) programs.

5.2.2 OPTICAL SPECTROSCOPY

With the aim of constructing composite SEDs, we collected flux calibrated spectroscopic data for each GRB afterglow listed in Table 5.1 (see also F09). The sample includes GRB afterglows from April 2005 to September 2008. The longslit spectra were obtained with either the FORS1 or FORS2 spectrographs (Appenzeller et al. 1998) using either the 300V or 600I grisms. This yields a spectral resolution of $R = \lambda/\Delta\lambda = 440$ and 1500 in the 300V and 600I grisms, respectively, with a slit of 1 arcsec. The data were reduced using standard tasks in IRAF and corrected for cosmic rays using the method developed by van Dokkum (2001). All the spectra were flux calibrated using spectrophotometric standard stars observed on the same night of the afterglow spectra. All FORS1/2 spectra from F09 are used except GRB 060526, GRB 060719, GRB 060807, GRB 070411, GRB 070508, GRB 070306, GRB 080411, GRB 080413B and GRB 080523. There were no suitable standard star spectra obtained near the time of observations of GRB 060526, GRB 080411 and GRB 080413B. The spectra of GRB 060719, GRB 070411, GRB 070508 and GRB 080523 have extremely low S/N ratios. GRB 060807 has no redshift estimation. The spectrum of GRB 070306 was dominated by the host galaxy. The spectrum of GRB 080607 was obtained with Keck using the Low Resolution Imaging Spectrometer (LRIS; Oke et al. 1995) and is therefore formally outside our sample. We include it here as a comparison object, since it is one of only two known GRB afterglows with a confirmed 2175 Å bump in the host galaxy prior to this sample. We used photometry from acquisition camera imaging, mostly performed using the R filter, to set the absolute flux level of the spectra. The time of the acquisition camera image was then used as the mean time of the SED. The magnitudes of the afterglows are obtained using ESO zero-points from the night of the observation.

To avoid contamination from absorption caused by the Ly α forest, data (both spectroscopic and photometric) with restframe wavelength $\lambda < 1216$ Å were excluded from the SED fitting. Furthermore, emission and absorption lines arising from different metal species and atmospheric molecular absorption lines were removed from the optical spectra.

5.2.3 PHOTOMETRY

The 30 cm Ultraviolet Optical Telescope (UVOT) onboard *Swift*, has six UV/optical filters: v , b , u , $uvw1$, $uvm2$ and $uvw2$ (Roming et al. 2005). The data are made available at the UK Swift Science Data Centre. The UVOT filter lightcurves were extracted using the UVOT imaging data tool UVOTMAGHIST. The fluxes in each band were obtained by using standard UVOT photometric calibration techniques defined by Poole et al. (2008). For the ground-based optical and NIR data, lightcurves for each filter were constructed using data either from refereed publications or from GRB Coordinates Network (GCN) circulars. For ease of access to the data published in GCN circulars for each GRB, the information was obtained via the GRBLog¹ database (Quimby et al. 2004). To generate SEDs at instantaneous epochs, the magnitudes in the relevant filters were obtained by interpolating or extrapolating the lightcurves to the time of interest. For this purpose, usually the R -band lightcurve decay index is used for extrapolation and interpolation in other bands since it is typically the most complete.

The optical spectra and optical/NIR photometry have been corrected for Galactic dust extinction using the Schlegel et al. (1998) dust extinction maps. The $E(B - V)$ values along the line of sight for each burst are given in Table 5.1 and were retrieved from the NASA Extragalactic database (NED²) web-calculator. Several works have attempted to verify the Schlegel et al. (1998) results (e.g. Dutra et al. 2003; Schlafly et al. 2010), finding overall a good agreement at low values of A_V . Some uncertainty is still present, e.g. recently Schlafly et al. (2010) suggested that these values might be systematically overestimated by $\sim 14\%$ on the average. For our analysis we corrected the Galactic $E(B - V)$ values of Schlegel et al. (1998) for the 14% overestimation (see Table 5.1). However, extinction at high redshift has a much greater effect for a given dust column on the observed spectrum since we are observing dust effects in the restframe UV of the GRB host. For example, for a GRB host at $z = 2$ with SMC extinction, the effective observer frame A_R is ~ 4 times larger than the equivalent Galactic A_R . Discrepancies between the Schlafly et al. (2010) and Schlegel et al. (1998) values in the Galactic extinction are therefore small compared to the typical uncertainty on the measured restframe absorption and extinction values.

5.2.4 X-RAY DATA

The GRB afterglows present in our sample have been all detected by *Swift*. The X-Ray Telescope (XRT; Burrows et al. 2007) onboard *Swift* performed the X-ray observations in each case and the X-ray data for each GRB have been obtained from the UK *Swift* science data center³. The X-ray spectrum for each GRB afterglow was reduced in the 0.3–10.0

¹<http://grblog.org/grblog.php>

²<http://nedwww.ipac.caltech.edu/>

³http://www.swift.ac.uk/swift_portal/archive.php

Table 5.1: Basic data on the flux calibrated spectroscopic sample. The details of the sample are provided in the columns as (1) burst names, (2) Galactic HI column density, (3) time of SED, time since GRB trigger, (4) Galactic $E(B - V)$ from the Schlegel et al. (1998) extinction maps corrected for 14% overestimation, (5) redshift, and (6) acquisition camera photometry measurement.

GRB	$N_{H\text{ Gal}}$ 10^{20} cm^{-2}	Δt hr	$E(B - V)_{\text{Gal}}$ mag	z	Mag_{acq} mag
050401	4.40	14.7	0.056	2.8983	23.27 ± 0.09
050730	2.99	4.10	0.044	3.9693	17.80 ± 0.04
050824	3.72	9.50	0.030	0.8278	20.60 ± 0.06
060115	9.48	8.90	0.114	3.5328	22.00 ± 0.07
060512	1.53	8.80	0.015	2.1000	20.40 ± 0.20
060614	1.87	21.1	0.019	0.1257	19.80 ± 0.05
060707	1.44	34.4	0.019	3.4240	22.40 ± 0.06
060708	2.10	43.0	0.009	1.9200	22.90 ± 0.07
060714	6.05	10.1	0.066	2.7108	20.90 ± 0.06
060729	4.49	13.2	0.046	0.5428	17.50 ± 0.05
060904B	11.3	5.10	0.149	0.7029	19.90 ± 0.05
060906	9.81	1.00	0.048	3.6856	20.00 ± 0.06
060926	7.58	7.70	0.135	3.2086	23.00 ± 0.06
060927	4.60	12.5	0.053	5.4636	24.00 ± 0.09
061007	1.77	17.4	0.018	1.2622	21.50 ± 0.06
061021	4.52	16.5	0.049	0.3463	20.50 ± 0.04
061110A	4.26	15.0	0.077	0.7578	23.10 ± 0.05
061110B	3.35	2.50	0.055	3.4344	22.50 ± 0.05
070110	1.61	17.6	0.012	2.3521	20.80 ± 0.04
070125	4.31	31.5	0.045	1.5471	18.80 ± 0.20
070129	6.96	2.20	0.118	2.3380	21.30 ± 0.05
070318	1.44	16.7	0.015	0.8397	20.20 ± 0.10
070506	3.80	4.00	0.034	2.3090	21.00 ± 0.04
070611	1.38	7.70	0.010	2.0394	21.00 ± 0.04
070721B	2.33	21.6	0.027	3.6298	24.30 ± 0.07
070802	2.90	2.00	0.023	2.4541	22.60 ± 0.06
071020	5.12	5.12	0.052	2.1462	20.33 ± 0.04
071031	1.22	1.20	0.010	2.6918	18.90 ± 0.04
071112C	7.44	9.50	0.101	0.8227	22.20 ± 0.11
071117	2.33	9.00	0.021	1.3308	23.58 ± 0.09
080210	5.47	1.69	0.071	2.6419	19.57 ± 0.05
080319B	1.12	26.0	0.009	0.9382	20.36 ± 0.04
080520	6.82	7.30	0.071	1.5457	23.00 ± 0.06
080605	6.67	1.70	0.117	1.6403	23.00 ± 0.06
080707	6.99	1.10	0.086	1.2322	19.60 ± 0.04

GRB	$N_{H\text{ Gal}}$ 10^{20} cm^{-2}	Δt hr	$E(B - V)_{\text{Gal}}$ mag	z	Mag_{acq} mag
080721	6.94	10.2	0.086	2.5914	20.20 ± 0.12
080805	3.46	1.00	0.037	1.5042	21.50 ± 0.05
080905B	3.50	8.30	0.040	2.3739	20.20 ± 0.05
080913	3.17	1.88	0.037	6.6950	23.36 ± 0.13
080916A	1.84	17.1	0.016	0.6887	22.30 ± 0.05
080928	5.59	15.5	0.058	1.6919	21.07 ± 0.07
080607 ^a	1.69	0.08	0.060	3.0368	17.97 ± 0.07

^aKeck spectrum.

keV energy range using the HEASoft software (version 6.10). For each afterglow, the X-ray lightcurves were produced from the XRT data (Evans et al. 2007, 2009). To get a better estimate of the X-ray flux, we fitted a decay model (Beuermann et al. 1999) to the X-ray lightcurves. For X-ray spectral analysis we used photon counting (PC) mode data and source counts were extracted within a circular region centered on the source, and background counts from a circular region ~ 10 times greater than the source region. We used XSELECT (v2.4) to extract spectral files from the event data in the 0.3–10 keV energy band. To avoid pile-up all X-ray spectra were taken from time intervals where the measured count rate is less than 0.6 counts s^{-1} . The X-ray spectral files were grouped to 12–20 counts per energy channel. Effective area files for each spectrum were created using the FTOOLS XRTMKARF recipe and bad columns were corrected by using the exposure maps. Response matrices (v11) from the *Swift* XRT calibration files were used. The X-ray spectra were obtained over an interval as close as possible to the mid-time of the optical spectra. The flux of the final X-ray spectrum was corrected to the SED time by taking the ratio of the X-ray lightcurve model fits at the photon weighted mean time (PWMT) of the X-ray spectrum and the SED time. The spectra were fitted within XSPEC (v12.6.0; Arnaud 1996) with a Galactic-absorbed power-law, with absorption from the Galactic neutral hydrogen column density taken from Kalberla et al. (2005, using the nH FTOOL), and additional absorption from the GRB host galaxy. The Galactic column density value used for each GRB is given in Table 5.5. The equivalent neutral hydrogen column density from the host galaxy of each GRB was estimated from the soft X-ray absorption and is denoted here as $N_{\text{H,X}}$. $N_{\text{H,X}}$ is modeled with XSPEC where solar abundances were assumed from Asplund et al. (2006). $N_{\text{H,X}}$, presented in units of equivalent hydrogen column density for a solar abundance of the elements, is essentially a direct measure of the metal column density.

Table 5.2: Results of fits to the SEDs. The columns give the burst name, and then for each model the χ^2_ν/dof and the null hypothesis probability (NHP) for the fit are provided. The F-test probability is computed for each SED comparing the single (PL) and broken power-law (BPL) models. The best fit models are denoted \dagger .

SMC					
	PL		BPL		
GRB	χ^2_ν/dof	NHP%	χ^2_ν/dof	NHP%	F-test prob.
050401	1.09/1011	2.0	1.08/1009 [†]	2.6	0.02
050730	1.23/659	0.003	0.98/657 [†]	60	< 0.01
050824	1.13/958	0.2	0.97/956 [†]	71	< 0.01
060115	1.15/1014 [†]	0.06	1.15/1012	0.05	1.00
060512	1.02/1452	33	0.93/1450 [†]	96	< 0.01
060614	1.01/1254	37	0.82/1252 [†]	100	< 0.01
060707	0.98/1088 [†]	65	0.98/1086	64	1.00
060708	0.86/867	100	0.85/865 [†]	100	< 0.01
060714	1.02/1043	35	0.97/1041 [†]	72	< 0.01
060729	0.99/1140 [†]	54	0.99/1138	53	1.00
060904B	0.80/1198 [†]	100	0.80/1196	100	1.00
060906	1.01/786	42	0.94/784 [†]	87	< 0.01
060926	0.95/907 [†]	86	0.95/905	85	1.00
060927	1.03/274 [†]	35	1.03/272	32	1.00
061007	0.97/1341 [†]	78	0.97/1339	77	1.00
061021	1.26/1703	0.0	0.98/1701 [†]	70	< 0.01
061110A	0.98/1093 [†]	63	0.98/1091	61	1.00
061110B	0.95/896	85	0.94/894 [†]	88	0.02
070110	1.09/1087	0.17	1.04/1085 [†]	18	< 0.01
070125	1.03/790	25	0.97/788 [†]	72	< 0.01
070129	0.93/1017	94	0.91/1015 [†]	98	< 0.01
070506	0.99/775	57	0.98/773 [†]	65	< 0.01
070611	0.77/1248 [†]	100	0.77/1246	100	0.77
070721B	1.00/830 [†]	47	1.00/828	46	0.76
071020	1.09/1020	2.1	1.06/1018 [†]	10	< 0.01
071031	2.13/614	0	1.05/612 [†]	17	< 0.01
071112C	1.67/1287	0	1.00/1285 [†]	48	< 0.01
071117	0.99/1171	56	0.98/1169 [†]	71	< 0.01
080210	1.10/964	1.7	1.00/962 [†]	45	< 0.01
080319B	0.83/1468 [†]	100	0.83 /1466	100	1.00
080520	1.00/1028 [†]	54	1.00/1026	51	1.00
080707	1.07/743	9.3	1.03/741 [†]	30	< 0.01
080721	0.96/731 [†]	76	0.96/729	74	1.00
080905B	0.98/1029 [†]	68	0.98/1027	66	1.00

SMC					
GRB	PL		BPL		F-test prob.
	χ^2_ν/dof	NHP%	χ^2_ν/dof	NHP%	
080913	0.58/81 [†]	100	0.58/79	100	1.00
080916A	0.93/1170	96	0.91/1168 [†]	99	< 0.01
080928	0.99/1157 [†]	57	0.99/1155	55	1.00
FM					
GRB	PL		BPL		F-test prob.
	χ^2_ν/dof	NHP%	χ^2_ν/dof	NHP%	
070318	1.15/1392	0.001	0.88/1390 [†]	100	< 0.01
070802	0.54/1381 [†]	100	0.54/1379	100	1.00
080605	0.86/859 [†]	100	0.86/857	100	1.00
080805	0.93/1391 [†]	98	0.93/1389	97	1.00
080607 ^a	1.79/39 [†]	0.19	1.79/37	0.17	1.00

^aKeck spectrum.

5.3 DATA ANALYSIS

We describe the afterglow continuum emission with single or broken power-law models. For each burst, we tried both laws to fit the observed data, where the spectral break must be in the observing window ($10^{14} \text{ Hz} \lesssim \nu_{\text{break}} \lesssim 10^{18} \text{ Hz}$). On top of the power-law fits, we added empirical extinction laws corresponding to the SMC (Pei 1992), MW (Fitzpatrick & Massa 1986; Cardelli et al. 1989), or LMC (Pei 1992) (see §5.3.1 for details), in order to account for the effect of dust in the GRB local environment. The X-ray to optical/NIR GRB afterglow SEDs were generated at specific epochs (the time of the acquisition image of the spectrum), and modeled in `IDL`. To get errors on each parameter we used 1000 Monte Carlo (MC) realizations of the data, with the mean value of each datapoint set to the observed value and a gaussian distribution with a width corresponding to the 1σ measured error on that datapoint. For each simulated set we fitted the function and estimated the best fit parameters. The error for each parameter was calculated using the standard deviation of this distribution. To determine whether the use of a broken power-law was required over a single power-law, we used an F-test probability < 5% as the threshold. The results from the spectral analysis of our spectroscopic GRB sample are provided in Table 5.2.

5.3.1 DUST MODELS

The dust extinction was modeled with empirical extinction laws (Fitzpatrick & Massa 1986; Cardelli et al. 1989; Pei 1992) to determine the absolute extinction and the characteristics of the extinction. From the Pei (1992) extinction laws we used only the SMC

extinction law. Hereafter, we will refer to these three extinction models as FM (Fitzpatrick & Massa 1986), CCM (Cardelli et al. 1989) and SMC (Pei 1992). The important characteristic of the SMC law used here is the lack of the graphite 2175 Å bump and the even steeper rise in the far UV, rising faster than $1/\lambda$ (Prevot et al. 1984; Gordon et al. 2003). Cardelli et al. (1989) showed that Galactic sightlines could typically be well-fit with a parameterization of the extinction curve that relied only on a single parameter, the ratio of selective to absolute extinction, $R_V = A_V/E(B - V)$. Comparable to CCM, FM provides greater freedom in reproducing the extinction curves. To investigate rest-frame visual extinction, we fit all three extinction laws for each case and found that the best fitting results and null hypothesis probabilities for SMC and FM were similar in most cases. We therefore selected the SMC model to represent extinction where the null hypothesis probability for the fit with FM was not significantly better. The FM parameterization is used for the cases where the SMC could not provide a good fit (see Table 5.2). It transpired that the CCM curve was a poorer fit to the observed data in every case (see below).

The continuum emission from an afterglow is believed to be dominated by synchrotron radiation (Sari et al. 1998) described by a power-law given as

$$F_\nu = F_0 \nu^{-\beta} \quad (5.1)$$

where F_0 is the flux normalization, ν is the frequency and β is the intrinsic spectral slope. The observed flux is extinguished due to dust in the Milky Way, and in objects between our Galaxy and the GRB, the latter typically dominated by the GRB host galaxy (though see GRB 060418; Ellison et al. 2006). As explained above (Sect. 5.2.3), we corrected the optical/NIR data for Galactic foreground extinction maps (Schlegel et al. 1998). With knowledge of the unextinguished flux from X-rays and the redshift, the extinction corrected spectral slope and restframe A_V can be obtained. Therefore the extinguished flux will be given as

$$F_\nu^{\text{obs}} = F_\nu 10^{-0.4A_\lambda} \quad (5.2)$$

Here A_λ is the extinction in the host galaxy of the GRB as a function of wavelength λ . The wavelength dependence on dust extinction observed in SMC, LMC and MW environments is well reproduced by the standard dust models (Fitzpatrick & Massa 1986; Cardelli et al. 1989; Pei 1992). For SMC, LMC and MW the extinction law introduced by Pei (1992) is given as

$$A_\lambda = A_V \left(\frac{1}{R_V} + 1 \right) \sum_{i=1}^6 \frac{a_i}{(\lambda/\lambda_i)^{n_i} + (\lambda_i/\lambda)^{n_i} + b_i} \quad (5.3)$$

For SED modeling we used the SMC parameterization where $R_V = 2.93$ for the SMC extinction law (Pei 1992). The parameters a_i , b_i and n_i are different for each extinction

model (see Pei 1992 for the parameter list). A parameterization for extinction in the Milky Way was advocated by Cardelli et al. (1989). It provides a better estimation of far UV curvature with fixed bump strength and varying R_V . It is defined as

$$A_\lambda = A_V \left(a(x) + \frac{b(x)}{R_V} \right) \quad \text{where } x = \lambda^{-1} \quad (5.4)$$

$a(x)$ and $b(x)$ are wavelength dependent polynomials controlling the UV, optical and NIR regimes of the extinction curve. Finally, we fitted the data with an FM extinction model. The parameterization for the FM extinction curve in the UV range is given as

$$A_\lambda = A_V \left(\frac{1}{R_V} k(\lambda - V) + 1 \right) \quad (5.5)$$

where

$$k(\lambda - V) = \begin{cases} c_1 + c_2x + c_3D(x, x_0, \gamma) & x \leq c_5 \\ c_1 + c_2x + c_3D(x, x_0, \gamma) + c_4(x - c_5)^2 & x > c_5 \end{cases}$$

and the Lorentzian-like Drude profile, which represents the 2175 Å bump, is given as

$$D(x, x_0, \gamma) = \frac{x^2}{(x^2 - x_0^2)^2 + x^2\gamma^2}$$

The underlying UV linear component is specified by the intercept, c_1 , and the slope, c_2 . The ~ 2175 Å absorption bump is controlled by c_3 (bump strength), x_0 (central wave number), and γ (the width of the bump). The parameters c_4 and c_5 give the far-UV curvature. The extinction properties in the NIR and optical are determined using spline interpolation points (see Fitzpatrick & Massa 2007). The FM parameterization provides greater freedom for fitting the extinction curve; in particular, it allows characterization of the curve, for example in the strength, width and position of the 2175 Å bump.

5.4 RESULTS

5.4.1 THE SED OF THE AFTERGLOW

GRB afterglows are well described by a coherent synchrotron emission from accelerated electrons with a power-law distribution of energies promptly behind the shock. These electrons then cool both adiabatically and by emitting synchrotron and inverse Compton radiation. At late times, the electron population accelerated by shock mechanisms is expected to radiate in the slow cooling regime (see Sari et al. 1998). The GRB spectrum in that regime is defined by a broken power-law model. The transfer to the slow cooling regime causes a cooling break in the intrinsic spectrum, typically occurring between the X-ray and the optical/NIR wavelengths. The broken power-law model is given as

$$F_\nu = \begin{cases} F_0\nu^{-\beta_1} & \nu \leq \nu_{\text{break}} \\ F_0\nu_{\text{break}}^{\beta_2-\beta_1}\nu^{-\beta_2} & \nu \geq \nu_{\text{break}} \end{cases} \quad (5.6)$$

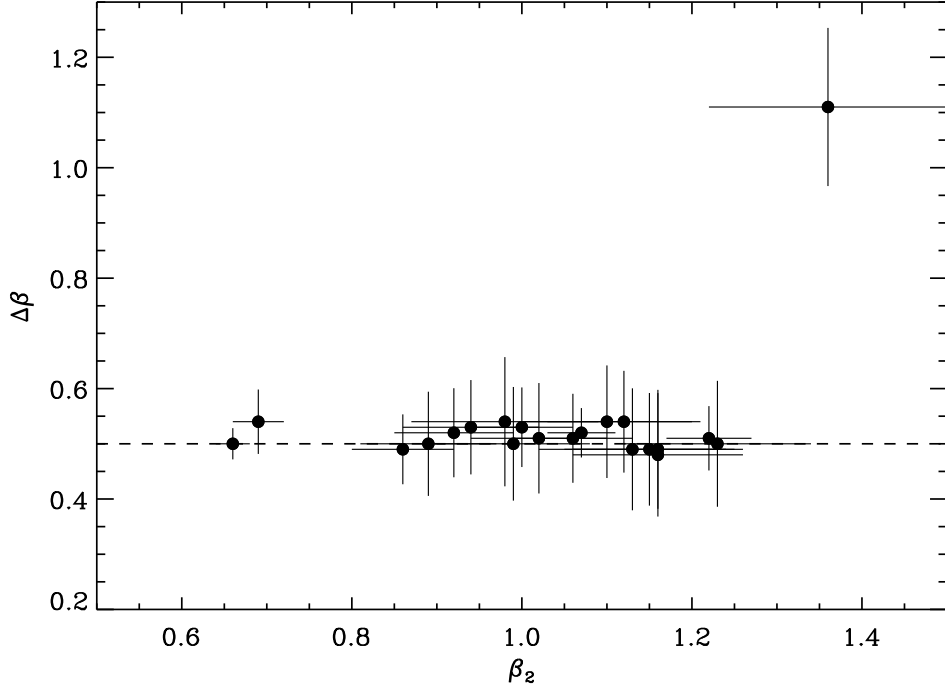


Figure 5.1: $\Delta\beta$ against the X-ray spectral slope. The dashed line corresponds to $\Delta\beta = 0.5$. GRB 080210 is an outlier and has a softer X-ray slope compared to the rest of the sample.

where β_1 and β_2 are the slopes of the optical and X-ray segments in our model respectively. The parameter ν_{break} is the cooling break frequency joining the two power-law segments. In accordance with the theory outlined by Sari et al. (1998), this additional break in the spectrum will give a spectral change of $\beta_1 = \beta_2 - \Delta\beta$, where $\Delta\beta = 0.5$. In our SED modeling we treat $\Delta\beta$ as a free parameter by allowing both slopes to vary independently in order to test the compatibility of the synchrotron model with our observed SED sample. From our sample, 21 SEDs have a spectral break between the X-ray and optical wavelengths. We find that 95% of the spectral breaks have a spectral change of $\Delta\beta \sim 0.5$, in agreement with the synchrotron emission model. The mean $\Delta\beta$ of all 21 GRBs is 0.54 with a standard deviation of 0.13. This large standard deviation is dominated by a single outlier, GRB 080210, which has a $\Delta\beta = 1.1 \pm 0.1$. Of the 21 GRBs, GRB 080210 is the only case that deviates from $\Delta\beta = 0.5$ (see De Cia et al. 2010, for a detailed analysis of the SED of GRB 080210). Considering only the remaining SEDs, $\langle\Delta\beta\rangle = 0.51$ with a standard deviation of 0.02. This agreement with the prediction of Sari et al. (1998) is remarkable, and indicates that for the vast majority of SEDs taken at similar epochs, it is valid to assume that the amplitude of the spectral break is equal to exactly 0.5. In the future, for broad-band SED analysis, this should remove a degree of freedom in deriving extinction curves using GRBs, making the process more robust.

5.4.2 DUST EXTINCTION

The restframe visual extinction, A_V , is determined for the forty one afterglows in our sample, plus GRB 080607. Approximately two thirds (26/41), have moderate extinction values with A_V ranging from 0.06 ± 0.02 to 0.65 ± 0.04 , and are well-fit with SMC-type extinction. The mean visual extinction for these 26 GRB afterglows is $\langle A_V \rangle = 0.24$ with a standard deviation of 0.14. Roughly one quarter of the sample (11/41) is consistent with no dust reddening, with a mean 2σ upper limit $\langle A_V \rangle < 0.10$ assuming an SMC type dust extinction curve. More than 7% of the full sample ($\sim 9\%$ of the extinguished afterglows) are found to have a well-defined bump consistent with the 2175 Å feature. Of these bursts, GRB 070802 was known before (Elíasdóttir et al. 2009; Krühler et al. 2008), while GRB 080605 and GRB 080805 are new (but see F09), doubling the number of such bumps unequivocally known in GRB host galaxies. We also include the other definite case of a bump in a GRB host extinction curve, GRB 080607, in our analysis as a comparison extinction curve. All of these cases have $A_V \gtrsim 1$, and are by far the most extinguished bursts in our sample, with a mean extinction more than five times the average extinction of extinguished bursts in the sample. Finally, GRB 070318 was not well fit by the SMC curve and does not have a 2175 Å bump. Its extinction curve seems very unusual and is the subject of a separate investigation (Watson et al. in prep.). We find no evidence in our sample for the extinction curve of Maiolino et al. (2004) associated with dust from supernovae.

5.5 DISCUSSION

5.5.1 THE 2175 Å FEATURE

The 2175 Å absorption feature, as mentioned above, has been robustly detected in the optical spectra of four GRB afterglows (see Table 5.4). The feature is a broad dip centered at 2175 Å due to excess extinction and was first discovered by Stecher (1965). Notable characteristics are the width ($\sim 1\mu\text{m}^{-1}$ and its variability ($\sim 20\%$), contrasted to the tight observed central wavelength of the bump (to within ~ 10 Å, i.e. $< 1\%$). Several candidates have been considered to explain the 2175 Å bump, ranging from carbonaceous materials (Henrard et al. 1997) to iron poor silicate grains in the form of partially hydrogenated amorphous Mg_2SiO_4 particles (Steel & Duley 1987). The dominant hypothesis is some form of carbonaceous material in small grains ($\lesssim 50$ Å), with polycyclic aromatic hydrocarbons (Duley & Seahra 1998; Duley 2006; Cecchi-Pestellini et al. 2008; Duley 2009; Cecchi-Pestellini et al. 2010) and graphite being popular choices (Stecher & Donn 1965; Mathis et al. 1977; Draine & Lee 1984; Draine 1989; Sorrell 1990; Mathis 1994; Rouleau et al. 1997; Will & Aannestad 1999; Andersen et al. 2002; Clayton et al. 2003; Fitzpatrick & Massa 2007). The absence or weakness of the bump in SMC and LMC sightlines can be explained by a difference in the relative abundances

Table 5.3: Parameters of the best fit with the SMC extinction curve ($R_V = 2.93$) of Pei (1992). The values of β_2 and ν_{break} are provided for the cases where a broken power-law is the best fit.

GRB	β_1	β_2	$\log \nu_{\text{break}}$ Hz	A_V mag
050401	0.39 ± 0.05	0.89 ± 0.08	16.32 ± 0.89	0.65 ± 0.04
050730	0.16 ± 0.02	0.66 ± 0.02	16.00 ± 0.17	0.12 ± 0.02
050824	0.40 ± 0.04	0.92 ± 0.07	15.20 ± 0.33	0.15 ± 0.03
060115	0.77 ± 0.03	0.10 ± 0.02
060512	0.68 ± 0.05	1.16 ± 0.10	15.37 ± 0.45	< 0.12
060614	0.47 ± 0.04	1.00 ± 0.05	16.06 ± 0.21	0.11 ± 0.03
060707	0.59 ± 0.02	0.08 ± 0.02
060708	0.67 ± 0.04	1.16 ± 0.11	16.92 ± 1.04	0.14 ± 0.02
060714	0.44 ± 0.04	0.98 ± 0.11	15.86 ± 0.53	0.21 ± 0.02
060729	0.78 ± 0.03	0.07 ± 0.02
060904B	0.90 ± 0.02	0.34 ± 0.03
060906	0.56 ± 0.02	1.10 ± 0.10	17.10 ± 0.14	< 0.09
060926	0.82 ± 0.01	0.32 ± 0.02
060927	0.86 ± 0.03	< 0.12
061007	0.78 ± 0.02	0.34 ± 0.03
061021	0.55 ± 0.02	1.07 ± 0.04	16.93 ± 0.24	< 0.10
061110A	0.79 ± 0.02	< 0.10
061110B	0.73 ± 0.03	1.23 ± 0.11	16.90 ± 0.15	0.23 ± 0.03
070110	0.66 ± 0.02	1.15 ± 0.10	16.84 ± 0.18	< 0.10
070125	0.55 ± 0.04	1.06 ± 0.07	14.95 ± 0.48	0.30 ± 0.04
070129	0.58 ± 0.02	1.12 ± 0.09	16.98 ± 0.13	0.28 ± 0.02
070506	0.51 ± 0.06	1.02 ± 0.08	16.00 ± 0.69	0.44 ± 0.05
070611	0.95 ± 0.02	0.06 ± 0.02
070721B	0.88 ± 0.02	0.20 ± 0.02
071020	0.15 ± 0.05	0.69 ± 0.03	14.79 ± 0.25	0.43 ± 0.04
071031	0.64 ± 0.01	1.13 ± 0.11	15.35 ± 0.55	< 0.07
071112C	0.37 ± 0.02	0.86 ± 0.06	15.67 ± 0.22	< 0.08
071117	0.41 ± 0.03	0.94 ± 0.08	16.95 ± 0.92	0.28 ± 0.02
080210	0.25 ± 0.03	1.36 ± 0.14	16.03 ± 0.15	0.33 ± 0.03
080319B	0.77 ± 0.02	< 0.11
080520	0.78 ± 0.02	0.22 ± 0.02
080707	0.71 ± 0.03	1.22 ± 0.05	16.90 ± 0.16	< 0.12
080721	0.68 ± 0.02	< 0.12
080905B	0.80 ± 0.07	0.42 ± 0.03
080913	0.79 ± 0.03	0.12 ± 0.03
080916A	0.49 ± 0.05	0.99 ± 0.09	17.00 ± 0.88	0.15 ± 0.04
080928	1.08 ± 0.02	0.29 ± 0.03

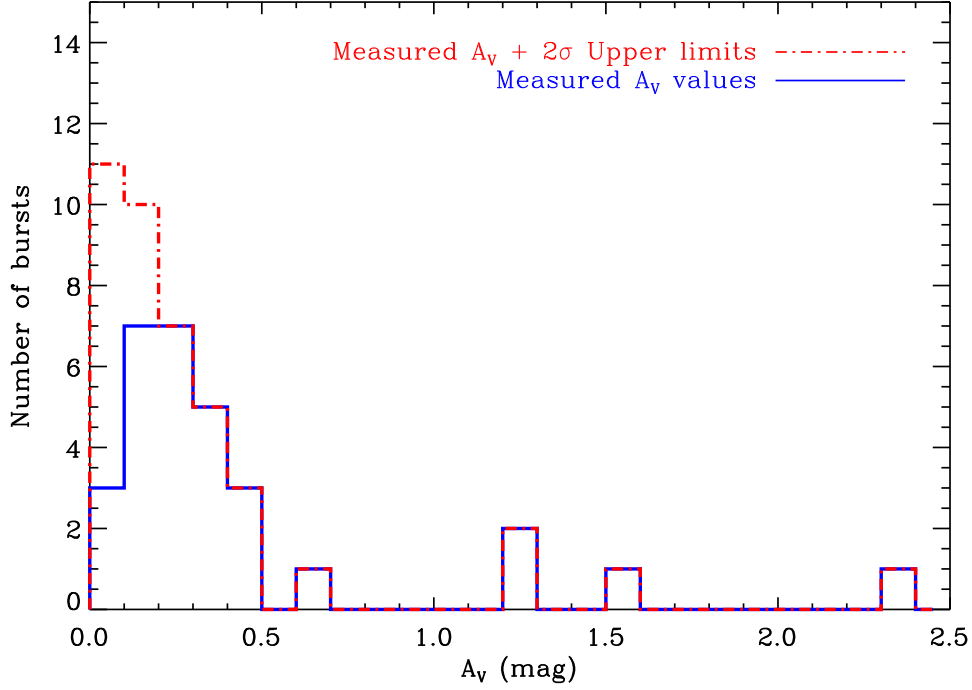


Figure 5.2: Distribution of the restframe visual extinction, A_V , of our flux calibrated spectroscopic sample. The solid curve corresponds to detections; the dot-dashed curve to detections and 2σ upper limits.

Table 5.4: Best fit extinction curve parameters for the afterglow cases where FM is the best model (see Table. 5.2). GRB 080607 is obtained with Keck telescope and is not a part of our spectroscopic sample.

Parameter	070802	080605	080805	080607
c_1	0.02 ± 0.25	-0.81 ± 0.16	0.26 ± 0.15	1.19 ± 0.43
c_2 (μm)	0.82 ± 0.16	0.86 ± 0.07	0.57 ± 0.06	0.37 ± 0.10
c_3	1.46 ± 0.29	0.35 ± 0.04	0.89 ± 0.11	2.96 ± 0.66
c_4 (μm^2)	0.26 ± 0.08	0.26 ± 0.10	0.15 ± 0.14	0.17 ± 0.10
c_5 (μm^{-1})	5.03 ± 0.31	6.30 ± 0.41	6.50 ± 0.14	5.88 ± 0.34
γ (μm^{-1})	0.99 ± 0.01	0.90 ± 0.02	0.90 ± 0.02	1.20 ± 0.04
R_V	$2.81^{+0.67}_{-0.68}$	$2.93^{+0.17}_{-0.20}$	2.48 ± 0.39	$3.75^{+1.02}_{-1.06}$
x_0 (μm^{-1})	4.64 ± 0.01	4.55 ± 0.01	4.57 ± 0.01	4.52 ± 0.02
β_1	0.88 ± 0.06	0.76 ± 0.03	0.81 ± 0.02	$0.96^{+0.05}_{-0.06}$
A_V (mag)	1.19 ± 0.15	$1.20^{+0.09}_{-0.10}$	1.53 ± 0.13	$2.33^{+0.46}_{-0.43}$

of graphite and silicate grains (Pei 1992; Prevot et al. 1984). The presence of the 2175 Å bump in GRB afterglow SEDs indicates that these GRBs occur in more evolved and massive galaxies and have dust properties similar to our local disk galaxies. Beyond our Local Group these distant GRBs can provide information on the graphite content

of small grains in the surrounding circumburst environments.

It is notable that less than 9% of the GRB extinction curves show an unequivocal 2175 Å bump. This is a small fraction, consistent with the prevailing notion that strongly star-forming galaxies, and in particular GRB hosts, have featureless dust extinction curves like the SMC (e.g. Pei 1992; Calzetti et al. 1994; Schady et al. 2010; Kann et al. 2010; Krühler et al. 2010; Greiner et al. 2011). However, there are only five known extinction curves toward the SMC, and one in fact does have a 2175 Å bump (Pei 1992). Furthermore, the starburst sample of Calzetti et al. (1994) with SMC-like attenuation curves is very small, containing only six objects. Therefore we examined our sample to see in how many SEDs a bump could have been detected. We found that for 12 cases the bump region is not significantly covered by our spectra or photometry and in a few more the signal-to-noise ratio is very low. This is approximately 40–50% of the *extinguished* sample. It could be argued therefore, that in only about a quarter of the sample are we reasonably certain that no bump is present. Furthermore, there is very clear evidence in this sample that afterglows with a 2175 Å bump are preferentially heavily extinguished ($A_V \gtrsim 1$).

It is apparent that our spectroscopic sample is heavily reliant on optically bright afterglows; the bulk of bursts in the sample have an average magnitude of 21.1 with a standard deviation of 1.7 magnitudes. But a MW style extinction gives 2–3 magnitudes of extinction in the *BVRI* bands for $A_V = 1$ at $z = 2$. A restframe $A_V \gtrsim 1$ would make spectroscopy unfeasible for the overwhelmingly majority of these bursts and a redshift would almost certainly not have been found for any except the brightest few (apart from emission lines from the host galaxy). It is obvious that we are heavily biased against these high extinction sightlines. F09 report a dark burst fraction of 25–42% for that sample. If most of those dark bursts are similar to the most heavily extinguished bursts in our sample, many, if not all, may have a 2175 Å bump in their extinction curves. Our conclusion is that the apparent prevalence of the SMC extinction curve in GRB hosts is very likely an artifact of the bias in favour of low extinction sightlines and the frequent lack of good coverage of the bump region. We can only say that the bump is not present in about a quarter of our sample, and that it is present in 7%, and that we know there is a clear preference for the bump to be detected in the most extinguished sightlines. Currently it is therefore not possible to say whether a featureless extinction curve or one with a bump is more common in GRB host galaxies. But it seems likely that the 2175 Å bump is far more prevalent than previously believed.

5.5.2 CONSTRAINTS ON R_V

We attempted to constrain R_V specifically for the extinction curves that were well fit with SMC-type extinction. We fitted the data again with the FM model, this time fixing the FM parameters to the SMC average extinction curve values given in Gordon

Table 5.5: Table listing the spectroscopic GRB sample with their name, Galactic column density, neutral hydrogen column density when available from the literature, equivalent column density ($N_{H,X}$) determined from the X-ray spectral fits and the $N_{H,X}/A_V$ ratio. We reported 2σ upper limits for $N_{H,X}$ where detection is $< 2\sigma$ significant.

GRB	A_V mag	$\log N_{H\text{I}}$ cm^{-2}	$N_{H,X}$ 10^{22} cm^{-2}	$N_{H,X}/A_V$ $10^{22} \text{ cm}^{-2} \text{ mag}^{-1}$
050401	0.65 ± 0.04	22.60 ± 0.30	$1.56^{+0.19}_{-0.18}$	$2.40^{+0.33}_{-0.32}$
050730	0.12 ± 0.02	22.10 ± 0.10	< 0.70	< 5.83
050824	0.15 ± 0.03	...	< 0.20	< 1.33
060115	0.10 ± 0.02	21.50 ± 0.10	< 0.84	< 8.40
060512	< 0.12	...	< 0.07	...
060614	0.11 ± 0.03	...	< 0.05	< 0.45
060707	0.08 ± 0.02	21.00 ± 0.20	< 1.03	< 12.9
060708	0.14 ± 0.02	...	< 0.46	< 3.29
060714	0.21 ± 0.02	21.80 ± 0.10	$1.39^{+0.20}_{-0.19}$	$6.62^{+1.14}_{-1.10}$
060729	0.07 ± 0.02	...	0.13 ± 0.02	1.89 ± 0.61
060904B	0.34 ± 0.03	...	0.47 ± 0.04	1.38 ± 0.17
060906	< 0.09	21.85 ± 0.10	< 5.3	...
060926	0.32 ± 0.02	22.70 ± 0.10	< 8.00	< 25.0
060927	< 0.12	22.50 ± 0.15	< 5.7	...
061007	0.34 ± 0.03	...	0.45 ± 0.03	1.29 ± 0.14
061021	< 0.10	...	$0.07^{+0.02}_{-0.01}$	> 0.70
061110A	< 0.10	...	< 0.03	...
061110B	0.23 ± 0.03	22.35 ± 0.10	< 8.40	< 36.52
070110	< 0.10	21.70 ± 0.10	< 0.34	...
070125	0.30 ± 0.04	...	$0.39^{+0.20}_{-0.17}$	$1.30^{+0.69}_{-0.59}$
070129	0.28 ± 0.02	...	$0.78^{+0.22}_{-0.20}$	$2.79^{+0.81}_{-0.74}$
070318	0.45 ± 0.05	...
070506	0.44 ± 0.05	22.00 ± 0.30	< 1.26	< 2.86
070611	0.06 ± 0.02	21.30 ± 0.20	< 0.94	< 15.7
070721B	0.20 ± 0.02	21.50 ± 0.20	< 1.57	< 7.85
070802	1.19 ± 0.15	21.50 ± 0.20	< 2.90	< 2.44
071020	0.43 ± 0.04	< 20.30	0.46 ± 0.02	1.07 ± 0.11
071031	< 0.07	22.15 ± 0.05	< 1.20	...
071112C	< 0.08	...	< 0.16	...
071117	0.28 ± 0.02	...	$1.18^{+0.20}_{-0.30}$	$4.21^{+0.77}_{-1.11}$
080210	0.33 ± 0.03	21.90 ± 0.10	$2.15^{+0.62}_{-0.54}$	$6.52^{+1.97}_{-1.74}$
080319B	< 0.11	...	0.12 ± 0.01	> 1.10
080520	0.22 ± 0.02	...	$1.38^{+0.40}_{-0.59}$	$6.27^{+1.90}_{-2.74}$
080605	$1.20^{+0.09}_{-0.10}$...	0.71 ± 0.08	0.59 ± 0.08
080707	< 0.12	...	0.38 ± 0.19	> 3.17
080721	< 0.12	21.60 ± 0.10	0.86 ± 0.02	> 7.17

GRB	A_V mag	$\log N_{\text{HI}}$ cm^{-2}	$N_{\text{H,X}}$ 10^{22} cm^{-2}	$N_{\text{H,X}}/A_V$ $10^{22} \text{ cm}^{-2} \text{ mag}^{-1}$
080805	1.53 ± 0.13	...	$1.22^{+0.35}_{-0.45}$	$0.80^{+0.24}_{-0.30}$
080905B	0.42 ± 0.03	< 22.15	$2.38^{+0.51}_{-0.43}$	$5.67^{+1.28}_{-1.10}$
080913	0.12 ± 0.03	< 21.14	< 9.30	< 77.5
080916A	0.15 ± 0.04	...	0.68 ± 0.07	4.53 ± 1.29
080928	0.29 ± 0.03	...	$0.30^{+0.13}_{-0.12}$	$1.03^{+0.46}_{-0.43}$
080607 ^a	$2.33^{+0.46}_{-0.43}$	22.70 ± 0.15	$3.77^{+0.23}_{-0.22}$	$1.62^{+0.33}_{-0.31}$

^aKeck spectrum.

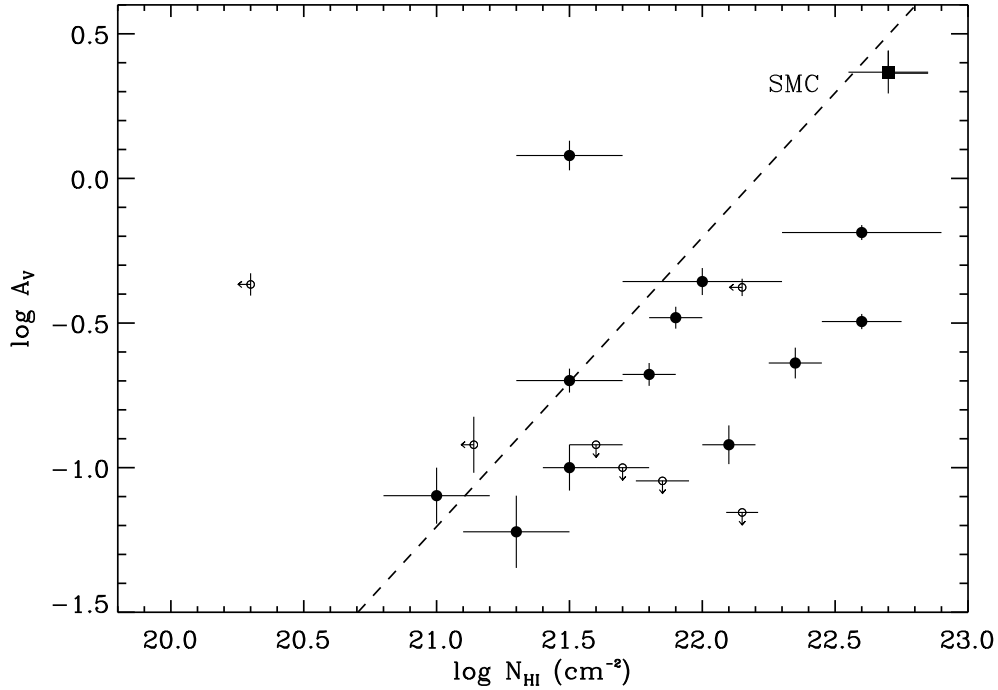


Figure 5.3: A_V against spectroscopically measured HI column density in log-log space. N_{HI} values are obtained from the literature and given in Table 5.5. The dashed line corresponds to the $N_{\text{H,I}}/A_V$ ratio for the SMC environment given by Weingartner & Draine (2001).

et al. (2003) and fixing $\Delta\beta$ to 0.5 for the 20 relevant spectral break cases (see §5.4.1), but allowing R_V to vary freely. In most cases R_V is degenerate with A_V , so that we cannot constrain R_V in any useful sense. For GRB 071020 and 080928 we can constrain R_V to $3.0^{+0.7}_{-0.8}$ and $2.0^{+0.5}_{-0.7}$ respectively (1σ errors for two parameters of interest). From these cases, we can determine that it is the strong constraint on the absolute optical flux level that allows the constraint on R_V . In the former case it is because the spectral break is very close to the optical, and in the latter because the X-ray and optical fluxes are so similar. In both cases the extinction is relatively high – $A_V = 0.43 \pm 0.04$ and

0.29 ± 0.03 respectively – and the X-ray spectrum fairly well-defined. To fix R_V in future observations will require that the unextinguished power-law is well-constrained, either through infrared spectroscopy or better X-ray observations. The ideal way to do this is to use mid-infrared data in concert with good X-ray data. To date this has been published for only one GRB afterglow using observations with *Spitzer* (Heng et al. 2008), albeit with a low S/N result. While more mid-infrared observations are now unlikely, and better X-ray observations will not be routinely available in the foreseeable future, near-infrared spectra are now regularly obtained with the X-shooter spectrograph on the VLT and may allow us to obtain reasonably well-constrained R_V values for GRB extinction sightlines in the next few years.

5.5.3 GAS-TO-DUST RATIOS

The H I column densities for these lines of sight have been measured from the 1216 Å Ly α absorption line in F09. The ratio of A_V to H I gives, in principle, an estimate of the gas-to-dust ratio in the host galaxy of the GRB (Fig. 5.3). However, the potential ionizing and destructive effect of the GRB and its afterglow may substantially complicate this picture. The vast majority of data points lie at values greater than the SMC gas-to-dust ratio – the dashed line in Fig. 5.3 corresponds to the gas-to-dust ratio of the SMC environment with a value of $N_{\text{HI}}/A_V = 1.6 \times 10^{22} \text{ cm}^{-2} \text{ mag}^{-1}$ (Weingartner & Draine 2001). The only clear outlier is GRB 071021, with a very small neutral hydrogen column density quoted in F09. However, the burst is at $z = 2.1$, and the spectrum is cut off in the blue. On close re-inspection of the 2D spectrum, it seems unlikely that such a strong limit can indeed be placed on the Ly α line in the afterglow of this burst. Indeed, it seems possible that this burst could have a large enough neutral column density in hydrogen to make it perfectly consistent with the SMC value. Therefore, the only burst in our sample that securely yields a gas-to-dust ratio lower than the SMC is GRB 070802, with a gas-to-dust ratio consistent with Galactic sightline values. As pointed out by Elíasdóttir et al. (2009), this afterglow sightline is highly unusual among GRBs in this regard, a fact strengthened by our results. However, it is clearly not a property of all sightlines with the 2175 Å bump, since GRB 080607 has a gas-to-dust ratio a factor of ten higher. We do not have H I column density measurements for GRB 080605 and GRB 080805. The overall distribution suggests that gas-to-dust ratios in GRB environments are typically SMC-like or higher. An obvious idea is that metallicities that are SMC-like or lower are responsible for the high gas-to-dust ratios. However two arguments point against such a conclusion: first, the metals-to-dust ratio, where the metal column density is derived from soft X-ray absorption is typically an order of magnitude or more above the values from the Local Group (see below and Watson et al. 2007; Schady et al. 2010); second, when we correct the H I column for the metallicity in Fig. 5.4, we show that even corrected for metallicity, most GRB sightlines

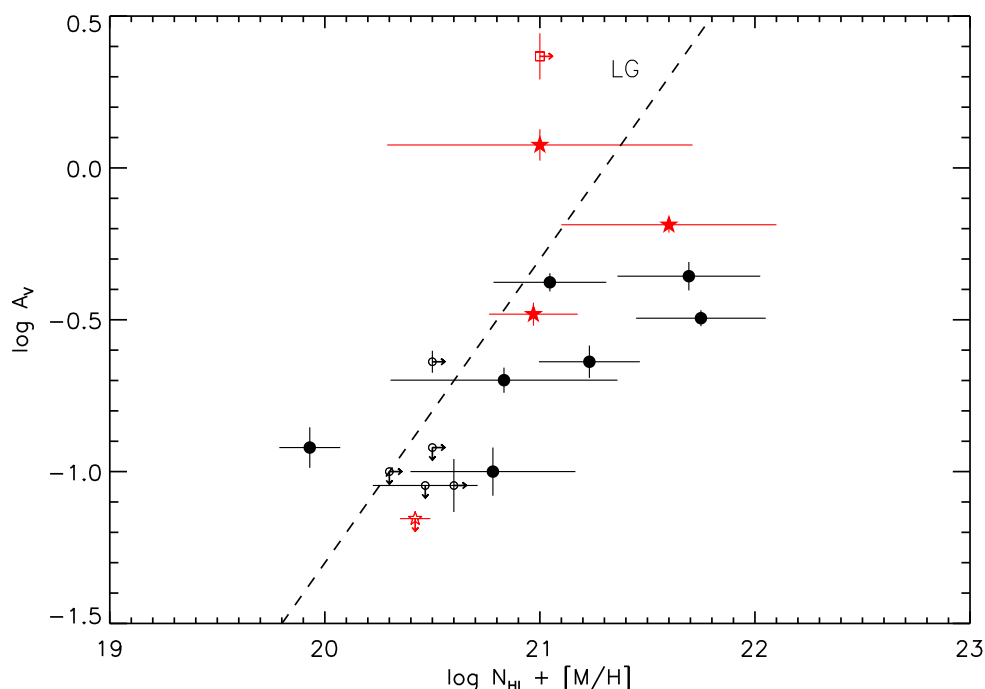


Figure 5.4: Visual extinction against UV metal abundances in solar units. The metallicities obtained from the literature based on Zn element are marked with red stars. The rest of the data points are based on Si element metallicities (see Table 5.6). GRB 080607 is indicated with a red square. The metallicity or A_V upper limits are represented by small circles or stars. The dashed line indicates metals-to-dust relation for the Local Group (indicated as LG).

have a super-Local-Group gas-to-dust ratio.

In Fig. 5.4 we check if metallicity effects alone could be responsible for the high gas-to-dust ratios without reference to the X-ray absorption. We derived a metal column density in solar units using $\log (N_{\text{H I}}/\text{cm}^{-2}) + [\text{M}/\text{H}]$ (equivalent to $N_{\text{H,X}}$). The $[\text{M}/\text{H}]$ values are given in Table 5.6 and the $N_{\text{H I}}$ values for the corresponding GRBs are taken from Table 5.5. These are metal column densities in the gas phase, derived from the low ionization species, based on the non-refractory elements Zn and Si. In Fig. 5.4 we see that the low ionization metals-to-dust ratios are closer to the Local Group value than the gas-to-dust ratios, but are still typically higher. Conclusions on the gas-to-dust ratio of the host galaxies of GRBs are inevitably complicated by the fact that we know a majority of the gas along the line of sight to a GRB is ionized close to the burst (Watson et al. 2007; Schady et al. 2010; Prochaska et al. 2007; Vreeswijk et al. 2007; Ledoux et al. 2009), and it is suspected that any dust near the GRB will be either sublimated or cracked by the GRB (e.g. Fruchter et al. 2001; Perna & Lazzati 2002). The X-ray absorption, by contrast is far less affected by photo-ionization, and so GRBs show much larger metals-to-dust ratios (Fig. 5.5). The most probable interpretation is that the column has

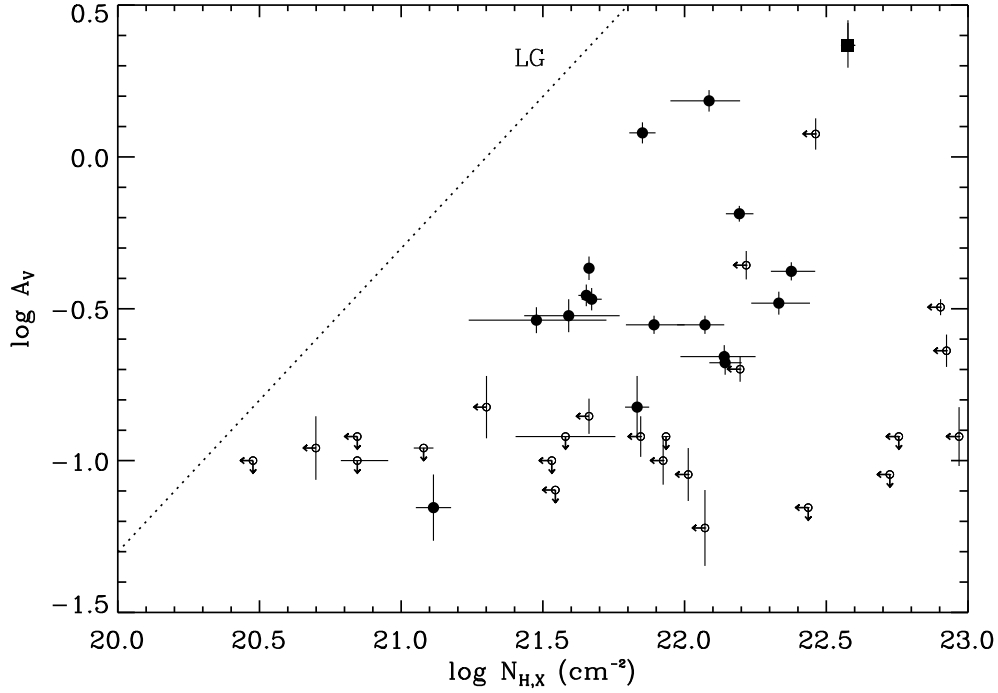


Figure 5.5: A_V measurements versus $N_{H,X}$ for the spectroscopic GRB sample determined from X-ray spectral analysis and SED fitting. The dotted curve represents the metals-to-dust ratio for the Local Group environments (indicated as LG) assuming solar abundances.

been strongly affected by the GRB/afterglow, and the ionization distance and the dust sublimation distance are different. Therefore the metals-to-dust and gas-to-dust ratios derived from the optical/UV are not representative of the intrinsic ratios for the GRB host, but instead are due to the interaction of the distribution of the gas and dust along the column and the luminosity and spectrum of the GRB and its afterglow. Thus, the SMC-like and higher gas-to-dust ratios found in GRB afterglows, even after accounting for metallicity, seem to be due to the competing effects of gas ionization and dust destruction. The ratios found are closer to the values in the Local Group than are the metals-to-dust ratios derived from X-rays. An obvious explanation for this is that since we know that hydrogen ionization certainly occurs in the surroundings of the GRB, the H I column densities are simply lower limits to the actual gas column. So far we have no unequivocal evidence for dust destruction in GRB surroundings, but it seems probable that it occurs; what we can at least say from these results is that hydrogen ionization in the GRB surroundings is a more efficient process than dust-destruction, drawing the gas values closer to the Local Group ratio.

5.5.4 METALS-TO-DUST RATIOS

Metal column densities ($N_{H,X}$) from soft X-ray absorption in excess of the Galactic absorption (e.g. Galama & Wijers 2001; Watson et al. 2002; Stratta et al. 2004; Starling et al. 2005, 2007; Gendre et al. 2006; Butler & Kocevski 2007; Watson et al. 2007; Schady et al. 2010; Campana et al. 2010b; Evans et al. 2007) have been detected in most GRB afterglows; a rather surprising fact, since the absorption becomes harder to detect with increasing redshift. The effective X-ray absorption is dominated by various species, mostly oxygen and silicon K-shell absorption and including helium and iron L-shell (Morrison & McCammon 1983). At higher redshifts (i.e. $z > 2.5$) the soft X-ray absorption becomes increasingly dominated by the heavier elements such as iron, silicon and sulphur (Kallman et al. 2003; Gou et al. 2005; Butler 2007; Hurkett et al. 2008). It is important to note that the X-ray column densities are typically reported in units of equivalent hydrogen column density assuming solar abundances. The upper limits and measured $N_{H,X}$ values of our spectroscopic GRB sample are given in Table 5.5. Significant excess X-ray absorption was detected for 21 GRBs in our sample. The X-ray column densities are effectively metal column densities in both gas and dust, and would have to be corrected by the metallicity to obtain the gas column density. However, this is not enough. Due to a lack of information on the precise ionization state and structure of the gas, the absorption is invariably fit with a neutral gas model. We are well aware that the gas surrounding the GRB that causes the majority of the absorption is highly ionized (Watson et al. 2007; Schady et al. 2011; Prochaska et al. 2007). The metal column densities derived from the fits using neutral models are therefore strictly lower limits to the actual metal column densities. How close they are to the real value of the total column density depends strongly on the ionization state of the gas. It is reasonable to assume we are not underestimating the column densities by a factor of more than ten, since in the cases with the highest column densities, Compton scattering effects would become significant (Watson & Laursen 2010; Campana et al. 2011), and we would not detect some bursts in X-rays.

In Fig. 5.5 we plot the dust extinction and soft X-ray–derived metal column densities for the sample. It is immediately apparent that all of the dust extinctions lie far below the expectation for the Local Group metals-to-dust ratios. For the Galaxy, $N_{H,X}/A_V$ has been measured for many sightlines and using different techniques (e.g. Güver & Özel 2009; Predehl & Schmitt 1995; Gorenstein 1975). For the LMC and SMC, the gas-to-dust ratio (N_{HI}/A_V) can be converted to the same units ($N_{H,X}/A_V$) by correcting for the metallicity. The N_{HI}/A_V relation for the MW varies in the range $(1.7 - 2.2) \times 10^{21} \text{ cm}^{-2} \text{ mag}^{-1}$. Correcting for metallicities, the LMC (Fitzpatrick 1985) and SMC (Weingartner & Draine 2001) values are consistent with this range (see for a review Draine 2003). Therefore, we use a canonical value of $N_{H,X}/A_V \approx 0.2 \times 10^{22} \text{ cm}^{-2} \text{ mag}^{-1}$ for the metals-to-dust ratio of the Local Group of galaxies for comparison to our sample.

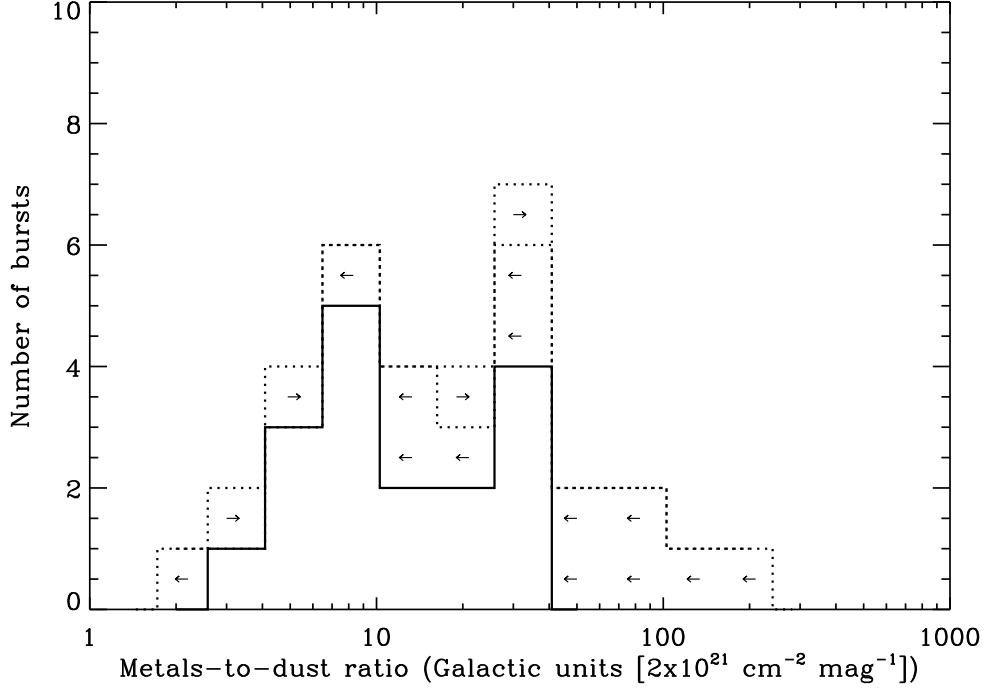


Figure 5.6: Metals-to-dust ratio ($N_{H,X}/A_V$) distribution of our spectroscopic GRB sample in Galactic units. The solid line show the cases where both $N_{H,X}$ and A_V are significantly measured. The upper and lower limits to the metals-to-dust ratios are shown by the dotted histogram and the limits in each bin are marked by left or right arrow.

Dai & Kochanek (2009) showed that in lensing galaxies, the metals-to-dust ratio is also consistent with values in the Local Group. Together, those results hint that there may be an almost universal metals-to-dust ratio, at least in galaxies that are somewhat evolved.

In apparent contrast to this, our sample shows a spread of metals-to-dust ratios that covers a range from approximately three to thirty times the Local Group value (Fig. 5.6). The fact that none of our objects have a metals-to-dust ratio below the Local Group value suggests that the Local Group ratio may at least be a minimum. Indeed, our result here, which confirm much previous work (e.g., Galama & Wijers 2001; Schady et al. 2010, 2011; Stratta et al. 2007), may be consistent with a universal metals-to-dust ratio if dust destruction by the GRB and afterglow is responsible for the lack of dust that leads to these large metals-to-dust ratios. Under this hypothesis, the GRB would have to destroy the equivalent of between 1 and 10 magnitudes of extinction (A_V) of dust within a few pc of the burst (Watson et al. 2007), which seems feasible (Fruchter et al. 2001; Waxman & Draine 2000; Perna et al. 2003). As pointed out by Fruchter et al. (2001), Waxman & Draine (2000), and Perna et al. (2003), observations within the first few seconds of a burst should, for most GRBs, show a colour change related to the destruction of the dust. Based on these data and the assumption of a universal metal-

to-dust ratio, such a colour change would be very large; however, given that we rely on bright restframe UV emission for detection, and it is precisely the bright UV emission that is primarily responsible for the dust destruction, it seems unlikely that we will be able to detect such a colour change before it is complete.

It is worth noting here again that neither ionization nor metallicity can resolve the dust-poor nature of these absorptions. In the former case we know the gas must already be highly ionized; the dust would not survive in such an environment. As to the latter, we are directly observing the metal absorption, changes to the overall metallicity therefore have no effect on this ratio.

We examined the possibility of a relationship between the metals-to-dust ratio and the line-of-sight extinction (Fig. 5.7). While it might be anticipated that GRB hosts that possessed high extinction sightlines might be dust-enriched and have low metals-to-dust ratios, we see no clear correlation here either. Even the highly extinguished events with a 2175 Å bump have metals-to-dust ratios similar to the rest of the sample.

We briefly compared the metals-to-dust ratios of our spectroscopic sample with the burst redshift. We see no obvious trend of the ratio with redshift except what might be expected from the detectability limits of the X-ray absorption increasing with redshift and while the limit for A_V essentially decreases with redshift (see Sect. 5.8).

5.5.5 THE EFFECT OF METALLICITY

Metallicities measured in GRBs vary from less than 1/100 to nearly solar values, and are usually higher than the values found in QSO-DLA sightlines (see Fynbo et al. 2006d; Prochaska et al. 2007; Fynbo et al. 2008c; Ledoux et al. 2009). This trend supports the idea that GRBs occur in low mass or dwarf galaxies, representing the largest fraction of galaxies in the local Universe with large star formation rates. This favours the currently accepted scenario of long duration GRBs, the collapse of massive, rotating Wolf-Rayet star (Woosley 1993; MacFadyen & Woosley 1999). The metallicities are obtained from Voigt-profile fitting to mildly saturated lines arising from non-refractory elements using mid/high resolution spectroscopy. In our metallicity sub-sample we obtained metallicities for the GRBs from the literature (see Table 5.6). The metallicities based on Zn are given for GRB 050401, GRB 070802, GRB 071030 and GRB 080210. In addition, we derived Si column densities, and hence, metallicities, for GRB 060707, GRB 060714, GRB 070110, using the optically thin limit approximation (e.g. Petitjean 1998) with oscillator strengths from Morton (1991). For these three bursts we used the equivalent width of the weak and hence likely only mildly saturated Si II (1808 Å) line to estimate the Si II column density. For a few more GRBs there is no detection of Si II (1808 Å) whereas Si II (1526 Å) is well-detected (see F09). We inferred metallicities for eight GRB hosts using the restframe equivalent widths of Si II (1526 Å). The equivalent widths for all

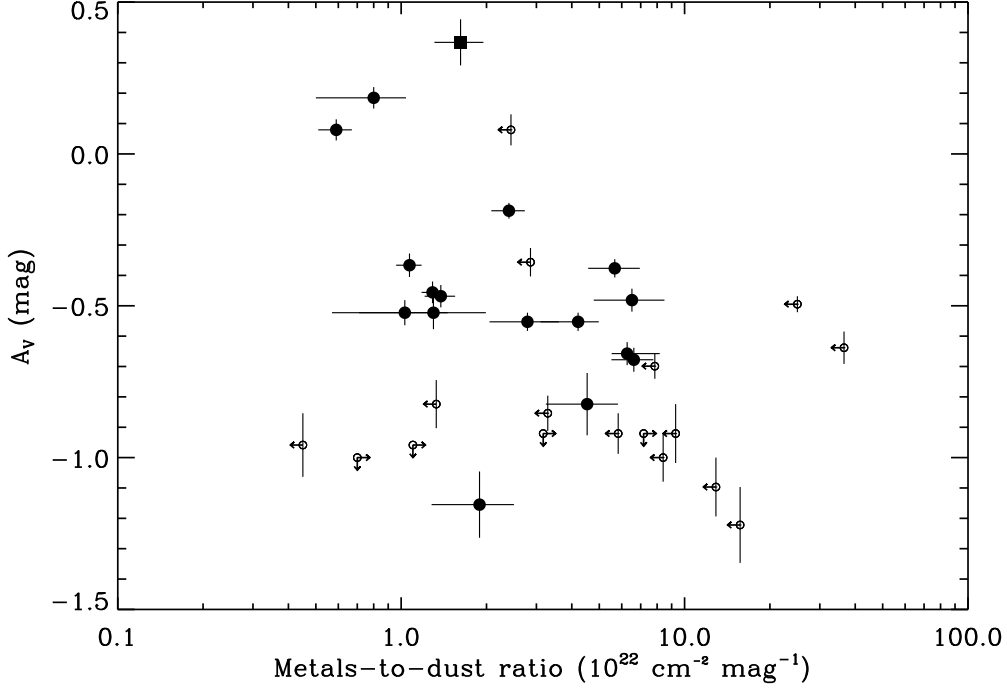


Figure 5.7: Restframe A_V and metals-to-dust ratio ($N_{H,X}/A_V$) for our GRB sample. The solid circles are for the cases where $N_{H,X}$ and A_V are $\geq 2\sigma$ significant. The open circles represent upper limits either obtained for $N_{H,X}$ or A_V . The solid square corresponds to GRB 080607 observed with the Keck telescope.

these GRBs are obtained from F09. The metallicities are derived in these cases using the metallicity– EW_{1526} correlation for QSO-DLAs (Prochaska et al. 2008a, Eq. 1). Other independent QSO-DLA studies also confirm this tight trend between EW_{1526} and $[M/H]$ (Kaplan et al. 2010); GRB-DLAs also exhibit the same trend (Prochaska et al. 2008a). For GRB 080607 the absorption line features are highly saturated, therefore only lower limits are obtained (Prochaska et al. 2009). The metallicity for this burst could be solar or even super solar. The reported metallicity here is a lower limit based on Zn. No metallicity measurements are available for 60% of our sample, mainly due to a lack of high- or medium-resolution spectroscopy or a redshift $\lesssim 2$, placing the $Ly\alpha$ line outside the observed wavelength range.

In Fig. 5.8 we plot metallicities for our GRB sub-sample versus the visual dust extinction, A_V . Fig. 5.8 shows that there may be a slight trend between the metallicity and dust extinction. We see somewhat higher dust with increasing metallicity, suggesting that more metal rich systems may be more dusty. However we do not claim this correlation here with any confidence.

Schady et al. (2010) also found high X-ray–derived metals-to-dust ratios and proposed that these ratios could be related to the metallicity of the GRB environment. They suggested that there might be an anti-correlation between the cold, gas-phase

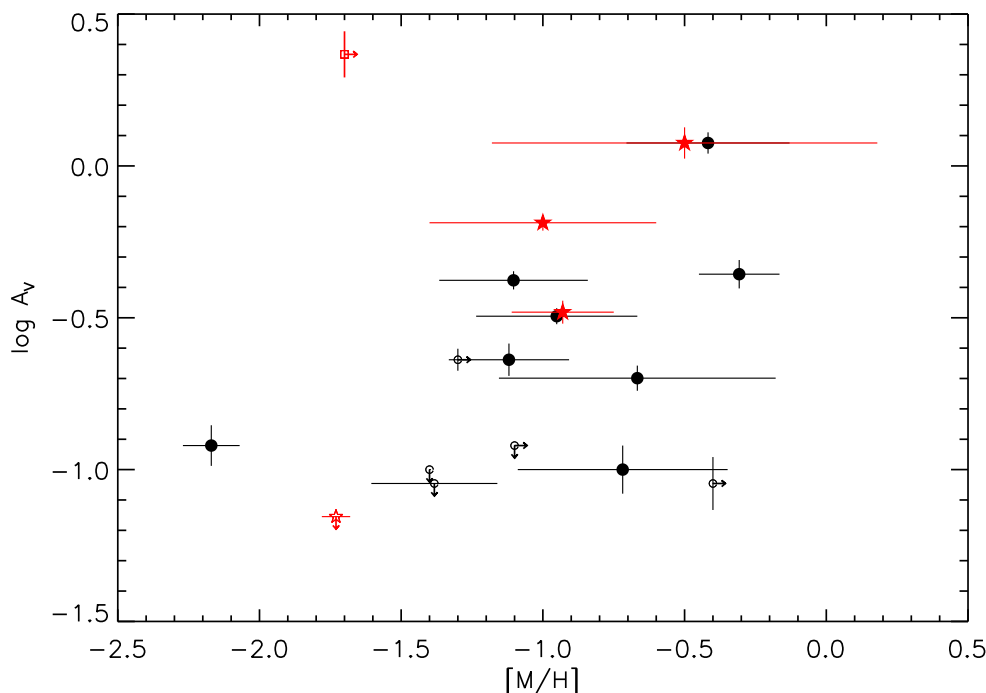


Figure 5.8: Restframe A_V measurements versus GRB metallicity. The metallicities obtained from the literature based on Zn are marked with red stars. The remaining data points are based on Si element metallicities (see Table 5.6). GRB 080607 is shown as an open square. The small circles or stars represent metallicity or A_V upper limits.

metallicity and the metals-to-dust ratios; i.e. metal poor galaxies forming dust less efficiently from their metals than the metal rich ones. Fig. 5.10 shows the relation using the data in our sample. We see no obvious trend between the metals-to-dust ratios and the gas-phase metallicities and cannot confirm the relation. For the Spitzer Infrared Nearby Galaxies Survey (SINGS) sample Draine et al. (2007) found that the *gas*-to-dust ratio was anti-correlated with metallicity. The anti-correlation was also found for dwarf galaxies (Lisenfeld & Ferrara 1998). Such a correlation would not be terribly surprising since the dust is composed of metals. In Fig. 5.9 we plot the gas-to-dust ratios of our GRB sub-sample versus metallicity. There is an anti-correlation between the two values; a Spearman rank test for a random origin for such an anti-correlation yields a $< 1\%$ probability. So, while there is some evidence of an anti-correlation between the gas-to-dust ratio and metallicity in GRB host galaxy sightlines, we find no evidence for a relationship between the metals-to-dust ratio and the metallicity. GRB environments have consistently higher metals-to-dust ratios than the Local Group but at the same time their metallicities cover the range as observed in the Local Group with a large scatter. Fig. 5.10 in fact shows the large gap between the Local Group and GRB hosts in metals-to-dust ratios.

Table 5.6: GRB sub-sample metallicity measurements taken either from the literature or based on the Si II lines strength. The Si II ($\lambda = 1808 \text{ \AA}$, 1526 \AA) absorption lines are used to obtain metallicity by using the optically thin approximation and the Prochaska et al. (2008a) correlation. The metallicity for GRB 080607 is based on Zn element. The metallicity could be solar or even super-solar for this burst (Prochaska et al. 2009).

GRB	[M/H]	Reference
050401	-1.00 ± 0.40	Watson et al. (2006a)
050730	-2.17 ± 0.10	Ledoux et al. (2009)
060115	-0.72 ± 0.37	Prochaska et al. (2008a) correlation
060707	> -0.40	From Si II(1808)
060714	> -1.30	From Si II(1808)
060906	-1.38 ± 0.22	Prochaska et al. (2008a) correlation
060926	-0.95 ± 0.28	Prochaska et al. (2008a) correlation
061110B	-1.12 ± 0.21	Prochaska et al. (2008a) correlation
070110	> -1.40	From Si II(1808)
070506	-0.31 ± 0.14	Prochaska et al. (2008a) correlation
070721B	-0.67 ± 0.49	Prochaska et al. (2008a) correlation
070802	-0.50 ± 0.68	Elíasdóttir et al. (2009)
071031	-1.73 ± 0.05	Ledoux et al. (2009)
080210	-0.93 ± 0.18	De Cia et al. (2010)
080605 ^a	-0.42 ± 0.29	Prochaska et al. (2008a) correlation
080607	> -1.70	Prochaska et al. (2009)
080721	> -1.10	Starling et al. (2009)
080905B	-1.10 ± 0.26	Prochaska et al. (2008a) correlation

^aThe metallicity for GRB 080605 is based on the Si II line EW. Being at $z < 2$, H I is not detected for this burst. Therefore it is not included in Fig. 5.4 and 5.9.

5.6 CONCLUSIONS

In this work we have presented the results of our analyses of 41 GRB afterglows from X-ray to NIR. This is not only the first spectroscopic study of *absolute* extinction curves in distant galaxies, but also the largest extinction sample outside the Local Group. The SEDs are almost universally well-described by a power-law or broken power-law with absorption in soft X-rays and extinction in the optical/UV. Our analysis shows that a break occurs between optical and X-ray in about half of all SEDs at times typically between a few hours and a day after the burst. The mean spectral change excluding one outlier, is $\Delta\beta = \beta_2 - \beta_1 = 0.51$, with a very small scatter (0.02), suggesting that in future afterglow SED analyses, the spectral change can typically be fixed to 0.5.

63% (26/41) of the bursts in the sample are well-fit with an SMC extinction curve,

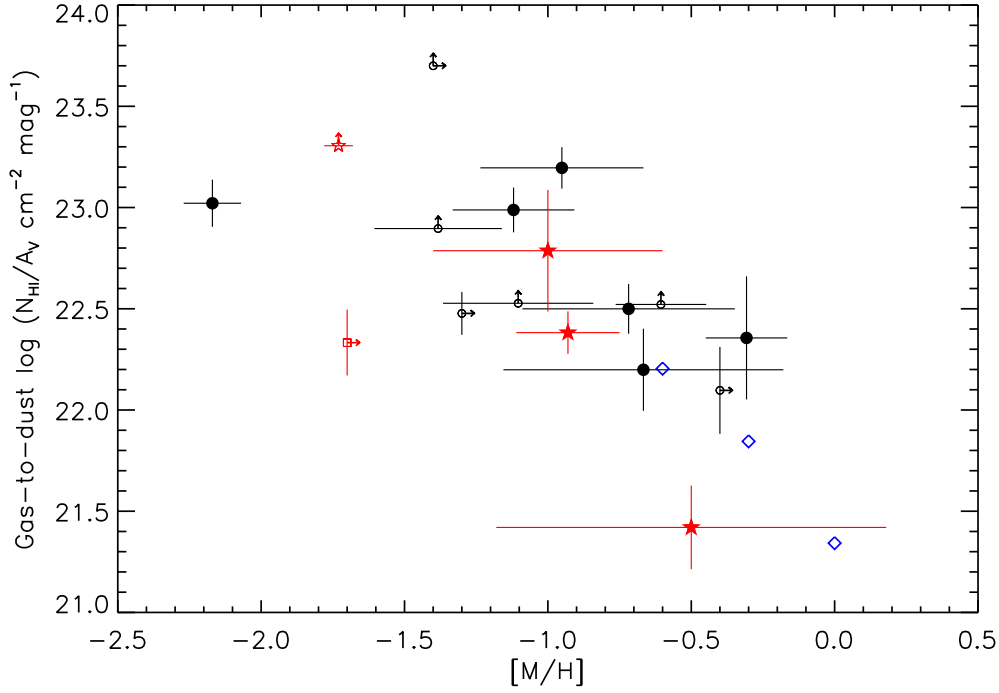


Figure 5.9: Gas-to-dust ratio versus metallicity for GRB sub sample. The metallicities obtained from the literature based on Zn are marked with red stars. The remaining data points are based on Si (see Table 5.6). GRB 080607 is indicated with a red square. The small circles and stars denote metallicity or gas-to-dust ratio upper limits. MW, LMC and SMC environments are denoted with blue diamonds from right to left.

with 27% (11/41) of the afterglows found to have no significant extinction. Of the remaining 4, 3 have a 2175 Å bump and one has a very unusual extinction curve. The bump cases comprise 7% of our spectroscopic sample. Most bursts of our sample have moderate or low extinction, with $A_V < 0.65$. However cases with a 2175 Å bump all have $A_V > 1.0$. The predominance of the bump in the extinction curves of high-extinction sightlines allows us to claim that since our sample is heavily biased against high extinction sightlines, missing between a quarter and a half of all bursts, the percentages of extinction curves listed above are not at all representative of GRB hosts as a whole. Previous conclusions suggesting that the bump is a rare feature in extragalactic sightlines are also likely to be incorrect. An important conclusion from this work is that the most extinguished systems seem to correlate with the systems with a 2175 Å bump and possibly with high metallicity. Both facts point to the most extinguished systems being the most evolved, and therefore likely more massive. This is consistent with reports on work by Perley et al. (2011a) based on Spitzer data suggesting that dark bursts are more likely to have red, dusty host galaxies. Since a very substantial fraction ($\sim 25 - 42\%$) of GRB afterglows are dark and likely extinguished (F09; Greiner et al.

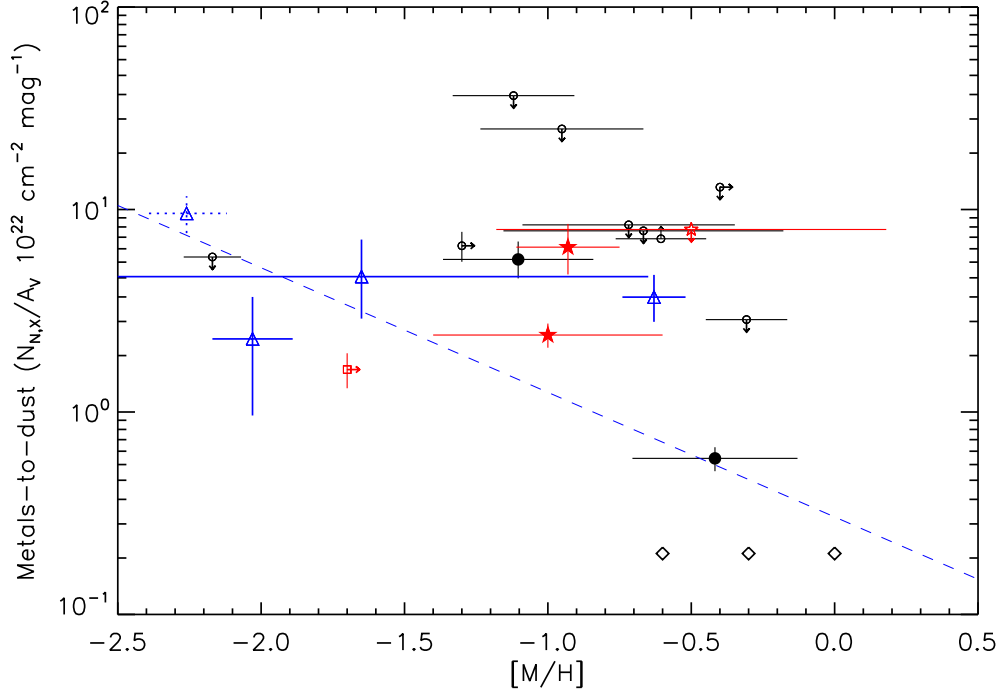


Figure 5.10: Metals-to-dust ratio versus metallicity for the GRB sub sample. The metallicities based on Zn are marked with red stars. The black circles represent Si-derived metallicity (see Table 5.6). GRB 080607 is marked by a red square. The small circles and stars illustrate metallicity or metals-to-dust ratio upper limits. MW, LMC and SMC environments are denoted with diamonds from right to left. The blue triangles correspond to four data points taken from Schady et al. (2010). The blue dashed line represents the best fit to the three Local Group environments and the four GRBs from Schady et al. (2010). The blue triangle with dotted error bar is GRB 050730 which is also included in our sample.

2011), and all four known 2175 Å systems have restframe $A_V > 1$, corresponding to >2 – 3 magnitudes of extinction in the observed BVR I bands, it is premature to claim unequivocally that GRBs reside in small, sub-luminous, blue galaxies, or even that they follow star-formation.

The gas-to-dust ratios of GRBs are typically higher than the SMC. Correcting for gas-phase metallicity does not provide an explanation for these high ratios, and we find that gas-to-dust ratios from optical/UV measures are likely to be dominated by ionization and dust-destruction effects by the GRB, and not indicative of the intrinsic ratios of the GRB host galaxies. Soft X-ray-derived metals-to-dust ratios are 3–30 times the Local Group values. This is not due to ionization or metallicity effects. GRB hosts may however be consistent with a universal metals-to-dust ratio if dust destruction by the GRB is responsible for the apparent paucity of dust. We find no correlation between the metals-to-dust ratios in GRBs and the cold, gas-phase metallicity, the redshift or the extinction.

5.7 DETAILS ON THE SPECTROSCOPIC GRB AFTERGLOW SAMPLE

5.7.1 GRB 050401

The optical spectrum of the afterglow of GRB 050401 was secured with the VLT/FORS2 instrument (Watson et al. 2006a; F09). The NIR photometry in the J , H and K bands from Watson et al. (2006a) is interpolated to the time of the SED using the R -band decay rate ($\alpha = 0.86 \pm 0.1$). We find that the SED of the afterglow can be well reproduced by a broken power-law with substantial amount of SMC-type dust extinction with a value of $A_V = 0.65 \pm 0.04$ mag. The best-fit parameters are given in Table 5.3.

GRB 050401 at $z = 2.8983$ is categorized as a “dark burst” as defined by Jakobsson et al. (2004a). Previously Watson et al. (2006a) found the afterglow SED is compatible with a broken power-law model and SMC type dust reddening with $A_V = 0.62 \pm 0.06$, in agreement with our results. This burst has remarkably one of the highest H I column densities with $\log \text{NH I}/\text{cm}^{-2} = 22.60 \pm 0.3$ (Watson et al. 2006a).

5.7.2 GRB 050730

The optical spectrum of the afterglow of GRB 050730 ($z = 3.9693$) presented in this paper was carried out with the VLT/FORS2 (F09). The afterglow SED is constructed at 4.1 hr after the burst. The SED can be explained by a broken power-law, consistent with a $\Delta\beta \sim 0.5$, plus a small amount of SMC type extinction with $A_V = 0.12 \pm 0.02$ mag.

Optical spectra of GRB 050730 were also acquired by the Magellan Inamori Kyocera Echelle (MIKE) echelle spectrograph on the Magellan Telescopes (Chen et al. 2005), the Intermediate-dispersion Spectroscopic and Imaging System (ISIS) on the William Herschel Telescope (WHT; Starling et al. 2005) and VLT UV-visual Echelle Spectrograph (UVES; D’Elia et al. 2007; Ledoux et al. 2009). The derived H I column density is $\log \text{NH I}/\text{cm}^{-2} = 22.1 \pm 0.1$ (Starling et al. 2005; D’Elia et al. 2007; Ledoux et al. 2009). A foreground QSO is also detected in the 2D spectrum at an impact parameter of 20 arcsec (F09). Previously (Oates et al. 2009) derived $A_V = 0.15$ from a fit of UVOT and X-ray data. Kann et al. (2010) find $A_V = 0.10 \pm 0.02$ from their optical/NIR SED fitting. Both results are consistent with our findings. Starling et al. (2005) find $A_V = 0.01$ from spectral fitting. Schady et al. (2010) find that no extinction model is capable to fit of the NIR through X-ray SED, and derive $A_V \approx 0.16 - 0.23$ for the SMC model using single and broken power-laws.

5.7.3 GRB 050824

The optical spectrum of the afterglow of GRB 050824 ($z = 0.8278$) was taken with the VLT/FORS2 instrument (Sollerman et al. 2007; F09). GRB 050824 is an X-ray flash (XRF)

(Sollerman et al. 2007). The optical and X-ray spectrum are normalized to the level of acquisition image photometry taken at 9.5 hr after the burst trigger. The SED of the afterglow of GRB 050824 is well explained by a broken power-law and SMC extinction with $A_V = 0.14 \pm 0.04$ mag.

Schady et al. (2007b) find SMC dust fits the data best, but they are not able to discriminate among the single and broken power-law models. For both power-law models Schady et al. (2010) find $A_V \approx 0.12 - 0.16$, in excellent agreement with our values. Kann et al. (2010) also find that SMC model well fits the optical/NIR SED with an insignificant amount of dust ($A_V = 0.14 \pm 0.13$).

5.7.4 GRB 060115

The optical spectrum and the R -band photometry of the afterglow of GRB 060115 ($z = 3.5328$) were carried out with the VLT/FORS1 (Piranomonte et al. 2006b; F09). The SED is generated at $t_0 + 8.9$ hr after the burst. The afterglow SED of GRB 060115 is described by a single power-law and SMC type extinction with a very small amount of dust ($A_V = 0.10 \pm 0.02$ mag). The optical spectrum has very low S/N and this can be seen clearly in the extinction curve (see Fig. 5.12). F09 derived an H I column density of $\log \text{NH I}/\text{cm}^{-2} = 21.5 \pm 0.1$.

5.7.5 GRB 060512

The spectrum of the afterglow of GRB 060512 was carried out with the VLT/FORS2 (Starling et al. 2006a; F09). For this afterglow there is uncertainty about the redshift in the GCN circulars. The redshift of $z = 2.1$ comes from a single absorption line detected in the Telescopio Nazionale Galileo (TNG; Starling et al. 2006b) and the FORS1 spectra (F09). This redshift is also consistent with the spectral break detected by UVOT (de Pasquale & Cummings 2006; Oates et al. 2009). The R -band afterglow light curve is constructed by using magnitudes given by Mundell et al. (2006); Cenko (2006a); Milne (2006); Cenko & Baumgartner (2006). The K_s -band photometry is interpolated at the time of the SED by using observations given in Hearty et al. (2006); Tanaka et al. (2006). The J -band observations of the afterglow are taken from Sharapov et al. (2006). We reduced the UVOT data and the afterglow is clearly detected in the v , b and u bands. The interpolated lightcurve for each band is obtained by using the R -band lightcurve decay rate of $\alpha = 1.05 \pm 0.1$. The SED of the afterglow of GRB 060512 fits well with a broken power-law and no dust reddening (see Table 5.3). We estimated the 2σ upper limit for extinction in the rest-frame V -band (< 0.08 mag).

Previously Schady et al. (2010) find that no dust model is capable of fitting the NIR through X-ray data and derive high extinction using SMC model ($A_V \approx 0.47 - 0.66$). The extinction corrected data presented in Schady et al. (2010) do not match with their given intrinsic slope of the afterglow SED.

5.7.6 GRB 060614

The optical spectrum of the afterglow of GRB 060614 was obtained with the VLT/FORS2 (Della Valle et al. 2006; F09). GRB 060614 has a redshift of $z = 0.1257$, the lowest redshift in our flux calibrated GRB sample. The redshift is estimated from the emission lines from the GRB host galaxy (Della Valle et al. 2006). GRB 060614 is a nearby, long duration GRB but not accompanied by a bright supernova (Fynbo et al. 2006d; Della Valle et al. 2006; Gal-Yam et al. 2006; Gehrels et al. 2006). The UVOT data were previously published in Xu et al. (2009) and Mangano et al. (2007). We re-reduced the UVOT data for v , b , u , $uvw1$, $uvm2$ and calibrated the afterglow fluxes in these bands using the photometric technique given in Poole et al. (2008). The optical to the X-ray SED of the afterglow of GRB 060614 is well modeled with a broken power-law and low SMC type extinction with $A_V = 0.1 \pm 0.03$ mag.

Mangano et al. (2007) find that SMC dust well fits the optical through X-ray SED, with $A_V = 0.05 \pm 0.02$, values comparable to ours. Kann et al. (2008) find SMC dust model fits the optical data, and even higher extinction is obtained ($A_V = 0.28 \pm 0.07$). The SED is not provided in Kann et al. (2008), therefore a detailed comparison could not be made.

5.7.7 GRB 060707

The optical spectrum of the afterglow of GRB 060707 ($z = 3.4240$) together with R -band photometry are taken with the VLT/FORS1 (Jakobsson et al. 2006a; F09). The afterglow SED is constructed at 34.4 hr after the burst trigger. The optical to X-ray SED of the afterglow of GRB 060707 can be nicely reproduced with a single power-law and SMC type dust extinction ($A_V = 0.08 \pm 0.02$ mag). The derived HI column density is $\log \text{NH I}/\text{cm}^{-2} = 21.0 \pm 0.2$ (Jakobsson et al. 2006a).

5.7.8 GRB 060708

The optical spectrum and R -band photometry of the afterglow of GRB 060708 are obtained with the VLT/FORS2 (Jakobsson et al. 2006d; F09). A precise redshift of the burst is not obtained due to the low S/N of the optical spectrum (F09). The reported redshift of $z = 1.92$ was based on spectral break seen in UVOT data due to $\text{Ly}\alpha$ break (Schady & Moretti 2006). Together with the X-ray and optical spectrum we reduced the UVOT data in all bands obtained from the *Swift* science archive facility. The data were reduced using the standard UVOT photometric calibration technique described in Poole et al. (2008). The afterglow is clearly detected in the UVOT v , b and u photometric bands. The optical to X-ray SED of the afterglow is well fit with a broken power-law together with SMC type dust extinction, $A_V = 0.13 \pm 0.02$ mag.

5.7.9 GRB 060714

The optical spectrum of the afterglow of GRB 060714 ($z = 2.7108$) was carried out with the VLT/FORS1. The R -band lightcurve is obtained from the circulars spanning from 0.04 to 4 days after the burst. The I and J -band photometric magnitudes were obtained from the CTIO A Novel Dual Imaging CAMera (ANDICAM) instrument (Cobb 2006). The UVOT data of the afterglow is reduced and the source is well detected in the v and b bands. We modeled the intrinsic SED of the afterglow and found that the afterglow can be well explained by a broken power-law together with SMC type extinction with restframe extinction of $A_V = 0.22 \pm 0.02$ mag.

Previously Jakobsson et al. (2006a) obtained the redshift and the H I column density of $\log \text{NH I}/\text{cm}^{-2} = 21.8 \pm 0.1$ from the optical afterglow spectrum. Moreover extended Ly α emission in the center of the DLA trough is clearly detected (F09). Schady et al. (2010) find that no dust model is able to fit the optical/X-ray data. The least bad is the SMC-type dust and power-law with dust extinction $A_V = 0.46 \pm 0.17$, comparable to our results. The afterglow SED in Schady et al. (2010) is constructed from the Rvb band and X-ray data. While b band is clearly affected by the Ly α absorption at $z = 2.7108$ and might causes high amount of extinction.

5.7.10 GRB 060729

The optical spectrum of the afterglow of GRB 060729 at $z = 0.5428$ is obtained with the VLT/FORS2 (Thöne et al. 2006b; F09). The acquisition image photometry was carried out using the I -band filter as reported in Table 5.1. The UVOT data of the afterglow of GRB 060729 is previously published in Grupe et al. (2007). The *Swift* UVOT data of the afterglow of GRB 060729 have been re-reduced and the source is clearly detected in the v , b , u , $uvw1$ and $uvm2$ filters. The optical spectrum is not of good quality and has broad undulations, therefore, the true shape of the underlying continuum cannot be seen from the spectrum. The optical spectrum has very low S/N and is affected by the high airmass at the time of the observation (F09). The afterglow SED can be fitted by a single power-law and SMC type dust extinction, and resulted in a very small amount of dust ($A_V = 0.07 \pm 0.02$ mag).

Schady et al. (2010) find that SMC/power-law is the best model, resulting in low amount of extinction with $A_V = 0.03 \pm 0.01$ and consistent with our value.

5.7.11 GRB 060904B

The optical spectrum of the afterglow of GRB 060904B ($z = 0.7029$) was obtained with the VLT/FORS1 instrument (Fugazza et al. 2006; F09). In our sample GRB 060904B has the highest amount of foreground extinction and absorption (see Table 5.1). The SED of the afterglow is constructed at 5.1 hr after the burst. The SED fits well with a single

power-law and SMC type extinction with extinction of $A_V = 0.31 \pm 0.02$ mag. The SED seems like a broken power-law case with softer X-ray slope. However, due to large uncertainties on the X-ray spectrum the fitting routine cannot minimize both models accurately and prefers a single power-law.

Previously Schady et al. (2010) find no good fit for any dust model but find that single power-law is less likely, suggesting low extinction with $A_V = 0.12^{+0.05}_{-0.04}$. Kann et al. (2010) find that their optical-NIR SED is consistent with no dust reddening using any dust model. The SED is not provided in Kann et al. (2010), therefore a detailed comparison could not be made.

5.7.12 GRB 060906

The optical spectrum of the afterglow of GRB 060906 ($z = 3.6856$) was obtained with the VLT/FORS1 spectrograph (Jakobsson et al. 2006a; F09). The I -band observation was taken at the New Mexico Skies Observatory (Torii 2006) and corrected for the time using the R -band lightcurve power-law with shallow decay index $\alpha = 0.56 \pm 0.07$ (Cenko et al. 2006b; Cenko 2006b). The z' band observation is taken from the lightcurve presented in Cenko et al. (2009). The optical to X-ray SED can be fitted with a broken power-law with no dust extinction. The derived 2σ extinction upper limit is < 0.09 mag. The X-ray to optical slope differ by $\Delta\beta \sim 0.5$ which corresponds to the change in slope caused by the cooling frequency (Sari et al. 1998) lying within the observed frequency range.

The derived HI column density is $\log \text{NH I}/\text{cm}^{-2} = 21.85 \pm 0.1$ (Jakobsson et al. 2006a). Previously Cenko et al. (2009) fitted the SED and found dust extinction with $A_V = 0.20^{+0.01}_{-0.12}$. Kann et al. (2010) fit the optical afterglow SED and find insignificant dust extinction $A_V = 0.05 \pm 0.05$, in agreement with our results.

5.7.13 GRB 060926

The optical afterglow of GRB 060926 ($z = 3.2086$) was observed with the VLT/FORS1 (Piranomonte et al. 2006a; F09). The $\text{Ly}\alpha$ emission from the host galaxy of the GRB is detected in the trough of the DLA (F09). The estimated HI column density is $\log \text{NH I}/\text{cm}^{-2} = 22.7 \pm 0.1$ (Jakobsson et al. 2006a). The optical to X-ray SED is normalized to the acquisition image photometry at 7.7 hr after the burst. The optical to X-ray SED is well described by a single power-law and SMC type dust with a moderate extinction of $A_V = 0.31 \pm 0.02$ mag.

5.7.14 GRB 060927

The optical spectrum of the afterglow of GRB is carried out with the VLT/FORS1 spectrograph (Ruiz-Velasco et al. 2007; F09). GRB 060927 with a redshift of $z = 5.4636$ is the

second highest redshift GRB in our spectroscopic GRB sample. The redshift is based on a single Si II absorption line (Ruiz-Velasco et al. 2007). The K , J and I band observations of the afterglow were carried out with VLT filters (Ruiz-Velasco et al. 2007). We took NIR photometry and spectroscopy to construct the composite SED at 12.5 hr after the burst trigger. The SED of the afterglow can be fitted with a single power-law without any dust extinction. The estimated 2σ upper limit for the A_V is < 0.12 mag.

The optical spectrum of the afterglow is previously published in Ruiz-Velasco et al. (2007) reporting the H I column density of $\log \text{NH I}/\text{cm}^{-2} = 22.50 \pm 0.15$. Kann et al. (2010) fit the NIR SED of the afterglow and found $\leq 2.5\sigma$ significant dust with $A_V = 0.21 \pm 0.08$ for SMC dust. Due to the large uncertainties on the NIR data, no model could be able to fit the NIR segment alone.

5.7.15 GRB 061007

GRB 061007 is an extremely bright burst detected by *Swift* accompanied by a very luminous afterglow and similar decay rate in the X-ray and optical bands (Schady et al. 2007a). The spectrum of the optical afterglow of GRB 061007 at $z = 1.2622$ was obtained with the VLT/FORS1 (Jakobsson et al. 2006b; Paper). The I -band photometry is obtained from the lightcurve presented by Mundell et al. (2007). We reduced the UVOT data of the GRB afterglow and detected source in the v , b and u photometric bands. The SED of the afterglow is nicely fitted with a single power-law together with SMC extinction with a value of $A_V = 0.35 \pm 0.03$ mag.

Oates et al. (2009) and Schady et al. (2010) find high values of extinction varying from $A_V \approx 0.66 - 0.75$, while Schady et al. (2010) prefer LMC dust model. The results of Mundell et al. (2007) with $A_V = 0.48 \pm 0.19$ and Kann et al. (2010) with $A_V = 0.48 \pm 0.10$ are comparable with our values. There is an indication of a 2175 Å bump in the blue end of the optical spectrum. The central wavelength of the bump (i.e. $\lambda_{\text{obs}} \sim 4520$ Å) does not match with the redshift of the GRB. An intervening absorber at redshift $z = 1.066$ is also seen in the spectrum with strong Mg II and Ca OI lines. This absorption feature could be associated with the intervening absorber. Apart from the optical spectrum, no other sign of the intervening absorber is seen at this redshift.

5.7.16 GRB 061021

The spectrum of the GRB 061021 was secured with the VLT/FORS1 spectrograph (Thöne et al. 2006a; F09). The redshift of the burst (i.e. $z = 0.3463$) is obtained from Mg II absorption lines (Hjorth et al, in prep). This is the second lowest redshift of our flux calibrated GRB afterglow sample. The UVOT photometric data have been reduced and the afterglow is well detected in the v , b , u , $uvw1$ and $uvm2$ filters (see Fig. 5.11). The intrinsic SED of the afterglow can be explained by a broken power-law consistent with a cooling break as explained by Sari et al. (1998) and with no dust extinction. The esti-

mated 2σ extinction upper limit is < 0.1 mag.

5.7.17 GRB 061110A

The optical spectrum of the afterglow of GRB 061110A at $z = 0.7578$ was obtained with the VLT/FORS1 (Fynbo et al. 2007; F09). The intrinsic SED of the afterglow is scaled to the acquisition image photometry. The afterglow spectrum of this burst has low S/N. The optical to X-ray SED can be modeled with a single power-law with no dust reddening. We derived the 2σ extinction upper limit of $A_V < 0.1$ mag.

5.7.18 GRB 061110B

The VLT/FORS1 carried out the optical observation of the afterglow of GRB 061110B at $z = 3.4344$ (Fynbo et al. 2006a; F09). The afterglow SED is constructed at $t_0 + 2.5$ hr epoch scaling with the R -band flux. The estimated HI column density is $\log \text{NH I}/\text{cm}^{-2} = 22.35 \pm 0.1$ (F09). The intrinsic SED of the afterglow can be explained by a broken power-law all the way from optical to the X-ray with SMC type extinction with $A_V = 0.22 \pm 0.03$ mag.

5.7.19 GRB 070110

The optical spectrum of GRB 070110 ($z = 2.3521$) was obtained with the VLT/FORS2 spectrograph (Jaunsen et al. 2007b; F09). The UVOT data of this burst have been reduced by using UVOT calibration technique given by Poole et al. (2008). The afterglow is detected only in the v and b bands. The optical to X-ray SED of the afterglow is fitted with a broken power-law indicating a cooling break as suggested by Sari et al. (1998). We find no dust extinction in this burst. The derived 2σ extinction upper limit is $A_V < 0.11$ mag.

The estimated HI column density is $\log \text{NH I}/\text{cm}^{-2} = 21.7 \pm 0.1$ (F09). Previously Schady et al. (2010) find that broken power-law well fits the data, but they could not distinguish between the MW, LMC and SMC dust models, finding dust extinction of $A_V = 0.23^{+0.06}_{-0.05}$ with SMC model.

5.7.20 GRB 070125

The optical spectrum of the afterglow of GRB 070125 ($z = 1.5471$) was carried out with the VLT/FORS2 and previously published in F09. The broad undulations in the optical spectrum are due to systematics in the flux calibration. The redshift of the GRB is determined from the data obtained with Gemini North Telescope equipped with GMOS (Cenko et al. 2008). The R_c and I band observations have been collected by the MIT-SuME Telescope (Yoshida et al. 2007). The J , H and K_s band observations of the afterglow have been obtained with the robotic Peters Automatic Infrared Imaging Telescope

(PAIRITEL; Bloom et al. 2007b) and scaled to R_c -band flux level using the decay rate from a decent R -band lightcurve obtained from the circulars. The R -band lightcurve exhibits a plateau phase and a break to a steeper decay with decay indices $\alpha_1 = 1.4 \pm 0.1$ and $\alpha_2 = 2.55 \pm 0.07$ and break time at ~ 4 days after the burst. The optical spectrum is normalized to R_c -band flux level. The X-ray to optical/NIR SED can be fitted with a broken power-law and SMC-type linear extinction with $A_V = 0.27 \pm 0.03$ mag.

Previously Kann et al. (2010) carried out a fit to the optical/NIR data and found that SMC dust best fits the data with little amount of dust ($A_V = 0.11 \pm 0.04$). We find that the errors on the photometry are large and the NIR/optical X-ray joint fit suggests a cooling break in the SED and moderate extinction.

5.7.21 GRB 070129

The optical spectrum of the afterglow of GRB 070129 was obtained with the VLT/FORS2 spectrograph together with the R -band imaging (F09). We collected the I -band detection of the afterglow from Michigan-Dartmouth-MIT (MDM) Hiltner telescope (Halpern et al. 2007), which is close to the time of the SED. The redshift ($z = 2.338$) reported here was estimated from the host galaxy [O III] emission line (Bo Milvang-Jensen private comm.). The intrinsic SED of the afterglow is scaled to the level of the R -band observation. The X-ray to optical SED of the afterglow is reproduced well with a broken power-law with SMC type extinction with a typical value of $A_V = 0.30 \pm 0.02$ mag.

5.7.22 GRB 070318

The optical spectrum of the afterglow of GRB 070318 ($z = 0.8397$) was carried out with the VLT/FORS1 spectrograph (Jaunsen et al. 2007a; F09). The spectrum shows an unusual sharp break in the optical spectrum around $\lambda_{\text{obs}} \sim 5000 \text{ \AA}$. A spectrum simultaneously obtained at the Magellan telescope, showed the same optical break (Chen et al. 2007). The *Swift* UVOT data have been reduced together with the NIR data from ANDICAM. The UVOT slope is consistent with the downturn in the optical spectrum. The SED of the afterglow is generated at $t_0 + 16.7$ hr after the burst. There is clear evidence for dust attenuation in the NIR to X-ray afterglow SED. Due to the sharp break in the optical spectrum and peculiar dust reddening the data are not consistent with SMC-origin extinction curve. We fit the SED with FM-dust induced model and found that the SED fits with a sharp break in the optical spectrum. The extinction curve is very unusual due to the sharp optical break. The GRB is not included in our extinction sample due to non-consistency with the synchrotron model. This sharp break could be due to destruction of dust grains by the GRB. A more detailed and comprehensive analysis of the SED will be given in Watson et al. (in prep).

Previously Schady et al. (2010) implemented UVOT-XRT joint fit and found that a broken power-law is a slightly better fit to the data with dust extinction of $A_V =$

$$0.59^{+0.01}_{-0.06}.$$

5.7.23 GRB 070506

The optical spectrum of the afterglow of GRB 070506 ($z = 2.3090$) was taken with the VLT/FORS2 instrument (Thöne et al. 2007b; F09). The estimated H I column density is $\log \text{NH I}/\text{cm}^{-2} = 22.0 \pm 0.3$ (F09). The optical spectrum redwards of $\lambda_{\text{obs}} \approx 7000 \text{ \AA}$ is affected by strong fringing, therefore, this part is not included in our SED analysis. The intrinsic SED of the afterglow is modeled and we find a broken power-law to be a reasonable fit to the data. In addition to the broken power-law the data require dust using SMC type dust grains with $A_V = 0.44 \pm 0.05 \text{ mag}$.

5.7.24 GRB 070611

The optical spectrum of the afterglow of GRB 070611 ($z = 2.0394$) was obtained with the VLT/FORS2 (Thöne et al. 2007a; F09). The derived neutral hydrogen column density of the DLA is $\log \text{NH I}/\text{cm}^{-2} = 21.3 \pm 0.2$ (F09). The SED is scaled to the time of the *R*-band photometry at 7.7 hr. The X-ray to optical SED of the afterglow is defined by a single power-law and SMC type dust extinction ($A_V = 0.06 \pm 0.02 \text{ mag}$).

5.7.25 GRB 070721B

The optical spectrum of the afterglow of GRB 070721B ($z = 3.6298$) is carried out with the VLT/FORS2 spectrograph (Malesani et al. 2007; F09). The estimated H I column density is $\log \text{NH I}/\text{cm}^{-2} = 21.5 \pm 0.2$ (F09). The SED is scaled to the flux level of the *R*-band photometry. The intrinsic SED of the afterglow is nicely reproduced by using a broken power-law and SMC-type extinction with $A_V = 0.2 \pm 0.02 \text{ mag}$ (see Fig. 5.11).

5.7.26 GRB 070802

The optical observations of GRB 070802 ($z = 2.4541$) were obtained with the VLT/FORS2 spectrograph. The 2175 Å dust extinction feature is clearly seen in the optical spectrum of the afterglow (F09; Elíasdóttir et al. 2009). The burst is categorized as dark burst as defined by Jakobsson et al. (2004a). The *J*, *H* and *K* band observations are taken at $t_0 + 2.0 \text{ hr}$ from the lightcurves presented in Krühler et al. (2008) for each band. We reduced UVOT data using the calibration techniques defined by Poole et al. (2008). The afterglow is well detected in the *v* and *b* bands (see Fig. 5.11). Due to the presence of a strong 2175 Å bump feature, the SMC extinction curve gives the worst fit to the data. The observed bump is shallower than the MW, therefore, CCM is also not a good fit to the data. We fitted the SED using a FM extinction model with both single and broken power-laws. The intrinsic SED is well described with a single power-law and a large amount of dust observed in rest-frame *V*-band ($A_V = 1.19 \pm 0.15 \text{ mag}$) with total-to-

selective extinction of $R_V = 2.81 \pm 0.68$. The complete log of the best fit FM parameters is given in Table 5.4.

The neutral hydrogen column density of $\log \text{NH I}/\text{cm}^{-2} = 21.5 \pm 0.2$ is determined from the optical spectrum (Elíasdóttir et al. 2009). The rest-frame extinction curve of the afterglow is shown in Fig. 5.12. The NIR to X-ray SED has been previously fitted by Elíasdóttir et al. (2009); Krühler et al. (2008); Cenko et al. (2009); Greiner et al. (2011), finding high dust extinction ($A_V \gtrsim 1.0$) with a single power-law, similar to our results.

5.7.27 GRB 071020

There was no PC mode data available near the time of the optical spectrum of GRB 071020 ($z = 2.1462$), therefore, we reduced early and late time PC mode X-ray data for this burst using the procedure described in §5.2.4. We further checked that the X-ray spectral slope for early and late time are similar. The optical spectrum of the afterglow was obtained with the VLT/FORS2 instrument (Jakobsson et al. 2007c; F09). The derived H I column density is $\log \text{NH I}/\text{cm}^{-2} < 20.30$ (Nardini et al. in prep; F09). In our spectroscopic sample, this is the lowest column density obtained from the optical spectrum. The $\text{Ly}\alpha$ is in the very blue end of the spectrum and is not seen clearly (see F09). The R , J and K band observations are taken from Nardini et al. (in prep). The H -band photometry is carried out with PAIRITEL (Bloom et al. 2007a) and scaled to the time of the SED. A comprehensive analysis of the optical spectrum of GRB 071020 will be discussed in Nardini et al. (in prep). The SED of the afterglow of GRB 071020 can be modeled using a broken power-law with SMC type extinction with $A_V = 0.40 \pm 0.04$ mag. The change in slope is consistent with $\Delta\beta = 0.5$ (see Table 5.3).

The best fit of Kann et al. (2010) implies SMC-type dust with $A_V = 0.28 \pm 0.09$, comparable to our results within uncertainties.

5.7.28 GRB 071031

The acquisition image photometry and the spectroscopy of the afterglow of GRB 071031 ($z = 2.6918$) were carried out with the VLT/FORS2 instrument (Ledoux et al. 2007; F09). The i' , z' , J , H and K_s band photometry have been obtained from GROND (Krühler et al. 2009). We also compared acquisition camera photometry to the r' band photometry presented in Krühler et al. (2009) and taken at similar time, finding consistent values. The obtained column density of the GRB-DLA is $\log \text{NH I}/\text{cm}^{-2} = 22.15 \pm 0.05$ (Ledoux et al. 2009). The SED of the afterglow of GRB 071031 fits well with a broken power-law and no dust reddening. The estimated 2σ reddening upper limit in the V -band is < 0.07 mag.

Previously Kann et al. (2010) modeled the optical-NIR data and found that SMC model well fits the data with insignificant amount of dust $A_V = 0.14 \pm 0.13$. The SED presented in this paper clearly indicate no dust. Greiner et al. (2011) find no dust ex-

tion from the GROND-XRT joint fit, consistent with our results.

5.7.29 GRB 071112C

The optical spectrum of the afterglow of GRB 071112C at $z = 0.8227$ was carried out with the VLT/FORS2 instrument together with the acquisition image photometry (Jakobsson et al. 2007b; F09). The only available H band photometry has been taken with the MAGNUM (Minezaki et al. 2007). The R -band lightcurve is retrieved from the GRBLog and fitted with a decay index of $\alpha = 0.92 \pm 0.06$. We used the R -band lightcurve decay rate to obtain the NIR photometry at 10 hr after the burst. The SED and optical/NIR observations of the afterglow have been previously discussed in Uehara et al. (2010). The intrinsic SED of the afterglow is modeled well with a broken power-law and presents no dust extinction. The derived upper limit for dust reddening is < 0.08 mag.

Previously Kann et al. (2010) studied the optical-NIR afterglow SED and found that SMC dust best fit the data with an insignificant amount of dust ($A_V = 0.23 \pm 0.21$). On the contrary, NIR to X-ray afterglow SED studied in this paper suggests no dust extinction (see Fig. 5.11).

5.7.30 GRB 071117

The optical spectrum of the afterglow of GRB 071117 ($z = 1.3308$) was obtained with the VLT/FORS1 (Jakobsson et al. 2007a; F09). The estimated redshift of the afterglow comes from [O II] emission line. The optical and X-ray spectrum are normalized to the R -band acquisition camera photometry at 9 hr after the burst trigger. The NIR to X-ray data fit well with a single power-law and SMC type with dust reddening of $A_V = 0.26 \pm 0.02$ mag.

5.7.31 GRB 080210

The optical spectrum of the afterglow of GRB 080210 at $z = 2.6419$ was carried out using the VLT/FORS2 instrument (Jakobsson et al. 2008b; De Cia et al. 2010; F09). The early and late time R -band photometry has been acquired with FORS2 (see De Cia et al. 2010). We selected the R -band photometry at 1.69 hr which is near the mid time of the optical spectrum and scaled the afterglow SED to that level. The optical spectrum is corrected for slit losses and kindly provided by Annalisa De Cia (see also De Cia et al. 2010). In addition to the optical spectrum the optical/NIR data have been obtained by using the GROND telescope (Greiner et al. 2011). We obtained the g' , r' , i' , z' , J , H and K_s band photometry at the time of the SED (Krühler, private comm.). The i' and z' data show a spectral plateau and are clearly down compared to the rest of the photometry (see Fig. 5.11), therefore, the GROND photometry is not included in our SED fitting. The optical-XRT SED is modeled nicely with a broken power-law and SMC-type dust

reddening. The dust extinction is found to be $A_V = 0.33 \pm 0.03$. The change in the spectral slope for this afterglow is $\Delta\beta = 1.14 \pm 0.13$ (see Fig. 5.1).

The estimated HI column density for the DLA is of $\log \text{NH I}/\text{cm}^{-2} = 21.90 \pm 0.10$ (De Cia et al. 2010). Kann et al. (2010) fitted the GROND SED and assumed the i' and z' data as an indication of 2175 Å bump, resulting in some deviation from the dust model and give quite large extinction ($A_V = 0.7$). An independent analysis of De Cia et al. (2010) also confirms that the spectral change is around 1.0 and is inconsistent with the fireball model. This is the only outlier with twice the spectral slope change as compared to the other break frequency cases. The X-ray slope for this case is much softer than the other cases (see Fig. 5.1). We checked that the X-ray spectrum becomes gradually softer ($\Gamma = \beta + 1 > 2.0$) in the time interval ranging from 1000 to 10000 s, suggesting that energy injection from the central engine is likely to be decreasing at these times. For SMC type extinction De Cia et al. (2010) found $A_V = 0.18 \pm 0.03$. Greiner et al. (2011) employed a joint GROND-XRT fit to the data with fixed $\Delta\beta = 0.5$ and find $A_V = 0.24 \pm 0.03$.

5.7.32 GRB 080319B

The optical spectrum of the afterglow of GRB 080319B ($z = 0.9382$) was obtained with the VLT/FORS2 spectrograph almost one day after the burst trigger (F09). The GRB is commonly referred to as the “naked eye burst” due to its peak visual magnitude of 5.3 mag (Racusin et al. 2008; Woźniak et al. 2009; Bloom et al. 2009). The g' , r' , i' and z' band photometry has been obtained from the lightcurves for these filters presented in Tanvir et al. (2010). The UVOT data have been reduced and the magnitudes obtained for the v , b , u and $uvw1$ filters, where the afterglow is clearly detected. We generated the SED at 26 hr after the burst and modeled it using power-laws and dust extinction. We found the observed data fit very well with a single power-law all the way from optical to the X-ray and no dust reddening. The upper limit on the amount of dust is estimated to be < 0.11 mag.

Kann et al. (2010) find no dust extinction from optical-NIR SED fitting, in excellent agreement with our result.

5.7.33 GRB 080520

The optical spectrum of the afterglow of GRB 080520 ($z = 1.5457$) was obtained with the VLT/FORS2 spectrograph at the time when the afterglow was very faint. The UVOT data have been reduced and the afterglow is only detected in the v band. The SED of the afterglow is constructed and the data are well fitted with a single power-law and SMC-type dust extinction with $A_V = 0.23 \pm 0.02$ mag.

Greiner et al. (2011) fit the XRT through optical/NIR data and find weakly constrained high amount of extinction ($A_V = 0.53^{+0.40}_{-0.42}$). Our results are consistent to

Greiner et al. (2011) within 1σ .

5.7.34 GRB 080605

The optical spectrum of the afterglow of GRB 080605 ($z = 1.6403$) was carried out with the VLT/FORS2 in different grisms (Jakobsson et al. 2008c; F09). The 2175 Å absorption dip is clearly seen in two FORS2 grism spectra. Being at redshift $z < 2$ the Ly α is not detected for this burst due to the sensitivity range of the spectrograph. Therefore metal abundances cannot be obtained for this interesting case. We reduced the UVOT data of the afterglow and the source is detected in the v , b and u bands. A fair I -band lightcurve up to 1 day after the burst is available at GRBLog, obtained from GCN circulars. The I -band observation used here has been obtained from I -band lightcurve. The 2175 Å absorption dip is very weak and narrow. The SED is modeled with the FM extinction law. The SED is well described by a single power-law and large amount of dust extinction in restframe V band of $A_V = 1.2^{+0.09}_{-0.10}$ mag. The extinction curve of the afterglow suggests R_V consistent with its value in the MW (see Fig. 5.12). The metallicity obtained from the equivalent width of Si II (1526 Å) suggests a fairly high metallicity for this burst (see Table 5.6).

Greiner et al. (2011) find that the MW dust model best-fit the data with moderate amount of extinction ($A_V = 0.47 \pm 0.03$). The SED presented in this paper is not complete and lacking the NIR data, which could be in the restframe V -band. This particular case with other 2175 Å bump cases will be discussed in Zafar et al. (in prep).

5.7.35 GRB 080607

The optical spectrum of the afterglow of GRB 080607 ($z = 3.0368$) was obtained with the Keck telescope and previously published in Prochaska et al. (2009); Perley et al. (2011b) and F09. Because of being not observed with the VLT, this burst is not a part of our spectroscopic GRB sample. The derived neutral hydrogen column density of GRB-DLA is $\log \text{NH I}/\text{cm}^{-2} = 22.70 \pm 0.15$ (Prochaska et al. 2009; F09). Due to the occurrence of GRBs in star-forming molecular clouds, molecular hydrogen has been searched for many GRBs and resulted in non-detections (Vreeswijk et al. 2004; Tumlinson et al. 2007; Sheffer et al. 2009). Fynbo et al. (2006c) tentatively interpreted an absorption feature as H₂ in their spectrum of GRB 060206. For the first time, strong unambiguous H₂ and CO molecular absorption lines were detected in the optical afterglow spectrum of GRB 080607 (Prochaska et al. 2009; Perley et al. 2011b). Most of the 2175 Å extinction bump is clearly detected in the optical spectrum. The remaining part of the bump is covered by using the z and i filters. The afterglow is detected in the NIR J , H and K_s bands with PAIRITEL. The I and V band observations have been performed with the Katzman Automatic Imaging Telescope (KAIT) and the R , i and z band detection are from the robotic Palomar 60 inch telescope (see Table:1 Perley et al. 2011b). This burst

classifies as dark by the definition of Jakobsson et al. (2004a). The GRB afterglow is remarkably luminous in optical and NIR wavelengths. Since the optical data have strong H_2 molecular absorption lines which makes it hard to see the underlying continuum, therefore, we fit with the binned spectrum where lines are already taken out (see Table: 4; Perley et al. 2011b). We fit the data with the FM parameterization and the best fit parameters are given in Table 5.4. The intrinsic SED of the afterglow is nicely reproduced with $A_V = 2.31^{+0.46}_{-0.43}$ mag and a very high $R_V = 3.75 \pm 1.04$. The 2175 Å is the widest compared to all other bump cases (see Table 5.4). The host galaxy of the GRB afterglow is also extremely red in the optical and NIR bands (Chen et al. 2010).

Previously Prochaska et al. (2009) found $A_V \approx 3.2$ and Perley et al. (2011b) estimated $A_V = 3.3 \pm 0.4$ the optical/NIR data fit. Both authors found $R_V \sim 4$ which is consistent with our result of a shallower extinction curve.

5.7.36 GRB 080707

The optical spectrum of the afterglow of GRB 080707 ($z = 1.2322$) is obtained with the VLT/FORS1 under bad conditions (Fynbo et al. 2008b; F09). The SED is normalized to the R -band observation taken at 1.1 hr after the burst. The intrinsic SED of the afterglow is fitted with a broken power-law and no dust reddening. The upper limit on the dust content is $A_V < 0.13$ mag.

Greiner et al. (2011) implemented the GROND-XRT joint fit to the data and find that the data are consistent with no dust with an insignificant value of $A_V = 0.11^{+0.14}_{-0.08}$ mag.

5.7.37 GRB 080721

The optical spectrum of the afterglow of GRB 080721 at $z = 2.5914$ was obtained with the VLT/FORS1 spectrograph (Starling et al. 2009; F09). We extracted the UVOT data and the afterglow is detected in the v and b band. The I -band photometry is obtained at 10.2 hr using the I -band observations given by Starling et al. (2009). The neutral hydrogen column density of the DLA is $\log \text{NH I}/\text{cm}^{-2} = 21.6 \pm 0.1$ (F09). The intrinsic SED is scaled to the R -band acquisition camera photometry. The data is well described by using a single power-law and no dust reddening. The estimated upper limit for dust reddening is < 0.12 mag.

Previously Starling et al. (2009) found no cooling break between the X-ray and optical wavelengths. Despite the large errors on the photometry, Kann et al. (2010) fit the optical SED and find $A_V = 0.35 \pm 0.07$.

5.7.38 GRB 080805

The optical spectrum of the afterglow of GRB 080805 ($z = 1.5042$) was obtained with the VLT/FORS2 (Jakobsson et al. 2008a; F09). The spectrum clearly show a 2175 Å

absorption feature at the redshift of the GRB. Due to the relative faintness in the optical, the afterglow is not detected in any of the UVOT filters. The spectrum shows a pretty clear absorption dip and the extinction curve resembles that of the MW. The intrinsic SED of the afterglow is generated 1.0 hr after the burst trigger. The X-ray to optical SED is reproduced nicely with a single power-law plus FM extinction curve with a large amount of dust reddening of $A_V = 1.53 \pm 0.13$ mag and total-to-selective extinction of $R_V = 2.48 \pm 0.39$.

Previously Greiner et al. (2011) modeled the GROND-XRT data and found that MW dust model, with a 2175 Å bump, provides the best explanation to the data with $A_V = 1.01^{+0.19}_{-0.08}$. The value is consistent with the results we find from our analysis.

5.7.39 GRB 080905B

The optical spectroscopy of the afterglow of GRB 080905B at $z = 2.3739$ was taken with the VLT/FORS2 together with the R band acquisition image photometry (Vreeswijk et al. 2008b; F09). We implemented MIDAS package FITLYMAN (Fontana & Ballester 1995) to determine the neutral hydrogen column density. The derived H I column density of the afterglow of GRB 080905B is $\log \text{NH I}/\text{cm}^{-2} < 22.15$. Since the afterglow flux is contaminated by the light from another object on the slit, we suggest the column density to be an upper limit. We modeled the intrinsic afterglow SED and the data are well fitted with a single power-law and dust extinction with $A_V = 0.41 \pm 0.03$ mag

5.7.40 GRB 080913

The spectrum of the afterglow of GRB 080913 was taken with the VLT/FORS2 (Greiner et al. 2009; F09; Zafar et al. 2011). GRB 080913 is the highest redshift GRB in our spectroscopic sample. The acquisition image was taken with z -Gunn filter. The magnitude reported in Table 5.1 is strongly affected by Ly α absorption. We corrected the magnitude for Ly α absorption using spectro-photometric analysis (see Zafar et al. 2011 for detail). A comprehensive description of the SED analysis is given in Zafar et al. (2011). The neutral H I column density of the DLA is $\text{NH I}/\text{cm}^{-2} < 21.14$ (Greiner et al. 2009).

5.7.41 GRB 080916A

The optical spectrum of the optical afterglow of GRB 080916A ($z = 0.6887$) was carried out with the VLT/FORS2 (Fynbo et al. 2008a; F09). The SED is constructed at 17.1 hr i.e. the time of R -band acquisition image photometry. The intrinsic SED is nicely reproduced with a broken power-law and SMC type dust extinction with $A_V = 0.15 \pm 0.04$ mag.

5.7.42 GRB 080928

The optical spectrum of the afterglow of GRB 080928 at $z = 1.6919$ was obtained with the VLT/FORS2 (Vreeswijk et al. 2008a; F09). We collected the optical/NIR photometry at the time of the SED taken with GROND from Rossi et al. (2010). We scaled the spectrum to the level of the r' band photometry taken at 15.5 hr. In addition we reduced the UVOT data for this burst and fluxes are obtained for the v , b and u bands at the common SED epoch. The intrinsic SED is well fitted with a single power-law and SMC extinction. The best fit A_V value is 0.3 ± 0.03 mag.

Kann et al. (2010) find that a MW dust model best fits the optical-NIR data with a small amount of extinction ($A_V = 0.14 \pm 0.08$). We do not find any evidence for the 2175 Å bump in the optical spectrum.

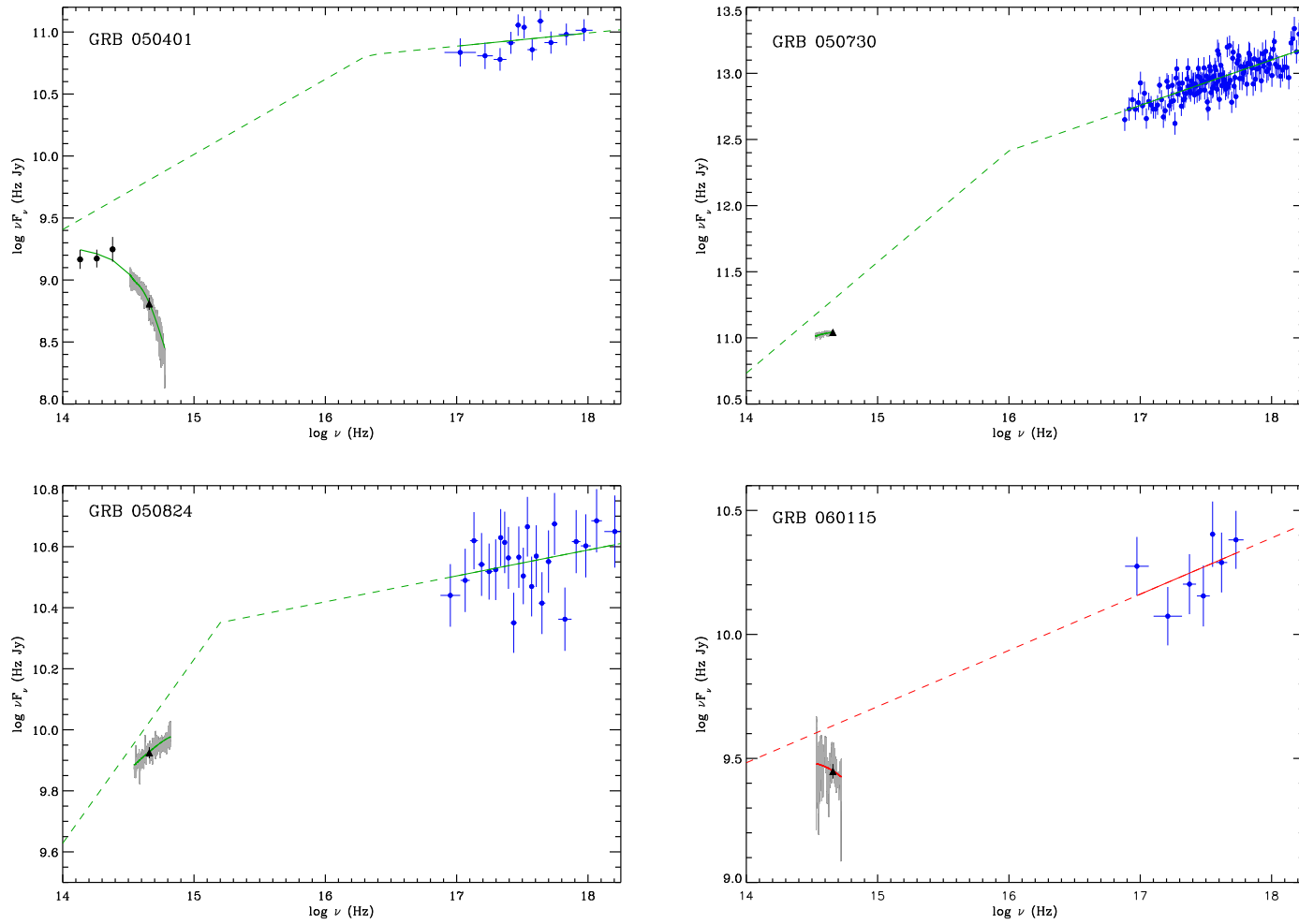


Figure 5.11: SED of GRB afterglows in νF_ν and ν space. The best fit extinguished and extinction corrected spectral model are shown by solid and dashed lines respectively. The grey curve represents the optical spectrum. The X-ray spectra are indicated by blue points. The black triangle corresponds to acquisition image photometry. Black open circles are not included in the SED fit because of the optical spectrum wavelength coverage in that region while solid circles represent the data points included in the SED modeling. The red curve shows the best fit single power-law model and the green curve illustrates the broken power-law model.

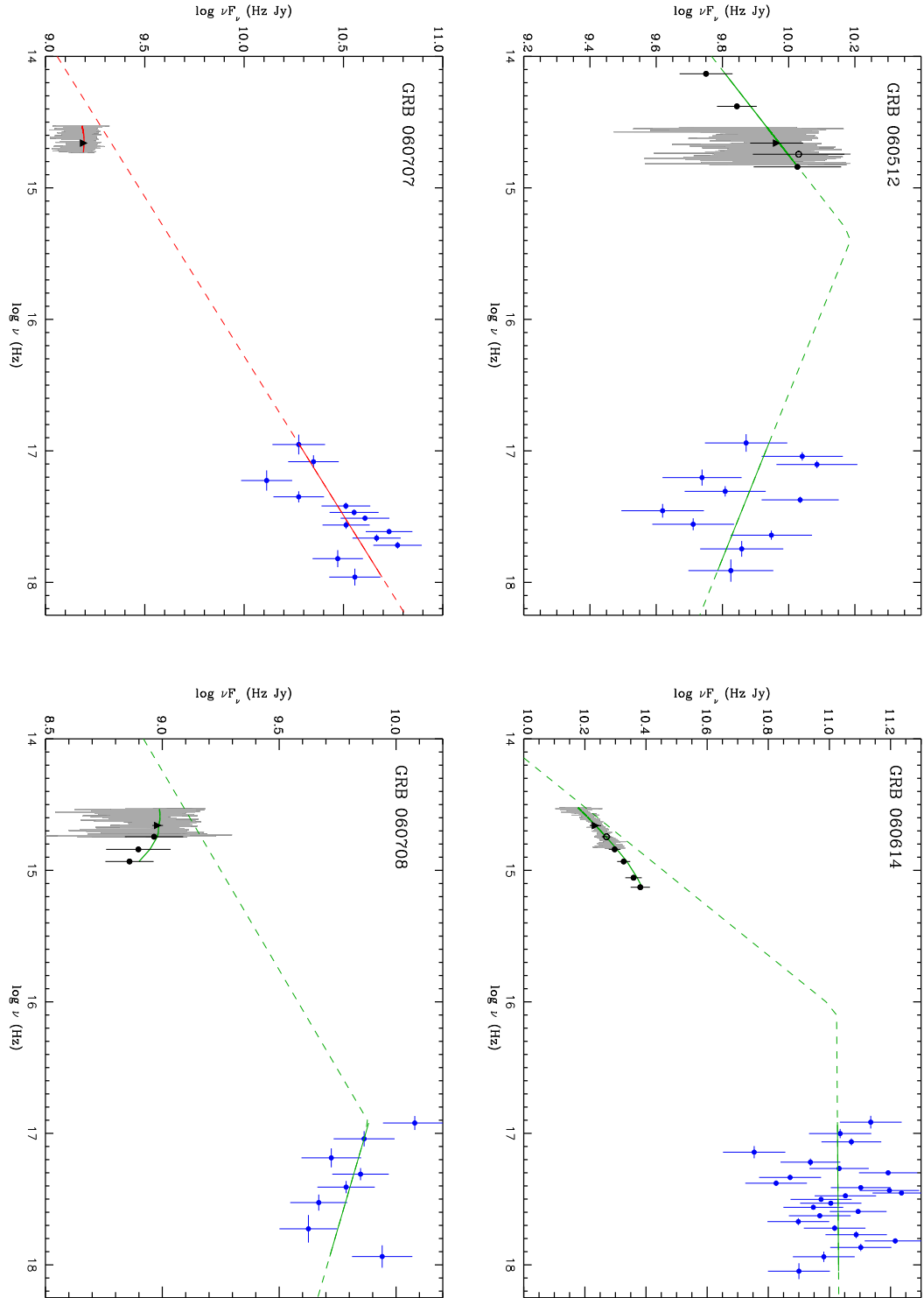


Figure 5.11: (continued)

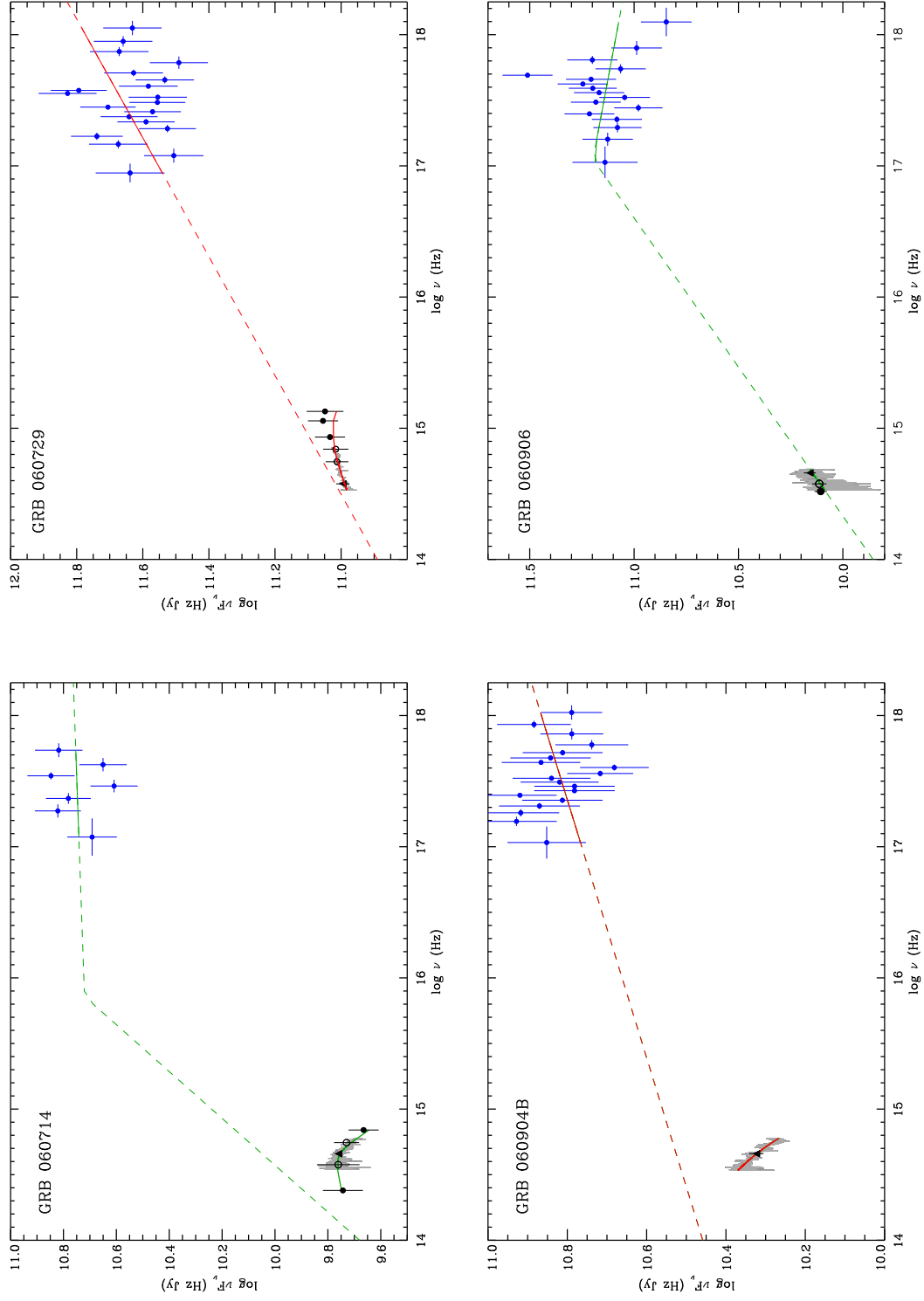


Figure 5.11: (continued)

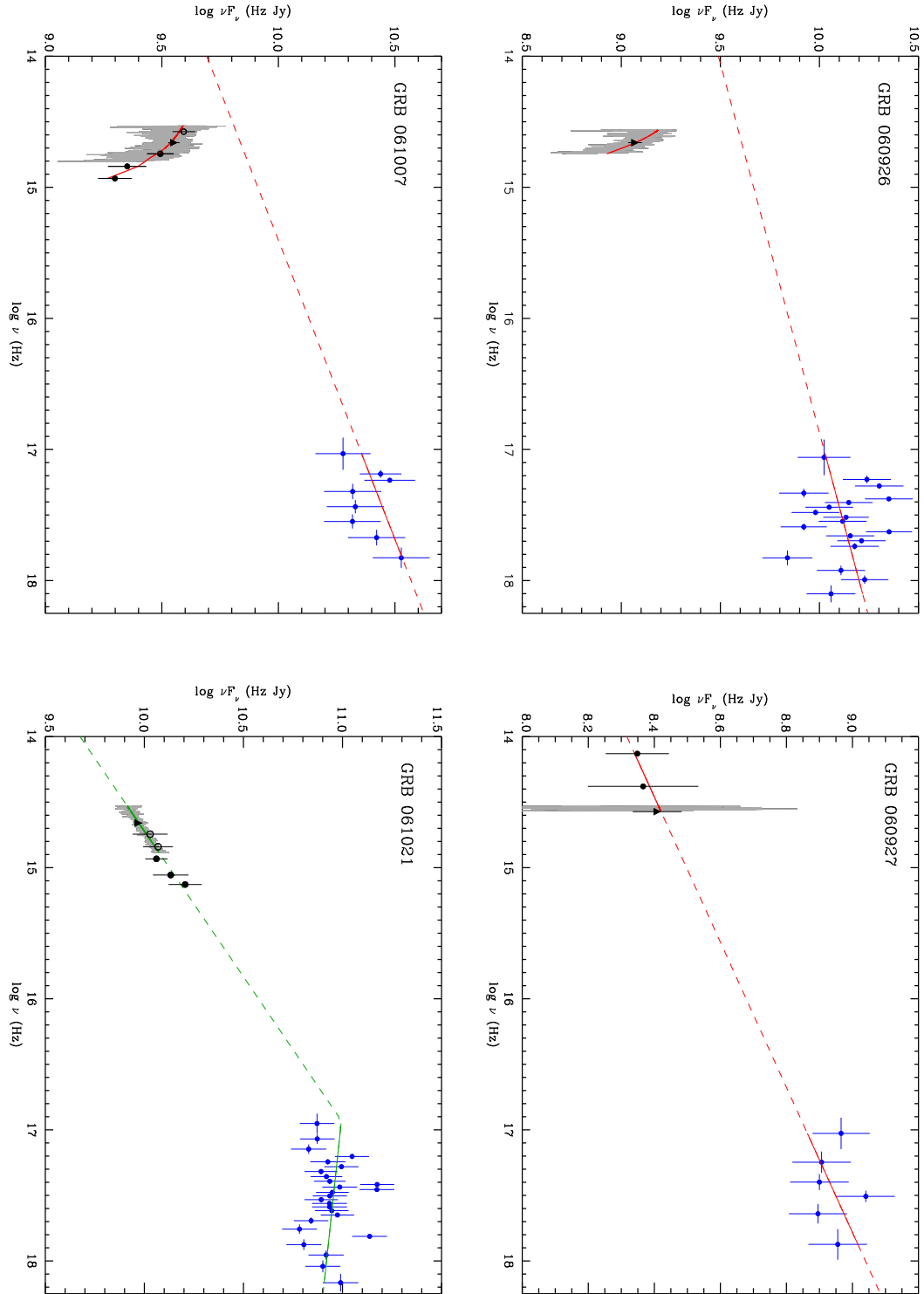


Figure 5.11: (continued)

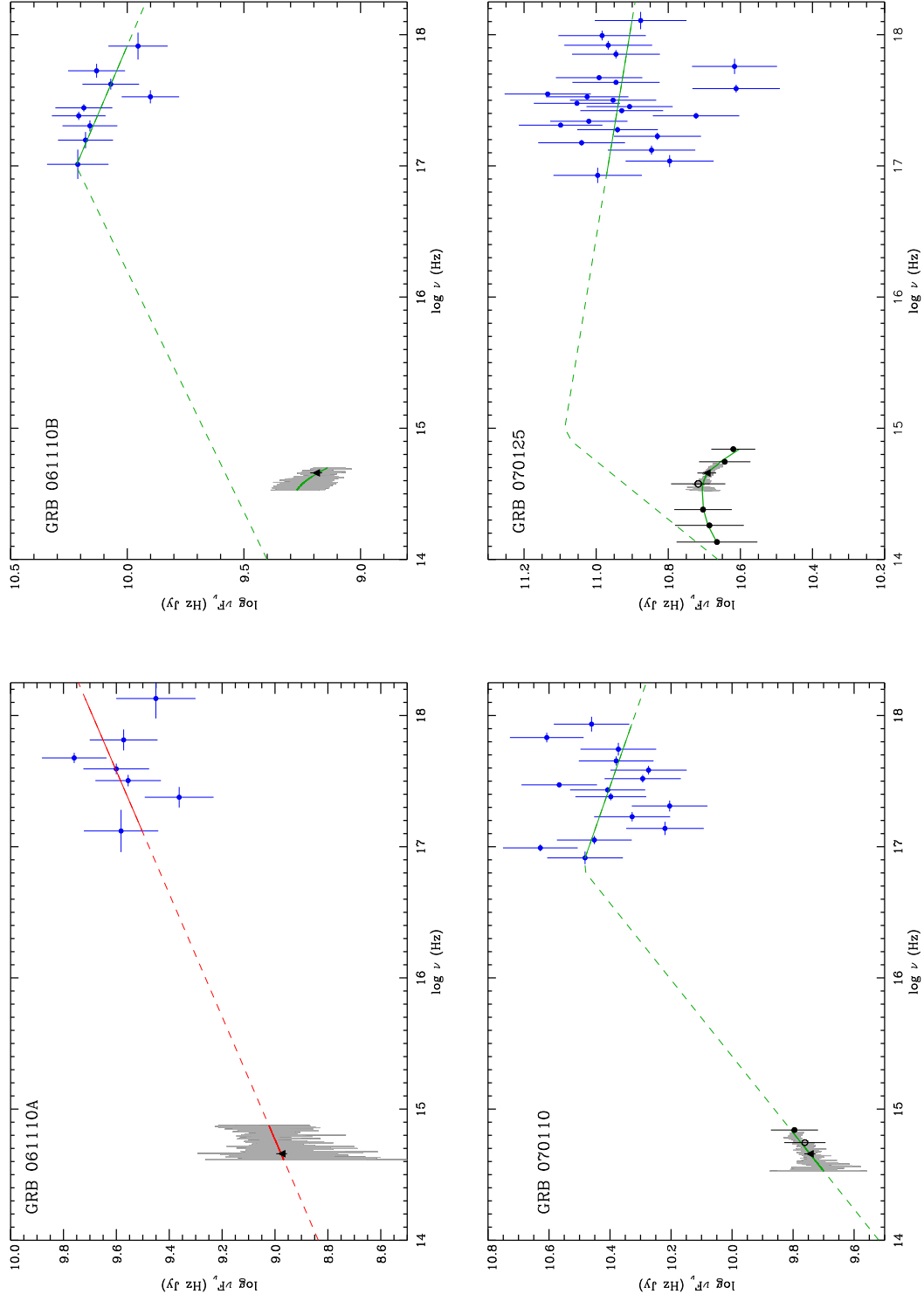


Figure 5.11: (continued)

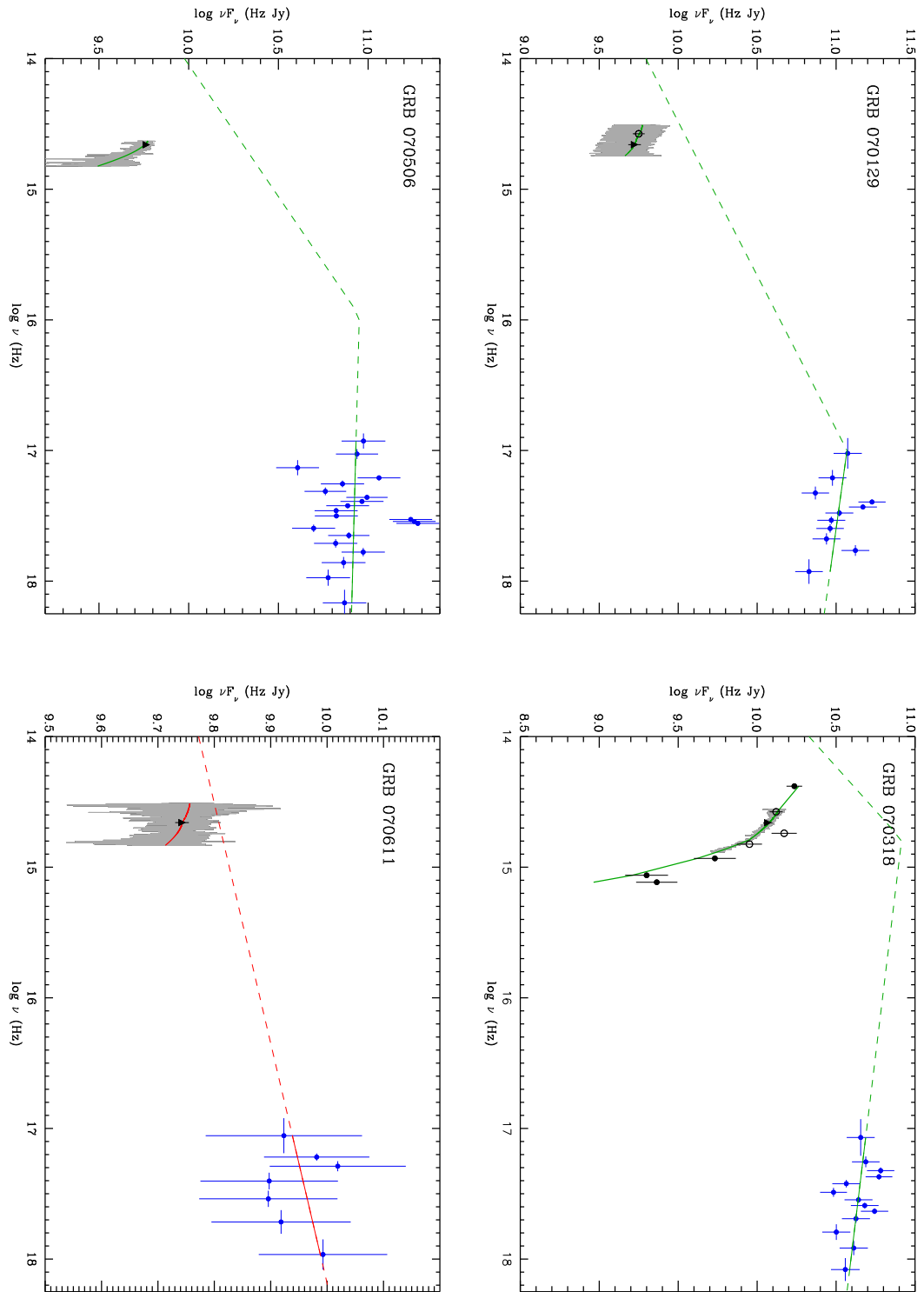


Figure 5.11: (continued)

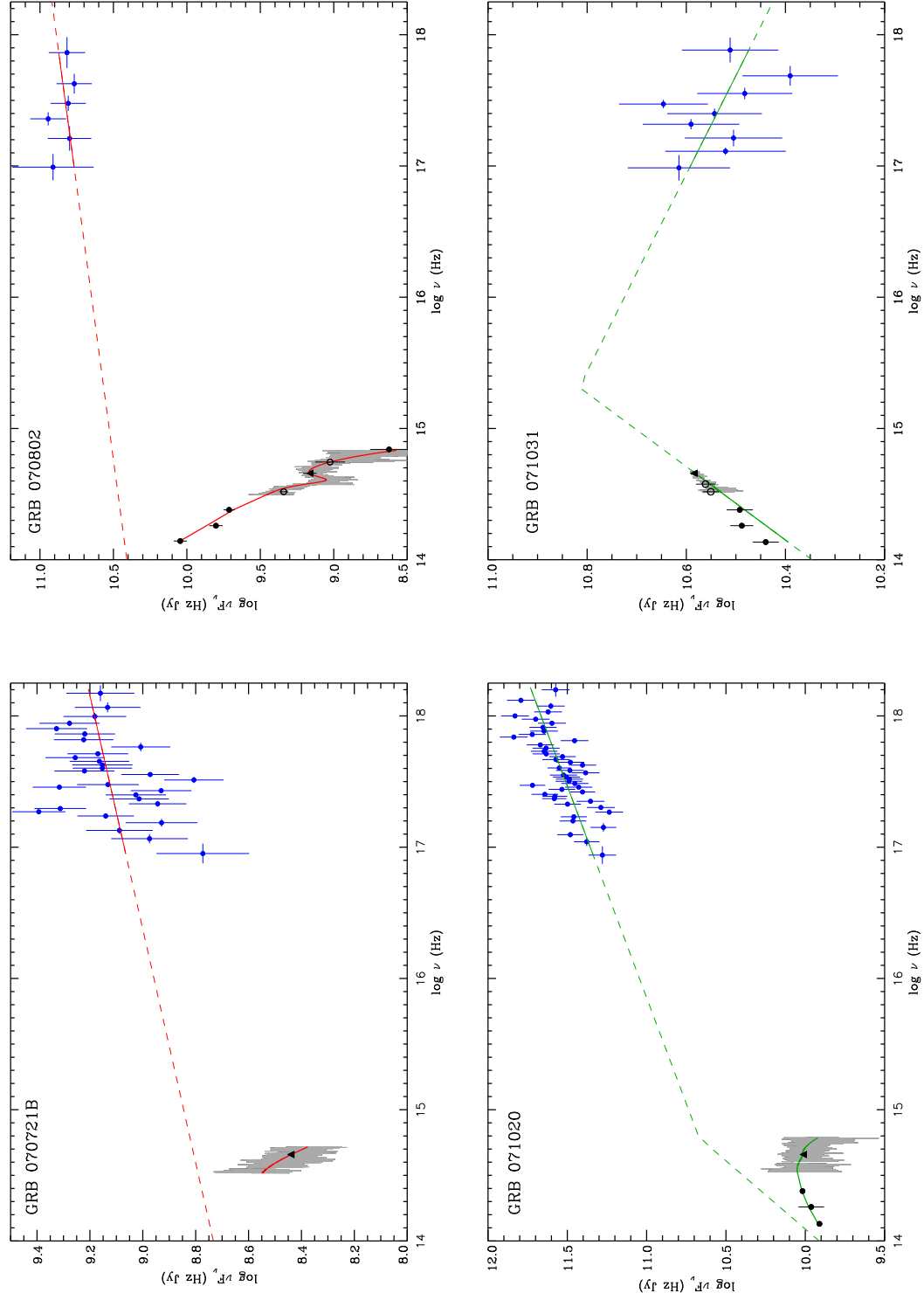


Figure 5.11: (continued)

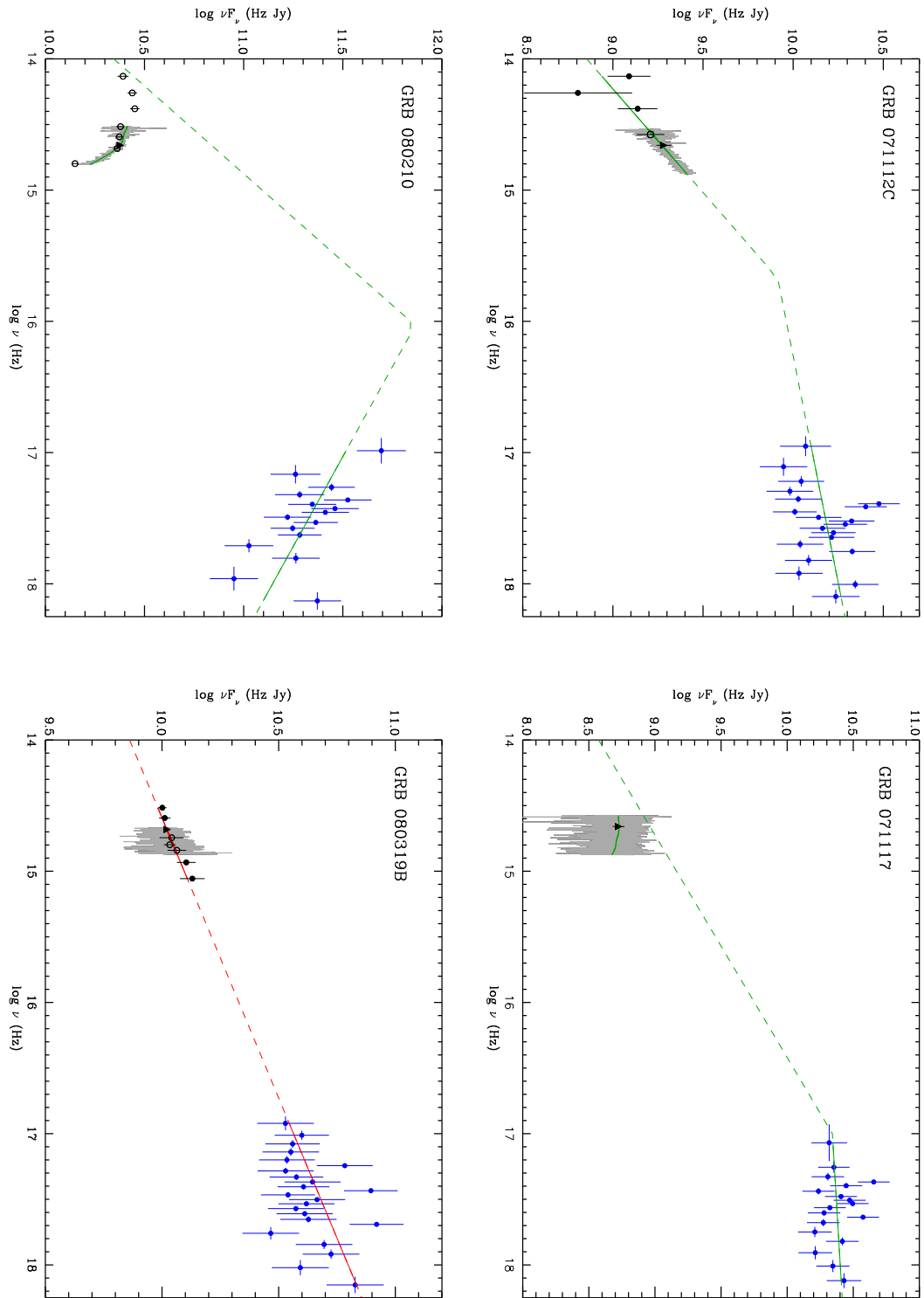


Figure 5.11: (continued)

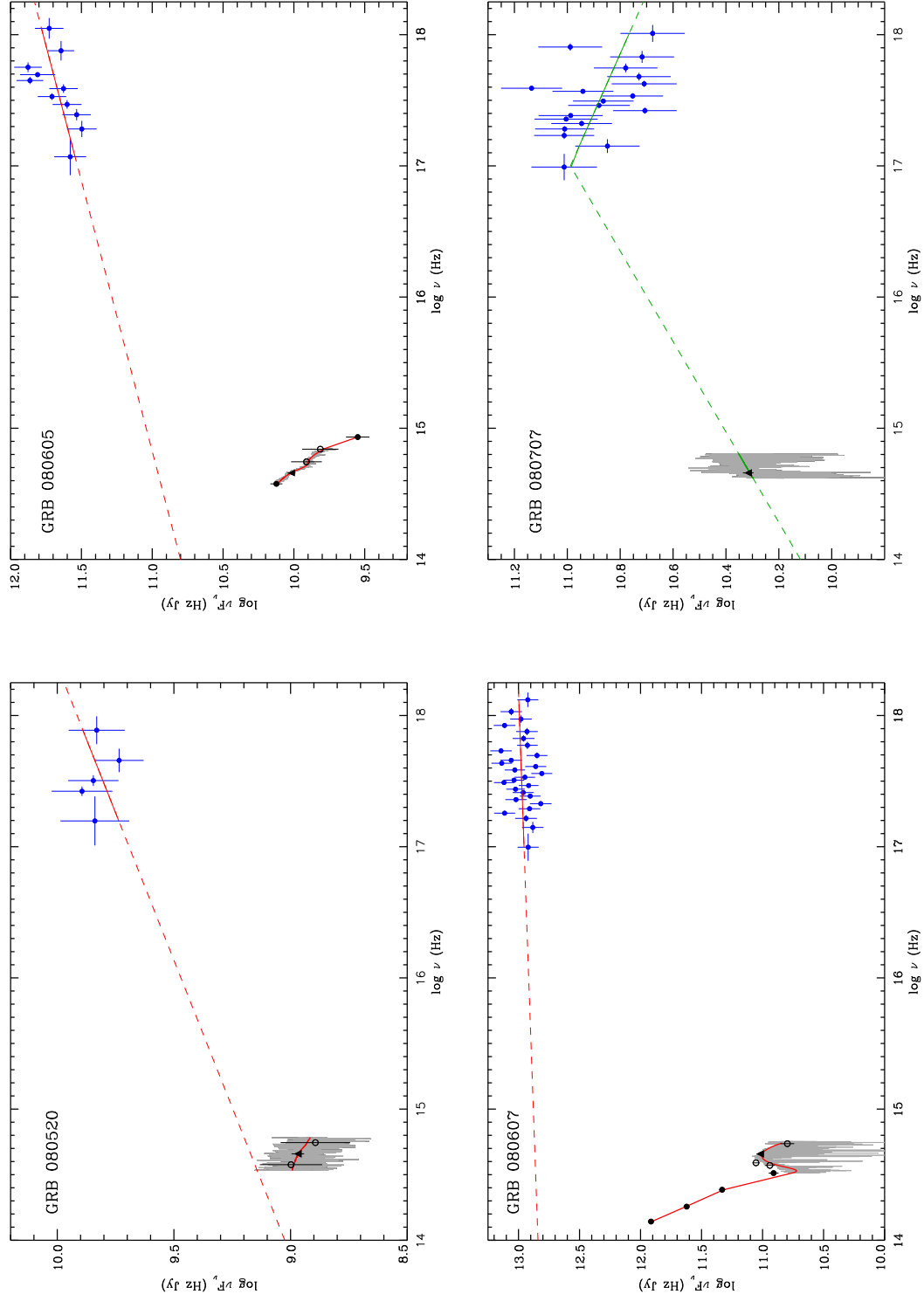


Figure 5.11: (continued)

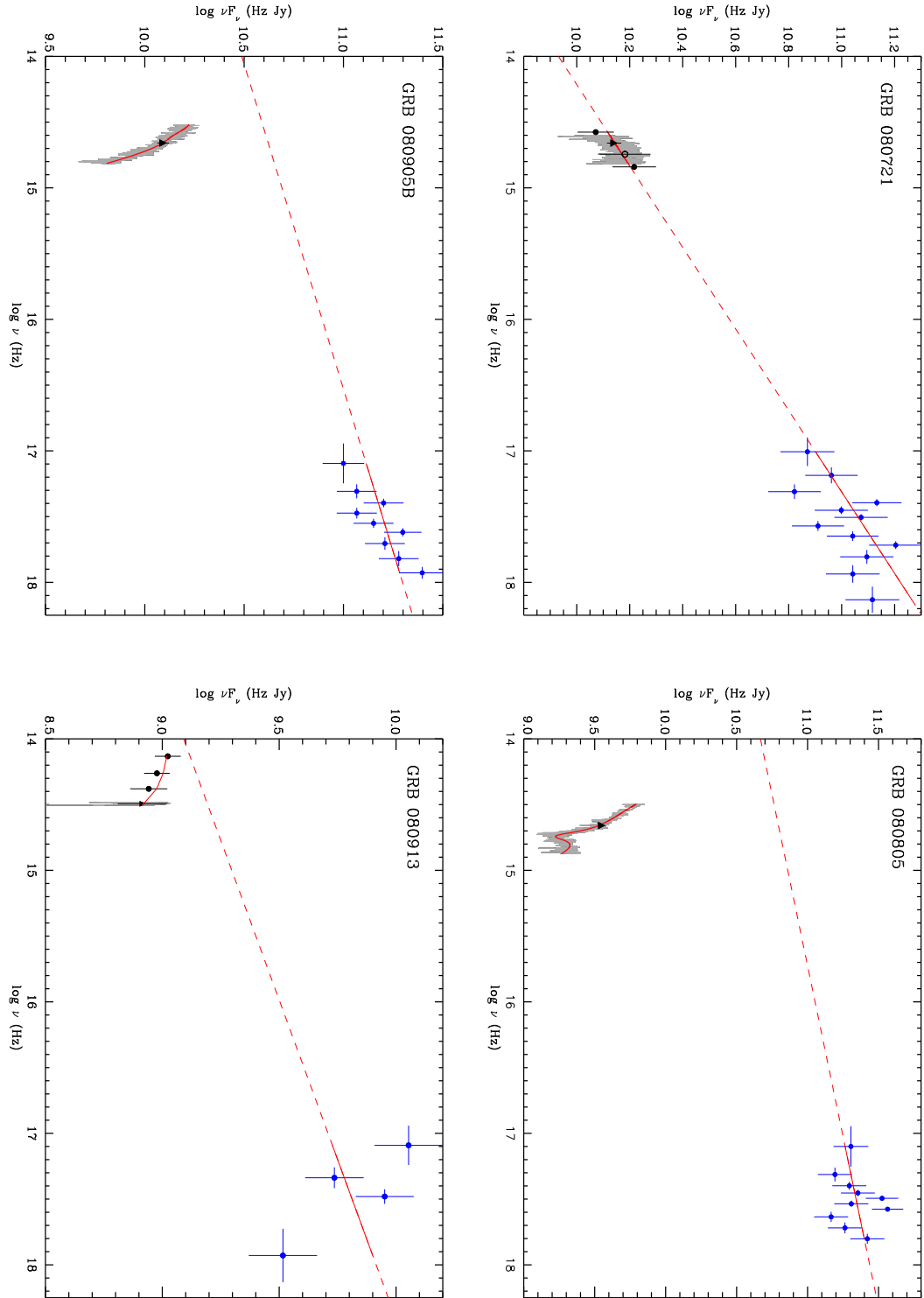


Figure 5.11: (continued)

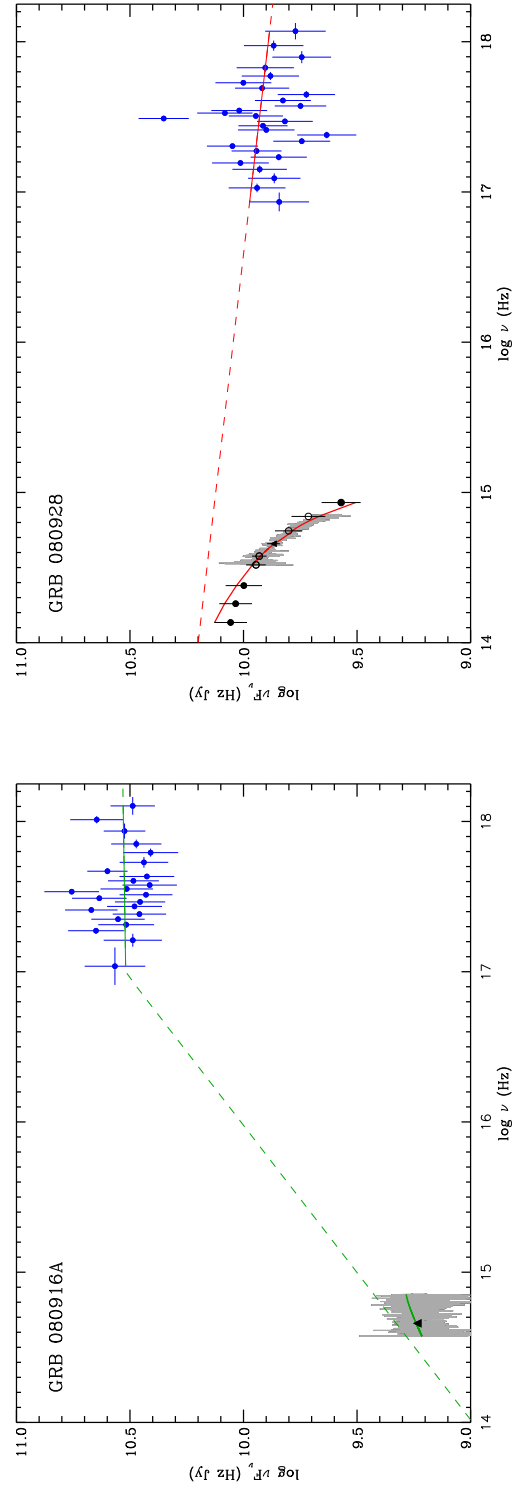


Figure 5.11: (continued)

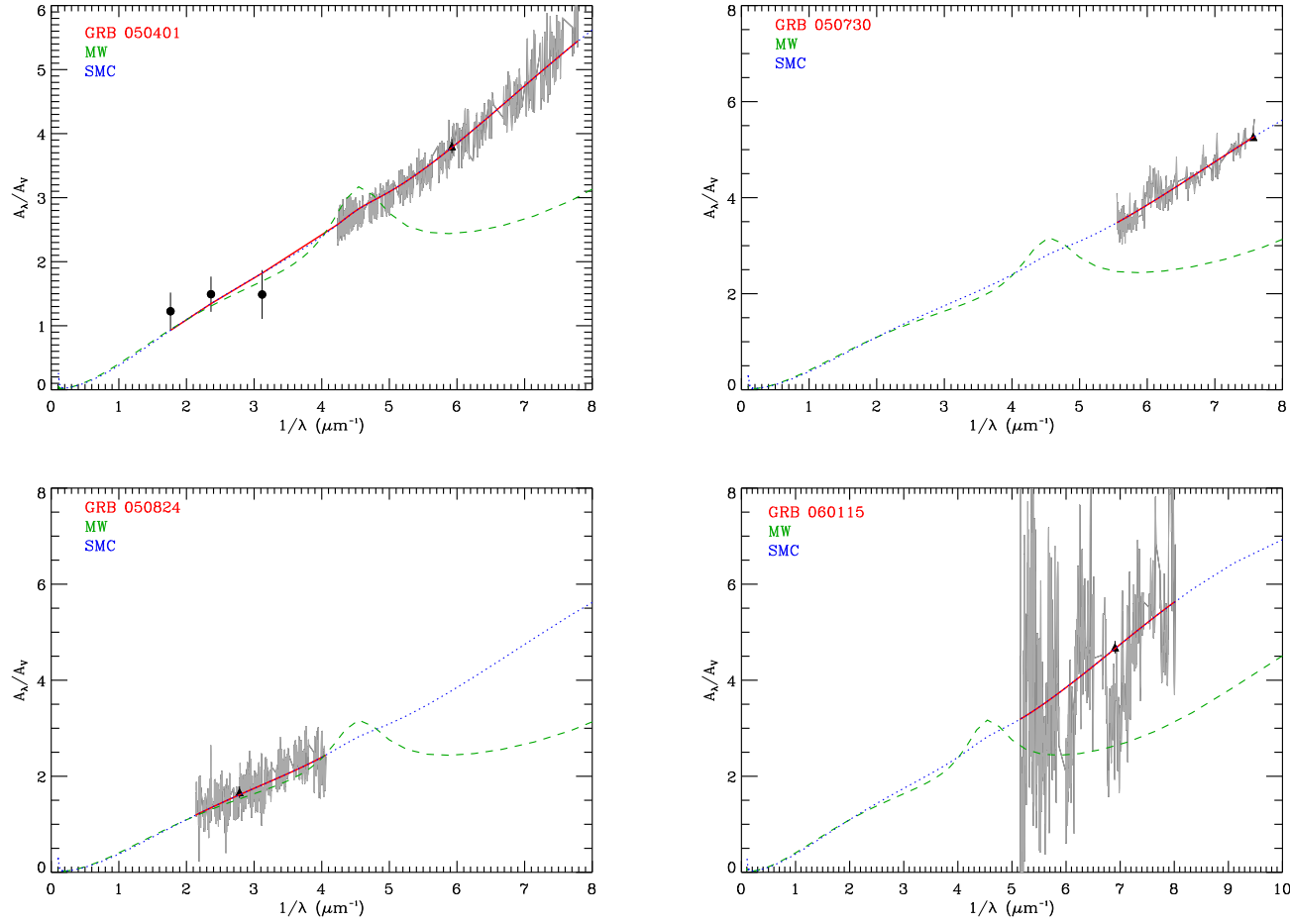


Figure 5.12: Absolute extinction curves of the GRB sample. The extinction curves are based on the best fit models given in Table 5.2. The grey curve represents the optical spectrum. The black triangles correspond to acquisition image photometry. Black open circles are not included in the spectral fitting because of the optical spectrum wavelength coverage in that region while solid circles represents the photometric data points included in the SED modeling. The red curve corresponds to the best dust model for each GRB. Also shown are the Milky Way (green line) and SMC (blue line) extinction models taken from Pei (1992).

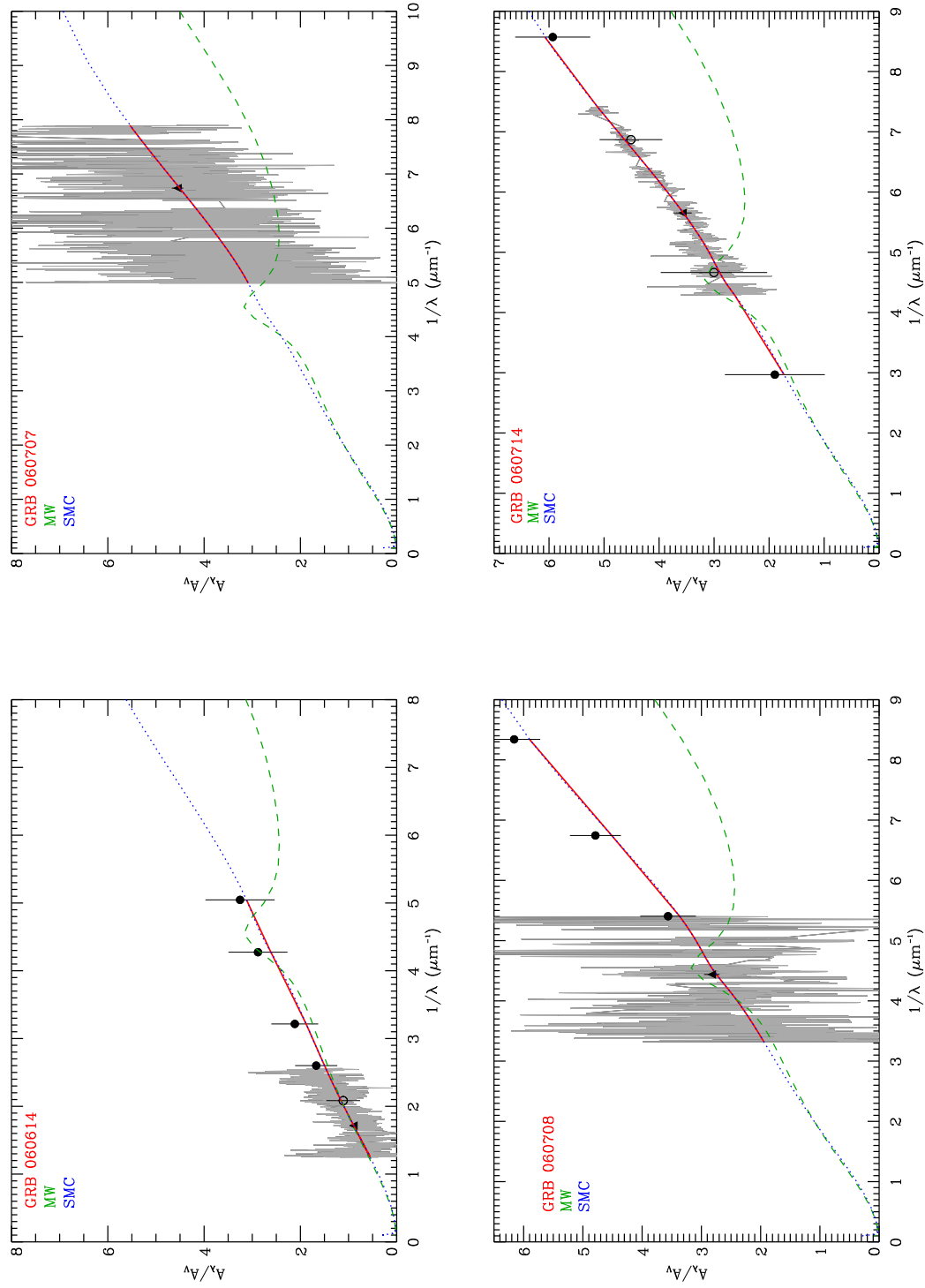


Figure 5.12: (continued)

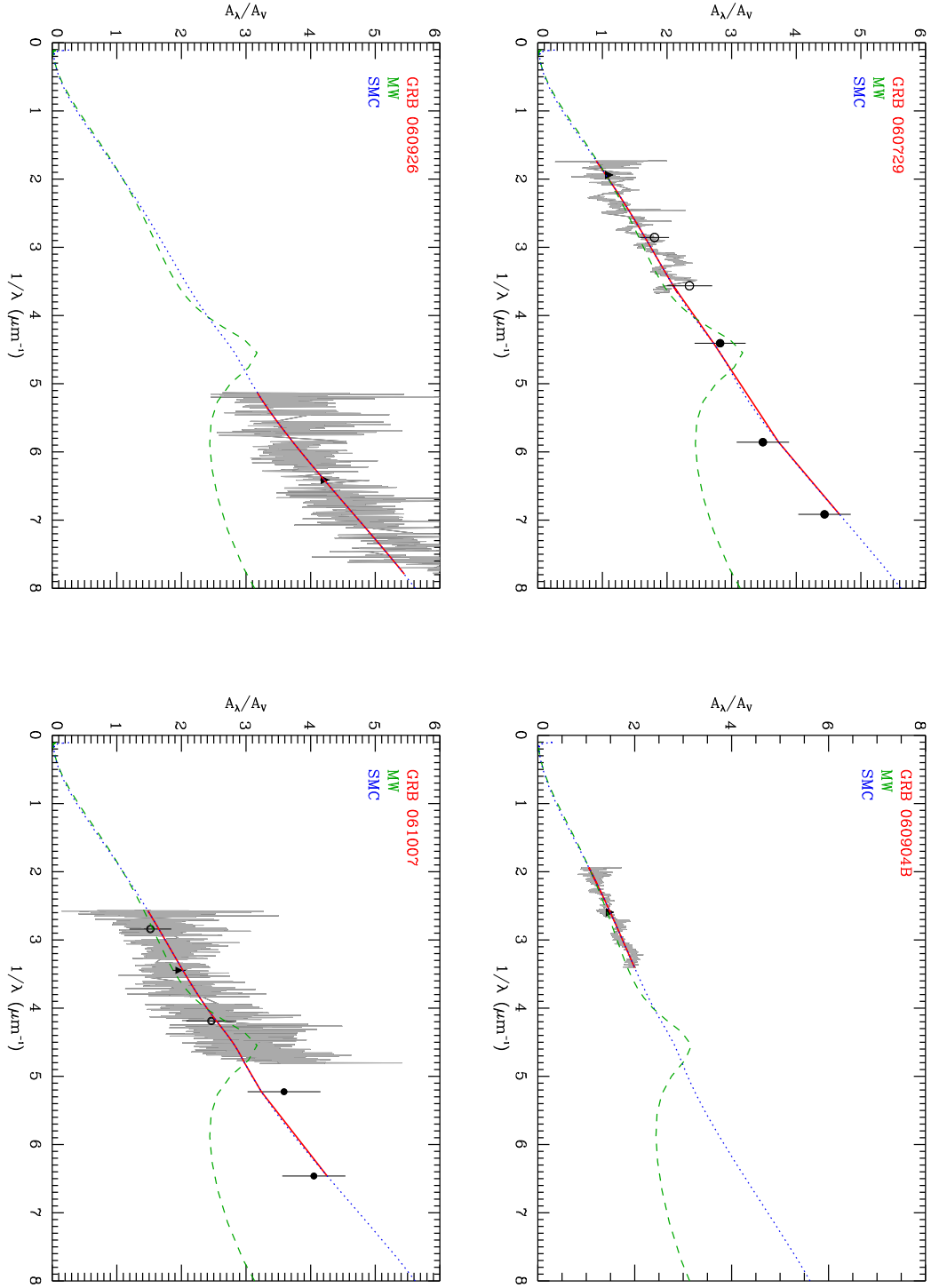


Figure 5.12: (continued)

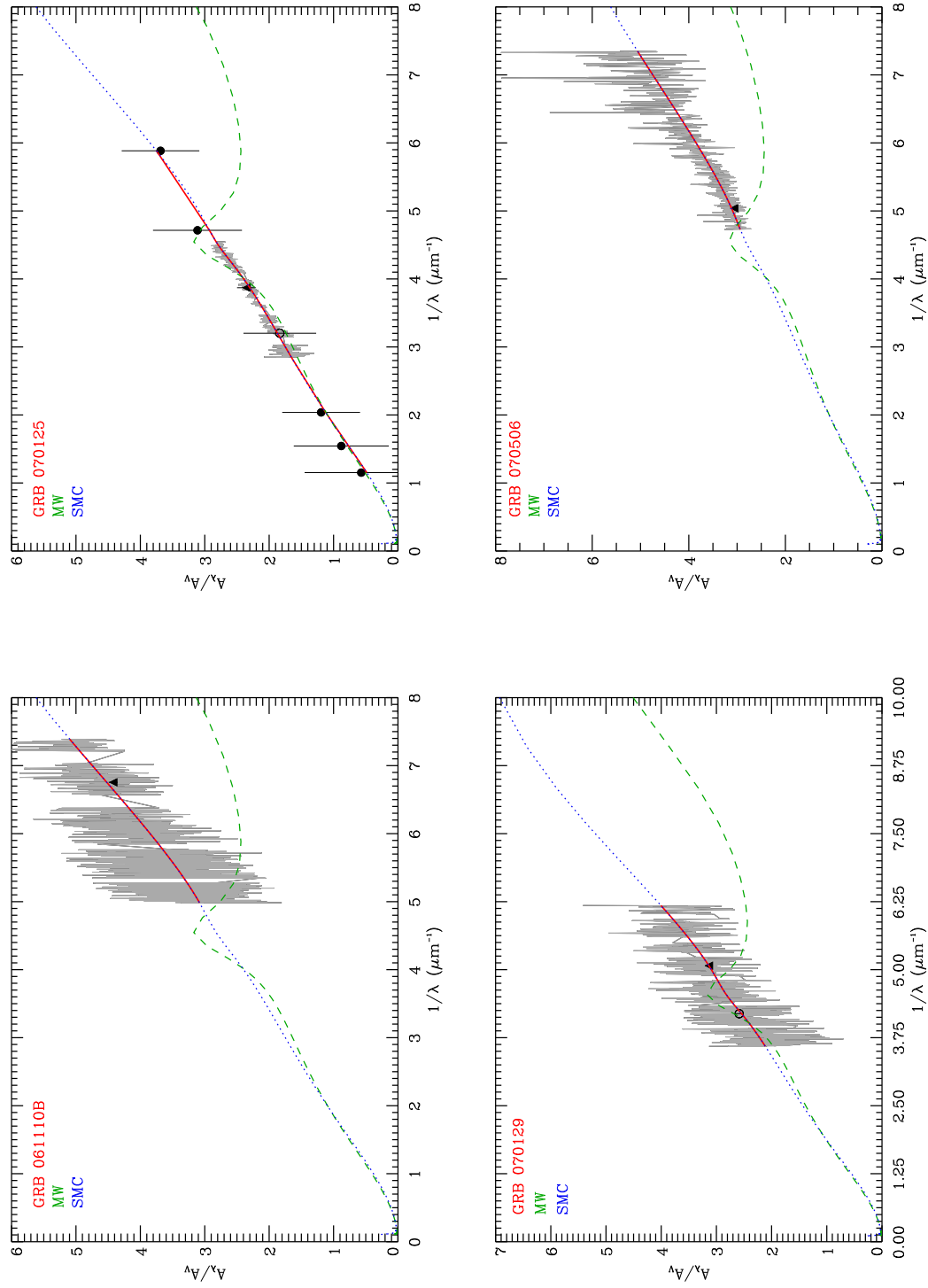


Figure 5.12: (continued)

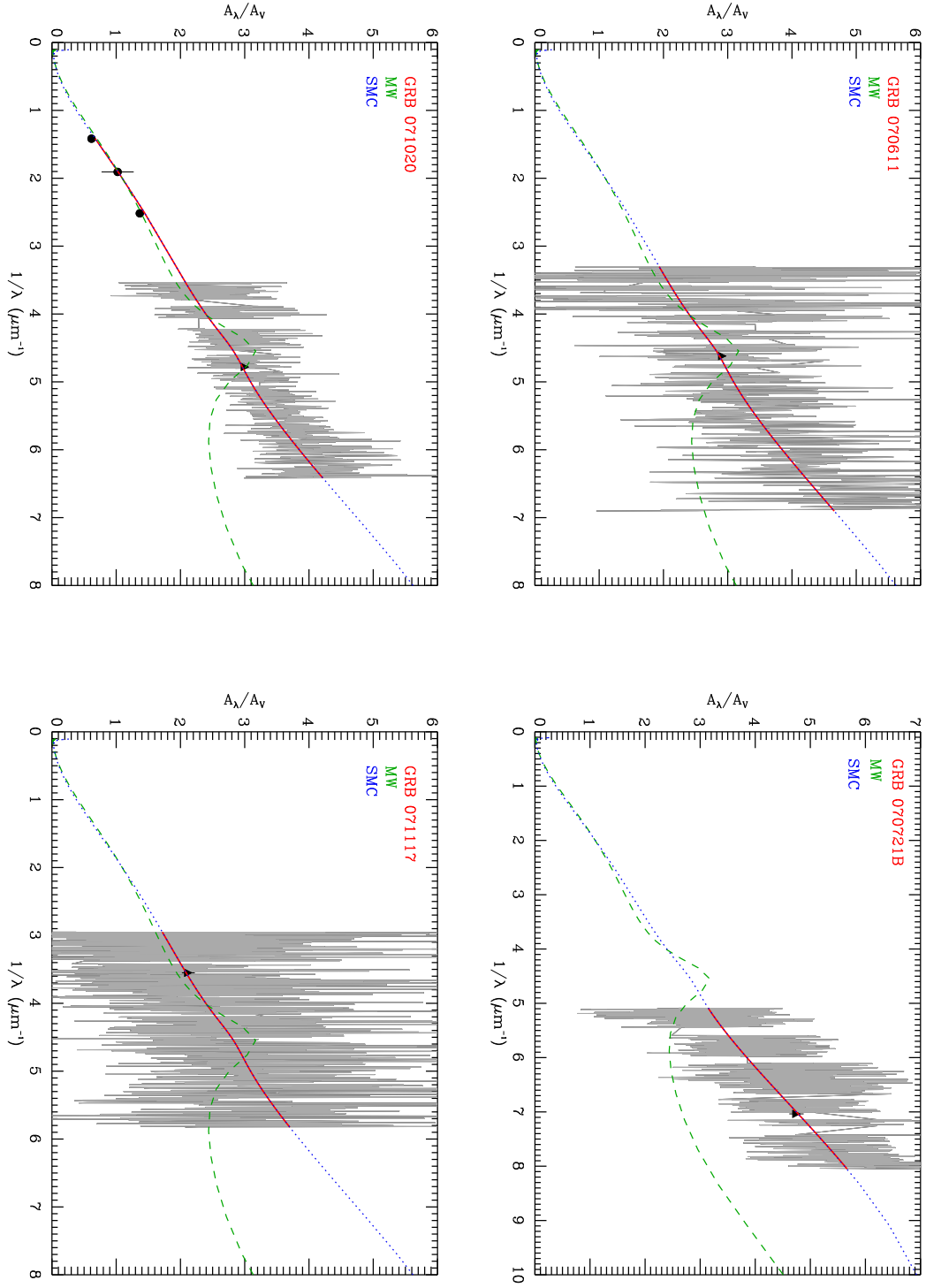


Figure 5.12: (continued)

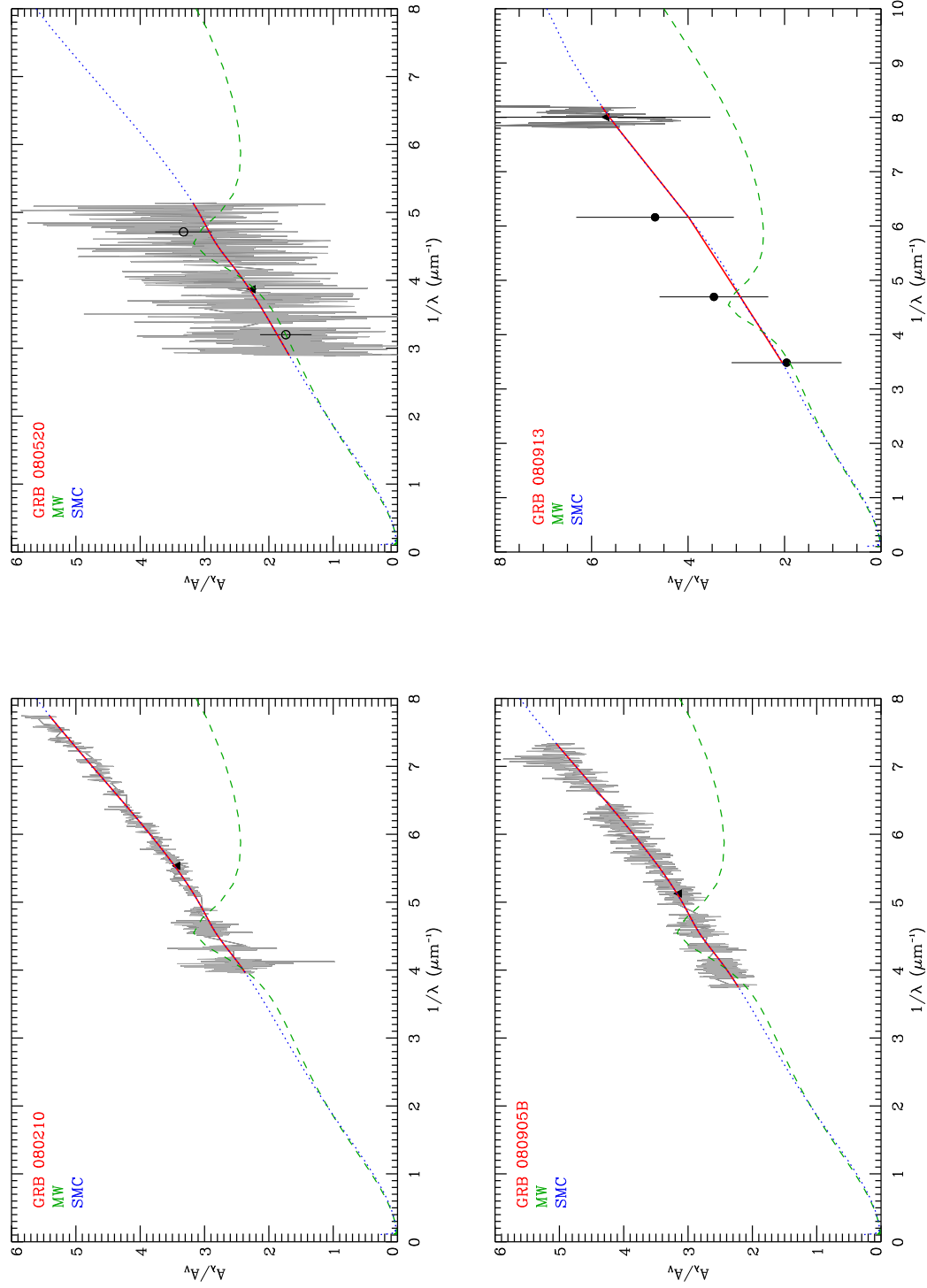


Figure 5.12: (continued)

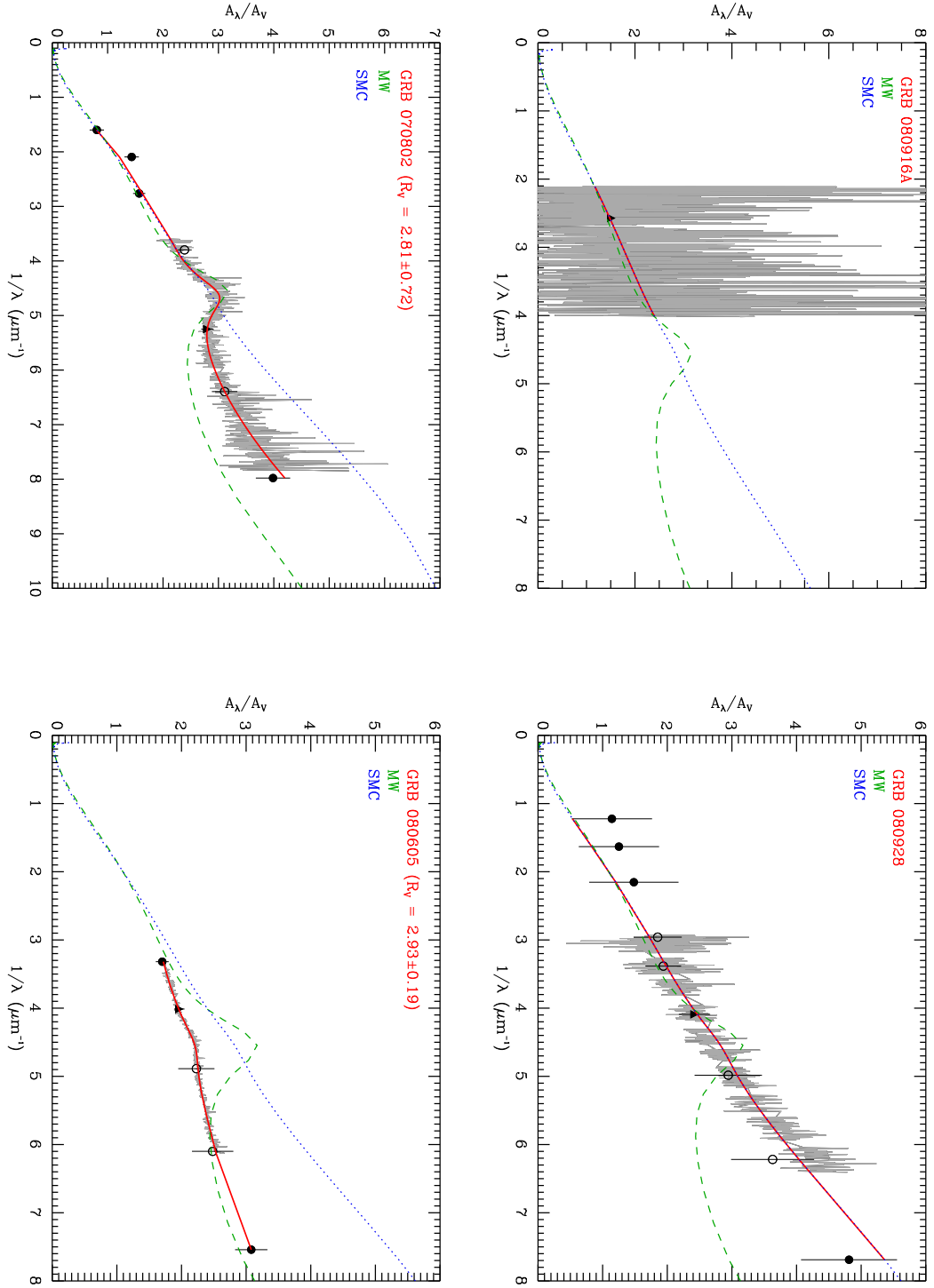


Figure 5.12: (continued)

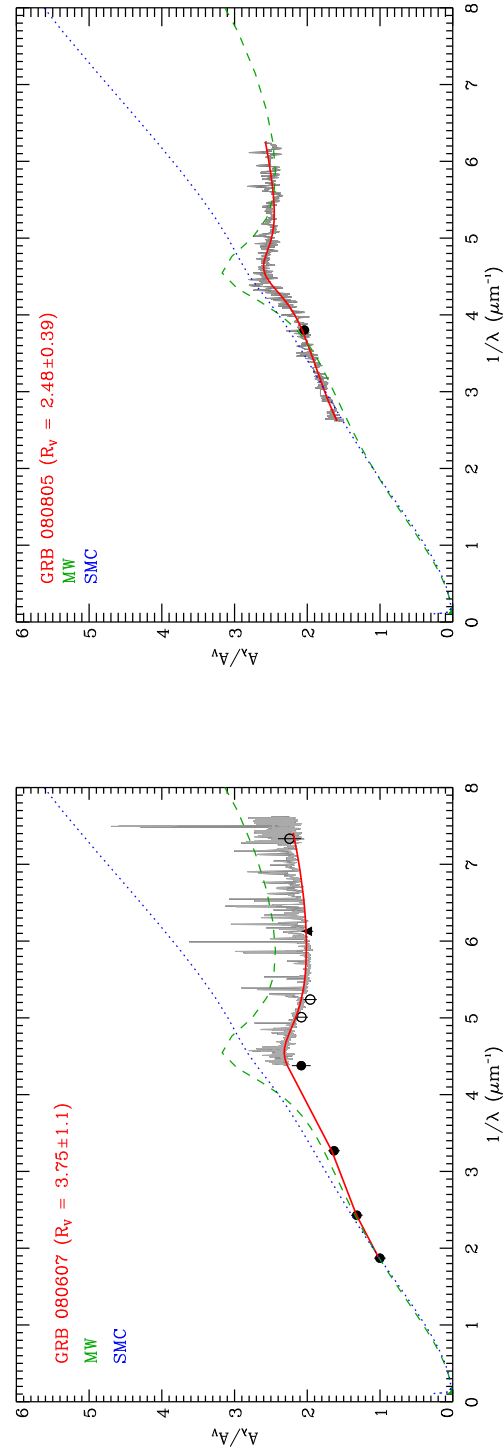


Figure 5.12: (continued)

5.8 ADDITIONAL NOTES

The study of a spectroscopic sample of 41 GRB afterglow provided many interesting results. This section provides additional information about the data and results of our spectroscopic GRB sample. The following information is not published in the paper.

5.8.1 PHOTOMETRIC DATA

The UV, optical and NIR photometry in different bands were gathered from the literature. For ease of access to the data published in GCN circulars for each GRB, the information was obtained via the GRBLog database (Quimby et al. 2004). The SEDs are constructed at specific epochs, therefore, the magnitudes in the relevant filters were obtained by interpolating or extrapolating the lightcurves to the time of interest. For this purpose, usually the R -band lightcurve decay index (α) is used for extrapolation and interpolation in other bands since it is typically the most complete. The details of the photometry used in afterglow SEDs are already given above for each individual case (see Sect. 5.7). The SED magnitudes in the relevant filters for the GRB afterglows are given in Table 5.7 to 5.32 below (see Table 5.1 for SED epochs). The R or I -band acquisition image magnitudes for the GRB afterglows are already provided in Table 5.1 above.

The X-ray to optical/NIR GRB afterglow SEDs were generated at specific epochs (the time of the acquisition image of the spectrum), and modeled in IDL using single and broken power-laws. On top of the single and broken power-laws, we fit the data of each GRB afterglow with different empirical dust extinction laws i.e. SMC (Pei 1992), CCM (Cardelli et al. 1989), and FM (Fitzpatrick & Massa 1986). After fitting the three empirical dust models, the best model for each case was selected from the null hypothesis probability. To determine whether the use of a broken power-law was required over a single power-law, we used an F-test probability $< 5\%$ as the threshold. The results from the spectral analysis of our spectroscopic GRB sample are provided in Table 5.33. For each dust model, the χ^2_ν , number of degrees of freedom, and null hypothesis probabilities are evaluated using single and broken power-laws (see Table 5.33).

Table 5.7: Photometric data for GRB 050401

Band	Magnitude
<i>J</i>	20.85 ± 0.25
<i>H</i>	20.27 ± 0.18
<i>K</i>	19.65 ± 0.12

Table 5.8: Photometric data for GRB 060512

Band	Magnitude
<i>b</i>	21.20 ± 0.38
<i>v</i>	20.80 ± 0.40
<i>J</i>	19.50 ± 0.15
<i>K</i>	18.02 ± 0.20

Table 5.9: Photometric data for GRB 060614

Band	Magnitude
<i>uvm2</i>	19.24 ± 0.07
<i>uvw1</i>	19.27 ± 0.07
<i>u</i>	19.51 ± 0.06
<i>b</i>	20.45 ± 0.06
<i>v</i>	20.15 ± 0.05

Table 5.10: Photometric data for GRB 060708

Band	Magnitude
<i>u</i>	23.20 ± 0.32
<i>b</i>	23.80 ± 0.35
<i>v</i>	23.40 ± 0.36

Table 5.11: Photometric data for GRB 060714

Band	Magnitude
<i>b</i>	22.30 ± 0.14
<i>v</i>	21.67 ± 0.12
<i>I</i>	20.72 ± 0.17
<i>J</i>	19.72 ± 0.18

Table 5.12: Photometric data for GRB 060729

Band	Magnitude
<i>uvm2</i>	17.90 ± 0.15
<i>uvw1</i>	17.60 ± 0.16
<i>u</i>	18.90 ± 0.12
<i>b</i>	18.80 ± 0.10
<i>v</i>	18.40 ± 0.08

Table 5.13: Photometric data for GRB 060906

Band	Magnitude
<i>I</i>	19.50 ± 0.10
<i>z'</i>	19.95 ± 0.07

Table 5.14: Photometric data for GRB 060927

Band	Magnitude
<i>J</i>	23.05 ± 0.42
<i>K</i>	21.45 ± 0.29

Table 5.15: Photometric data for GRB 061007

Band	Magnitude
<i>u</i>	22.15 ± 0.20
<i>b</i>	22.90 ± 0.16
<i>v</i>	22.15 ± 0.20
<i>I</i>	20.40 ± 0.12

Table 5.16: Photometric data for GRB 061021

Band	Magnitude
<i>uvm2</i>	20.10 ± 0.23
<i>uvw1</i>	20.20 ± 0.25
<i>u</i>	20.50 ± 0.16
<i>b</i>	21.20 ± 0.20
<i>v</i>	20.90 ± 0.24

Table 5.17: Photometric data for GRB 070110

Band	Magnitude
<i>b</i>	20.80 ± 0.20
<i>v</i>	21.40 ± 0.18

Table 5.18: Photometric data for GRB 070125

Band	Magnitude
b	19.75 ± 0.22
v	19.30 ± 0.29
I_c	18.00 ± 0.30
J	17.20 ± 0.20
H	16.50 ± 0.25
K	15.75 ± 0.25

Table 5.19: Photometric data for GRB 070129

Band	Magnitude
I	20.60 ± 0.04

Table 5.20: Photometric data for GRB 070318

Band	Magnitude
$uvm2$	21.75 ± 0.30
$uvw1$	21.85 ± 0.40
u	20.85 ± 0.18
b	21.26 ± 0.32
v	20.40 ± 0.24
i'	20.28 ± 0.06
J	19.25 ± 0.10

Table 5.21: Photometric data for GRB 070802

Band	Magnitude
b	24.60 ± 0.28
v	23.30 ± 0.15
z'	22.00 ± 0.15
J	20.60 ± 0.10
H	20.30 ± 0.08
K_s	19.20 ± 0.10

Table 5.22: Photometric data for GRB 071020

Band	Magnitude
J	18.87 ± 0.01
H	18.35 ± 0.25
K_s	17.62 ± 0.01

Table 5.23: Photometric data for GRB 071031

Band	Magnitude
i'	18.98 ± 0.05
z'	18.86 ± 0.06
J	18.65 ± 0.08
H	18.36 ± 0.08
K_s	18.17 ± 0.09

Table 5.24: Photometric data for GRB 071112C

Band	Magnitude
I	21.95 ± 0.17
J	21.10 ± 0.30
H	21.15 ± 0.80
K_s	19.61 ± 0.30

Table 5.25: Photometric data for GRB 080210

Band	Magnitude
g'	20.53 ± 0.04
i'	19.47 ± 0.04
z'	19.26 ± 0.05
J	18.74 ± 0.06
H	18.47 ± 0.06
K_s	18.27 ± 0.07

Table 5.26: Photometric data for GRB 080319B

Band	Magnitude
$uvw1$	19.80 ± 0.15
u	20.65 ± 0.10
g'	20.90 ± 0.06
b	20.95 ± 0.10
v	20.65 ± 0.10
i'	20.44 ± 0.03
z'	20.32 ± 0.04

Table 5.27: Photometric data for GRB 080520

Band	Magnitude
v	23.65 ± 0.40
i'	22.70 ± 0.40

Table 5.28: *Photometric data for GRB 080605*

Band	Magnitude
<i>u</i>	22.00 ± 0.15
<i>b</i>	22.15 ± 0.22
<i>v</i>	21.40 ± 0.23
<i>I</i>	19.65 ± 0.10

Table 5.29: *Photometric data for GRB 080607*

Band	Magnitude
<i>V</i>	18.89 ± 0.12
<i>i'</i>	17.86 ± 0.07
<i>I</i>	17.64 ± 0.10
<i>z'</i>	17.96 ± 0.10
<i>J</i>	15.66 ± 0.06
<i>H</i>	14.12 ± 0.06
<i>K_s</i>	12.64 ± 0.06

Table 5.30: *Photometric data for GRB 080721*

Band	Magnitude
<i>b</i>	20.65 ± 0.24
<i>v</i>	20.40 ± 0.25

Table 5.31: *Photometric data for GRB 080913*

Band	Magnitude
<i>J</i>	22.52 ± 0.20
<i>H</i>	22.14 ± 0.13
<i>K_s</i>	21.70 ± 0.14

Table 5.32: *Photometric data for GRB 080928*

Band	Magnitude
<i>u</i>	21.30 ± 0.23
<i>b</i>	21.83 ± 0.19
<i>v</i>	21.26 ± 0.16
<i>i'</i>	20.65 ± 0.08
<i>z'</i>	20.46 ± 0.09
<i>J</i>	19.93 ± 0.12
<i>H</i>	19.63 ± 0.18
<i>K_s</i>	19.14 ± 0.18

Table 5.33: Results of fits to the SEDs. The columns give the burst name, and then for each model the χ^2_{ν}/dof and the null hypothesis probability (NHP) for the fit are provided. The F-test probability (indicated as f) is computed for each SED comparing the single (PL) and broken power-law (BPL) models. The best fit models are denoted \dagger .

GRB	SMC					CCM					FM				
	PL		BPL		f	PL		BPL		f	PL		BPL		f
	χ^2_{ν}/dof	NH%	χ^2_{ν}/dof	NH%		χ^2_{ν}/dof	NH%	χ^2_{ν}/dof	NH%		χ^2_{ν}/dof	NH%	χ^2_{ν}/dof	NH%	
050401	1.09/1011	2.0	1.08/1009 \dagger	2.6	0.02	9.29/1010	0	9.29/1008	0	1.0	1.08/1005	2.0	1.07/1003	2.6	0.02
050730	1.23/659	0.003	0.98/657 \dagger	60	< 0.01	1.23/658	0.006	1.23/656	< 0.01	0.96	1.02/650	32	0.99/648	52	< 0.01
050824	1.13/958	0.2	0.97/956 \dagger	71	< 0.01	1.30/957	0	1.10/955	2.0	< 0.01	1.23/949	< 0.01	1.04/947	19	< 0.01
060115	1.15/1014 \dagger	0.06	1.15/1012	0.05	1.0	1.13/1013	0.2	1.13/1011	0.2	0.91	1.11/1005	0.8	1.11/1003	0.8	1.0
060512	1.02/1452	33	0.93/1450 \dagger	96	< 0.01	1.02/1451	33	0.94/1449	96	< 0.01	1.02/1443	32	0.94/1441	95	< 0.01
060614	1.01/1254	37	0.82/1252 \dagger	100	< 0.01	1.14/1253	0.03	0.84/1251	100	< 0.01	0.99/1245	61	0.84/1243	100	< 0.01
060707	0.98/1088 \dagger	65	0.98/1086	64	1.0	1.00/1087	52	1.00/1085	51	1.0	0.98/1082	71	0.98/1080	63	1.0
060708	0.86/867	100	0.85/865 \dagger	100	< 0.01	0.96/866	78	0.96/864	78	1.0	0.93/861	92	0.91/859	97	< 0.01
060714	1.02/1043	35	0.97/1041 \dagger	72	< 0.01	2.79/1042	0	2.79/1040	0	0	1.05/1034	14	0.99/1032	61	< 0.01
060729	0.99/1140 \dagger	54	0.99/1138	53	1.0	1.0/1139	49	1.0/1137	49	1.0	1.00/1131	50	1.00/1139	50	1.0
060904B	0.80/1198 \dagger	100	0.80/1196	100	1.0	0.79/1197	1197	1.08/1195	3.0	0.0	0.95/1189	88	0.95/1187	88	1.0
060906	1.01/786	42	0.94/784 \dagger	87	< 0.01	1.01/785	41	0.81/783	100	< 0.01	1.02/777	33	0.95/775	84	< 0.01
060926	0.95/907 \dagger	86	0.95/905	85	1.0	1.02/906	33	1.02/904	31	1.0	0.91/901	97	0.91/899	97	1.0
060927	1.03/274 \dagger	35	1.03/272	32	1.0	1.20/273	1.3	1.20/271	1.3	1.0	1.05/268	27	1.05/266	27	1.0
061007	0.97/1341 \dagger	78	0.97/1339	77	1.0	0.99/1340	60	0.99/1338	60	1.0	0.98/1335	69	0.98/1333	70	1.0
061021	1.26/1703	0.0	0.97/1701 \dagger	75	< 0.01	1.26/1702	0.0	0.97/1700	79	< 0.01	1.19/1694	< 0.01	0.98/1692	73	< 0.01
061110A	0.98/1093 \dagger	63	0.98/1091	61	1.0	0.98/1092	70	0.97/1090	72	0.1	0.98/1084	64	0.98/1062	71	0.2
061110B	0.95/896	85	0.94/894 \dagger	88	0.02	1.33/895	0.0	1.33/893	0.0	0.99	1.12/887	0.8	1.11/885	1.0	0.04
070110	1.09/1087	0.17	1.04/1085 \dagger	18	< 0.01	1.16/1086	0.02	1.10/1084	1.2	< 0.01	1.18/1078	0.003	1.12/1076	0.3	< 0.01
070125	1.03/790	25	0.97/788 \dagger	72	< 0.01	1.02/789	34	0.98/787	65	< 0.01	1.04/784	21	0.98/982	65	< 0.01

GRB	SMC					CCM					FM				
	PL		BPL		f	PL		BPL		f	PL		BPL		f
	χ^2_ν/dof	NH%	χ^2_ν/dof	NH%		χ^2_ν/dof	NH%	χ^2_ν/dof	NH%		χ^2_ν/dof	NH%	χ^2_ν/dof	NH%	
070129	0.93/1017	94	0.91/1015 [†]	98	< 0.01	1.18/1016	0.01	1.18/1014	< 0.01	0.0	1.02/1008	34	0.94/1006	89	< 0.01
070318	1.03/1477	18	1.03/1475	17	0.0	0.95/1476	92	0.95/1474	91	1.0	1.15/1392	< 0.01	0.88/1390 [†]	100	< 0.01
070506	0.99/775	57	0.98/773 [†]	65	< 0.01	3.38/774	0.0	3.38/772	0.0	0.0	1.04/766	22	1.03/764	28	< 0.01
070611	0.77/1248 [†]	100	0.77/1246	100	0.77	1.00/1247	45	1.00/1245	45	1.0	0.98/1242	65	0.98/1240	65	1.0
070721B	1.00/830 [†]	47	1.00/828	46	0.76	1.19/829	0.01	1.19/827	0.01	0.0	1.05/821	18	1.08/819	5.4	0.0
070802	1.48/1390	0.0	1.48/1388	0.0	0.0	0.89/1389	100	0.89/1387	100	0.0	0.54/1381 [†]	100	0.54/1379	100	1.0
071020	1.09/1020	2.1	1.06/1018 [†]	10	< 0.01	1.48/1019	0.0	1.48/1017	0.0	0.0	1.10/1014	1.4	1.07/1012	6.0	< 0.01
071031	2.13/614	0	1.05/612 [†]	17	< 0.01	2.20/613	0	1.06/611	16	< 0.01	1.80/608	0	1.07/606	11	< 0.01
071112C	1.67/1287	0	1.00/1285 [†]	48	< 0.01	1.76/1286	0	1.03/1284	22	< 0.01	1.76/1278	0	0.97/1276	76	< 0.01
071117	0.99/1171	56	0.98/1169 [†]	71	< 0.01	1.04/1170	17	1.02/1168	31	< 0.01	1.00/1165	49	0.98/1163	68	< 0.01
080210	1.10/964	1.7	1.00/962 [†]	45	< 0.01	4.51/963	0	4.51/961	0	1.0	1.17/955	0.02	1.11/953	1.1	< 0.01
080319B	0.83/1468 [†]	100	0.83 /1466	100	1.0	0.84/1467	100	0.84/1465	100	1.0	0.83/1458	100	0.83/1456	100	1.0
080520	1.00/1028 [†]	54	1.00/1026	51	1.0	1.01/1027	39	1.01/1025	37	1.0	1.01/1019	43	1.01/1017	43	1.0
080605	1.74/865	0.0	1.74/863	0.0	0.0	0.89/864	100	0.89/862	100	1.0	0.86/859 [†]	100	0.86/857	100	1.0
080707	1.07/743	9.3	1.03/741 [†]	30	< 0.01	1.10/742	2.9	1.06/740	13	< 0.01	1.07/737	9.2	1.04/737	22	< 0.01
080721	0.96/731 [†]	76	0.96/729	74	1.0	0.99/730	57	0.99/728	57	1.0	0.98/725	64	0.98/733	64	1.0
080805	2.84/1397	0.0	2.84/1396	0	1.0	2.05/1396	0	1.80/1395	0	0	0.93/1391 [†]	98	0.93/1389	97	1.0
080905B	0.98/1029 [†]	68	0.98/1027	66	1.0	7.34/1028	0	7.34/1026	0	0	0.99/1020	58	0.99/1018	58	1.0
080913	0.58/81 [†]	100	0.58/79	100	1.0	2.00/80	0	2.00/78	0	0	0.67/75	99	0.67/73	99	1.0
080916A	0.93/1170	96	0.91/1168 [†]	99	< 0.01	1.00/1169	49	0.97/1167	76	< 0.01	0.95/1164	89	0.92/1162	98	< 0.01
080928	0.99/1157 [†]	57	0.99/1155	55	1.0	1.42/1156	0	1.42/1154	0	0	0.99/1151	59	0.99/1149	59	1.0
080607	88.5/48 [†]	0	26.8/46	0.0	0	3.02/47	0	3.02/45	0	0	1.79/39 [†]	0.19	1.79/37	0.17	1.0

5.8.2 SPECTRAL CHANGE

As explained earlier, the continuum emission of GRB afterglows is described by a coherent synchrotron emission model. The synchrotron emission comes from the accelerated electrons with a power-law distribution of energies. At late times, the electron population is expected to radiate in the slow cooling regime and the GRB spectrum in that regime is defined by a broken power-law. According to the theory suggested by Sari et al. (1998), this cooling break in the spectrum will give a spectral change of $\Delta\beta = 0.5$. In our spectral analysis we treat this $\Delta\beta$ as a free parameter. We found from our SED analysis that 95% of the spectral breaks have a spectral change consistent with $\Delta\beta = 0.5$. The mean spectral change for 20 GRB afterglows out of 21 is found to be 0.51 with a very small standard deviation of 0.02.

Additional checks were made to verify the robustness of the $\Delta\beta = 0.5$ result. In our sample 21 GRB afterglows are found to have a spectral break between the optical/NIR and the X-ray wavelengths. All of these GRB afterglows are well fit with the SMC dust model. Our SED fitting method results in quite large errors on individual $\Delta\beta$ measurements but a very small standard deviation. This suggests an underestimate of errors. The large errors are due to the large uncertainties of the X-ray slopes. These large uncertainties could be due to the fact that the X-ray spectra is not as well defined as the optical segment. In order to test whether the result is robust, we made contour plots of confidence levels of the $\Delta\beta$ versus A_V and versus ν_{break} . For this we fit the data again with the SMC dust model. For each fit the $\Delta\beta$ and ν_{break} were stepped between 0–1.1 and log 14–18 Hz respectively. Only for GRB080210, was the $\Delta\beta$ grid taken from 0.5 to 1.5. The A_V was stepped to different values for each case. This was done to evaluate the χ^2 values at 30×30 grid points. These contours are another way of visualizing the range of acceptable parameters for the least squares fit. The least squares fit was carried out to fit the data using the IDL MPFITFUN routine. MPFITFUN fits the user supplied model using a least squares minimization algorithm. MPFITFUN returns the best fit parameters, errors on each quantity, degrees of freedom, and χ^2 . In Fig. 5.13 we plot the confidence contours of χ^2 as a function of $\Delta\beta$ and A_V . The best-fit minimum is indicated by a cross in each figure. The contour plots of $\Delta\beta$ and A_V clearly indicate that the spectral change is indeed 0.5. Fig. 5.14 show the confidence contours of χ^2 as a function of $\Delta\beta$ and ν_{break} . The contours are usually big but they too essentially show $\Delta\beta = 0.5$. The results clearly show that the $\Delta\beta = 0.5$ in all cases, except GRB080210, and are consistent with the prediction of Sari et al. (1998). In future this result can be used to help derive extinction curves and can reduce the uncertainty in extinction curves.

We briefly compared $\Delta\beta$ results with the optical slope β_1 and spectral break ν_{break} (see Fig. 5.15 and 5.16). The results are similar to the one shown above in Fig. 5.1. Out of the 21 GRB afterglows, GRB080210 is the only case that deviates from $\Delta\beta = 0.5$. Fig.

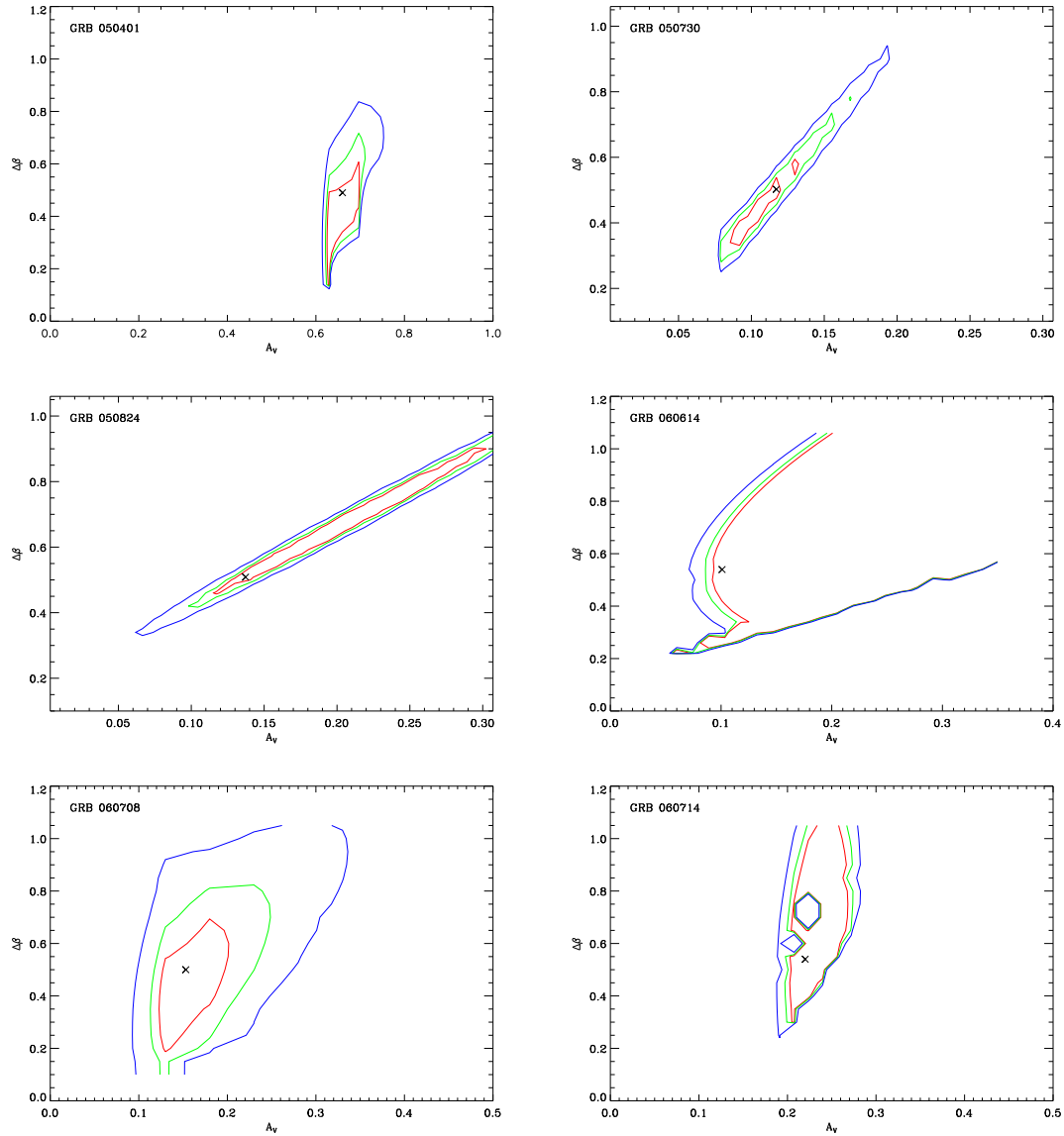
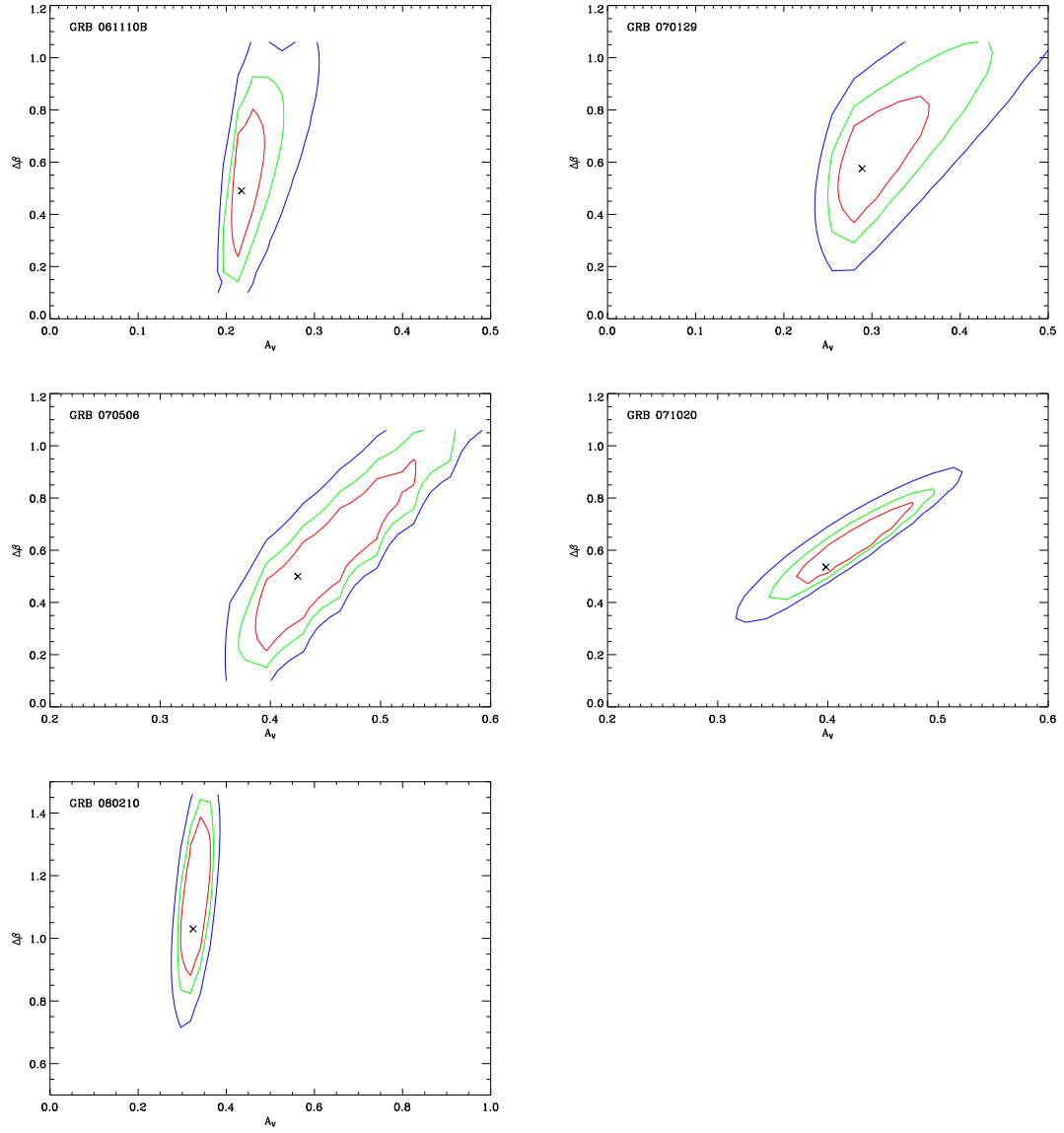


Figure 5.13: Contour plots of χ^2 as a function of A_V and $\Delta\beta$ for the three confidence levels of 68.3% (red), 95.4% (green), and 99.7% (blue). The cross indicate the best fit center positions for A_V and $\Delta\beta$ from MC fitting.

5.15 and 5.16 show that GRB080210 have optical slope and spectral break comparable to the rest of the sub-sample. While Fig. 5.1 show that only GRB080210 has a softer X-ray spectrum than the rest of the sub-sample.

Figure 5.13: *Continued.*

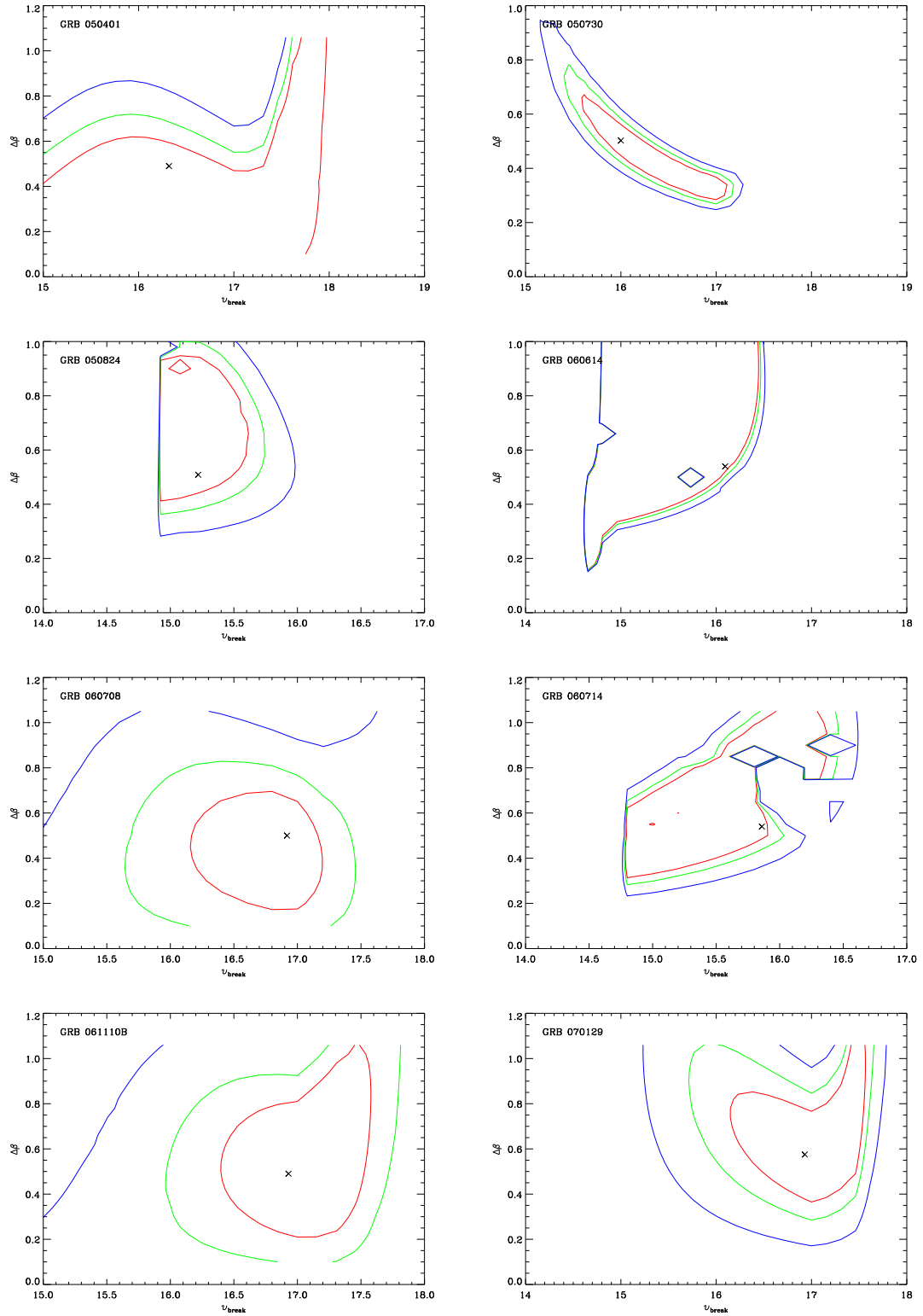
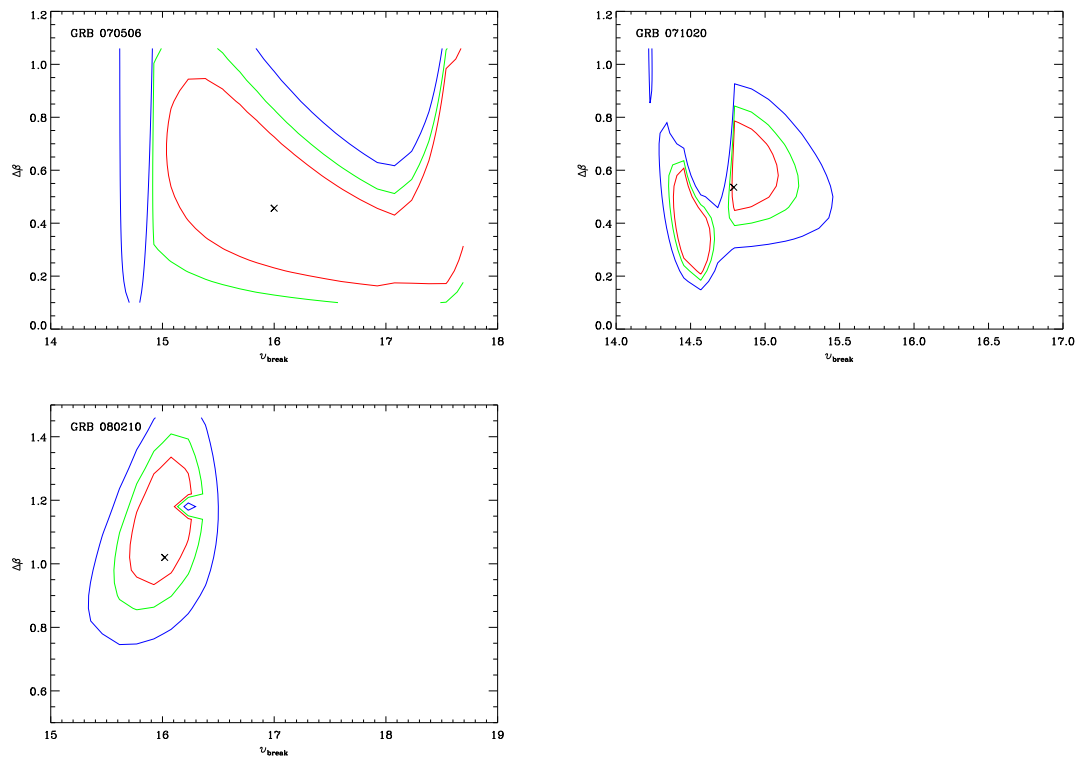


Figure 5.14: Contour plots of χ^2 as a function of A_V and ν_{break} for the three confidence levels of 68.3% (red), 95.4% (green), and 99.7% (blue). The cross indicate the best fit center positions for A_V and ν_{break} from MC fitting.

Figure 5.14: *Continued.*

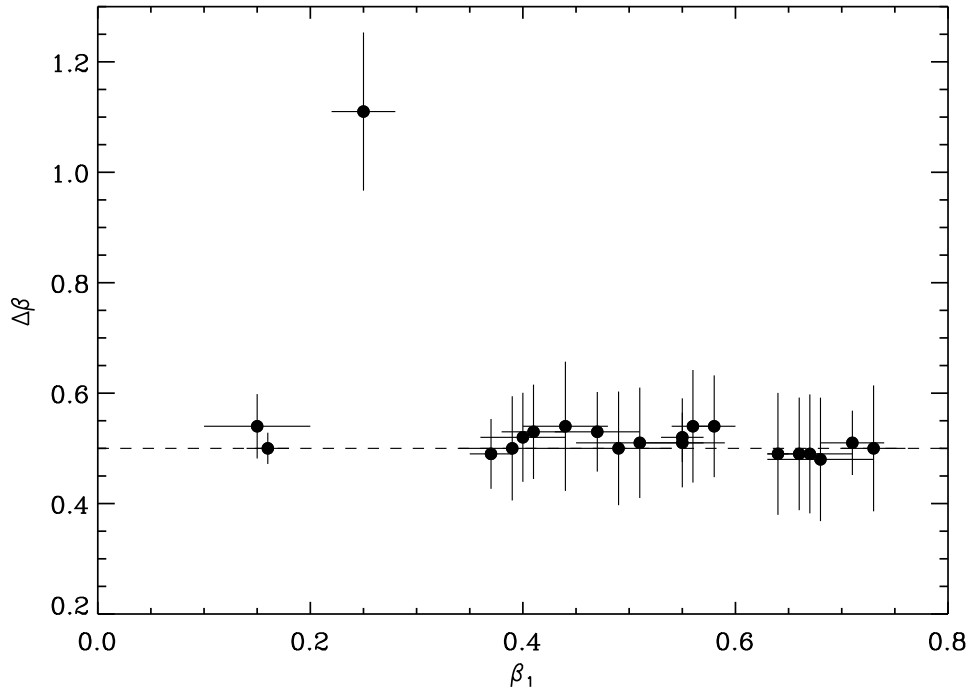


Figure 5.15: Spectral change $\Delta\beta$ against the optical spectral slope β_1 . The dashed line corresponds to $\Delta\beta = 0.5$.

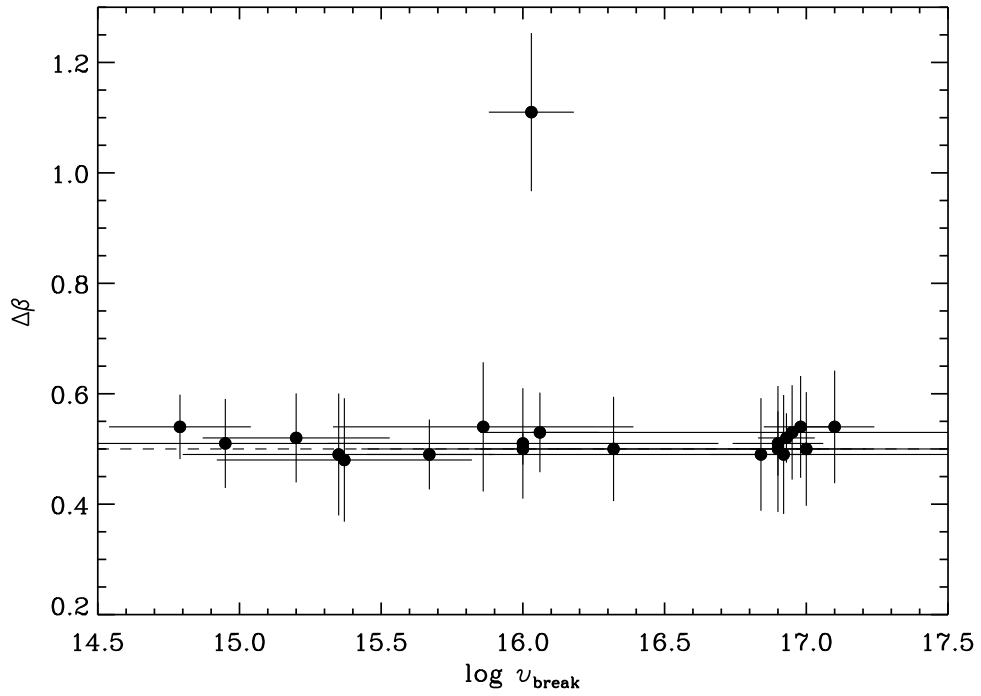


Figure 5.16: Spectral change $\Delta\beta$ against the spectral cooling break ν_{break} . The dashed line corresponds to $\Delta\beta = 0.5$.

5.8.3 CONSTRAINING R_V

From the information on $\Delta\beta$, we tried to constrain R_V for GRB environments. We fitted the data again with the FM model, this time fixing the FM parameters to the SMC average extinction curve values given in Gordon et al. (2003) and fixing $\Delta\beta$ to 0.5 for the 20 relevant spectral break cases, but allowing R_V to vary freely. We generated confidence contours of χ^2 as a function of R_V and A_V . In most cases, however, R_V is degenerate with A_V , so that we cannot constrain R_V in any useful sense.

The contour plots of χ^2 as a function of R_V and A_V are also obtained for the rest of the afterglows including the four 2175 Å bump cases. For GRB 070802 and GRB 080607 we can constrain R_V to 2.8 ± 0.7 and 3.8 ± 1.0 respectively. Previously Prochaska et al. (2009); Perley et al. (2011b) found the A_V for GRB 080607 to be ~ 3.3 mag. Their results were based on the optical data alone. We incorporated X-ray data in the SED which give the absolute flux level, resulting in a smaller A_V compared to Prochaska et al. (2009); Perley et al. (2011b). The A_V versus R_V contours for GRB 080607 show that the visual extinction A_V is less than 3 mag. The optical spectrum of GRB 080607 has strong molecular absorption lines. Therefore, to get the intrinsic continuum we removed the absorption lines and binned the continuum. Because of the fewer data points we found that the contours have several local minima. The other two cases, GRB 080605 and 080805, will be discussed in a future publication (Zafar et al. (in prep.)) with more data out to NIR wavelengths.

We briefly compared the metals-to-dust ratios with z and found no obvious trend (see Fig. 5.18). Such trend is expected because we cannot detect low values of $N_{H,X}$ at higher redshifts. Moreover we compared UV metal abundances in solar units to GRB metal column densities. We found no obvious trend either (see Fig. 5.19). Both values are metal abundances and therefore one might expect some trend. But it is also known that the origin of both values is not same. $N_{H,X}$ comes from the core of GRB and UV metal columns comes from the ISM.

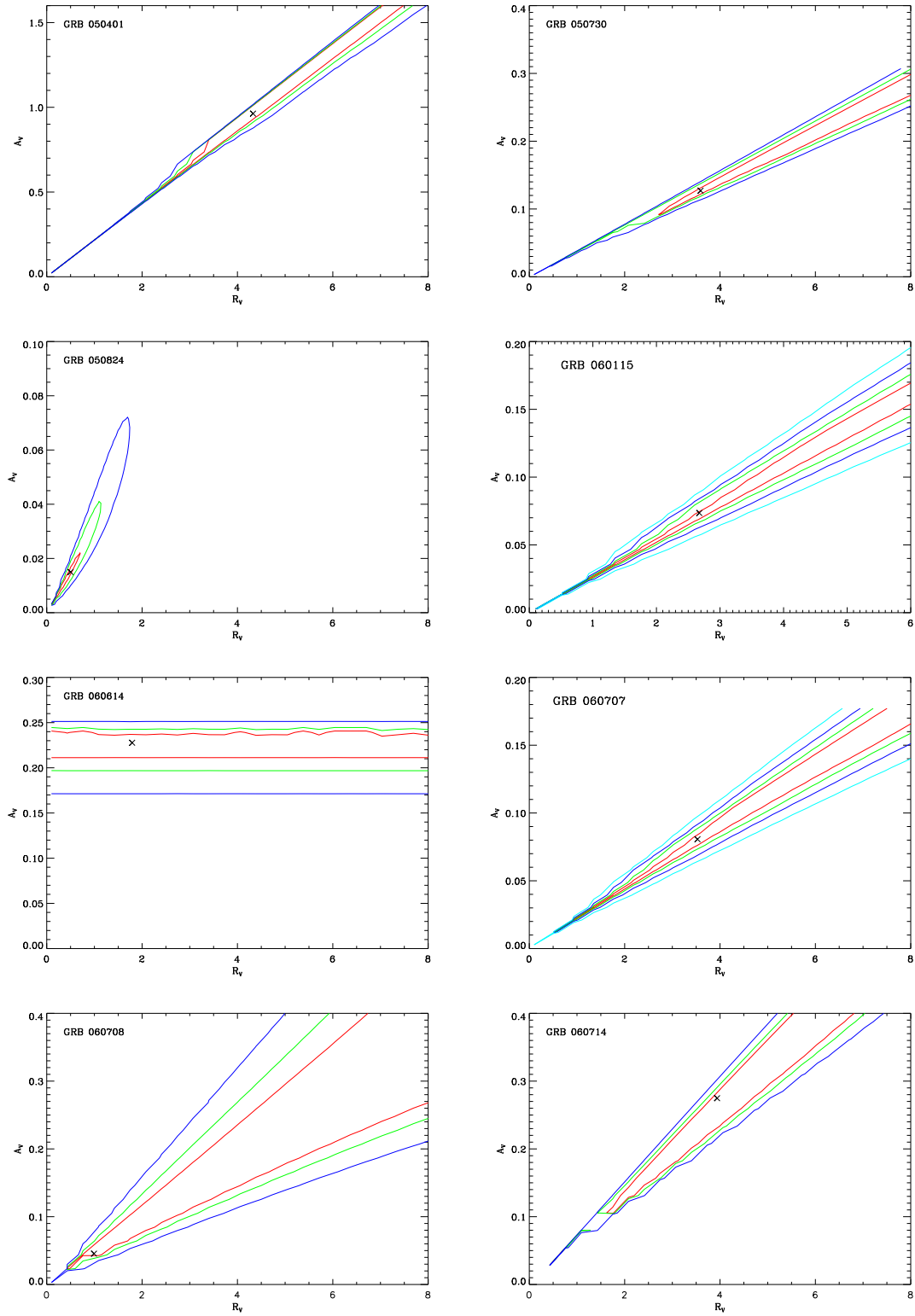
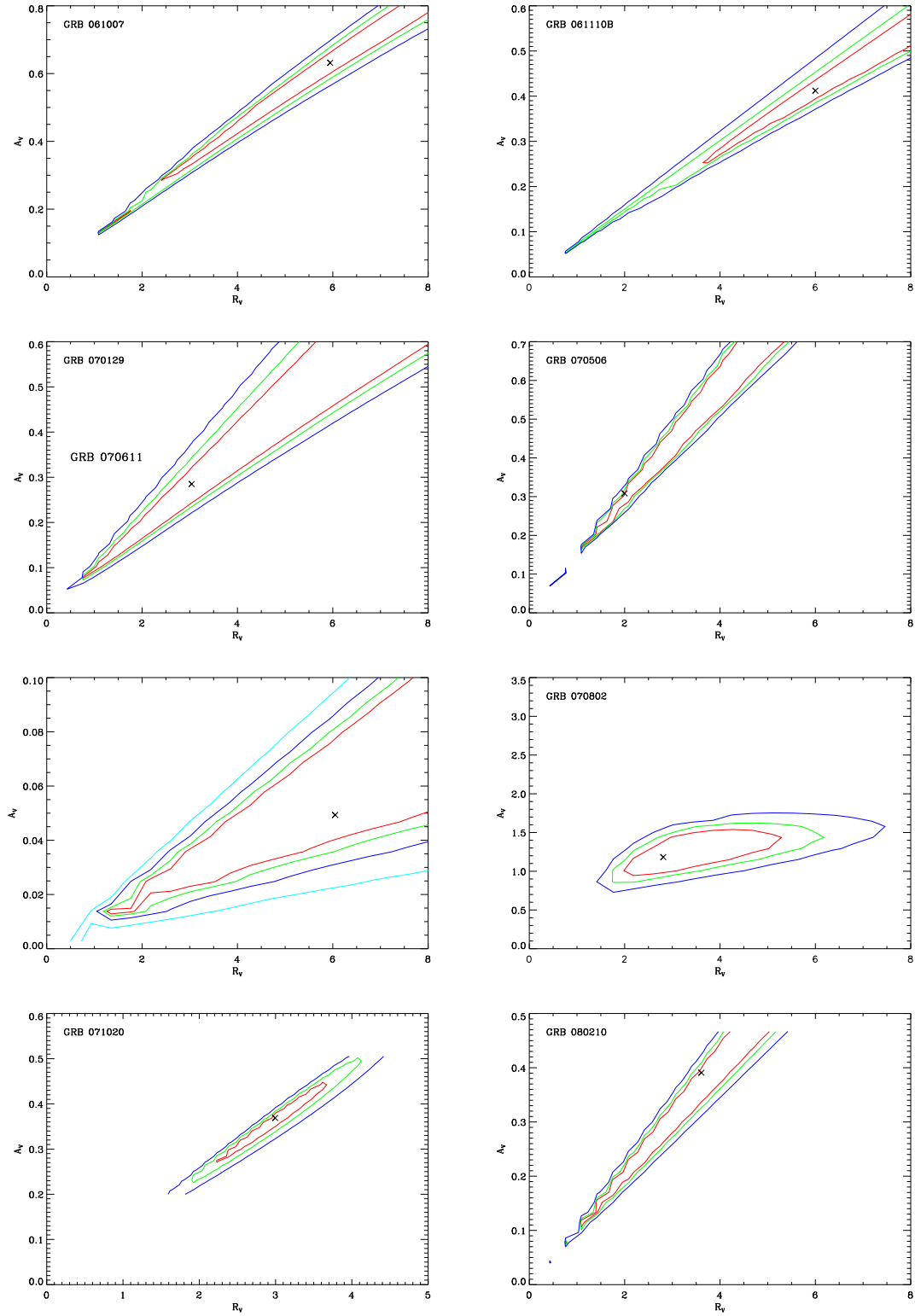
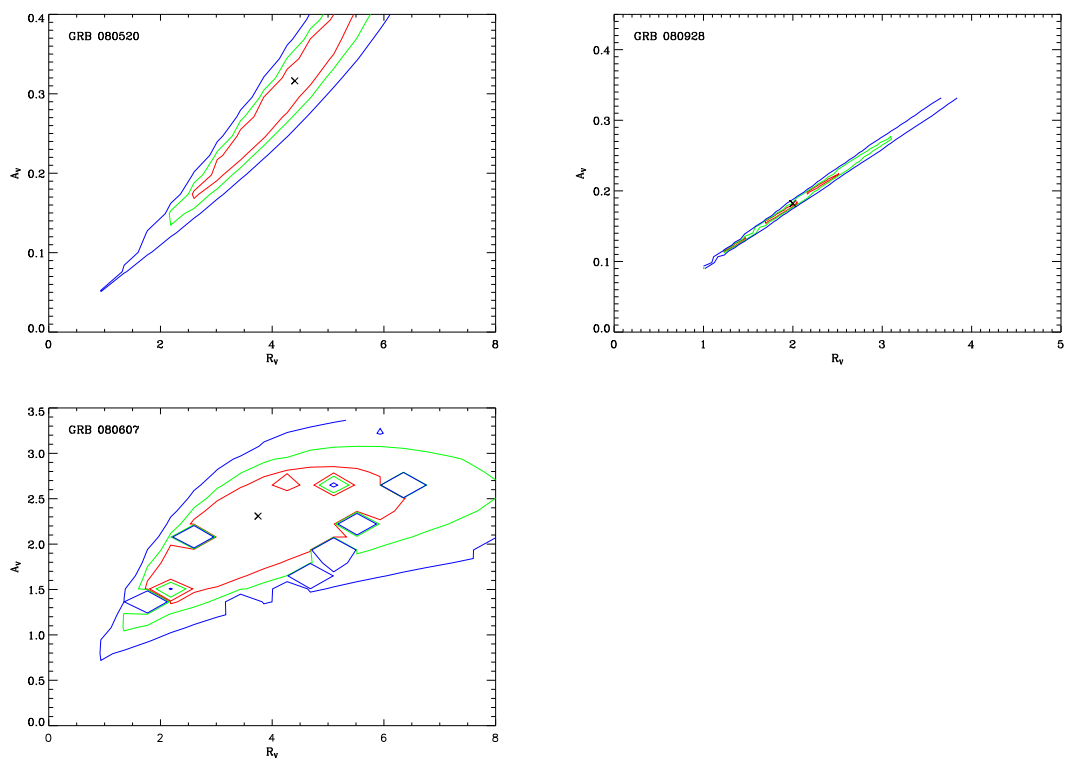


Figure 5.17: Contour plots of χ^2 as a function of A_V and R_V for the three confidence levels of 68.3% (red), 95.4% (green), and 99.7% (blue). The cross indicate the best fit center positions for A_V and R_V from MC fitting.

Figure 5.17: *Continued.*

Figure 5.17: *Continued.*

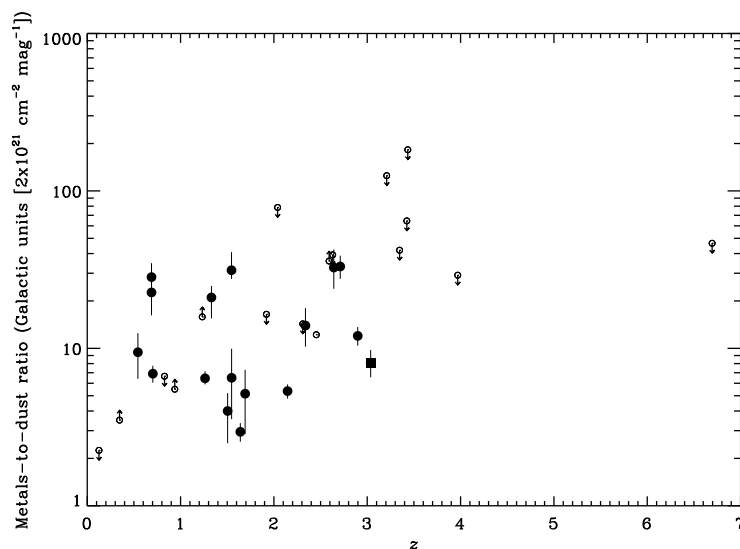


Figure 5.18: Metals-to-dust ratios ($N_{H,X}/A_V$) in Galactic units versus redshift. Filled circles denote the cases where both $N_{H,X}$ and A_V are $\geq 2\sigma$ significant, while the open circles show upper or lower limits for the rest of the sample. GRB 080607 is marked by filled square.

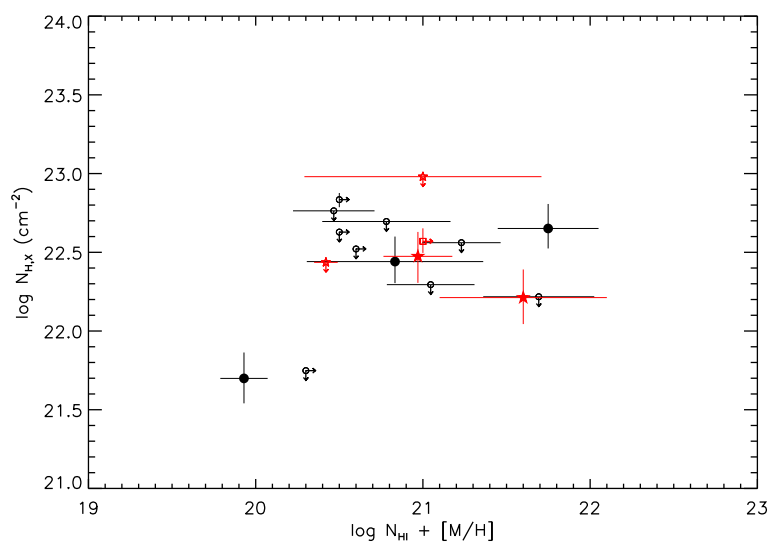


Figure 5.19: Metal column densities, $N_{H,X}$, of GRBs against UV metal abundances in solar Units. The metallicities obtained from the literature based on Zn are marked with red stars. The rest of the data points are based on Si element metallicities (see Table 5.6). GRB 080607 is indicated with a red square. The metallicity or $N_{H,X}$ upper limits are represented by small circles or stars.

6

SPECTROSCOPIC STUDIES OF QSO PAIR Q 0151+048

ABSTRACT –

Q 0151+048 is a physical quasar (QSO) pair at $z \sim 1.929$ with a separation of 3.3 arcsec on the sky. In the spectrum of the brighter member of this pair, Q 0151+048A, a damped Ly α absorber (DLA) is observed at a higher redshift. We have previously detected the host galaxies of both QSOs as well as a Ly α blob whose emission surrounding Q 0151+048A extends over 5×3.3 arcsec. We seek to constrain the geometry of the system and understand the possible relations between the DLA, the Ly α blob and the two QSOs. We also aim at characterizing the former two objects in more detail. To study the nature of the Ly α blob, we have performed low-resolution long-slit spectroscopy with the slit aligned with the extended emission. We have also observed the whole system using the medium-resolution VLT/X-shooter spectrograph and the slit aligned with the two QSOs. The systemic redshift of both QSOs is determined from rest-frame optical emission lines redshifted into the NIR. We employ line-profile fitting techniques, to measure metallicities and the velocity width of low-ionization metal absorption lines associated to the DLA, and photo-ionization modeling, to characterize the DLA further. We measure systemic redshifts of $z_{\text{em(A)}} = 1.92924 \pm 0.00036$ and $z_{\text{em(B)}} = 1.92863 \pm 0.00042$ from the H β and H α emission lines, respectively. In other words, the two QSOs have identical redshifts within 2σ . From the width of Balmer emission lines and the strength of the rest-frame optical continuum, we estimate the masses of the black holes of the two QSOs to be $10^{9.33} M_{\odot}$ and $10^{8.38} M_{\odot}$ for Q 0151+048A and Q 0151+048B, respectively. We then use the correlation between black hole mass and dark matter halo mass to infer the mass of the dark matter halos hosting the two QSOs: $10^{13.74} M_{\odot}$ and $10^{13.13} M_{\odot}$ for Q 0151+048A and Q 0151+048B, respectively. We observe a velocity gradient along the major axis of the Ly α blob consistent with the rotation curve of a large disk galaxy, but it may also be caused by gas inflow or outflow. We detect residual continuum in the DLA trough which we interpret as emission from the host galaxy of Q 0151+048A. The derived H I column density of the DLA is $\log \text{NH I} = 20.34 \pm 0.02 \text{ cm}^{-2}$. Metal column densities are also determined for a number of low-ionization species resulting in an overall metallicity of $0.01 Z_{\odot}$. We use the non-detection of C II* absorption to infer a lower limit on the distance between the DLA and Q 0151+048A of 190 kpc. From the systemic redshifts of the QSOs, we conclude that the Ly α blob is associated with

Q 0151+048A rather than with the DLA. The DLA must be located in front of both the Ly α blob and Q 0151+048A at a distance larger than 190 kpc and has a relative velocity of about 600 km s⁻¹. No absorption is detected in the spectrum of Q 0151+048B at or near the redshift of the DLA which implies that the extent of the DLA and any halo probed by MgII, SiIV or CIV absorption associated with the DLA must be smaller than about 28 kpc.

6.1 INTRODUCTION

Searches for Ly α emission in the high redshift Universe have in the last decade found many sources of a type called Ly α “blobs” (Fynbo et al. 1999; Keel et al. 1999; Steidel et al. 2000; Francis et al. 2001; Matsuda et al. 2004; Palunas et al. 2004; Weidinger et al. 2004; Dey et al. 2005; Villar-Martín et al. 2005; Nilsson et al. 2006). Ly α blobs must be considered the extreme end of the distribution of Ly α emitting sources, in that they are very extended (sizes more than several times ten kpc across), and unusually bright in the Ly α line ($\log Ly\alpha \gtrsim 43 \text{ erg s}^{-1}$). They are interesting and promising cosmological probes, partly because they are some of the largest cohesive structures at high redshift and partly because they hold key insights into the energetics of their source. Among the Ly α blobs, a number of sub-categories have emerged, sorting them based on the presumed main source of ionizing flux. Several blobs have been shown to be powered by vigorous star formation (Taniguchi et al. 2001; Ohyama et al. 2003; Mori et al. 2004; Matsuda et al. 2006), others by cold gas falling onto a dark matter (DM) halo (Nilsson et al. 2006; Smith & Jarvis 2007).

In this group of extreme objects, the most extreme sub-sample in terms of sizes and fluxes are those powered by active galactic nuclei (AGN), QSOs and radio galaxies. Gigantic Ly α haloes are routinely discovered around high redshift radio galaxies (see Miley & De Breuck (2008) for a review). Smaller blobs are also often powered by AGN activity; Geach et al. (2009) find that roughly 17% of narrow-band selected Ly α blobs are powered by AGN. In especially rare cases, multiple component systems including a QSO, a DLA, and a Ly α blob are found (Møller et al. 1998; Leibundgut & Robertson 1999; Hennawi et al. 2009). It is yet unclear how these systems interact, or even their actual spatial configurations.

One such system is the binary QSO Q 0151+048A & B (also called PHL1222), whose brightest member was first observed spectroscopically by Burbidge (1968) who measured its redshift to be $z = 1.943$ (at that time the other member of the binary was not yet discovered). Williams & Weymann (1976) were the first to discuss the nature of the $z_{\text{abs}} > z_{\text{em}}$ DLA in the spectrum of PHL1222 in some detail. They inferred a redshift of the absorber of more than 2000 km s^{-1} relative to the redshift of Q 0151+048A (hereafter qA). The DLA is hence a member of the class of $z_{\text{abs}} \approx z_{\text{em}}$ DLAs (see Møller et al. 1998) which later became proximate DLAs (PDLAs) (Ellison et al. (2010); see also Weymann et al. (1977); Prochaska et al. (2008c)). Compared to normal intervening DLAs PDLAs tend to have evidence for a higher radiation field (presumably the proximate QSO) and on average slightly higher metallicities (Ellison et al. 2010).

The QSO redshift reported in the above work was measured from the UV emission lines from N V, Si IV and C IV, which are now known to be systematically blueshifted relative to the systemic redshift (Tytler & Fan 1992). Williams & Weymann (1976) also inferred a minimum distance of 0.4 Mpc between the DLA and qA based on the absence

of fine structure lines from Si II and C II. Later Meylan et al. (1990) were the first to establish that PHL1222 has a fainter companion at nearly the same redshift. The pair was discussed in more detail in Møller et al. (1998) where Ly α emission was also detected in the DLA trough. Fynbo et al. (1999, hereafter FMW99) found using narrow band imaging that there is very extended Ly α emission close to the redshift of the DLA and in retrospect this appears to be one of the first detections of what is now known as Ly α blobs.

In this study we present new spectroscopic observations of both members of the QSO pair. Our main objectives are *i*) to characterize the DLA absorber (in particular its metallicity and velocity profile), *ii*) to determine the systemic redshift of both members of the pair using rest frame optical emission lines, *iii*) further constrain the geometry of the system by looking for absorption in the spectrum of Q 0151+048B (qB) at the redshift of the DLA, and *iv*) to further study the nature of the Ly α emission blob.

The outline of the paper is as follows: In §2 we describe our spectroscopic observations and data reduction. In §3 & 4 we analyze emission features (the Ly α emitting gas and QSO emission lines) and absorption signatures of the DLA respectively and in §5 we discuss how these new data change our interpretation of the geometry and dynamical state of the system. In §6 we briefly summarise our conclusions. Throughout this paper, we assume a Hubble constant of $H_0 = 72 \text{ km s}^{-1} \text{ Mpc}^{-1}$ (Freedman et al. 2001) and a universe with flat cosmology $\Omega_m = 0.27$, $\Omega_\Lambda = 0.73$ following the results presented in the initial WMAP data release (Spergel et al. 2003). At a redshift of 1.93 and with this cosmology, 1 arcsec corresponds to a proper length of 8.384 kpc. All wavelengths are corrected to vacuum heliocentric frame.

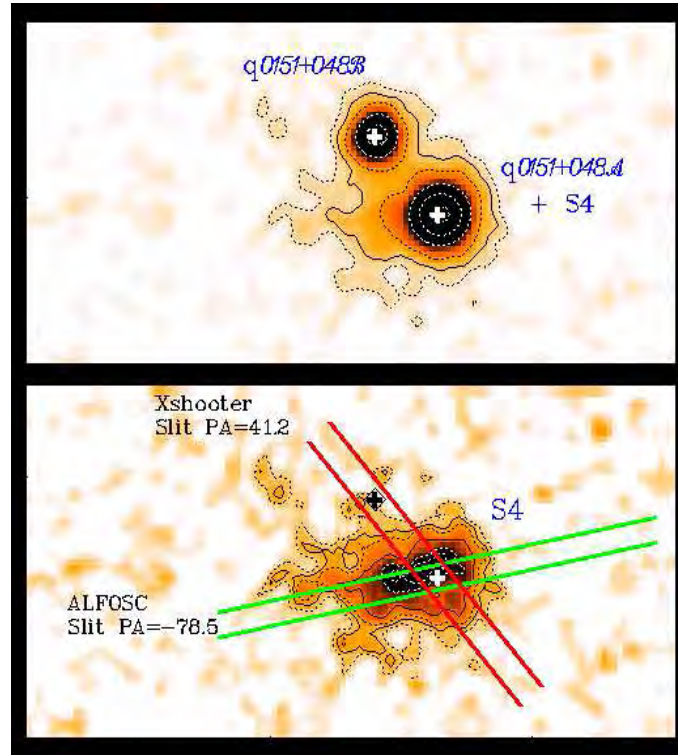
6.2 OBSERVATIONS AND DATA REDUCTION

6.2.1 THE NOT/ALFOSC DATA

On three nights in September 1997 we used the NOT equipped with Andalucia Faint Object Spectrograph and Camera (ALFOSC) to obtain a spectrum of the elongated Ly α emission line object discovered by FMW99 (see their Fig. 2) who named it S4. Our slit was centered on qA and aligned with the major axis of S4 at a position angle of -78.5° (see Fig. 6.1). We used ALFOSC grism G6 and a slit of $0.7''$ which provided a resolution of $R = \lambda/\Delta\lambda = 700$. We integrated for a total exposure time of 33000 sec at this slit position. A detailed log is provided in Table 6.1. The data were reduced using standard techniques for bias and flat-fielding and a final stack was obtained using optimal weights.

Table 6.1: Log of spectroscopic Observations of Q 0151+048 A & B with NOT (ALFOSC) and VLT/X-Shooter (XSH).

Date	Object	Exp. (sec)	Instrument	slit width	R	PA (deg)
2 Sep, 97	A+S4	14000	ALFOSC	0.7''	700	-78.5
3 Sep, 97	A+S4	15000	ALFOSC	0.7''	700	-78.5
4 Sep, 97	A+S4	4000	ALFOSC	0.7''	700	-78.5
18 Nov, 08	A+B	3600	XSH/UVB ¹	0.8''	6200	41.2
	A+B	3600	XSH/VIS ²	0.7''	11000	41.2
29 Sept, 09	A+B	960	XSH/UVB	1.0''	5100	41.2
	A+B	960	XSH/VIS	0.9''	8800	41.2
	A+B	480	XSH/NIR	0.9''	5600	41.2

**Figure 6.1:** Top frame is a cut-out of the original narrow band image (FMW99). The two QSOs are marked by a “+”, NE is to the upper left. The black solid and dashed line illustrate contour plot. In the bottom frame the QSOs were psf-subtracted and only the extended Ly α emission is seen. The “+”es still mark the position of the QSOs. The slit-position along the Ly α major axis used for the NOT/ALFOSC observations is shown in green, the X-shooter A+B slit-position is shown in red.

6.2.2 VLT/X-SHOOTER DATA

On November 18th 2008, during the first instrument commissioning run, we returned to this field, this time using the X-shooter on the VLT which allowed us to observe

both QSOs with higher spectral resolution and long wavelength coverage from ultra-violet (UV) to near-infrared (NIR). The ESO-VLT X-shooter is an Echelle spectrograph mounted at the VLT Cassegrain focus (D’Odorico et al. 2006). Here we used a slit PA of 41.2 deg which placed both QSOs on the slit (see Fig. 6.1) thereby allowing us to obtain a 3600 seconds exposure of both QSOs (Program ID: 60.A-9022(C)). During this early commissioning run only two of the three arms were operational and we obtained spectra in parallel with the UV-blue (UVB) and visual (VIS) arms of the spectrograph using slits of 0.8'' and 0.7'' respectively. The resulting resolutions are 6200 (UVB) and 11000 (VIS). Because the seeing was significantly larger than the slit widths the sky-line widths provide a good measure of the resolution.

On September 29, 2009, during a Science Verification run (Program ID: 60.A-9441(A)), we again integrated with the X-shooter slits on both QSOs. This time we could utilize all three arms (i.e. UVB, VIS, and NIR) and the log of observations is again provided in Table 6.1. Availability of the NIR arm during the September run allowed us to extend the wavelength coverage through to rest wavelength optical lines. We obtained 480 sec in the NIR arm with a resolution of $R = 5100$. All X-shooter data are available from the ESO archive.

The X-shooter data were processed using a preliminary version of the X-shooter data reduction pipeline (Goldoni et al. 2006; Modigliani et al. 2010). The pipeline first corrected UVB and VIS raw frames for bias and NIR frames for dark current. After division by the flat field, the pipeline performed background subtraction, corrected cosmic ray hits using the method developed by van Dokkum (2001) and subtracted sky emission lines using the Kelson (2003) method. The individual orders were extracted and rectified in wavelength space. This was done by using the previously obtained wavelength solution from calibration frames. The individual orders were merged afterwards and in the overlapping regions the merging was weighted by the errors which were being propagated during the reduction process. From the final 2D merged spectrum one dimensional spectra for qA & qB were extracted.

We obtained a spectrum of the hot B-type main sequence star Hip020971 with the NIR arm on the same night. The spectrum was extracted using the same procedure and was subsequently used for atmospheric absorption correction. No flux calibration was applied to either of the spectra.

6.3 RESULTS

6.3.1 THE NOT/ALFOSC DATA

The purpose of the NOT spectrum was to study the dynamics of the Ly α emitting gas (S4). The resolution of the spectrum is too low to provide any useful information about the DLA metallicity, so the primary interest is in the region around Ly α emission. In

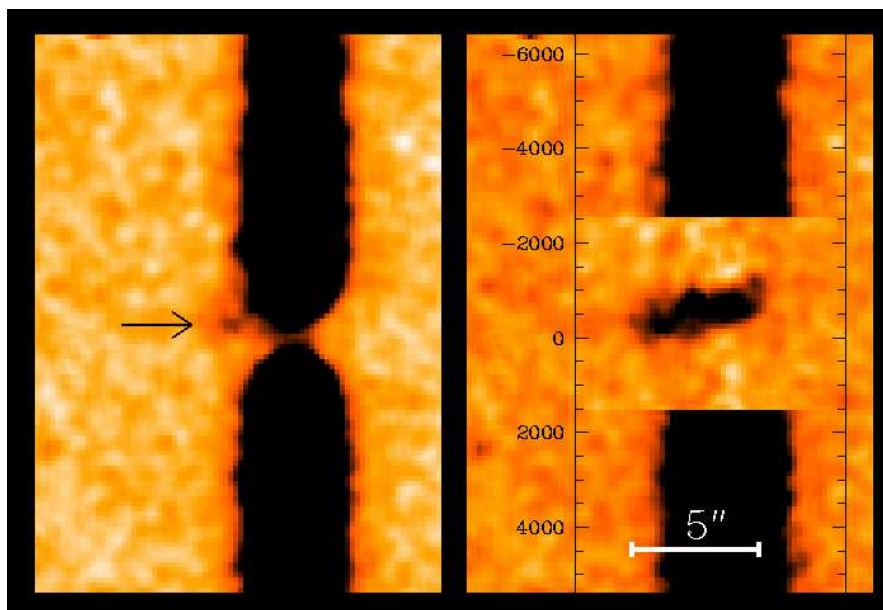


Figure 6.2: (Credit: Palle Møller) *Left panel: NOT/ALFOSC 2D spectrum of qA, the dispersion is vertical with short wavelengths at the top. The DLA line is at the centre, the arrow points to faint extended Ly α emission. Right panel: Same as left after SPSF subtraction. The full extent of the Ly α emission is now visible. It is seen to be tilted and shifted relative to the DLA. The vertical axis provides relative velocity (km/s) in the rest frame of the DLA absorber.*

Fig. 6.2 (left panel) we show this region of the 2D stacked, sky subtracted spectrum. We here use a negative representation where black is bright and orange is zero. In the centre the DLA absorption trough is a dominant feature, and the arrow points to a small but significant area of extended line emission. To examine the Ly α emission closer to the QSO it is necessary first to remove the emission from the QSO, a technique referred to as Spectral-PSF (or SPSF) subtraction (Møller 2000; Møller et al. 2000).

In the right panel of Fig. 6.2 we show the same part of the spectrum after SPSF subtraction around the extended Ly α emission. We clearly detect extended Ly α over a total region of about 5 arcsec (42 kpc proper), corresponding well to the extend of the emission seen in narrowband imaging (Fig. 6.1, lower panel). It is also clear that the emission is not symmetrically distributed around the QSO (also consistent with Fig. 6.1), that it is well separated (in redshift) from the DLA and, somewhat surprisingly, that the emission has a strong velocity gradient along the major axis which has a remarkable resemblance to a rotation curve. The velocity gradient as measured on the SPSF subtracted spectrum is shown in Fig. 6.3.

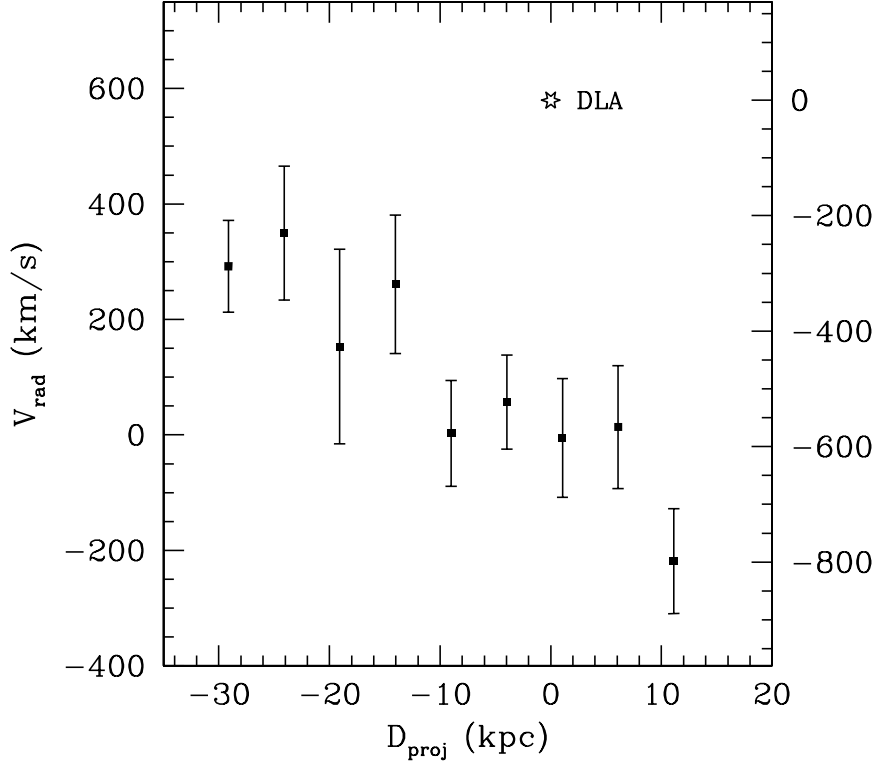


Figure 6.3: (Credit: Palle Møller) *Velocity field of the $\text{Ly}\alpha$ emission seen in the right panel of Fig. 6.2. The DLA absorption sightline towards the qA is marked with “☆”.*

6.3.2 VLT/X-SHOOTER DATA

Residual flux in the DLA trough

One of the most striking features of the X-shooter spectrum of qA is that the DLA absorption line does not go completely to zero. $\text{Ly}\alpha$ emission in or close to DLA absorption lines has been seen in several cases. Møller & Warren (1993); Pettini et al. (1995); Djorgovski et al. (2001); Leibundgut & Robertson (1999); Møller et al. (2002, 2004) and Fynbo et al. (2010) all reported a narrow emission line slightly offset from the position of the background quasar and consistent with being $\text{Ly}\alpha$ emission from the DLA host which absorb the QSO to zero flux at $\text{Ly}\alpha$. Cooke et al. (2010) report what they interpret as either a broad absorption line with emission at the centre or as two absorption lines separated by non-absorbed quasar continuum. Unfortunately they do not provide the detailed spatial information which would help the interpretation, but since a possible interpretation of the “feature” is that it is non-absorbed quasar continuum it must be centered on the position of the quasar and have the spatial profile of a point-source.

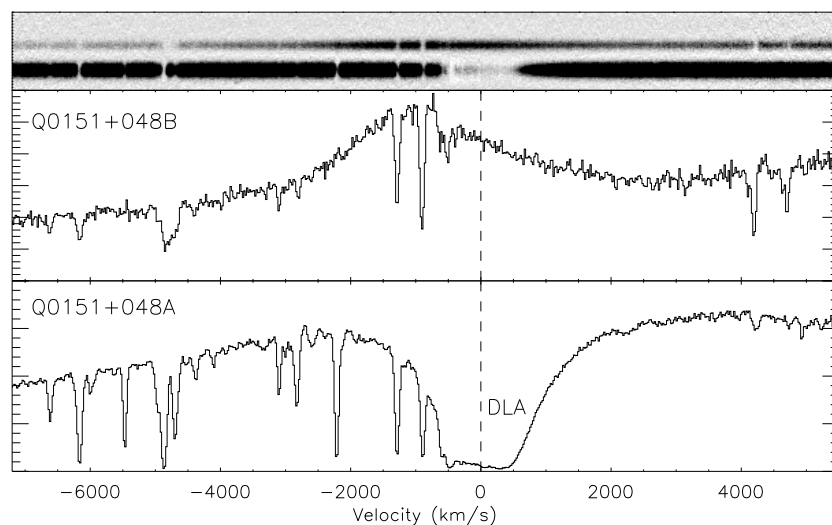


Figure 6.4: X-shooter spectra of both QSOs obtained on November, 18 2008 with a single exposure of 3600 sec. Upper panel: 2D UVB-arm spectra of both QSOs, qB is the fainter object and qA is the brighter object displaying strong DLA absorption. Middle panel: 1D spectrum of qB. Lower panel: 1D spectrum of qA showing the DLA absorption. Note that in both the 2D and the 1D spectrum of qA residual flux is clearly visible in the damped trough.

This makes it unlikely that it is $\text{Ly}\alpha$ emission as $\text{Ly}\alpha$ emission usually is more extended than a point-source and in addition it would be an unlikely coincidence that the $\text{Ly}\alpha$ emission by chance would be lined up exactly with the second image of the lens where the DLA covers only the first image.

Hennawi et al. (2009) also report an emission line in a damped absorption line. They do not provide any information about spatial offset, but the object has a large (5 arcsec) size along the slit. Hennawi et al. (2009) rule out that the emission is related to the DLA and instead interpret it as a $\text{Ly}\alpha$ blob physically connected to the quasar. This object has two features in common with the DLA in qA. Both are PDLAs and both have $\text{Ly}\alpha$ emission extending 5 arcsec. The extended $\text{Ly}\alpha$ of qA is however significantly offset in redshift from the PDLA and does not enter into the absorption line. Nevertheless in both the 2D and the 1D X-shooter spectrum of qA (Fig. 6.4) it is clearly seen that there is a smooth continuum providing a non-zero “floor” in the $\text{Ly}\alpha$ line. In this section we aim to determine the source of this residual flux in the damped absorption line.

There are two possible ways to explain this residual flux. Either the absorber is so small that it only partly covers the emitter (the central engine), or there are at least two different sources of emission and the DLA absorber is only covering one of those. In Fynbo et al. (2000) it was reported that qA is located inside a comparatively bright host

galaxy with a $B(AB)$ magnitude of 20.8 ± 0.2 and $I(AB)$ of 21.5 ± 0.2 . The host was best fitted by a de Vaucouleurs profile, and in $B(AB)$ it was found to be 3.0 magnitude fainter than qA while in $u(AB)$ and $I(AB)$ it was 3.9 and 4.0 magnitude fainter respectively. We now investigate if the residual flux in the DLA trough simply is the spectrum of the QSO host galaxy.

We first co-added the profile of all wavelength bins in the centre of the DLA line where it should be completely absorbed. We then did the same where the QSO continuum had recovered both on the blue side (3540–3545 Å) and on the red side (3595–3605 Å). The FWHM of the QSO profile along the slit on both the blue and the red side is 1.03 arcsec while the FWHM of the flux at the bottom of the DLA is 1.57 arcsec, i.e. significantly wider. Simple subtraction in squares gives an intrinsic FWHM of 1.2 arcsec for the object seen in the DLA line which immediately rules out that the residual could be caused by partial coverage of the QSO alone because in this case the profile should be the same as that of the QSO. The object that we see in the DLA trough is therefore a different object than the QSO, it is relatively large (1.2 arcsec FWHM) and could possibly be the host galaxy.

The spectrum was taken with a slit of $0.8''$ and we therefore have slit losses of both the QSO and of the other object. We have modeled the psf of the QSO such that the psf-on-slit is identical to that observed. Using this we measure a slit loss of 40%. Similarly we have modeled the profile of the object seen in the trough, and find slit losses of 60% in this case. The measured counts per bin of the extended object is a factor 27 less than of the QSO continuum. Correcting for the different slit losses this becomes a factor 18 fainter, i.e. 3.1 magnitudes fainter. This corresponds well to the reported magnitude difference as found via imaging (Fynbo et al. 2000).

From Fig. 6.4 upper panel (more clearly seen in Fig. 6.7) it is also seen that the two objects are centered on the same position. Summing up all of the evidence, extended profile, centered on the QSO, similar brightness relative to qA, we conclude that the flux seen in the DLA trough is the signature of the continuum of the qA host galaxy.

Emission line analysis of Q 0151+048A & B

The discovery of $\text{Ly}\alpha$ emission from this system was first reported in Møller et al. (1998) but the interpretation of the data in that paper was severely complicated by the large apparent blueshift of qA relative to the DLA (1250 km s^{-1}) and to the $\text{Ly}\alpha$ emitter (950 km s^{-1}) which remained even after the corrections suggested by Tytler & Fan (1992) were applied. Such shifts are common in QSOs spectra (see Grandi 1982; Wilkes 1986; Møller & Warren 1993; Laor et al. 1995; McIntosh et al. 1999; Vanden Berk et al. 2001; Richards et al. 2002), but even though there is a general pattern to the shifts it has not yet been possible to devise a method to successfully correct for this. We therefore had serious doubts about the accuracy of QSO systemic redshifts determined from UV

Table 6.2: Emission line properties of Q 0151+048A & B. The columns provide observed and restframe wavelengths, observed and restframe equivalent widths with their corresponding errors, line IDs and emission redshifts.

Object	λ_{obs} Å	λ_{rest} Å	EW_{obs} Å	σ_{EW} Å	EW_{rest} Å	ID	z_{em}
qA:	3612.441	1240.13	13.658	0.237	4.688	N V	1.91295 ± 0.00014
	3694.3012	1262.59	3.9	0.09	1.33	Si II	1.92597 ± 0.00027
	3814.9426	1304.35	11.4	0.113	3.9	O I	1.92478 ± 0.00035
	3894.3012	1334.5	3.8	0.087	1.3	C II	1.9182 ± 0.00016
	4063.8574	1399.7	40.35	0.198	13.9	Si IV + O IV	1.9034 ± 0.0003
	4504.9333	1549.06	62.7	0.266	21.56	C IV	1.9082 ± 0.0004
	6804.5376	UV 344(2325.38)	19.16	0.11	6.55	Fe II	1.92621 ± 0.00026
	7109.3696	UV 360(2433.436)	10.73	0.14	3.67	Fe II	1.92154 ± 0.00038
	8188.9807	2798.75	96.44	0.24	32.96	Mg II	1.92594 ± 0.0004
	14244.0	4862.68	119.8	0.28	40.9	H β	1.92924 ± 0.00036
	19231.4	6564.61	525.56	0.81	179.4	H α	1.92939 ± 0.00043
qB:	3557.5860	1215.67	243.7	0.923	83.3	Ly α	1.9264 ± 0.00034
	3628.5042	1240.14	8.29	0.631	2.83	N V	1.9270 ± 0.00042
	3678.3472	1262.59	2.13	0.409	0.73	Si II	1.9133 ± 0.00045
	3810.3911	1304.35	2.384	1.009	0.819	O I	1.9213 ± 0.00036
	4094.9756	1399.7	32.023	0.963	10.986	Si IV + O IV	1.9256 ± 0.00025
	4528.6998	1549.06	60.699	1.039	20.752	C IV	1.9235 ± 0.00043
	8198.6537	2798.75	89.8	0.27	30.65	Mg II	1.9294 ± 0.00039
	19225.3	6564.61	492.72	2.58	168.2	H α	1.92863 ± 0.00042

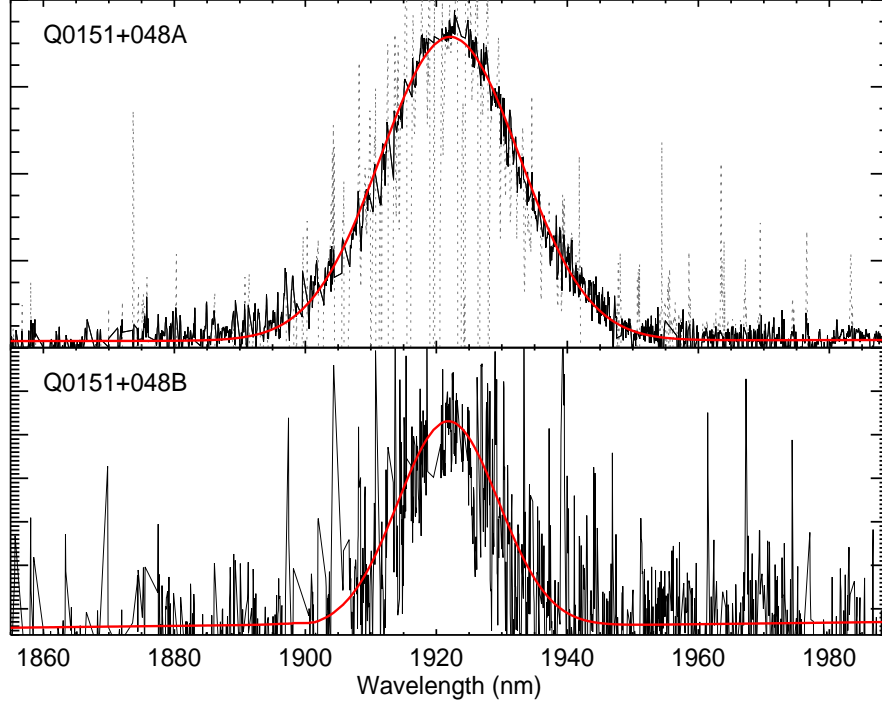


Figure 6.5: $H\alpha$ emission lines from Q0151+48 A & B after subtraction of the QSOs continuum. As described in the text only the good data intervals between the strong airglow residuals were used. The data, including airglow residuals are shown as a light dotted line, the solid black line is data with the not used parts removed. The solid red lines show the best gaussian profile fit to the used intervals. The inferred redshifts are $z_{H\alpha(A)} = 1.9294$ and $z_{H\alpha(B)} = 1.9286$.

emission lines, and one of the two main drivers for the X-shooter spectroscopy was to obtain systemic redshifts based on rest-frame optical emission lines. This is possible because of the X-shooter NIR arm. In Fig. 6.5 and 6.6 we show the $H\alpha$ and $H\beta$ emission lines respectively. For qB, the fainter of the two QSOs, only $H\alpha$ was detected. The blue part of the $H\alpha$ emission lines was affected by atmospheric absorption which corrected out well with the use of hot B-type main sequence stars.

In Table 6.2 we list observed and rest-frame parameters for the emission lines of the spectra of qA & qB. For the λ_{obs} and inferred z_{em} we use the same peak (or mode) definition as in Møller et al. (1998). It is seen that the inferred redshifts of qA range from 1.9034 to 1.92939 corresponding to a relative velocity of 2700 km s^{-1} vindicating our doubts about the previous redshift determination.

The narrow and unblended [O III] ($\lambda 5007$) emission line is presumed to trace the systemic (center of mass) redshift of the galaxy (Gaskell 1982; Vrtilik & Carleton 1985; McIntosh et al. 1999). Unfortunately the [O III] emission lines at our redshift are in a region of strong telluric absorption. The telluric absorption combined with the very

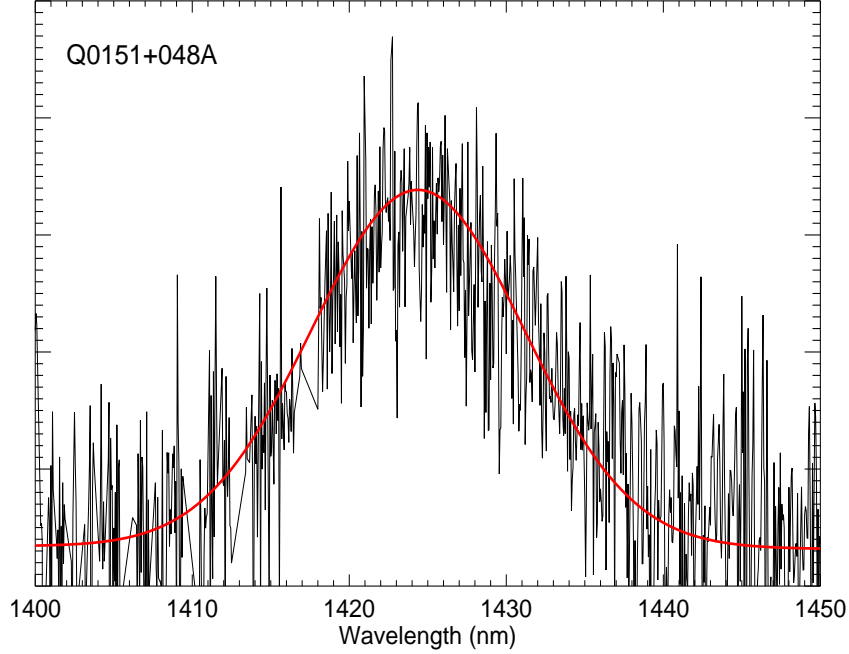


Figure 6.6: $H\beta$ emission line from Q0151+48 A after the continuum subtraction. The solid red line shows the best gaussian fit (see caption to Fig. 6.5 for details) providing an emission redshift of $z_{H\beta(A)} = 1.9292$.

narrow profile of [O III] makes it impossible to recover the lines via telluric correction. The $H\alpha$ line is in a part of the spectrum which is even stronger absorbed, but the width of the line is here helpful in recovering parts of the line. The $H\beta$ line is intrinsically fainter than the $H\alpha$ but in a region of less telluric absorption and therefore easier to recover.

In addition to the telluric absorption there are many strong sky emission lines present causing large residuals after sky subtraction. With the high resolution of X-shooter and for the wide $H\alpha$ and $H\beta$ lines this is not problematic as we simply masked out the affected intervals and used only the remaining sections (see Fig. 6.5). We subtracted continuum from the emission lines and then proceeded to fit a smooth profile to the central part of the lines using only the intervals not masked out. After the fit to the data we used the 1σ error spectrum to create 1,000 random realizations of errors, added those to the spectrum and repeated the process. In Table 6.2 we list the *standard deviation* of this distribution as statistical errors on the redshift. For qA we compute the optimally combined redshift as the weighted mean of the two lines and obtain $z_{em(A)} = 1.92930 \pm 0.00028$, for qB we only have $H\alpha$ and therefore simply adopt the redshift of that line as the systemic $z_{em(B)} = 1.92863 \pm 0.00042$. Redshifts determined from those lines are known to have an offset of only a few tens of km s^{-1} from the true systemic redshift of the QSO (Vanden Berk et al. 2001).

Table 6.3: Voigt profile fitting (best fits shown in Fig. 6.8) of metal ion transitions in the DLA using MIDAS FITLYMAN. Metal column densities were used to derive individual element abundances via comparison to the solar neighbourhood (Asplund et al. 2009). Multiplets were fitted with same column densities and Doppler width parameters. The Si II λ 1808, Si II λ 1611 and N V lines were not detected and for those we provide instead the 3σ column density upper limits.

λ_{obs}	EW_{obs}	σ_{EW}	EW_{rest}	ID	z_{abs}	$\log N$ cm^{-2}	b_{turb} km s^{-1}	[X/H]
3634.960	N V (1238)	1.93421	< 12.71	18.8	
3646.650	N V (1242)	1.93421	< 12.71	18.8	
3820.900	0.681	0.029	0.232	O I (1302)	1.93426	> 14.97	20.1 ± 2.1	[O/H] > -2.10
3915.800	0.724	0.037	0.247	C II (1334)	1.93421	> 14.46	18.8 ± 0.2	[C/H] > -2.30
3919.150	0.021	...	0.007	C II* (1335.7)	1.93414	≈ 12.85	18.8 ± 0.2	
4542.600	0.928	0.040	0.316	C IV (1548)	1.93413	> 14.56	18.9 ± 0.4	
4550.155	0.813	0.035	0.277	C IV (1550)	1.93413	> 14.56	18.9 ± 0.4	
3492.924	0.790	0.023	...	Si II (1190)	1.93421	13.92^a	18.8	
3501.357	0.362	0.014	0.123	Si II (1193)	1.93421	$\geq 13.92 \pm 0.03$	18.6 ± 0.4	
3698.343	0.767	0.034	0.261	Si II (1260)	1.93421	$\geq 13.92 \pm 0.03$	18.6 ± 0.4	
3827.300	0.265	0.030	0.100	Si II (1304)	1.93421	$\geq 13.92 \pm 0.03$	18.6 ± 0.4	
4479.678	0.459	0.026	0.156	Si II (1526)	1.93421	$\geq 13.92 \pm 0.03$	18.6 ± 0.4	
5305.090	Si II (1808)	1.93421	< 14.46	18.8	$-1.93 \leq [\text{Si}/\text{H}] < -1.39$
3540.130	0.804	0.030	0.270	Si III (1206)	1.93421	> 13.85	18.8 ± 0.3	
4089.480	0.640	0.065	0.218	Si IV (1393)	1.93415	> 13.75	19.2 ± 0.7	
4115.933	0.517	0.035	0.180	Si IV (1402)	1.93415	> 13.75	19.2 ± 0.7	
3359.492	0.103	0.024	0.035	Fe II (1144)	1.93421	$\geq 13.60 \pm 0.02$	18.8 ± 0.3	$-2.24 \leq [\text{Fe}/\text{H}] < -1.17$
4719.540	0.144	0.035	0.049	Fe II (1608)	1.93421	$\geq 13.60 \pm 0.02$	18.8 ± 0.3	

^aSi II λ 1190 line is blended with a Ly α forest line and therefore fit is poor. We fixed the column density value to fit the profile.

λ_{obs}	EW_{obs}	σ_{EW}	EW_{rest}	ID	z_{abs}	$\log N$ cm^{-2}	b_{turb} km s^{-1}	[X/H]
4727.600	Fe II (1611)	1.93421	< 14.67	18.8	
6967.170	0.138	0.010	0.047	Fe II (2374)	1.93421	$\geq 13.60 \pm 0.02$	18.8 ± 0.3	
6991.530	0.883	0.010	0.301	Fe II (2382)	1.93421	$\geq 13.60 \pm 0.02$	18.8 ± 0.3	
7589.770	0.410	0.013	0.140	Fe II (2586)	1.93421	$\geq 13.60 \pm 0.02$	18.8 ± 0.3	
4902.464	0.321	0.041	0.110	Al II (1670)	1.93423	$\geq 12.46 \pm 0.02$	18.8 ± 0.2	[Al/H] ≥ -2.33
5442.160	0.09	0.023	0.030	Al III (1854)	1.93423	12.15 ± 0.07	18.8 ± 0.2	
5465.850	0.060	0.030	0.020	Al III (1862)	1.93423	12.15 ± 0.07	18.8 ± 0.2	
8202.670	1.611	0.010	0.550	Mg II (2796)	1.93421	> 13.79	18.8 ± 0.3	[Mg/H] > -2.05
8223.730	1.380	0.011	0.470	Mg II (2802)	1.93421	> 13.79	18.8 ± 0.3	
8368.740	0.030	0.010	0.097	Mg I (2852)	1.93421	≈ 11.20	18.8 ± 0.2	

Extended emission in the X-shooter spectrum

In Fig. 6.1 it is seen that the X-shooter slit follows a line across the Ly α emitter more closely aligned with its minor axis. We would still expect to see some extended emission, but not extending as far away as for the NOT spectrum. To confirm this expectation we therefore also performed SPSF subtraction on the X-shooter spectrum. The result is shown in Fig. 6.7, where we have marked the redshifts of both QSOs relative to that of the DLA. SPSF subtraction of qA was only performed in the range -1300 to -200 km s $^{-1}$ (relative to the DLA redshift). This procedure left the flux from the host galaxy inside the DLA trough and clearly shows that the damped line does not at any point go to zero flux. Also it is seen that the host is precisely lined up with the position of qA. The extended Ly α is also here seen to be asymmetric (consistent with Fig. 6.1) and to stretch about half way towards qB. The emission is here offset 750 km s $^{-1}$ from the DLA, it has a FWHM of 200 km s $^{-1}$ and there is no obvious evidence for a rotation curve along this axis. There does seem to be marginal evidence for a double-emission profile with a splitting of 140 km s $^{-1}$ but the S/N of the data is too low to make any conclusive statements about this.

Double-peaked emission line profiles from Ly α were predicted by Neufeld (1990) from a static, un-absorbing, opaque scattering medium. Verhamme et al. (2006) obtained the same result using a 3D Ly α radiative transfer code with a Monte-Carlo fitting method, and subsequently used the code to fit Ly α lines in a sample of high redshift Lyman-break galaxies (LBGs; Verhamme et al. 2008). In this publication, two LBGs had double emission line peaks and were best fitted with a dust-free, nearly static medium. Thus, if it can be confirmed that the emission line profile is indeed double-peaked then this could be indicating that the blob is static rather than infalling or the signature of an expanding wind.

6.4 ABSORPTION LINE ANALYSIS

The X-shooter absorption line spectra are plotted in Fig. 6.14. The resolution of X-shooter is high enough to allow absorption line profile fitting and good column density determination of lines that are not heavily saturated. Our second main driver for the X-shooter spectroscopy was therefore to obtain element column densities and abundances for the DLA system in qA.

Element abundances are important for our understanding of this system, first because it is known that the DLA metallicity are related to the mass and luminosity of the DLA galaxy (Wolfe & Prochaska 1998; Møller et al. 2004; Ledoux et al. 2006; Fynbo et al. 2008d; Prochaska et al. 2008c) second because it can provide us with limits on the QSO/DLA distance (§6.4.2) which are needed in order to determine the arrangement of the QSO/DLA/Ly α emitter system in 3D space rather than redshift/space. In addition several systems at lower redshifts are also seen in the X-shooter spectra and for

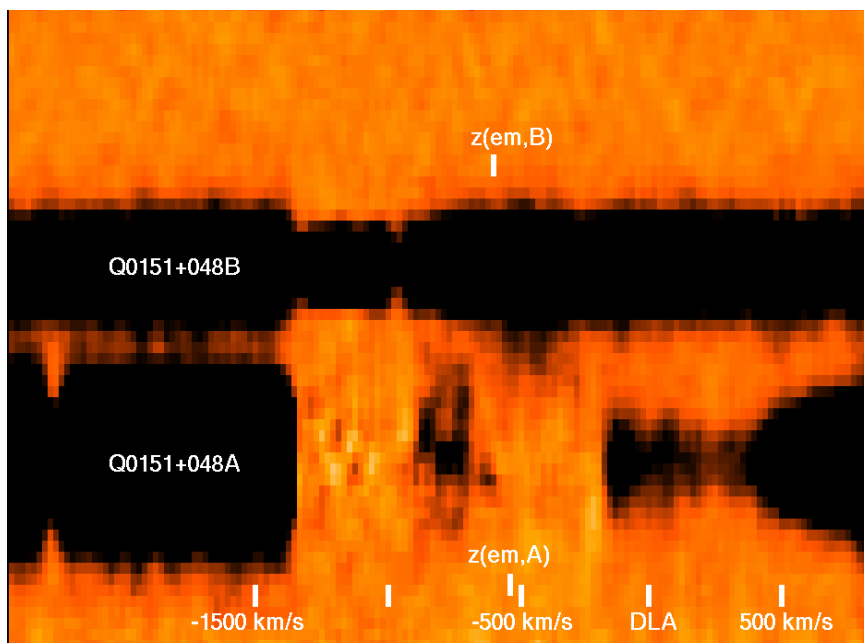


Figure 6.7: (Credit:Palle Møller) 2D X-shooter spectrum with the slit placed on both QSOs. Short wavelengths are to the left. The centre of the DLA line is marked and chosen as fiducial zero velocity. SPSF subtraction was done for the qA spectrum in the range -1300 to -200 km s $^{-1}$. There is a clear extended residual seen which we interpret as Ly α emission at -750 km s $^{-1}$. The redshifts of both QSOs based on H α and H β are also marked.

completeness we also identify those (§6.4.3).

6.4.1 ABSORPTION LINES OF THE DLA SYSTEM

Møller et al. (1998) reported an H I column density of the DLA of $\log \text{NH I} = 20.36$. In our higher quality data we determine a column of $\log \text{NH I} = 20.34 \pm 0.02$ cm $^{-2}$ at $z = 1.93421 \pm 0.00001$ from the fit which is overplotted in red on the spectrum in Fig. 6.14. At the same redshift we also identify several metal lines in the qA spectrum, of which none are seen in the spectrum of qB. We identify lines from O I, C II, C IV, Si II, Si III, Si IV, Fe II, Al II and Mg II. Equivalent widths and corresponding 1 sigma errors of those lines are listed in Table 6.3.

In order to determine accurate column densities we used the Voigt profile fitting FITLYMAN package in MIDAS (Fontana & Ballester 1995). We adopted the list of atomic data, laboratory wavelengths and oscillator strength for each transition from Morton (2003). FITLYMAN finds the best global fit using a χ^2 minimization algorithm which includes the spectral resolution and returns best fit parameters for redshift, column density and Doppler turbulent broadening as well as errors on each quantity. It may be used to fit single lines one at a time, or one may (optionally) choose to fit several lines with the same parameters (one may e.g. insist that all the chosen lines have the same

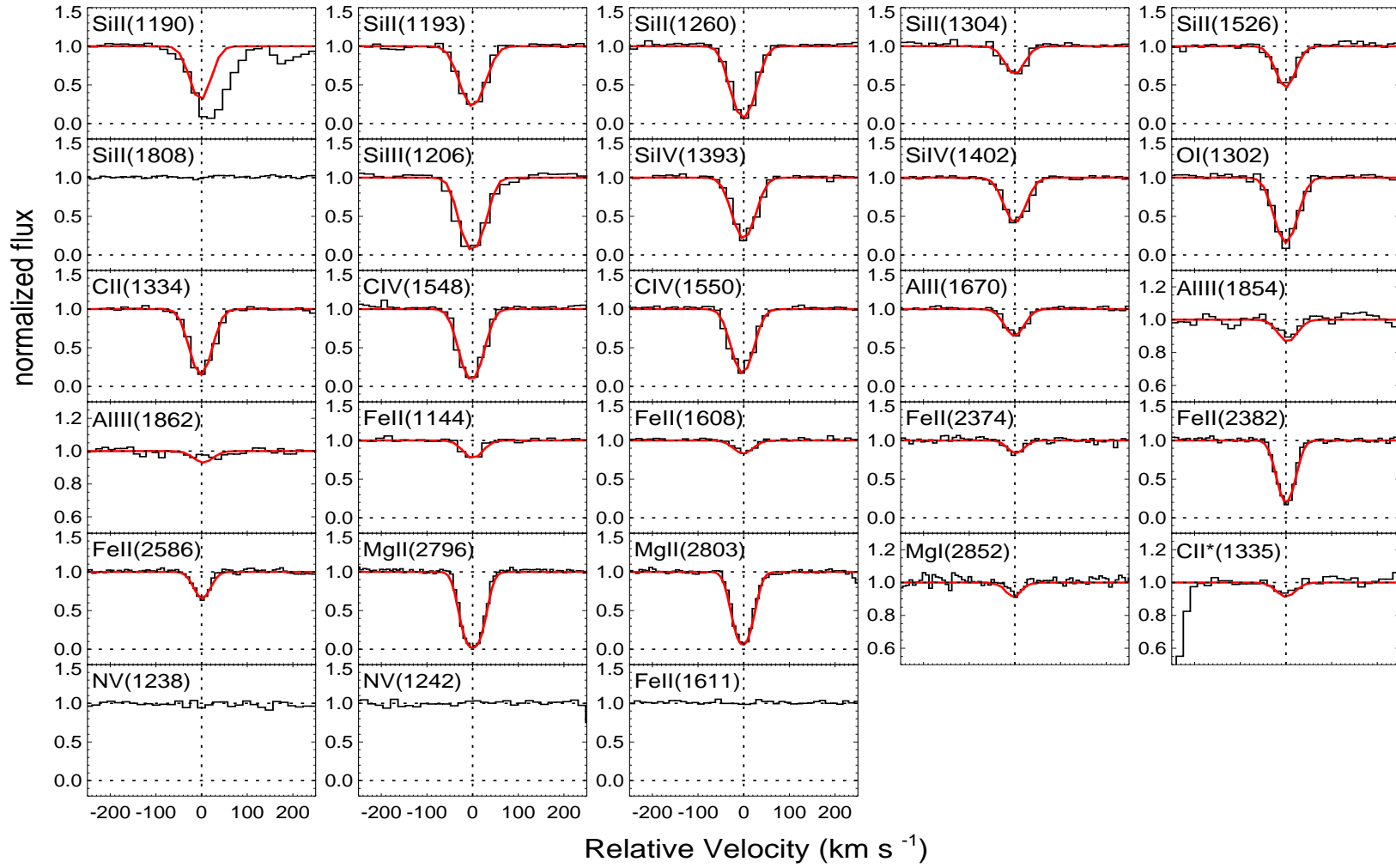


Figure 6.8: Voigt profile fits to the metal absorption lines of the damped absorber in the spectrum of qA. The red lines show the best fit in case of detections and the 3σ upper limit in case of non-detections (Si II λ 1808, Fe II λ 1611 and NV). The vertical dashed black line is our adopted zero velocity corresponding to $z = 1.93421$. The derived absorber parameters are provided in Table 6.3.

redshift or turbulent broadening).

We employed FITLYMAN in two ways. First we chose to fit all lines with the same redshift and turbulent broadening. The resulting fits were mostly very good, but for a few ions (e.g. O I and Si IV) the fits were slightly offset from the data. We therefore chose to fit each ionic species independently allowing them to have different redshifts and turbulent broadening. The resulting column densities did not change significantly from one procedure to the other so our results are not depending on this choice. The FITLYMAN output parameters are listed in Table 6.3 and the resulting fits (red) are shown overlaid on the data in Fig. 6.8. Note that the Si II λ 1190 line is in the Lyman forest and clearly blended with an intervening line. That line was not used for the fit, but the predicted line is plotted for completeness. In Table 6.3, we consider all column density measurements as lower limits due to the likelihood of hidden saturation as the absorption profiles could be made of multiple narrow components. We note however that in the cases of Fe II and Fe II hidden saturation can be present but is less of an issue because weaker transition lines are observed. Moreover, from the non-detection of Si II λ 1808 and Fe II λ 1611 we can infer column density upper limits (see Table 6.3) and hence constrain the abundances of these two elements to lie within conservative albeit relatively narrow ranges.

In the last column of Table 6.3 we adopted the solar abundances from Asplund et al. (2009) to obtain metallicities relative to solar. We find a silicon abundance of $-1.93 \leq [\text{Si}/\text{H}] < -1.39$ which is commonly used to define the DLA system metallicity, suggesting a metal-poor system (see Fig. 6.10, Ledoux et al. 2006; Prochaska et al. 2008b). We determine a ΔV of 64 km s^{-1} as defined in Ledoux et al. (2006) using Fe II λ 2382 which, after correction for the spectral resolution of 27 km s^{-1} , gives 58 km s^{-1} . In Fig. 6.10 we plot this together with the 35 DLA's in the redshift range 1.7 to 2.43 taken from Ledoux et al. (2006).

It is seen that the point follows the general metallicity/velocity width relation at $z = 2$, but that it falls within the 10–15% lowest metallicities, and that it lies on the high ΔV side of the bisector fit (in the widest 15%).

6.4.2 PHOTO-IONIZATION MODEL OF THE DLA

The well determined column densities of several ionization stages of the same elements makes it possible to make a simple photo-ionization model of the absorbing cloud. We know that the cloud is situated between us and qA, and it could in principle be lying very close to qA. The main question we seek answered is: "What is the minimum distance that the DLA cloud must be from Q0151+048A?" For this we follow an approach similar to that used in Williams & Weymann (1976) and perform Cloudy photo-ionization model with version 07.02, described by Ferland et al. (1998). The Cloudy calculations were based on the following assumptions. The cloud is a plane-parallel

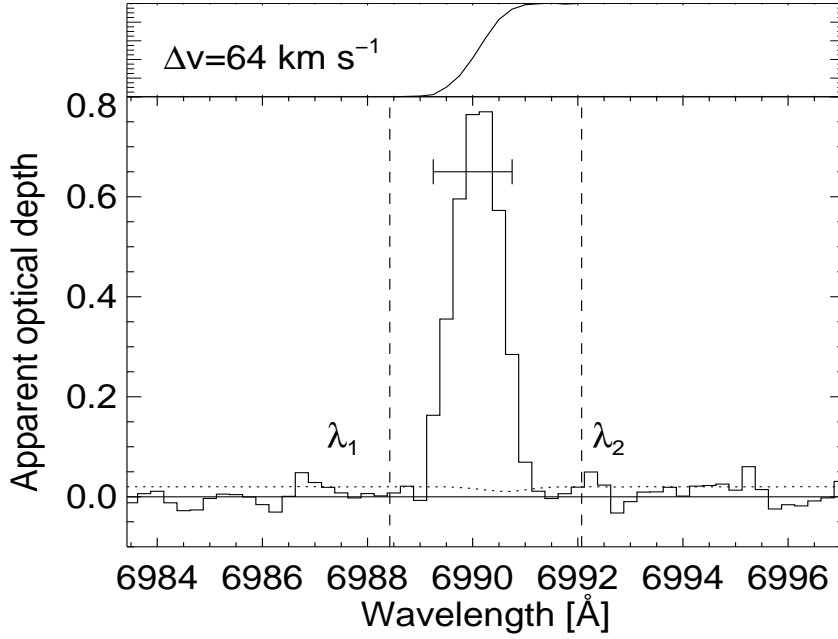


Figure 6.9: (Credit: Johan Fynbo) *Determination of ΔV as defined in Ledoux et al. (2006). The ΔV measured must be corrected for the spectral resolution of 27 km s^{-1} .*

slab of gas with total neutral hydrogen column density $\log \text{NH I} = 20.34$, metallicity 1/100th of solar, and solar abundance ratios. The radiation field is composed of the Cosmic Microwave Background at $z = 1.934$ and, towards one side of the cloud, the radiation spectrum of a typical AGN with specific luminosity at the Lyman limit $L_{\nu_0} = 30.9 \text{ erg s}^{-1} \text{ Hz}^{-1}$. The latter value has been determined using the flux calibrated spectrum obtained from NOT during August 2008 and a best matched spectral slope of -1.76 between rest frame 750 and 1600 Å (see Telfer et al. (2002)). This typical spectral slope was used because of the uncertainties present in the flux calibration of the NOT spectrum. We performed a series of photo-ionization equilibrium calculations for a range of QSO-absorbing cloud distances. The calculations show that the temperature throughout the region producing the C II ions does not differ much from 10^4 K , and that collisions with electrons are the dominant excitation mechanism to populate the upper fine-structure energy level of the C II ground state (see also Williams & Weymann 1976). The non-detection of the C II* $\lambda 1335.7$ line can therefore be used to set an upper limit on the electronic density n_e . The absorption line profile of the system spans a total width ($2 \times \text{FWHM}$) of 90 km s^{-1} , and the S/N ratio per pixel of the spectrum at the expected location of the C II* $\lambda 1335.7$ line is 56. This results in a 1σ EW (in the observer's frame) of 0.021 Å and, based on the optically thin approximation, a C II* 3σ column density upper limit of 12.85. From Fig. 4 of (Silva & Viegas 2002), we find that $n_e \sim n_{\text{H}} \lesssim 2 \text{ cm}^{-3}$. Ionic column densities predicted by the model for such particle densities are plotted as a function of QSO-absorbing cloud distances in Fig. 6.11. The

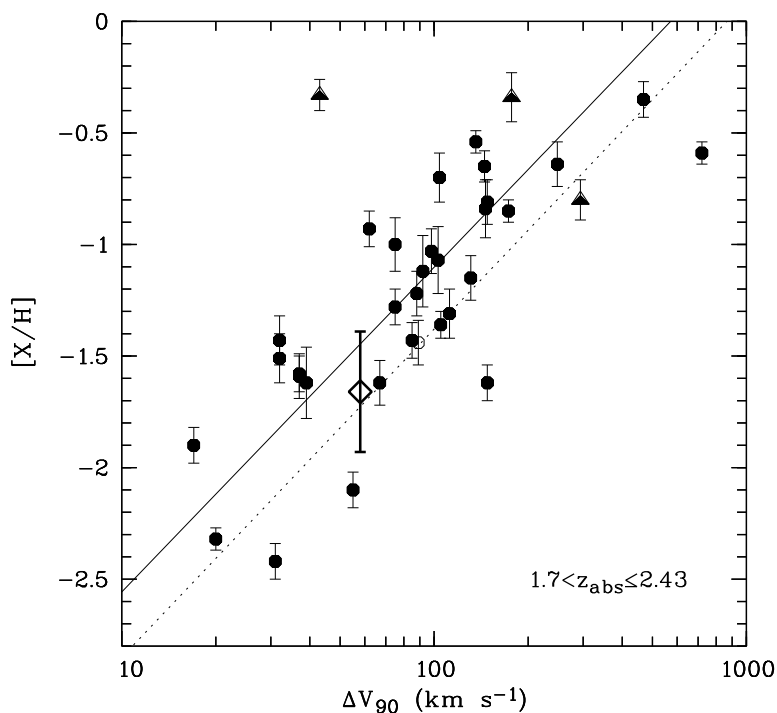


Figure 6.10: Average metallicity vs. velocity width of 35 DLA low ionization line profiles from Ledoux et al. (2006). The solid line represents the linear least square bisector fit. The DLA from the present work is marked by the large diamond. For details on this figure see Ledoux et al. (2006).

column densities measured observationally, in particular those of Si III, Si IV and C IV, are reproduced quite well (see Fig. 6.11) for a distance of ~ 190 kpc. Since the particle density can be lower, this distance estimate represents a lower limit on the actual distance of the absorbing cloud from the QSO, implying that the two objects are not directly physically associated.

6.4.3 INTERVENING ABSORBERS

The primary purpose of the X-shooter spectroscopy was to characterize the DLA and the QSO. In addition to the DLA four other C IV absorption systems at redshifts 1.2939, 1.3360, 1.5613, and 1.6192 were identified in the spectra. All four C IV doublets are seen in both spectra (as seen in Fig. 6.14) indicating that C IV absorbers at those redshifts typically have sizes larger than 30 kpc and covering factors close to unity. This is consistent with previous studies (Rauch et al. 2001; Ellison et al. 2004). One of the absorbers ($z = 1.6192$) is also seen as Si IV absorber in the sightline towards qA, but not towards qB, which might indicate that Si IV absorbers extend to smaller distances than C IV absorbers.

It is striking in Fig. 6.14 to see the one-to-one correspondence between the lines in the Lyman forest of the two QSOs (see Smette et al. 1992, 1995). The few lines which

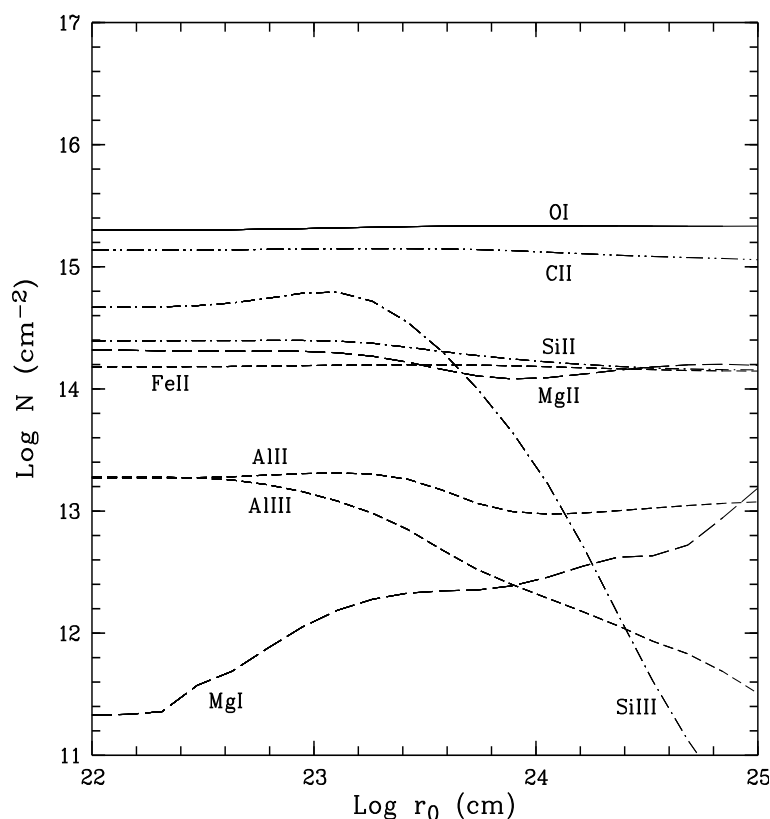


Figure 6.11: (Credit: Cédric Ledoux) *Cloudy photo-ionization model calculations for a $\log N_{\text{HI}} = 20.34$ cloud at $z_{\text{abs}} = 1.934$ illuminated on one side by Q 0151+048A (see text for details). Predicted ionic column densities are plotted for different QSO-absorbing cloud distances.*

are not reproduced in the qB spectrum all belong to the DLA system.

6.5 DISCUSSION: WHAT IS THE Q 0151+048A&B/DLA/LY α -BLOB SYSTEM?

This complex system has been the target of several studies because it brings together several types of objects which at this redshift are usually seen only separately. The mix of objects has made the interpretation difficult, yet at the same time the interaction between the objects allow us to extract information which is not normally accessible and can only be obtained for this unique system. Earlier interpretations were hampered by the lack of certain vital information but the new X-shooter data have now allowed us a more complete view of this system.

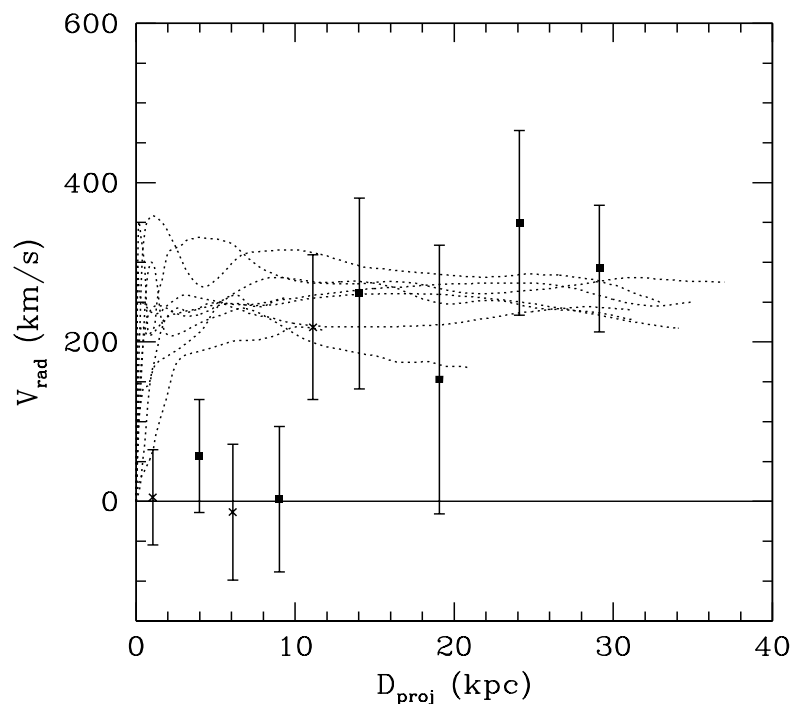


Figure 6.12: (Credit: Palle Møller) Rotation curves of large spiral galaxies at low redshift overplotted on the Ly α rotation curve inferred from Fig. 6.3.

6.5.1 GEOMETRY OF THE SYSTEM

Fig. 6.7 summarizes what we know about the redshifts of the components. The issue with the redshifts of the QSOs has been resolved causing qA to be moved 740 km s^{-1} towards higher redshift. This means that qA is now offset only 100 km s^{-1} from the Ly α emission (at the position of qA) in the NOT spectrum, and 200 km s^{-1} in the X-shooter spectrum. The difference is presumably arising from the different way the velocity field of the emitter has been averaged over the slit in the two observations. The velocity offset between the DLA and the Ly α blob is much larger (600 km s^{-1} and 750 km s^{-1}). All taken together the logical conclusion is that the blob is associated with qA and its host galaxy rather than with the DLA as it was previously thought. The end-to-end size of the blob along its major axis is about 5 arcseconds corresponding to 42 kpc, and 28 kpc along its minor axis while the projected distance from qA to qB is 27.7 kpc. Based on the ionization state of the gas we find that the DLA cloud is placed along our line of sight towards qA at a minimum distance of 190 kpc.

Table 6.4: *BH and total masses of the QSOs. Masses are provided in logarithmic scale.*

QSO	FWHM H β km s $^{-1}$	FWHM Mg II km s $^{-1}$	FWHM C IV km s $^{-1}$	$\lambda L_{\lambda}(5100\text{\AA})$ 10 44 erg s $^{-1}$	$\lambda L_{\lambda}(3000\text{\AA})$ 10 44 erg s $^{-1}$	$\lambda L_{\lambda}(1450\text{\AA})$ 10 44 erg s $^{-1}$	M_{BH}/M_{\odot} (H β)	M_{BH}/M_{\odot} (Mg II)	M_{BH}/M_{\odot} (C IV)	M_{tot}/M_{\odot}
qA	3577 \pm 150	2790 \pm 110	3875 \pm 130	170	2100	1400	9.12	9.37	9.5	13.74
qB	...	1840 \pm 130	2480 \pm 110	5.8	105	67	...	8.38	8.36	13.13

6.5.2 DYNAMICAL STATE OF THE SYSTEM

The systemic redshift difference between qA and qB is very small (60 km s^{-1} and consistent with zero to within less than 2σ) suggesting that their relative movement is in the plane of the sky. This would imply that their projected separation is their physical separation. The Ly α blob has a velocity gradient along its major axis and through qA. This may be caused by infalling gas which is being ionized where it falls into the ionizing cones of qA as it was described in the models by Weidinger et al. (2004, 2005) but it could also be the signature of a rotating disk. To test the latter possibility we have combined the data points on both sides of qA in Fig.6.3 into a single rotation curve along the major axis. In Fig. 6.12 we overplot several spiral galaxy rotation curves from Sofue et al. (2010) on those points. It is seen that for large radii there is a very good resemblance. At small radii Sofue et al. (2010) report that a very steep nuclear rise is a generic feature of spiral galaxies. This steep rise is not seen in our data but our resolution along the slit corresponds to a smoothing length of 13 kpc so the current data are indeed consistent with the rotation curve of a large spiral galaxy in today's universe. A spectrum with better spatial resolution, and along the major axis of the blob, would be needed to discriminate between the two possibilities.

The DLA absorber is a separate object which is moving towards the host galaxy with a relative velocity of 600 km s^{-1} .

6.5.3 BLACK HOLE AND DARK MATTER HALO MASSES

The mass of the DM halo of the QSO Q1205-30 at $z = 3.04$ was determined from a model of the gas falling into its potential well and was found to be in the range $\log M_{\text{tot}}/M_{\odot} = 12.3 - 12.8$ (Weidinger et al. 2004). As discussed in §6.5.2 it is not clear in our case if the dynamical signature of the gas is caused by infall or rotation so we shall use a different method to determine the DM halo mass.

First we derive Black hole (BH) masses following Vestergaard & Peterson (2006, formulae 5 & 7) and use the relation between BH mass, H β and C IV emission lines width and the continuum luminosity at 5100\AA and 1450\AA rest wavelength. We also estimated BH mass using the relation between Mg II and continuum luminosity at rest-frame 3000\AA (Vestergaard & Osmer 2009, formula 1). For the line widths we use the FWHM of the fitted gaussian for each emission line and we list those in Table 6.4. We corrected the FWHM of each line for spectral resolution as described in Peterson et al. (2004). For qB we do not have the H β emission line width, therefore, we have no mass estimation from that line.

To obtain the continuum luminosity at 5100 , 3000 and 1450\AA we use the H -band magnitudes of the two QSOs from Warren et al. (2001) and I and B -band magnitudes from Fynbo et al. (2000). We also checked for line contamination in these band and for this we used composite spectrum from Vanden Berk et al. (2001). We subtracted

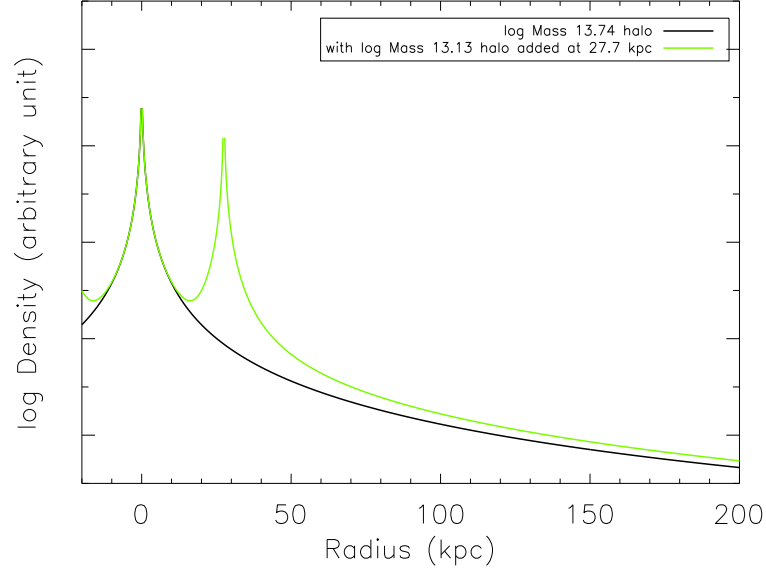


Figure 6.13: (Credit: Kim Nilsson) *Density profile of the two DM halos around qA and qB assuming that they have standard NFW profiles.*

emission line components from the spectrum and found the contamination to be 14, 15 and 7% in H , I and B bands respectively. After subtracting the contamination the resulting BH masses are listed in Table 6.4. It has recently been established that BH mass correlates well with the underlying total gravitational mass (presumably dominated by the dark matter) of the host halo (Bandara et al. 2009). We use this correlation to finally obtain the corresponding halo mass of each QSO by using their mean BH mass and those are also listed in Table 6.4.

In Fig. 6.13 we plot the density profile of the two halos assuming that they have NFW profiles (Navarro et al. 1997) and that their projected distance (27.7 kpc) is also their real proper distance as argued in §6.5.2. It is seen that qB is inside the halo of qA, but that it is still clearly defined as a separate sub-halo.

6.6 CONCLUSIONS

In this paper we have presented spectra of the two QSOs Q 0151+048A and Q 0151+048B as well as of a $\text{Ly}\alpha$ blob at the same position. We obtained spectra of the blob at two different position angles. QSO redshifts determined from $\text{H}\beta$ and $\text{H}\alpha$ change the previously reported redshifts by an additional 740 km s^{-1} . This is in addition to the much smaller corrections previously suggested by Tytler & Fan (1992). Our first conclusion is that the corrections to QSO redshifts based on rest-frame UV lines can be much larger than previously thought and that other QSO absorption systems of this kind (i.e. with

large inverted redshift offsets) presumably will turn out to find the same resolution.

The new redshift of qA means that the Ly α blob is now more likely belonging to this QSO. We determine a Black Hole mass of qA of $10^{9.33} M_{\odot}$ and a corresponding DM halo mass of $10^{13.74} M_{\odot}$. The Ly α blob is sitting in the potential well of this halo. The blob has a size of 42 by 28 kpc, it has a clear signature of a strong velocity gradient along its major axis which is consistent with the rotation curve of a large disk galaxy in today's universe but may alternatively be caused by in- or out-flow. In the X-shooter spectrum along the minor axis which has higher spatial resolution there is no velocity gradient of the blob, but there is a hint that the Ly α emission may be double peaked.

The metallicity of the DLA inferred from the X-shooter medium resolution spectrum is $-1.93 \leq [\text{Si}/\text{H}] < -1.39$, in the lowest 15% of DLAs at this redshift. This stands in contrast to the recent result by Ellison et al. (2010) who reported that PDLAs in general have higher metallicity than intervening DLAs.

The DLA falls nicely on the predicted relation of velocity-width vs metallicity Ledoux et al. (2006) even though it is somewhat broader than DLAs of similar metallicity, indicating that it probably has a slightly more complex internal velocity structure than other low metallicity DLAs. We speculate that the DLA is one of many small metal-poor clouds infalling onto the dark matter halo hosting the two QSOs.

Based on the constraining non-detection of C II* we model the physical state of the DLA and find that it must be at minimum 190 kpc from qA. The DLA is therefore not associated with the Ly α blob as previously thought but is a separate object.

We briefly report the detection of four intervening C IV systems seen in both sightlines of which one system has Si IV absorption seen only in a single sightline. Also we see rich Lyman forests with near identical absorption signatures. This QSO pair is therefore well suited for a multi-sightline study of both Lyman forest absorbers and of intervening metal absorbers.

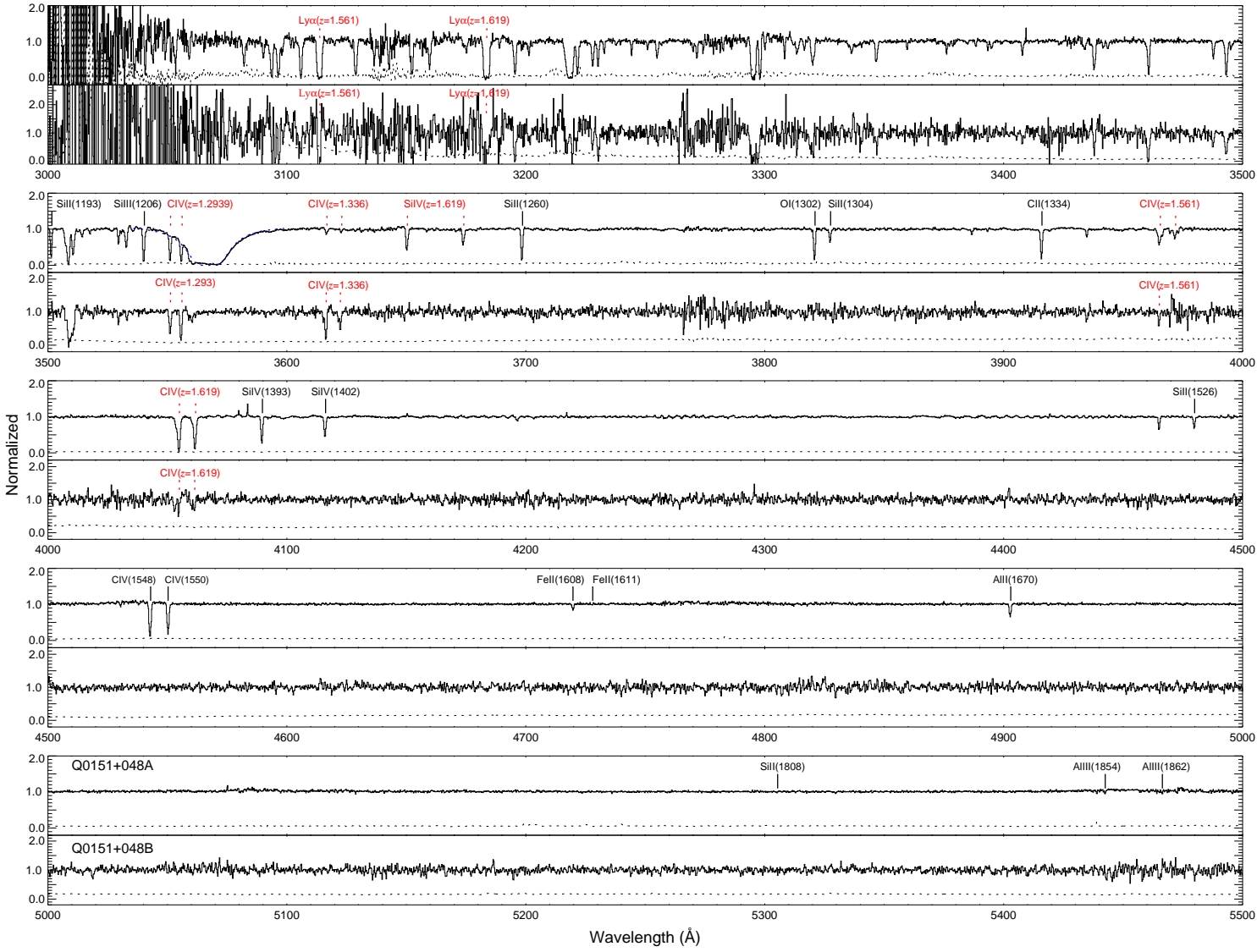


Figure 6.14: X-shooter UVB-arm spectra from 3000 – 5500 Å of qA in top panel and qB in bottom panel in each grid. Solid black lines with corresponding IDs in qA spectrum are from the DLA. The dashed blue line in qA spectrum shows the Voigt profile fit to the DLA with an derived column density of $\log \text{NH I} = 20.34 \pm 0.02$ for a redshift of 1.93421. Dashed red lines in both spectra are from the intervening absorbers with their corresponding IDs. The dotted line represents 1σ error on each spectra.

7

CONCLUSIONS AND FUTURE PROSPECTS

7.1 CONCLUSIONS

In this thesis I have performed studies of the dust outside the Local Group and on the origin and evolution of dust in the early Universe using GRB afterglows as probes. The study of a QSO pair together with a Ly α blob and a DLA at similar redshift was also conducted.

Dust formation in the local Universe mainly takes place in evolved AGB stars (Dwek 1998; Tielens 1998) which require ~ 1 Gyr to produce dust. Large dust masses ($> 10^8 M_{\odot}$) are discovered in quasar host galaxies at $z \sim 6$ from mm and sub-mm observations (e.g., Wang et al. 2008). To explain the huge amounts of dust inferred from observations of high redshift objects, different sources of dust have been invoked, such as SNe or QSO winds. Theoretical studies have long suggested that dust can condense in the ejecta from core collapse SNe (Gehrz 1989; Dwek et al. 2007). A small amount of dust from supernovae is sufficient to initiate grain growth in the ISM. Predictions for the extinction curve, produced due to dust condensation in quasar outflow winds (Elvis et al. 2002), have not been yet developed.

Theoretically, several authors have proposed that the ejecta of core-collapse SNe (and also pair instability SNe, PISNe) are efficient dust formation sites at high redshift (Todini & Ferrara 2001; Bianchi & Schneider 2007; Hirashita et al. 2008). These models predict both the core-collapse SNe/PISNe extinction curves and the masses of dust produced by each class of SN. The signature of SN-synthesized dust has been claimed for a BAL QSO, SDSS J1048+46, at $z = 6.2$ (Maiolino et al. 2004; but see also Gallerani et al. 2010). The observed extinction curve is in agreement with the core-collapse SN-origin curve proposed by Todini & Ferrara (2001). In a sample of 33 quasars Gallerani et al. (2010) found that the seven reddened quasars are best fit with the extinction curves defined by Hirashita et al. (2008), mainly the PISNe extinction curve. Gallerani et al. (2010) found no strong evidence for core-collapse SN-origin extinction curves defined by Todini & Ferrara (2001); Bianchi & Schneider (2007). Previously Stratta et al. (2007) and Perley et al. (2010) claimed evidence for a SN-origin extinction curve, similar to

the Maiolino et al. (2004) extinction curve, in GRB 050904 and 071025 respectively. In this thesis the result claimed by Stratta et al. (2007) was revisited and ruled out with a detailed analysis.

The thesis focuses on the origin of dust and the expected transition in dust producers at $z \gtrsim 5$. The claimed evidence for a SN-origin extinction curve in the host galaxy of GRB 050904 is addressed by multi-epoch SED analysis. The claim largely relies on the UKIRT Z band photometry at 0.47 days. It is found that the photometry of this band has calibration difficulties. The intrinsic SED of the afterglow is derived at 0.47, 1.25 and 3.4 days after the burst. Since the z' -band observations are strongly affected by Ly α absorption, the flux densities at $\lambda_{\text{rest}} = 1250 \text{ \AA}$ were computed from the observed counts at all epochs. No evidence for dust extinction is found in GRB 050904 ($z = 6.295$) at any epoch. In particular at 1.25 days, significant dust extinction can be ruled out. The afterglow SED is consistent with a single power-law from the X-ray to the NIR.

Gallerani et al. (2010) modelled the spectrum of the BAL QSO SDSS J1048+46 again and found that for this particular case differences from the other PISNe cases are not large. After this analysis, the only strong observational evidence in the literature is for GRB 071025 (Perley et al. 2010). That claim is strongly dependent on the H -band observation. The issue of H -band suppression cannot be revised because this case suffer from the lack of spectroscopy which could show the intrinsic continuum.

Observationally, large dust masses at high redshift are seen in high redshift quasars. However quasar host galaxies are not representative of the dominant star forming populations. It is known that GRBs occur in young star forming galaxies. To explore dust in star forming regions, the thesis discusses the analysis of all $z > 6$ GRB afterglows. GRB 050904 ($z = 6.295$), GRB 080913 ($z = 6.695$) and GRB 090423 ($z = 8.2$) are reinvestigated to probe stellar environments and interstellar dust at high redshift. Like GRB 050904 (see above), GRB 090423 is also consistent with no dust reddening. The data are well fitted with a broken power-law and no dust reddening at all epochs. A small amount of dust extinction with $A_V = 0.12 \pm 0.03$ is found from the afterglow SED fit of GRB 080913, dependent on the origin of the X-ray emission. A comparison with the larger sample of lower redshift GRBs show that there seems to be a decrease in the dust content in star forming environments above $z \gtrsim 4$, despite the low number statistics. This result is also consistent with the studies of other star forming environments at high redshift, i.e. LAEs and LBGs (Verma et al. 2007; Lai et al. 2007; Finkelstein et al. 2009; Douglas et al. 2010). The high redshift GRB sample might be biased towards low extinction sightlines. High redshift GRBs are observed farther into the restframe UV where extinction is more severe, possibly preventing more extinguished afterglows from being detected. However the comparison with low redshift GRBs shows that even high redshift GRBs with moderate extinction, $A_V = 0.3$, could be observed. Ultimately, the issues of bias and low number statistics are clearly important and they cannot be resolved them with this sample. In future, observation of more high redshift GRB after-

glows will allow me to say more about dust in high redshift star forming environments. Again, in no case do I find evidence for a SN-origin extinction curve.

GRB afterglows are excellent and sensitive probes of gas and dust in star-forming galaxies at all cosmic epochs. GRBs shine through the host galaxy, which leaves imprints from its ISM on the afterglow spectrum. This thesis has covered multi wavelength observations and SED analysis of GRB afterglows from the ($z = 0.1257$) to high ($z = 8.2$) redshift Universe. The absolute dust extinction curves in distant galaxies have been studied for the first time using GRB afterglow spectroscopy in a sample of 41 GRB afterglows. The thesis presents the largest sample of extinction curves outside the Local Group.

The SEDs of GRB afterglows are universally well described by a single or broken power-law with absorption in the soft X-rays and dust extinction at UV/optical wavelength. A significant conclusion of my study is that a cooling break occurs between the optical and X-ray wavelengths in about half of the GRB sample. The mean spectral change is $\Delta\beta = 0.51$ with a very small scatter of 0.02 for 95% of the spectral break cases. This result is in remarkable agreement with the prediction of the synchrotron emission model given by Sari et al. (1998). The spectral change in future studies could therefore reasonably be fixed to 0.5 for GRB afterglow SED analysis. This should make the SED analysis process more robust in future by removing one extra degree of freedom in deriving extinction curves. The synchrotron emission model has been accepted by the GRB community and $\Delta\beta = 0.5$ used without substantial observational confirmation. This thesis puts the model to a test and confirms its consistency.

63% of the bursts in the sample are well-fit with the SMC-type extinction curve with moderate extinction values of $\langle A_V \rangle = 0.24$ mag with a standard deviation of 0.14 mag. This two thirds of the sample have extinction values with A_V ranging from 0.06 ± 0.02 to 0.65 ± 0.04 mag. So far the 2175 Å extinction bump has been seen in the spectra of four GRB afterglows, (three observed with the VLT and one with Keck). The bump cases comprise 7% of the full spectroscopic sample and 9% of the extinguished sample, with all bump cases having $A_V > 1.0$ mag (including GRB 080607, which is strictly outside the VLT sample). The bump region, however, is not covered in twelve cases. The sample is based on good-quality optical spectra and therefore, it is likely to be heavily biased toward low extinction sightlines. This suggests that a larger fraction of dark GRBs might reside in the denser environments associated with the 2175 Å feature. However, the luminosity, redshift and viewing angle to the GRB also certainly affect the observed optical flux, and are factors that also need to be considered when determining the origin of dark GRBs.

Using the information on $\Delta\beta$ an attempt was made to constrain R_V . Only in two non-bump cases could R_V be constrained. In both cases, the underlying flux level of the optical power-law is well constrained which in turn constrained the R_V . The ideal way to obtain extinction curves is to fit the power-law from the X-ray to mid IR because

both wavelengths are largely unaltered by dust. To date only one afterglow observation out to mid-IR is reported in the literature: GRB 050525A (Heng et al. 2008).

The gas-to-dust ratios of GRBs are higher than in SMC environments. The gas-phase metallicity correction helps, but does not provide an explanation of these high gas-to-dust ratios. The gas-to-dust ratios derived here are likely to be affected by the gas photo-ionization and dust destruction effects from the GRB. Therefore, these ratios are not necessarily the intrinsic ratios of GRB hosts. The metals-to-dust ratios derived from the soft X-ray absorption below ~ 3 keV for the bright and dark population of GRBs are 3–30 times the Local Group values. These higher values are not due to metallicity or ionization effects but may in part be due to dust destruction which reduced the visual extinction. Furthermore I found no obvious correlation between the metals-to-dust ratios and the metallicity, the redshift or the visual extinction in GRBs.

For the SINGS sample (containing galaxies of different morphologies) and a sample of dwarf galaxies, the gas-to-dust ratio was found to be inversely proportional to the metallicity (Lisenfeld & Ferrara 1998; Draine et al. 2007). I found GRBs to have a similar anti-correlation between the two quantities. In future a larger sample with metallicity estimates will help to probe the trend better.

Schady et al. (2010) found that metals-to-dust ratios could be related to the cold, gas-phase metallicity of the GRB environment. Their anti-correlation suggests that metal poor galaxies form dust less efficiently than metal rich ones. This thesis finds that metal rich galaxies also have high metals-to-dust ratios and no obvious relation between the metals-to-dust ratios and metallicity.

The study of the QSO-pair Q 0151+048 has provided information about the geometry of the system. The system is at redshift $z \sim 2$ and includes a QSO-pair, a Ly α blob, and a DLA. The spectra of the QSO-pair were obtained with the NOT and VLT telescopes. In the spectrum of the brightest member of the QSO-pair, Q 0151+048A, a DLA is observed at higher redshift than the QSO itself due to peculiar velocity. Line-profile fitting techniques are employed to determine the metallicity. The metallicity of the DLA is found to be $-1.93 \lesssim [\text{Si}/\text{H}] < -1.39$, suggesting a metal poor system. Photo-ionization modelling based on the non-detection of the C II* $\lambda 1335.7$ Å line characterize that the distance between the DLA and Q 0151+048A is 190 kpc. No absorption at or near the redshift of the DLA is detected in the spectrum of Q 0151+048B which implies that the spatial extent of the DLA must be smaller than about 28 kpc. The systematic redshifts of both QSOs are determined to be $z_{\text{em(A)}} = 1.92924 \pm 0.00036$ and $z_{\text{em(B)}} = 1.92863 \pm 0.00042$ from the H β and H α emission lines, respectively. BH and DM halo masses are also inferred for both quasars. It is seen that qB is inside the halo of qA, but that it is likely defined as a separate sub-halo.

In summary the notable conclusions are:

- The simplest synchrotron emission model describes GRB afterglow SEDs quite well in the vast majority of cases.

- The SMC type extinction curve is not universal for GRB sightlines.
- No evidence for a SN-origin extinction curve is found in any GRB afterglow, particularly in high redshift afterglows.
- There is a possible decrease in the dust content in star forming environments above $z \gtrsim 4$.
- An anti-correlation between gas-to-dust ratio and metallicity is found for GRB environments which is consistent with the Local Group relation.

7.2 FUTURE PROSPECTS

The discovery of GRBs revealed many new enigmas and we are still trying to understand what exactly happens when a GRB goes off. This thesis sheds light on few aspects but there are many more to be explored.

Many interesting notions and ideas emerged during the dust studies in GRB afterglows. Below I will propose a few projects devoted to further studies, which could further help to explore the environments of GRBs.

7.2.1 EXTENSION OF THE SAMPLE

The GRB spectroscopic sample presented in this thesis cover observations of afterglows from April 2005 to September 2008. The GRB afterglow SED sample can be extended by using the VLT spectroscopic observations of GRB afterglows after September 2008. The spectra of 27 GRB afterglows is available where 10 are observed with VLT-FORS1/2 and 17 with VLT/X-shooter. This will help to know more about the properties of GRBs. The fitting model developed for GRB afterglow SEDs can be used to provide more information about the distant Universe and host galaxies environments.

7.2.2 X-SHOOTER

The quantity and quality of the observational data is increasing at an unprecedented rate with new facilities coming online. The wide wavelength coverage and better resolution of X-shooter will help us to study more about the GRB afterglows with 2175 Å bump. The wavelength coverage of X-shooter allows the detection of the bump even in the NIR. Moreover the observations of extinguished GRB afterglows with X-shooter into the NIR should help to constrain the R_V parameter in the future. This will also help us to understand more about the extinction curves in GRB environments. Although the observational research may seems challenging, the future looks promising.

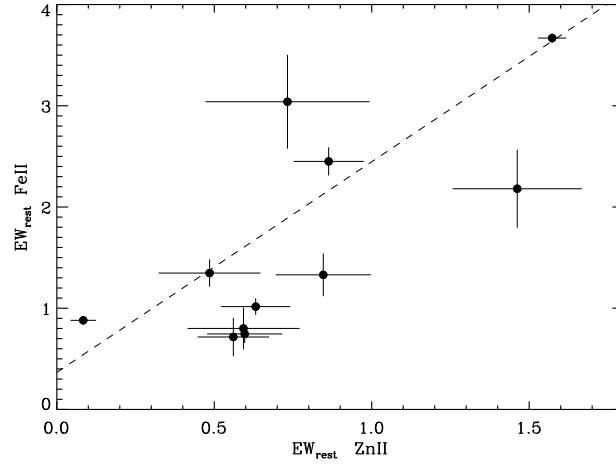


Figure 7.1: Restframe equivalent widths of Fe II 1608 Å versus Zn II 2026 Å of GRB afterglows.

7.2.3 POSSIBLE MASS-DUST RELATION

GRB-DLAs have metallicities ranging from 1/100 solar to around solar values, usually higher than galaxies probed by QSO sightlines. GRB hosts might be more metal enriched, evolved, massive and dusty as compared to QSO absorbers, or at least, the sightlines probed are. Analogous to absorption line studies of QSOs, the observations of GRBs reveal the H I column density, metallicity, chemical abundances, dust extinction, and kinematics of the gas along the sightline. GRB-DLAs and QSO-DLAs both trace the ISM in high redshift galaxies. In Fig. 7.1 the GRB-DLA equivalent widths of Fe II 1608 Å absorption line are plotted against the equivalent widths of Zn II 2026 Å, indicating that both equivalent widths are weakly correlated. The study of non-refractory elements (such as Zn) and refractory elements (like Fe) can provide information about the dust. Usually such a correlation is not expected because of the depletion of dust onto the dust grains. One would expect a turn-over while moving towards dusty environments. A tight correlation between these quantities was previously seen in QSO-DLAs (e.g., Ledoux et al. 2006). This hints that the kinematics of GRB absorbers is similar to that of QSO-DLAs and hence that the immediate environment of the GRB is not strongly dominating the kinematics and metallicity of the system. Since equivalent widths are associated with the velocity widths, hinting that GRB absorbers might also mimic the properties of QSO absorbers i.e. GRB absorbers might follow the metallicity-velocity relation like QSO absorbers. This in turn could give clues about the metallicity-mass and mass-dust relations. Fig. 7.2 also show that there is another correlation between the visual extinction and Zn II equivalent width, a possible indication of velocity dust relation. High resolution GRB spectra will allow me to determine metal abundances and H I column densities. The sample is small because of the small number of high resolution spectroscopic observations but it hints at the possibility of a relationship between

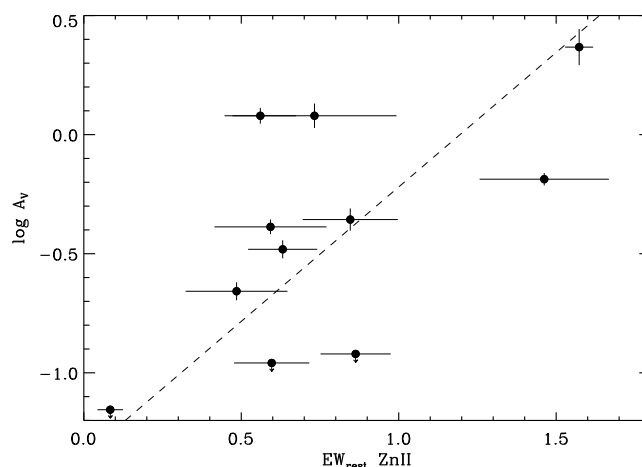


Figure 7.2: Visual extinction, A_V , of GRB afterglows against restframe equivalent widths Zn II 2026 Å.

dusty afterglows and more massive galaxies.

7.2.4 METAL RICH GRBS

Current observations of host galaxies of long GRBs suggest that they are, sub-luminous galaxies with a young stellar population. However, the statistics suffer greatly from selection affects that are biased towards those GRBs with an optical or NIR afterglow detection. Initially it was assumed that GRBs occur in low metallicity environments, but the solar-like metallicity and evidence of bumps in GRB 070802 (Elíasdóttir et al. 2009; Krühler et al. 2008) and GRB 080607 (Prochaska et al. 2009; Perley et al. 2011b) indicate that GRBs occur in diverse environments. This suggests that the SMC-type extinction in GRB environments is not as nearly-universal as previously believed. So far the 2175 Å bump feature is found in four GRB afterglow spectra, hinting that GRBs occur not only in young, low mass, less dusty and blue galaxies but also in more evolved, massive, dusty and red galaxies. The column density and chemical abundance measurements of elements present in the bump cases will help to characterize the properties of the ISM of dusty and metal rich galaxies. The column densities have been already measured for the two bump cases i.e. GRB 070802 (Elíasdóttir et al. 2009) and GRB 080607 (Prochaska et al. 2009). The rough estimates of the column densities of the other two cases (GRB 080605 and GRB 080805) indicate that these GRBs also reside in metal rich galaxies. Furthermore, and very interestingly, the strength and width of the bump is also different in these four GRB afterglows. The bump properties will also be discussed in an up-coming work.

BIBLIOGRAPHY

- Abbasi, R., Abdou, Y., Abu-Zayyad, T., et al. 2010, *ApJ*, 710, 346
- Andersen, A. C., Sotelo, J. A., Pustovit, V. N., & Niklasson, G. A. 2002, *A&A*, 386, 296
- Appenzeller, I., Fricke, K., Fürtig, W., et al. 1998, *The Messenger*, 94, 1
- Armstrong, B. H. 1967, *Journal of Quantitative Spectroscopy and Radiative Transfer*, 7, 61
- Arnaud, K. A. 1996, in *Astronomical Society of the Pacific Conference Series*, Vol. 101, *Astronomical Data Analysis Software and Systems V*, ed. G. H. Jacoby & J. Barnes, 17
- Asplund, M., Grevesse, N., & Jacques Sauval, A. 2006, *Nuclear Physics A*, 777, 1
- Asplund, M., Grevesse, N., Sauval, A. J., & Scott, P. 2009, *ARA&A*, 47, 481
- Baba, H., Yasuda, N., Ichikawa, S., et al. 2002, in *Astronomical Society of the Pacific Conference Series*, Vol. 281, *Astronomical Data Analysis Software and Systems XI*, ed. D. A. Bohlender, D. Durand, & T. H. Handley, 298
- Bahcall, J. N., Kirhakos, S., & Schneider, D. P. 1994, *ApJ*, 435, L11
- Bahcall, J. N., Kirhakos, S., & Schneider, D. P. 1995, *ApJ*, 454, L175
- Band, D., Matteson, J., Ford, L., et al. 1993, *ApJ*, 413, 281
- Bandara, K., Crampton, D., & Simard, L. 2009, *ApJ*, 704, 1135
- Beelen, A., Cox, P., Benford, D. J., et al. 2006, *ApJ*, 642, 694
- Belczynski, K., Benacquista, M., & Bulik, T. 2010, *ApJ*, 725, 816
- Bertoldi, F., Carilli, C. L., Cox, P., et al. 2003, *A&A*, 406, L55
- Beuermann, K., Hessman, F. V., Reinsch, K., et al. 1999, *A&A*, 352, L26
- Bianchi, S. & Schneider, R. 2007, *MNRAS*, 378, 973
- Blair, W. P., Ghavamian, P., Long, K. S., et al. 2007, *ApJ*, 662, 998
- Bloom, J. S., Frail, D. A., Kulkarni, S. R., et al. 1998, *ApJ*, 508, L21
- Bloom, J. S., Perley, D. A., Li, W., et al. 2009, *ApJ*, 691, 723

- Bloom, J. S., Perley, D. A., & Starr, D. L. 2007a, GRB Coordinates Network, 6953, 1
- Bloom, J. S., Starr, D., & Blake, C. H. 2007b, GRB Coordinates Network, 6054, 1
- Boella, G., Butler, R. C., Perola, G. C., et al. 1997, *A&AS*, 122, 299
- Briggs, M. S., Paciesas, W. S., Brock, M. N., et al. 1993, in *American Institute of Physics Conference Series*, Vol. 280, American Institute of Physics Conference Series, ed. M. Friedlander, N. Gehrels, & D. J. Macomb, 691–693
- Briggs, M. S., Paciesas, W. S., Pendleton, G. N., et al. 1996, *ApJ*, 459, 40
- Burbidge, E. M. 1968, *ApJ*, 154, L109
- Burrows, D. N., Falcone, A., Chincarini, G., et al. 2007, *Royal Society of London Philosophical Transactions Series A*, 365, 1213
- Butler, N. R. 2007, *ApJ*, 656, 1001
- Butler, N. R. & Kocevski, D. 2007, *ApJ*, 663, 407
- Butler, N. R., Li, W., Perley, D., et al. 2006, *ApJ*, 652, 1390
- Calzetti, D., Kinney, A. L., & Storchi-Bergmann, T. 1994, *ApJ*, 429, 582
- Campana, S., Lazzati, D., Ripamonti, E., et al. 2007, *ApJ*, 654, L17
- Campana, S., Mangano, V., Blustin, A. J., et al. 2006, *Nature*, 442, 1008
- Campana, S., Salvaterra, R., Tagliaferri, G., Kouveliotou, C., & Grindlay, J. 2010a, *MNRAS*, 1491
- Campana, S., Salvaterra, R., Tagliaferri, G., Kouveliotou, C., & Grindlay, J. 2011, *MNRAS*, 410, 1611
- Campana, S., Thöne, C. C., de Ugarte Postigo, A., et al. 2010b, *MNRAS*, 402, 2429
- Cardelli, J. A., Clayton, G. C., & Mathis, J. S. 1989, *ApJ*, 345, 245
- Carilli, C. L., Bertoldi, F., Omont, A., et al. 2001, *AJ*, 122, 1679
- Castro Cerón, J. M., Michałowski, M. J., Hjorth, J., et al. 2010, *ApJ*, 721, 1919
- Cecchi-Pestellini, C., Cacciola, A., Iatì, M. A., et al. 2010, *MNRAS*, 408, 535
- Cecchi-Pestellini, C., Mallocci, G., Mulas, G., Joblin, C., & Williams, D. A. 2008, *A&A*, 486, L25
- Cenko, S. B. 2006a, GRB Coordinates Network, 5125, 1
- Cenko, S. B. 2006b, GRB Coordinates Network, 5531, 1
- Cenko, S. B. & Baumgartner, W. H. 2006, GRB Coordinates Network, 5156, 1
- Cenko, S. B., Berger, E., Djorgovski, S. G., Mahabal, A. A., & Fox, D. B. 2006a, GRB Coordinates Network, 5155, 1

- Cenko, S. B., Fox, D. B., Penprase, B. E., et al. 2008, *ApJ*, 677, 441
- Cenko, S. B., Kelemen, J., Harrison, F. A., et al. 2009, *ApJ*, 693, 1484
- Cenko, S. B., Ofek, E. O., & Fox, D. B. 2006b, *GRB Coordinates Network*, 5529, 1
- Chen, H., Perley, D. A., Wilson, C. D., et al. 2010, *ApJ*, 723, L218
- Chen, H., Prochaska, J. X., Bloom, J. S., & Thompson, I. B. 2005, *ApJ*, 634, L25
- Chen, H., Prochaska, J. X., Herbert-Fort, S., Christlein, D., & Cortes, S. 2007, *GRB Coordinates Network*, 6217, 1
- Cherchneff, I. & Dwek, E. 2009, *ApJ*, 703, 642
- Christensen, L., Hjorth, J., & Gorosabel, J. 2004, *A&A*, 425, 913
- Clayton, G. C., Gordon, K. D., Salama, F., et al. 2003, *ApJ*, 592, 947
- Clayton, G. C., Gordon, K. D., & Wolff, M. J. 2000, *ApJS*, 129, 147
- Cobb, B. E. 2006, *GRB Coordinates Network*, 5323, 1
- Cobb, B. E. 2009, *GRB Coordinates Network, Circular Service*, 10113, 1 (2009), 113, 1
- Cooke, R., Pettini, M., Steidel, C. C., et al. 2010, *MNRAS*, 409, 679
- Costa, E., Frontera, F., Heise, J., et al. 1997, *Nature*, 387, 783
- Courty, S., Björnsson, G., & Gudmundsson, E. H. 2004, *MNRAS*, 354, 581
- Cummings, J., Angelini, L., Barthelmy, S., et al. 2005, *GRB Coordinates Network*, 3910, 1
- Cusumano, G., Mangano, V., Chincarini, G., et al. 2006, *Nature*, 440, 164
- Dai, X. & Kochanek, C. S. 2009, *ApJ*, 692, 677
- Dayal, P., Ferrara, A., & Saro, A. 2010, *MNRAS*, 402, 1449
- De Cia, A., Jakobsson, P., Björnsson, G., et al. 2010, in press *MNRAS*, arXiv:1011.42390
- de Pasquale, M. & Cummings, J. 2006, *GRB Coordinates Network*, 5130, 1
- de Ugarte Postigo, A., Fatkhullin, T. A., Jóhannesson, G., et al. 2007, *A&A*, 462, L57
- Dekel, A. & Birnboim, Y. 2006, *MNRAS*, 368, 2
- D’Elia, V., Fiore, F., Goldoni, P., et al. 2010, *MNRAS*, 401, 385
- D’Elia, V., Fiore, F., Meurs, E. J. A., et al. 2007, *A&A*, 467, 629
- Della Valle, M., Chincarini, G., Panagia, N., et al. 2006, *Nature*, 444, 1050
- Della Valle, M., Malesani, D., Benetti, S., et al. 2003, *A&A*, 406, L33

- Dey, A., Bian, C., Soifer, B. T., et al. 2005, *ApJ*, 629, 654
- Dezalay, J., Barat, C., Talon, R., et al. 1992, in *American Institute of Physics Conference Series*, Vol. 265, *American Institute of Physics Conference Series*, ed. W. S. Paciesas & G. J. Fishman, 304–309
- Dickey, J. M. & Lockman, F. J. 1990, *ARA&A*, 28, 215
- Dijkstra, M., Haiman, Z., & Spaans, M. 2006a, *ApJ*, 649, 14
- Dijkstra, M., Haiman, Z., & Spaans, M. 2006b, *ApJ*, 649, 37
- Diplas, A. & Savage, B. D. 1994, *ApJ*, 427, 274
- Djorgovski, S. G., Frail, D. A., Kulkarni, S. R., et al. 2001, *ApJ*, 562, 654
- D’Odorico, S., Dekker, H., Mazzoleni, R., et al. 2006, in *Presented at the Society of Photo-Optical Instrumentation Engineers (SPIE) Conference*, Vol. 6269, *SPIE Conference Series*
- Douglas, L. S., Bremer, M. N., Lehnert, M. D., Stanway, E. R., & Milvang-Jensen, B. 2010, *MNRAS*, 1588
- Draine, B. 1989, in *IAU Symposium*, Vol. 135, *Interstellar Dust*, ed. L. J. Allamandola & A. G. G. M. Tielens, 313
- Draine, B. T. 2003, *ARA&A*, 41, 241
- Draine, B. T. 2009, in *Astronomical Society of the Pacific Conference Series*, Vol. 414, *Astronomical Society of the Pacific Conference Series*, ed. T. Henning, E. Grün, & J. Steinacker, 453
- Draine, B. T., Dale, D. A., Bendo, G., et al. 2007, *ApJ*, 663, 866
- Draine, B. T. & Lee, H. M. 1984, *ApJ*, 285, 89
- Duley, W. W. 2006, *ApJ*, 639, L59
- Duley, W. W. 2009, *ApJ*, 705, 446
- Duley, W. W. & Seahra, S. 1998, *ApJ*, 507, 874
- Dutra, C. M., Ahumada, A. V., Clariá, J. J., Bica, E., & Barbuy, B. 2003, *A&A*, 408, 287
- Dwek, E. 1998, *ApJ*, 501, 643
- Dwek, E., Galliano, F., & Jones, A. P. 2007, *ApJ*, 662, 927
- Edge, D. O., Shakeshaft, J. R., McAdam, W. B., Baldwin, J. E., & Archer, S. 1959, *MmRAS*, 68, 37
- Eichler, D., Livio, M., Piran, T., & Schramm, D. N. 1989, *Nature*, 340, 126
- Elíasdóttir, Á., Fynbo, J. P. U., Hjorth, J., et al. 2009, *ApJ*, 697, 1725
- Ellison, S. L., Ibata, R., Pettini, M., et al. 2004, *A&A*, 414, 79

- Ellison, S. L., Prochaska, J. X., Hennawi, J., et al. 2010, *MNRAS*, 814
- Ellison, S. L., Vreeswijk, P., Ledoux, C., et al. 2006, *MNRAS*, 372, L38
- Elmhamdi, A., Danziger, I. J., Chugai, N., et al. 2003, *MNRAS*, 338, 939
- Elvis, M., Marengo, M., & Karovska, M. 2002, *ApJ*, 567, L107
- Evans, P. A., Beardmore, A. P., Page, K. L., et al. 2009, *MNRAS*, 397, 1177
- Evans, P. A., Beardmore, A. P., Page, K. L., et al. 2007, *A&A*, 469, 379
- Evans, P. A., Willingale, R., Osborne, J. P., et al. 2010, *A&A*, 519, A102
- Fan, X., Hennawi, J. F., Richards, G. T., et al. 2004, *AJ*, 128, 515
- Fan, X., Strauss, M. A., Richards, G. T., et al. 2006, *AJ*, 131, 1203
- Fan, X., Strauss, M. A., Schneider, D. P., et al. 2003, *AJ*, 125, 1649
- Fardal, M. A., Katz, N., Gardner, J. P., et al. 2001, *ApJ*, 562, 605
- Ferland, G. J., Korista, K. T., Verner, D. A., et al. 1998, *PASP*, 110, 761
- Finkelstein, S. L., Rhoads, J. E., Malhotra, S., & Grogan, N. 2009, *ApJ*, 691, 465
- Fishman, G. J. & Meegan, C. A. 1995, *ARA&A*, 33, 415
- Fishman, G. J., Meegan, C. A., Wilson, R. B., et al. 1989, in *Bulletin of the American Astronomical Society*, Vol. 21, *Bulletin of the American Astronomical Society*, 860
- Fitzpatrick, E. L. 1985, *ApJ*, 299, 219
- Fitzpatrick, E. L. 2004, in *Astronomical Society of the Pacific Conference Series*, Vol. 309, *Astrophysics of Dust*, ed. A. N. Witt, G. C. Clayton, & B. T. Draine, 33
- Fitzpatrick, E. L. & Massa, D. 1986, *ApJ*, 307, 286
- Fitzpatrick, E. L. & Massa, D. 2007, *ApJ*, 663, 320
- Foley, R. J., Perley, D. A., Pooley, D., et al. 2006, *ApJ*, 645, 450
- Fontana, A. & Ballester, P. 1995, *The Messenger*, 80, 37
- Fox, A. J., Ledoux, C., Petitjean, P., & Srianand, R. 2007a, *A&A*, 473, 791
- Fox, A. J., Ledoux, C., Vreeswijk, P. M., Smette, A., & Jaunsen, A. O. 2008, *A&A*, 491, 189
- Fox, A. J., Petitjean, P., Ledoux, C., & Srianand, R. 2007b, *A&A*, 465, 171
- Fox, D. B., Frail, D. A., Price, P. A., et al. 2005, *Nature*, 437, 845
- Fox, D. W., Yost, S., Kulkarni, S. R., et al. 2003, *Nature*, 422, 284
- Franceschini, A., Rodighiero, G., & Vaccari, M. 2008, *A&A*, 487, 837

- Francis, P. J., Williger, G. M., Collins, N. R., et al. 2001, *ApJ*, 554, 1001
- Freedman, W. L., Madore, B. F., Gibson, B. K., et al. 2001, *ApJ*, 553, 47
- Fruchter, A., Krolik, J. H., & Rhoads, J. E. 2001, *ApJ*, 563, 597
- Fugazza, D., D'Avanzo, P., Malesani, D., et al. 2006, *GRB Coordinates Network*, 5513, 1
- Fukugita, M., Ichikawa, T., Gunn, J. E., et al. 1996, *AJ*, 111, 1748
- Fynbo, J. P. U., Jakobsson, P., Prochaska, J. X., et al. 2009, *ApJS*, 185, 526
- Fynbo, J. P. U., Laursen, P., Ledoux, C., et al. 2010, *MNRAS*, 408, 2128
- Fynbo, J. P. U., Ledoux, C., Möller, P., Thomsen, B., & Burud, I. 2003, *A&A*, 407, 147
- Fynbo, J. P. U., Malesani, D., Hjorth, J., Sollerman, J., & Thoene, C. C. 2008a, *GRB Coordinates Network*, 8254, 1
- Fynbo, J. P. U., Malesani, D., & Milvang-Jensen, B. 2008b, *GRB Coordinates Network*, 7949, 1
- Fynbo, J. P. U., Malesani, D., Thoene, C. C., et al. 2006a, *GRB Coordinates Network*, 5809, 1
- Fynbo, J. P. U., Prochaska, J. X., Sommer-Larsen, J., Dessauges-Zavadsky, M., & Møller, P. 2008c, *ApJ*, 683, 321
- Fynbo, J. P. U., Prochaska, J. X., Sommer-Larsen, J., Dessauges-Zavadsky, M., & Møller, P. 2008d, *ApJ*, 683, 321
- Fynbo, J. P. U., Starling, R. L. C., Ledoux, C., et al. 2006b, *A&A*, 451, L47
- Fynbo, J. P. U., Starling, R. L. C., Ledoux, C., et al. 2006c, *A&A*, 451, L47
- Fynbo, J. P. U., Thoene, C. C., Malesani, D., et al. 2007, *GRB Coordinates Network*, 6759, 1
- Fynbo, J. P. U., Watson, D., Thöne, C. C., et al. 2006d, *Nature*, 444, 1047
- Fynbo, J. U., Burud, I., & Møller, P. 2000, *A&A*, 358, 88
- Fynbo, J. U., Gorosabel, J., Dall, T. H., et al. 2001a, *A&A*, 373, 796
- Fynbo, J. U., Jensen, B. L., Gorosabel, J., et al. 2001b, *A&A*, 369, 373
- Fynbo, J. U., Møller, P., & Warren, S. J. 1999, *MNRAS*, 305, 849
- Gal-Yam, A., Fox, D. B., Price, P. A., et al. 2006, *Nature*, 444, 1053
- Galama, T. J., Reichart, D., Brown, T. M., et al. 2003, *ApJ*, 587, 135
- Galama, T. J., Vreeswijk, P. M., van Paradijs, J., et al. 1998a, *Nature*, 395, 670
- Galama, T. J. & Wijers, R. A. M. J. 2001, *ApJ*, 549, L209
- Galama, T. J., Wijers, R. A. M. J., Bremer, M., et al. 1998b, *ApJ*, 500, L97

- Gall, C., Andersen, A. C., & Hjorth, J. 2010, *A&A* accepted, arXiv:1011.3157
- Gall, C., Andersen, A. C., & Hjorth, J. 2011, *aap* accepted, arxiv:1101.1553
- Gallerani, S., Maiolino, R., Juarez, Y., et al. 2010, *A&A*, 523, A85
- Gallerani, S., Salvaterra, R., Ferrara, A., & Choudhury, T. R. 2008, *MNRAS*, 388, L84
- Gaskell, C. M. 1982, *ApJ*, 263, 79
- Geach, J. E., Alexander, D. M., Lehmer, B. D., et al. 2009, *ApJ*, 700, 1
- Gehrels, N., Chincarini, G., Giommi, P., et al. 2004, *ApJ*, 611, 1005
- Gehrels, N., Norris, J. P., Barthelmy, S. D., et al. 2006, *Nature*, 444, 1044
- Gehrz, R. 1989, in *IAU Symposium*, Vol. 135, *Interstellar Dust*, ed. L. J. Allamandola & A. G. G. M. Tielens, 445
- Gendre, B., Corsi, A., & Piro, L. 2006, *A&A*, 455, 803
- Goldoni, P., Royer, F., François, P., et al. 2006, in *Presented at the Society of Photo-Optical Instrumentation Engineers (SPIE) Conference Series*, Vol. 6269
- González, V., Labbé, I., Bouwens, R. J., et al. 2010, *ApJ*, 713, 115
- Gordon, K. D., Calzetti, D., & Witt, A. N. 1997, *ApJ*, 487, 625
- Gordon, K. D., Clayton, G. C., Misselt, K. A., Landolt, A. U., & Wolff, M. J. 2003, *ApJ*, 594, 279
- Gordon, K. D., Clayton, G. C., Witt, A. N., & Misselt, K. A. 2000, *ApJ*, 533, 236
- Gorenstein, P. 1975, *ApJ*, 198, 95
- Gou, L., Fox, D. B., & Mészáros, P. 2007, *ApJ*, 668, 1083
- Gou, L. J., Mészáros, P., & Kallman, T. R. 2005, *ApJ*, 624, 889
- Grandi, S. A. 1982, *ApJ*, 255, 25
- Granot, J. & Sari, R. 2002, *ApJ*, 568, 820
- Greenstein, J. L. 1963, *Nature*, 197, 1041
- Greiner, J., Krühler, T., Fynbo, J. P. U., et al. 2009, *ApJ*, 693, 1610
- Greiner, J., Krühler, T., Klose, S., et al. 2011, *A&A*, 526, A30
- Grupe, D., Gronwall, C., Wang, X., et al. 2007, *ApJ*, 662, 443
- Güver, T. & Özel, F. 2009, *MNRAS*, 400, 2050
- Haiman, Z. & Rees, M. J. 2001, *ApJ*, 556, 87
- Haiman, Z., Spaans, M., & Quataert, E. 2000, *ApJ*, 537, L5

- Haislip, J. B., Nysewander, M. C., Reichart, D. E., et al. 2006, *Nature*, 440, 181
- Halpern, J. P., Mirabal, N., & Thorstensen, J. R. 2007, *GRB Coordinates Network*, 6097, 1
- Hearty, F., Lamb, D. Q., McMillan, R., et al. 2006, *GRB Coordinates Network*, 5126, 1
- Heng, K., Lazzati, D., Perna, R., et al. 2008, *ApJ*, 681, 1116
- Hennawi, J. F., Prochaska, J. X., Kollmeier, J., & Zheng, Z. 2009, *ApJ*, 693, L49
- Henrard, L., Lambin, P., & Lucas, A. A. 1997, *ApJ*, 487, 719
- Hirashita, H., Nozawa, T., Kozasa, T., Ishii, T. T., & Takeuchi, T. T. 2005, *MNRAS*, 357, 1077
- Hirashita, H., Nozawa, T., Takeuchi, T. T., & Kozasa, T. 2008, *MNRAS*, 384, 1725
- Hjorth, J., Møller, P., Gorosabel, J., et al. 2003a, *ApJ*, 597, 699
- Hjorth, J., Sollerman, J., Møller, P., et al. 2003b, *Nature*, 423, 847
- Hjorth, J., Watson, D., Fynbo, J. P. U., et al. 2005, *Nature*, 437, 859
- Hopkins, P. F., Strauss, M. A., Hall, P. B., et al. 2004, *AJ*, 128, 1112
- Hurkett, C. P., Vaughan, S., Osborne, J. P., et al. 2008, *ApJ*, 679, 587
- Impey, C. D., Petry, C. E., & Flint, K. P. 1999, *ApJ*, 524, 536
- Iye, M., Karoji, H., Ando, H., et al. 2004, *PASJ*, 56, 381
- Jakobsson, P., Fynbo, J. P. U., Ledoux, C., et al. 2006a, *A&A*, 460, L13
- Jakobsson, P., Fynbo, J. P. U., Malesani, D., et al. 2007a, *GRB Coordinates Network*, 7117, 1
- Jakobsson, P., Fynbo, J. P. U., Tanvir, N., & Rol, E. 2006b, *GRB Coordinates Network*, 5716, 1
- Jakobsson, P., Fynbo, J. P. U., Vreeswijk, P. M., & de Ugarte Postigo, A. 2008a, *GRB Coordinates Network*, 8077, 1
- Jakobsson, P., Fynbo, J. P. U., Vreeswijk, P. M., Malesani, D., & Sollerman, J. 2007b, *GRB Coordinates Network*, 7076, 1
- Jakobsson, P., Hjorth, J., Fynbo, J. P. U., et al. 2004a, *ApJ*, 617, L21
- Jakobsson, P., Hjorth, J., Fynbo, J. P. U., et al. 2004b, *A&A*, 427, 785
- Jakobsson, P., Levan, A., Fynbo, J. P. U., et al. 2006c, *A&A*, 447, 897
- Jakobsson, P., Vreeswijk, P., Ellison, S., et al. 2006d, *GRB Coordinates Network*, 5319, 1
- Jakobsson, P., Vreeswijk, P. M., Hjorth, J., et al. 2007c, *GRB Coordinates Network*, 6952, 1
- Jakobsson, P., Vreeswijk, P. M., Malesani, D., et al. 2008b, *GRB Coordinates Network*, 7286, 1

- Jakobsson, P., Vreeswijk, P. M., Xu, D., & Thoene, C. C. 2008c, GRB Coordinates Network, 7832, 1
- Jaunsen, A. O., Fynbo, J. P. U., Andersen, M. I., & Vreeswijk, P. 2007a, GRB Coordinates Network, 6216, 1
- Jaunsen, A. O., Malesani, D., Fynbo, J. P. U., Sollerman, J., & Vreeswijk, P. M. 2007b, GRB Coordinates Network, 6010, 1
- Jenkins, E. B. 2004, *Origin and Evolution of the Elements*, 336
- Jensen, B. L., Fynbo, J. U., Gorosabel, J., et al. 2001, *A&A*, 370, 909
- Jiang, L., Fan, X., Brandt, W. N., et al. 2010, *Nature*, 464, 380
- Kalberla, P. M. W., Burton, W. B., Hartmann, D., et al. 2005, *A&A*, 440, 775
- Kallman, T. R., Mészáros, P., & Rees, M. J. 2003, *ApJ*, 593, 946
- Kann, D. A., Klose, S., & Zeh, A. 2006, *ApJ*, 641, 993
- Kann, D. A., Klose, S., Zhang, B., et al. 2010, *ApJ*, 720, 1513
- Kann, D. A., Klose, S., Zhang, B., et al. 2008, arxiv:0804.1959
- Kann, D. A., Masetti, N., & Klose, S. 2007, *AJ*, 133, 1187
- Kaplan, K. F., Prochaska, J. X., Herbert-Fort, S., Ellison, S. L., & Dessauges-Zavadsky, M. 2010, *PASP*, 122, 619
- Kashikawa, N., Aoki, K., Asai, R., et al. 2002, *PASJ*, 54, 819
- Kawai, N., Kosugi, G., Aoki, K., et al. 2006, *Nature*, 440, 184
- Keel, W. C., Cohen, S. H., Windhorst, R. A., & Waddington, I. 1999, *AJ*, 118, 2547
- Kelson, D. D. 2003, *PASP*, 115, 688
- Klebesadel, R. W., Strong, I. B., & Olson, R. A. 1973, *ApJ*, 182, L85
- Koornneef, J. & Code, A. D. 1981, *ApJ*, 247, 860
- Kouveliotou, C., Meegan, C. A., Fishman, G. J., et al. 1993, *ApJ*, 413, L101
- Kozasa, T., Hasegawa, H., & Nomoto, K. 1991, *A&A*, 249, 474
- Krühler, T., Greiner, J., McBreen, S., et al. 2009, *ApJ*, 697, 758
- Krühler, T., Küpcü Yoldaş, A., Greiner, J., et al. 2008, *ApJ*, 685, 376
- Krühler, T., Schady, P., Greiner, J., et al. 2010, arXiv:1011.1205
- Kulkarni, S. R., Frail, D. A., Wieringa, M. H., et al. 1998, *Nature*, 395, 663

- Kumar, P. & Narayan, R. 2003, *ApJ*, 584, 895
- Lagache, G., Puget, J., & Dole, H. 2005, *ARA&A*, 43, 727
- Lai, K., Huang, J., Fazio, G., et al. 2007, *ApJ*, 655, 704
- Lamb, D. Q. & Reichart, D. E. 2000, *ApJ*, 536, 1
- Laor, A., Bahcall, J. N., Jannuzi, B. T., Schneider, D. P., & Green, R. F. 1995, *ApJS*, 99, 1
- Le Floch, E., Duc, P., Mirabel, I. F., et al. 2003, *A&A*, 400, 499
- Ledoux, C., Bergeron, J., & Petitjean, P. 2002, *A&A*, 385, 802
- Ledoux, C., Jakobsson, P., Jaunsen, A. O., et al. 2007, *GRB Coordinates Network*, 7023, 1
- Ledoux, C., Petitjean, P., Fynbo, J. P. U., Møller, P., & Srianand, R. 2006, *A&A*, 457, 71
- Ledoux, C., Vreeswijk, P. M., Smette, A., et al. 2009, *A&A*, 506, 661
- Leibundgut, B. & Robertson, J. G. 1999, *MNRAS*, 303, 711
- Lequeux, J., Maurice, E., Prevot-Burnichon, M., Prevot, L., & Rocca-Volmerange, B. 1982, *A&A*, 113, L15
- Lindblad, B. 1935, *Nature*, 135, 133
- Lisenfeld, U. & Ferrara, A. 1998, *ApJ*, 496, 145
- MacFadyen, A. I. & Woosley, S. E. 1999, *ApJ*, 524, 262
- Maiolino, R., Schneider, R., Oliva, E., et al. 2004, *Nature*, 431, 533
- Malesani, D., Jakobsson, P., Fynbo, J. P. U., Hjorth, J., & Vreeswijk, P. M. 2007, *GRB Coordinates Network*, 6651, 1
- Malesani, D., Tagliaferri, G., Chincarini, G., et al. 2004, *ApJ*, 609, L5
- Malkan, M. A., Margon, B., & Chanan, G. A. 1984, *ApJ*, 280, 66
- Mangano, V., Holland, S. T., Malesani, D., et al. 2007, *A&A*, 470, 105
- Marchenko, S. V. 2006, in *Astronomical Society of the Pacific Conference Series*, Vol. 353, *Stellar Evolution at Low Metallicity: Mass Loss, Explosions, Cosmology*, ed. H. J. G. L. M. Lamers, N. Langer, T. Nugis, & K. Annuk, 299
- Mathis, J. S. 1994, *ApJ*, 422, 176
- Mathis, J. S., Rimpl, W., & Nordsieck, K. H. 1977, *ApJ*, 217, 425
- Matsuda, Y., Yamada, T., Hayashino, T., et al. 2004, *AJ*, 128, 569
- Matsuda, Y., Yamada, T., Hayashino, T., Yamauchi, R., & Nakamura, Y. 2006, *ApJ*, 640, L123

- McIntosh, D. H., Rix, H., Rieke, M. J., & Foltz, C. B. 1999, *ApJ*, 517, L73
- Meegan, C., Fishman, G., Wilson, R., et al. 1993, in *American Institute of Physics Conference Series*, Vol. 280, *American Institute of Physics Conference Series*, ed. M. Friedlander, N. Gehrels, & D. J. Macomb, 681–685
- Meikle, W. P. S., Mattila, S., Gerardy, C. L., et al. 2006, *ApJ*, 649, 332
- Mészáros, P. 2002, *ARA&A*, 40, 137
- Mészáros, P. & Rees, M. J. 1992, *ApJ*, 397, 570
- Meszáros, P. & Rees, M. J. 1997, *ApJ*, 476, 232
- Metzger, M. R. 1997, in *Bulletin of the American Astronomical Society*, Vol. 29, *Bulletin of the American Astronomical Society*, 1303
- Metzger, M. R., Djorgovski, S. G., Kulkarni, S. R., et al. 1997, *Nature*, 387, 878
- Meurer, G. R., Heckman, T. M., & Calzetti, D. 1999, *ApJ*, 521, 64
- Meylan, G., Djorgovski, S., Weir, N., & Shaver, P. 1990, *The Messenger*, 59, 47
- Michałowski, M. J., Murphy, E. J., Hjorth, J., et al. 2010a, *A&A*, 522, A15
- Michałowski, M. J., Watson, D., & Hjorth, J. 2010b, *ApJ*, 712, 942
- Miley, G. & De Breuck, C. 2008, *A&A Rev.*, 15, 67
- Miller, J. S. & Sheinis, A. I. 2003, *ApJ*, 588, L9
- Milne, P. A. 2006, *GRB Coordinates Network*, 5127, 1
- Minezaki, T., Price, P. A., Yoshii, Y., & Cowie, L. L. 2007, *GRB Coordinates Network*, 7135, 1
- Misselt, K. A., Clayton, G. C., & Gordon, K. D. 1999, *ApJ*, 515, 128
- Modigliani, A., Goldoni, P., Royer, F., et al. 2010, in *Society of Photo-Optical Instrumentation Engineers (SPIE) Conference Series*, Vol. 7737
- Møller, P. 2000, *The Messenger*, 99, 31
- Møller, P., Fynbo, J. P. U., & Fall, S. M. 2004, *A&A*, 422, L33
- Møller, P. & Warren, S. J. 1993, *A&A*, 270, 43
- Møller, P., Warren, S. J., Fall, S. M., Fynbo, J. U., & Jakobsen, P. 2002, *ApJ*, 574, 51
- Møller, P., Warren, S. J., Fall, S. M., Jakobsen, P., & Fynbo, J. U. 2000, *The Messenger*, 99, 33
- Møller, P., Warren, S. J., & Fynbo, J. U. 1998, *A&A*, 330, 19
- Morgan, H. L. & Edmunds, M. G. 2003, *MNRAS*, 343, 427

- Mori, M., Umemura, M., & Ferrara, A. 2004, *ApJ*, 613, L97
- Morrison, R. & McCammon, D. 1983, *ApJ*, 270, 119
- Morton, D. C. 1991, *ApJS*, 77, 119
- Morton, D. C. 2003, *ApJS*, 149, 205
- Mundell, C. G., Melandri, A., Guidorzi, C., et al. 2007, *ApJ*, 660, 489
- Mundell, C. G., Steele, I. A., & Cummings, J. R. 2006, *GRB Coordinates Network*, 5118, 1
- Nagamine, K., Springel, V., Hernquist, L., & Machacek, M. 2004, *MNRAS*, 355, 638
- Nandy, K., Morgan, D. H., Willis, A. J., Wilson, R., & Gondhalekar, P. M. 1981, *MNRAS*, 196, 955
- Narayan, R., Paczynski, B., & Piran, T. 1992, *ApJ*, 395, L83
- Nardini, M., Ghisellini, G., & Ghirlanda, G. 2008, *MNRAS*, 386, L87
- Navarro, J. F., Frenk, C. S., & White, S. D. M. 1997, *ApJ*, 490, 493
- Neufeld, D. A. 1990, *ApJ*, 350, 216
- Nilsson, K. K., Fynbo, J. P. U., Møller, P., Sommer-Larsen, J., & Ledoux, C. 2006, *A&A*, 452, L23
- Noterdaeme, P., Petitjean, P., Ledoux, C., & Srianand, R. 2009, *A&A*, 505, 1087
- Nozawa, T., Kozasa, T., Umeda, H., Maeda, K., & Nomoto, K. 2003, *ApJ*, 598, 785
- Oates, S. R., Page, M. J., Schady, P., et al. 2009, *MNRAS*, 395, 490
- Ohyama, Y., Taniguchi, Y., Kawabata, K. S., et al. 2003, *ApJ*, 591, L9
- Oke, J. B., Cohen, J. G., Carr, M., et al. 1995, *PASP*, 107, 375
- Omont, A., Cox, P., Bertoldi, F., et al. 2001, *A&A*, 374, 371
- Paczynski, B. 1990, *ApJ*, 348, 485
- Paczynski, B. 1995, *PASP*, 107, 1167
- Paczynski, B. 1998, *ApJ*, 494, L45
- Palunas, P., Teplitz, H. I., Francis, P. J., Williger, G. M., & Woodgate, B. E. 2004, *ApJ*, 602, 545
- Patel, M., Warren, S. J., Mortlock, D. J., & Fynbo, J. P. U. 2010, *A&A*, 512, L3
- Pei, Y. C. 1992, *ApJ*, 395, 130
- Pei, Y. C. & Fall, S. M. 1995, *ApJ*, 454, 69
- Perley, D. A., Bloom, J. S., Butler, N. R., et al. 2008, *ApJ*, 672, 449

- Perley, D. A., Bloom, J. S., Cenko, S. B., et al. 2011a, in American Astronomical Society Meeting Abstracts, Vol. 217, American Astronomical Society Meeting Abstracts, 108.02
- Perley, D. A., Bloom, J. S., Klein, C. R., et al. 2010, *MNRAS*, 406, 2473
- Perley, D. A., Morgan, A. N., Updike, A., et al. 2011b, *AJ*, 141, 36
- Perna, R. & Lazzati, D. 2002, *ApJ*, 580, 261
- Perna, R., Lazzati, D., & Fiore, F. 2003, *ApJ*, 585, 775
- Perna, R. & Loeb, A. 1998, *ApJ*, 501, 467
- Péroux, C., McMahon, R. G., Storrie-Lombardi, L. J., & Irwin, M. J. 2003, *MNRAS*, 346, 1103
- Peterson, B. M., Ferrarese, L., Gilbert, K. M., et al. 2004, *ApJ*, 613, 682
- Petitjean, P. 1998, arXiv:9810418
- Pettini, M., Hunstead, R. W., King, D. L., & Smith, L. J. 1995, in *QSO Absorption Lines*, ed. G. Meylan, 55
- Pettini, M., Smith, L. J., Hunstead, R. W., & King, D. L. 1994, *ApJ*, 426, 79
- Pettini, M., Smith, L. J., King, D. L., & Hunstead, R. W. 1997, *ApJ*, 486, 665
- Pipino, A., Fan, X. L., Matteucci, F., et al. 2011, *A&A*, 525, A61
- Piran, T. 1992, *ApJ*, 389, L45
- Piran, T. 1999, *Phys. Rep.*, 314, 575
- Piran, T. 2004, *Reviews of Modern Physics*, 76, 1143
- Piranomonte, S., Covino, S., Malesani, D., et al. 2006a, *GRB Coordinates Network*, 5626, 1
- Piranomonte, S., D’Elia, V., Fiore, F., et al. 2006b, *GRB Coordinates Network*, 4520, 1
- Piro, L. 2000, in *Bulletin of the American Astronomical Society*, Vol. 32, *Bulletin of the American Astronomical Society*, 1231
- Poole, T. S., Breeveld, A. A., Page, M. J., et al. 2008, *MNRAS*, 383, 627
- Predehl, P. & Schmitt, J. H. M. M. 1995, *A&A*, 293, 889
- Prevot, M. L., Lequeux, J., Prevot, L., Maurice, E., & Rocca-Volmerange, B. 1984, *A&A*, 132, 389
- Price, P. A., Cowie, L. L., Minezaki, T., et al. 2006, *ApJ*, 645, 851
- Price, P. A., Harrison, F. A., Galama, T. J., et al. 2001, *ApJ*, 549, L7
- Prochaska, J. X., Bloom, J. S., Chen, H., et al. 2004, *ApJ*, 611, 200
- Prochaska, J. X., Chen, H., & Bloom, J. S. 2006, *ApJ*, 648, 95

- Prochaska, J. X., Chen, H., Dessauges-Zavadsky, M., & Bloom, J. S. 2007, *ApJ*, 666, 267
- Prochaska, J. X., Chen, H., Wolfe, A. M., Dessauges-Zavadsky, M., & Bloom, J. S. 2008a, *ApJ*, 672, 59
- Prochaska, J. X., Chen, H., Wolfe, A. M., Dessauges-Zavadsky, M., & Bloom, J. S. 2008b, *ApJ*, 672, 59
- Prochaska, J. X., Hennawi, J. F., & Herbert-Fort, S. 2008c, *ApJ*, 675, 1002
- Prochaska, J. X., Sheffer, Y., Perley, D. A., et al. 2009, *ApJ*, 691, L27
- Prochaska, J. X. & Wolfe, A. M. 2002, *ApJ*, 566, 68
- Quimby, R., McMahon, E., & Murphy, J. 2004, in American Institute of Physics Conference Series, Vol. 727, *Gamma-Ray Bursts: 30 Years of Discovery*, ed. E. Fenimore & M. Galassi, 529–532
- Racusin, J. L., Karpov, S. V., Sokolowski, M., et al. 2008, *Nature*, 455, 183
- Rauch, M. 1998, *ARA&A*, 36, 267
- Rauch, M., Sargent, W. L. W., & Barlow, T. A. 2001, *ApJ*, 554, 823
- Rees, M. J. & Meszaros, P. 1992, *MNRAS*, 258, 41P
- Richards, G. T., Vanden Berk, D. E., Reichard, T. A., et al. 2002, *AJ*, 124, 1
- Roming, P. W. A., Kennedy, T. E., Mason, K. O., et al. 2005, *Space Sci. Rev.*, 120, 95
- Rossi, A., Schulze, S., Klose, S., et al. 2010, *arXiv:1007.0383*
- Rouleau, F., Henning, T., & Stognienko, R. 1997, *A&A*, 322, 633
- Ruiz-Velasco, A. E., Swan, H., Troja, E., et al. 2007, *ApJ*, 669, 1
- Sakon, I., Onaka, T., Wada, T., et al. 2009, *ApJ*, 692, 546
- Salvaterra, R., Della Valle, M., Campana, S., et al. 2009, *Nature*, 461, 1258
- Sargent, W. L. W., Young, P. J., Boksenberg, A., & Tytler, D. 1980, *ApJS*, 42, 41
- Sari, R., Piran, T., & Narayan, R. 1998, *ApJ*, 497, L17
- Savaglio, S. & Fall, S. M. 2004, *ApJ*, 614, 293
- Savaglio, S., Glazebrook, K., & Le Borgne, D. 2009, *ApJ*, 691, 182
- Schady, P., de Pasquale, M., Page, M. J., et al. 2007a, *MNRAS*, 380, 1041
- Schady, P., Mason, K. O., Page, M. J., et al. 2007b, *MNRAS*, 377, 273
- Schady, P. & Moretti, A. 2006, *GRB Coordinates Network*, 5296, 1

- Schady, P., Page, M. J., Oates, S. R., et al. 2010, *MNRAS*, 401, 2773
- Schady, P., Savaglio, S., Krühler, T., Greiner, J., & Rau, A. 2011, *A&A*, 525, A113
- Schaerer, D. & de Barros, S. 2010, *A&A*, 515, A73
- Schlafly, E. F., Finkbeiner, D. P., Schlegel, D. J., et al. 2010, *ApJ*, 725, 1175
- Schlegel, D. J., Finkbeiner, D. P., & Davis, M. 1998, *ApJ*, 500, 525
- Schmidt, M. 1963, *Nature*, 197, 1040
- Sharapov, D., Djupvik, A., Pozanenko, A., & Cummings, J. 2006, *GRB Coordinates Network*, 5267, 1
- Sheffer, Y., Prochaska, J. X., Draine, B. T., Perley, D. A., & Bloom, J. S. 2009, *ApJ*, 701, L63
- Silva, A. I. & Viegas, S. M. 2002, *MNRAS*, 329, 135
- Skrutskie, M. F., Cutri, R. M., Stiening, R., et al. 2006, *AJ*, 131, 1163
- Smette, A., Robertson, J. G., Shaver, P. A., et al. 1995, *A&AS*, 113, 199
- Smette, A., Surdej, J., Shaver, P. A., et al. 1992, *ApJ*, 389, 39
- Smith, D. J. B. & Jarvis, M. J. 2007, *MNRAS*, 378, L49
- Smith, N., Foley, R. J., & Filippenko, A. V. 2008, *ApJ*, 680, 568
- Sofue, Y., Machida, M., & Kudoh, T. 2010, *PASJ*, 62, 1191
- Sollerman, J., Fynbo, J. P. U., Gorosabel, J., et al. 2007, *A&A*, 466, 839
- Sommer-Larsen, J. & Fynbo, J. P. U. 2008, *MNRAS*, 385, 3
- Sorrell, W. H. 1990, *MNRAS*, 243, 570
- Spergel, D. N., Verde, L., Peiris, H. V., et al. 2003, *ApJS*, 148, 175
- Stanek, K. Z., Matheson, T., Garnavich, P. M., et al. 2003, *ApJ*, 591, L17
- Starling, R., Thoene, C. C., Fynbo, J. P. U., Vreeswijk, P., & Hjorth, J. 2006a, *GRB Coordinates Network*, 5131, 1
- Starling, R. L. C., Rol, E., van der Horst, A. J., et al. 2009, *MNRAS*, 400, 90
- Starling, R. L. C., Vreeswijk, P. M., Ellison, S. L., et al. 2005, *A&A*, 442, L21
- Starling, R. L. C., Wiersema, K., Levan, A. J., et al. 2010, *arXiv:1004.2919*
- Starling, R. L. C., Wijers, R. A. M. J., Wiersema, K., et al. 2007, *ApJ*, 661, 787
- Starling, R. L. C. L. C., D'Elia, V., Piranomonte, S., et al. 2006b, *GRB Coordinates Network*, 5149
- Stecher, T. P. 1965, *ApJ*, 142, 1683

- Stecher, T. P. & Donn, B. 1965, *ApJ*, 142, 1681
- Steel, T. M. & Duley, W. W. 1987, *ApJ*, 315, 337
- Steidel, C. C., Adelberger, K. L., Shapley, A. E., et al. 2000, *ApJ*, 532, 170
- Stratta, G., Fiore, F., Antonelli, L. A., Piro, L., & De Pasquale, M. 2004, *ApJ*, 608, 846
- Stratta, G., Maiolino, R., Fiore, F., & D'Elia, V. 2007, *ApJ*, 661, L9
- Tagliaferri, G., Antonelli, L. A., Chincarini, G., et al. 2005, *A&A*, 443, L1
- Tanaka, I., Kawai, N., Tokoku, C., et al. 2006, *GRB Coordinates Network*, 5129, 1
- Taniguchi, Y., Shioya, Y., & Kakazu, Y. 2001, *ApJ*, 562, L15
- Tanvir, N. R., Chapman, R., Levan, A. J., & Priddey, R. S. 2005, *Nature*, 438, 991
- Tanvir, N. R., Fox, D. B., Levan, A. J., et al. 2009, *Nature*, 461, 1254
- Tanvir, N. R., Levan, A. J., Rol, E., et al. 2008, *MNRAS*, 388, 1743
- Tanvir, N. R., Rol, E., Levan, A. J., et al. 2010, *ApJ*, 725, 625
- Telfer, R. C., Zheng, W., Kriss, G. A., & Davidsen, A. F. 2002, *ApJ*, 565, 773
- Thöne, C. C., Fynbo, J. P. U., & Jakobsson, P. 2006a, *GRB Coordinates Network*, 5747, 1
- Thöne, C. C., Jakobsson, P., Fynbo, J. P. U., et al. 2007a, *GRB Coordinates Network*, 6499, 1
- Thöne, C. C., Jaunsen, A. O., Fynbo, J. P. U., Jakobsson, P., & Vreeswijk, P. M. 2007b, *GRB Coordinates Network*, 6379, 1
- Thöne, C. C., Levan, A., Jakobsson, P., et al. 2006b, *GRB Coordinates Network*, 5373, 1
- Tielens, A. G. G. M. 1998, *ApJ*, 499, 267
- Todini, P. & Ferrara, A. 2001, *MNRAS*, 325, 726
- Torii, K. 2006, *GRB Coordinates Network*, 5540, 1
- Totani, T., Kawai, N., Kosugi, G., et al. 2006, *PASJ*, 58, 485
- Trumpler, R. J. 1930, *PASP*, 42, 214
- Tumlinson, J., Prochaska, J. X., Chen, H., Dessauges-Zavadsky, M., & Bloom, J. S. 2007, *ApJ*, 668, 667
- Tytler, D. & Fan, X. 1992, *ApJS*, 79, 1
- Uehara, T., Uemura, M., Kawabata, K. S., et al. 2010, *A&A*, 519, A56
- Valencic, L. A., Clayton, G. C., Gordon, K. D., & Smith, T. L. 2003, *ApJ*, 598, 369
- Valiante, R., Schneider, R., Bianchi, S., & Andersen, A. C. 2009, *MNRAS*, 397, 1661

- van Dokkum, P. G. 2001, *PASP*, 113, 1420
- Vanden Berk, D. E., Richards, G. T., Bauer, A., et al. 2001, *AJ*, 122, 549
- Verhamme, A., Schaerer, D., Atek, H., & Tapken, C. 2008, *A&A*, 491, 89
- Verhamme, A., Schaerer, D., & Maselli, A. 2006, *A&A*, 460, 397
- Verma, A., Lehnert, M. D., Förster Schreiber, N. M., Bremer, M. N., & Douglas, L. 2007, *MNRAS*, 377, 1024
- Vestergaard, M. & Osmer, P. S. 2009, *ApJ*, 699, 800
- Vestergaard, M. & Peterson, B. M. 2006, *ApJ*, 641, 689
- Villar-Martín, M., Tadhunter, C., Morganti, R., & Holt, J. 2005, *MNRAS*, 359, L5
- Vreeswijk, P., Malesani, D., Fynbo, J., et al. 2008a, GRB Coordinates Network, 8301, 1
- Vreeswijk, P. M., Ellison, S. L., Ledoux, C., et al. 2004, *A&A*, 419, 927
- Vreeswijk, P. M., Fynbo, J. P. U., Malesani, D., Hjorth, J., & de Ugarte Postigo, A. 2008b, GRB Coordinates Network, 8191, 1
- Vreeswijk, P. M., Ledoux, C., Smette, A., et al. 2007, *A&A*, 468, 83
- Vreeswijk, P. M., Smette, A., Fruchter, A. S., et al. 2006, *A&A*, 447, 145
- Vrtilek, J. M. & Carleton, N. P. 1985, *ApJ*, 294, 106
- Wang, R., Carilli, C. L., Wagg, J., et al. 2008, *ApJ*, 687, 848
- Warren, S. J., Møller, P., Fall, S. M., & Jakobsen, P. 2001, *MNRAS*, 326, 759
- Watson, D., French, J., Christensen, L., et al. 2010, *ApJ*, submitted, arXiv:1010.1783
- Watson, D., Fynbo, J. P. U., Ledoux, C., et al. 2006a, *ApJ*, 652, 1011
- Watson, D., Hjorth, J., Fynbo, J. P. U., et al. 2007, *ApJ*, 660, L101
- Watson, D. & Laursen, P. 2010, arXiv:1011.1009
- Watson, D., Reeves, J. N., Hjorth, J., et al. 2006b, *ApJ*, 637, L69
- Watson, D., Reeves, J. N., Osborne, J. P., et al. 2002, *A&A*, 395, L41
- Waxman, E. & Draine, B. T. 2000, *ApJ*, 537, 796
- Weidinger, M., Møller, P., & Fynbo, J. P. U. 2004, *Nature*, 430, 999
- Weidinger, M., Møller, P., Fynbo, J. P. U., & Thomsen, B. 2005, *A&A*, 436, 825
- Weingartner, J. C. & Draine, B. T. 2001, *ApJ*, 548, 296
- Weymann, R. J., Williams, R. E., Beaver, E. A., & Miller, J. S. 1977, *ApJ*, 213, 619

- Weymann, R. J., Williams, R. E., Peterson, B. M., & Turnshek, D. A. 1979, *ApJ*, 234, 33
- Wijers, R. A. M. J., Bloom, J. S., Bagla, J. S., & Natarajan, P. 1998, *MNRAS*, 294, L13
- Wilkes, B. J. 1986, *MNRAS*, 218, 331
- Will, L. M. & Aannestad, P. A. 1999, *ApJ*, 526, 242
- Williams, R. E. & Weymann, R. J. 1976, *ApJ*, 207, L143
- Wolf, M. J. & Sheinis, A. I. 2008, *AJ*, 136, 1587
- Wolfe, A. M., Gawiser, E., & Prochaska, J. X. 2005, *ARA&A*, 43, 861
- Wolfe, A. M. & Prochaska, J. X. 1998, *ApJ*, 494, L15
- Wolfe, A. M. & Prochaska, J. X. 2000, *ApJ*, 545, 591
- Wolfire, M. G., McKee, C. F., Hollenbach, D., & Tielens, A. G. G. M. 2003, *ApJ*, 587, 278
- Wooden, D. H., Rank, D. M., Bregman, J. D., et al. 1993, *ApJS*, 88, 477
- Woosley, S. E. 1993, *ApJ*, 405, 273
- Woźniak, P. R., Vestrand, W. T., Panaitescu, A. D., et al. 2009, *ApJ*, 691, 495
- Xu, D., Starling, R. L. C., Fynbo, J. P. U., et al. 2009, *ApJ*, 696, 971
- Yoshida, M., Yanagisawa, K., & Kawai, N. 2007, *GRB Coordinates Network*, 6050, 1
- Zafar, T., Watson, D., Fynbo, J. P. U., et al. 2011, *ApJsubmitted*, arxiv:1102.1469
- Zafar, T., Watson, D. J., Malesani, D., et al. 2010, *A&A*, 515, A94
- Zel'Dovich, Y. B. & Novikov, I. D. 1964, *Soviet Physics Doklady*, 9, 246
- Zhang, B., Fan, Y. Z., Dyks, J., et al. 2006, *ApJ*, 642, 354
- Zhang, B., Zhang, B., Liang, E., et al. 2007, *ApJ*, 655, L25

CO-AUTHOR STATEMENTS



Declaration of co-authorship


Name: Tayyaba Zafar	
Civ. Reg. No. (CPR. No.): 290583 2940	E-mail: tayyaba@dark-cosmology.dk
Department: Dark Cosmology Centre, Niels Bohr Institute	
Principal supervisor: Darach Watson	E-mail: darach@dark-cosmology.dk
Title of PhD thesis: Spectroscopy of high redshift sightlines	

<p>This co-authorship declaration applies to the following paper: No evidence for dust extinction in GRB 050904 at $z \sim 6.3$</p>

The student's contribution to the paper
Reduced the X-ray and optical spectra and the critical z-band photometry at each epoch, constructed multi-epoch SED, fitted the data and obtained results, made figures and wrote the paper.

Signatures of co-authors		
Date (dd/mm/yy)	Name	Signature
08/02/2011	Darach Watson	
08/02/2011	Daniele Malesani	



PhD student:		Date:	08/02/2011 (dd/mm/yy)
	Signature		

A copy must be sent to the Department.

When completed, the form with signatures must be forwarded by e-mail, preferably in PDF format, to:

E-mail: PhD@science.ku.dk

*PhD School at the Faculty of Science,
University of Copenhagen,
Tagensvej 16, DK-2200 Copenhagen N.*



Declaration of co-authorship

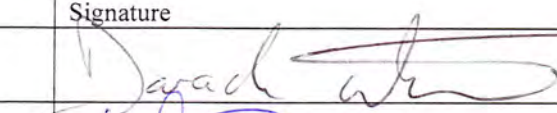
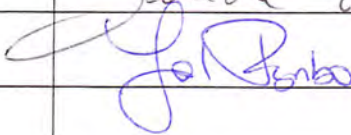
Name: Tayyaba Zafar	
Civ. Reg. No. (CPR. No.): 290583 2940	E-mail: tayyaba@dark-cosmology.dk
Department: Dark Cosmology Centre, Niels Bohr Institute	
Principal supervisor: Darach Watson	E-mail: darach@dark-cosmology.dk
Title of PhD thesis: Spectroscopy of high redshift sightlines	

This co-authorship declaration applies to the following paper:
Exploring dust extinction at the edge of reionization


The student's contribution to the paper

Reduced the X-ray spectra, constructed SEDs using NIR photometry and spectra, performed analysis, made figures and wrote the paper.

Signatures of co-authors

Date (dd/mm/yy)	Name	Signature
08/02/2011	Darach Watson	
08/02/2011	Johan P. U. Fynbo	



PhD student:		Date:	08/02/2011
	Signature		(dd/mm/yy)

A copy must be sent to the Department.

When completed, the form with signatures must be forwarded by e-mail, preferably in PDF format, to:

E-mail: PhD@science.ku.dk

*PhD School at the Faculty of Science,
University of Copenhagen,
Tagensvej 16, DK-2200 Copenhagen N.*



Declaration of co-authorship

Name: Tayyaba Zafar	
Civ. Reg. No. (CPR. No.): 290583 2940	E-mail: tayyaba@dark-cosmology.dk
Department: Dark Cosmology Centre, Niels Bohr Institute	
Principal supervisor: Darach Watson	E-mail: darach@dark-cosmology.dk
Title of PhD thesis: Spectroscopy of high redshift sightlines	


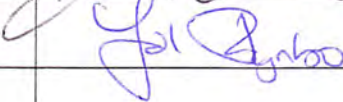
This co-authorship declaration applies to the following paper:

The extinction curves of star-forming regions from $z=0.1$ to 6.7 using GRB afterglow spectroscopy

The student's contribution to the paper

Reduced the X-ray spectra and UVOT data, collected photometry and optical spectra, constructed the fitting code, generated afterglow SEDs, fitted the data with different dust models, compared different results to understand GRB environments, made figures and wrote the paper.

Signatures of co-authors

Date (dd/mm/yy)	Name	Signature
08/02/2011	Darach Watson	
08/02/2011	Johan P. U. Fynbo	



PhD student:

Signature

Date: 08/02/2011

(dd/mm/yy)

A copy must be sent to the Department.

When completed, the form with signatures must be forwarded by e-mail, preferably in PDF format, to:

E-mail: PhD@science.ku.dk

*PhD School at the Faculty of Science,
University of Copenhagen,
Tagensvej 16, DK-2200 Copenhagen N.*



Declaration of co-authorship

Name: Tayyaba Zafar	
Civ. Reg. No. (CPR. No.): 290583 2940	E-mail: tayyaba@dark-cosmology.dk
Department: Dark Cosmology Centre, Niels Bohr Institute	
Principal supervisor: Darach Watson	E-mail: darach@dark-cosmology.dk
Title of PhD thesis: Spectroscopy of high redshift sightlines	


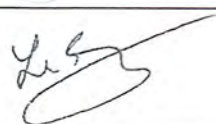
This co-authorship declaration applies to the following paper:

A Ly α blob and zabs \approx zem damped Ly α absorber in the dark matter halo of the binary quasar Q0151+048

The student's contribution to the paper

Reduced the X-shooter spectra, performed line profile fitting to the DLA, estimated redshift of the QSO-pair, made figures related to this work.

Signatures of co-authors

Date (dd/mm/yy)	Name	Signature
08/02/2011	Palle Møller	
08/02/2011	Cedric Ledoux	



PhD student: Signature		Date: 08/02/2011 (dd/mm/yy)
----------------------------------	---	---------------------------------------

A copy must be sent to the Department.

When completed, the form with signatures must be forwarded by e-mail, preferably in PDF format, to:

E-mail: PhD@science.ku.dk

*PhD School at the Faculty of Science,
University of Copenhagen,
Tagensvej 16, DK-2200 Copenhagen N.*